

SPRINGER BRIEFS IN MATERIALS

Suli Wu  
Zaifa Pan  
Runfeng Chen  
Xiaogang Liu

# Long Afterglow Phosphorescent Materials

# **SpringerBriefs in Materials**

The SpringerBriefs Series in Materials presents highly relevant, concise monographs on a wide range of topics covering fundamental advances and new applications in the field. Areas of interest include topical information on innovative, structural and functional materials and composites as well as fundamental principles, physical properties, materials theory and design. SpringerBriefs present succinct summaries of cutting-edge research and practical applications across a wide spectrum of fields. Featuring compact volumes of 50 to 125 pages, the series covers a range of content from professional to academic. Typical topics might include

- A timely report of state-of-the art analytical techniques
- A bridge between new research results, as published in journal articles, and a contextual literature review
- A snapshot of a hot or emerging topic
- An in-depth case study or clinical example
- A presentation of core concepts that students must understand in order to make independent contributions

Briefs are characterized by fast, global electronic dissemination, standard publishing contracts, standardized manuscript preparation and formatting guidelines, and expedited production schedules.

More information about this series at <http://www.springer.com/series/10111>

Suli Wu • Zaifa Pan • Runfeng Chen  
Xiaogang Liu

# Long Afterglow Phosphorescent Materials

Suli Wu  
Dalian University of Technology  
Dalian, China

Zaifa Pan  
Zhejiang University of Technology  
Hangzhou, China

Runfeng Chen  
Nanjing University of Posts  
and Telecommunication  
Nanjing, China

Xiaogang Liu  
National University of Singapore  
Singapore, Singapore

ISSN 2192-1091

ISSN 2192-1105 (electronic)

SpringerBriefs in Materials

ISBN 978-3-319-60419-0

ISBN 978-3-319-60421-3 (eBook)

DOI 10.1007/978-3-319-60421-3

Library of Congress Control Number: 2017945671

© The Author(s) 2017

This work is subject to copyright. All rights are reserved by the Publisher, whether the whole or part of the material is concerned, specifically the rights of translation, reprinting, reuse of illustrations, recitation, broadcasting, reproduction on microfilms or in any other physical way, and transmission or information storage and retrieval, electronic adaptation, computer software, or by similar or dissimilar methodology now known or hereafter developed.

The use of general descriptive names, registered names, trademarks, service marks, etc. in this publication does not imply, even in the absence of a specific statement, that such names are exempt from the relevant protective laws and regulations and therefore free for general use.

The publisher, the authors and the editors are safe to assume that the advice and information in this book are believed to be true and accurate at the date of publication. Neither the publisher nor the authors or the editors give a warranty, express or implied, with respect to the material contained herein or for any errors or omissions that may have been made. The publisher remains neutral with regard to jurisdictional claims in published maps and institutional affiliations.

Printed on acid-free paper

This Springer imprint is published by Springer Nature

The registered company is Springer International Publishing AG

The registered company address is: Gewerbestrasse 11, 6330 Cham, Switzerland

# Contents

<b>1</b>	<b>Fundamentals of Luminescent Materials</b>	<b>1</b>
1.1	Fundamentals of Luminescence	1
1.1.1	Absorption	2
1.1.2	Emission	2
1.1.3	Afterglow	6
1.2	Inorganic Afterglow Phosphors	7
1.2.1	Band Structure of Inorganic Host	7
1.2.2	Energy Levels of Isolated Ions in Solids	9
1.2.3	Luminescent Centers	12
1.2.4	Influence of Defects and Impurities	16
	References	18
<b>2</b>	<b>Inorganic Long Persistent Phosphor</b>	<b>21</b>
2.1	Introduction	21
2.2	Classification of Inorganic Long Persistent Phosphors	22
2.2.1	Lanthanide-Activated Phosphor	22
2.2.2	Transition Metal-Activated Persistent Phosphor	42
2.2.3	Summary	51
2.3	Synthetic Strategies	52
2.3.1	High-Temperature Solid-State Reaction	52
2.3.2	Sol-Gel Processing	53
2.3.3	Combustion Technique	55
2.3.4	Hydrothermal Treatment	56
2.3.5	Other Emerging Methods	58
2.3.6	Summary	60
2.4	Optical Properties	60
2.5	Commercially Available Long Persistent Phosphor	62
2.6	Factors Affecting Afterglow Properties	64
2.6.1	Emitting ion	64
2.6.2	Host	65
2.6.3	Codopant	67

2.6.4	Fluxing Agent	69
2.6.5	Preparation Condition	70
2.7	Surface Modification	70
2.7.1	Inorganic Coating	71
2.7.2	Small Molecule Modification	72
2.7.3	Polymer Modification	74
	References	77
<b>3</b>	<b>Material Characterizations</b>	<b>87</b>
3.1	Optical Properties	87
3.1.1	Excitation and Emission	87
3.1.2	Reflection and Absorption	88
3.1.3	Thermoluminescence	90
3.1.4	Luminescence Decay	93
3.2	Structural Characteristics	95
3.2.1	Size and Morphology	95
3.2.2	Crystal Structure	97
	References	99
<b>4</b>	<b>Applications of Inorganic Afterglow Phosphors</b>	<b>101</b>
4.1	Display and Lighting	102
4.1.1	Fire Safety Signs	103
4.1.2	Road Traffic Signs	104
4.1.3	Luminous Watch	104
4.1.4	Luminous Fibers	105
4.2	Biological Applications	106
4.2.1	In Vivo Imaging	106
4.2.2	Molecular Sensing	111
4.2.3	Lateral Flow Assay	113
	References	114
<b>5</b>	<b>Organic Afterglow Phosphors</b>	<b>117</b>
5.1	Principle of Organic Luminescence	118
5.1.1	Fluorescence	118
5.1.2	Phosphorescence	119
5.1.3	Thermally Activated Delayed Fluorescence (TADF)	120
5.1.4	Hybridized Local and Charge Transfer	121
5.1.5	Triplet-Triplet Annihilation and Singlet Fission	121
5.1.6	Organic Ultra-long Room-Temperature Phosphorescence (OURTP)	122
5.2	Materials for Organic Afterglow	124
5.2.1	Single-Component Small Molecules	125
5.2.2	Multicomponent Materials	128
5.2.3	Polymers	129
5.2.4	Carbon Dots	132

5.2.5	Metal-Organic Frameworks (MOFs) . . . . .	132
5.2.6	Complexes . . . . .	134
5.3	Applications of Organic Afterglow Phosphors . . . . .	134
5.3.1	Afterglow OLEDs . . . . .	135
5.3.2	Anti-counterfeiting . . . . .	136
5.3.3	Optical Recording . . . . .	139
5.3.4	Sensors . . . . .	141
5.3.5	Bioimaging . . . . .	143
5.4	Concluding Remarks . . . . .	144
	References . . . . .	148
	Index . . . . .	153



# Chapter 1

## Fundamentals of Luminescent Materials

### 1.1 Fundamentals of Luminescence

Luminescent materials have attracted tremendous research interest due to their widespread applications, ranging from lamps for home use to radars in civil defense. Inorganic luminescent materials usually feature a crystalline host and encapsulated dopants serving as light-emitting centers. Taking the commercialized white-light-emitting diodes (WLEDs) for instance [1],  $\text{Y}_3\text{Al}_5\text{O}_{12}$  is generally used as the host while a small amount of  $\text{Ce}^{3+}$  dopants serves as the luminescent centers. These luminescent materials can be utilized for frequency conversion, as evidenced in  $\text{Y}_3\text{Al}_5\text{O}_{12}:\text{Ce}^{3+}$  phosphors capable of turning blue irradiation into yellow emission.

A recent development in the luminescent materials field is the emergence of lanthanide-doped luminescent inorganic nanoparticles (NPs) as a new generation of bioprobes, relative to conventional molecular probes (i.e., organic dyes and lanthanide chelates). Particularly, significant progress has recently been achieved for up-conversion nanoparticles (UCNPs) in tumor biomarker detection and imaging, due to their superior physicochemical features such as long lifetime luminescence, large anti-Stokes shifts, narrow emission bands, high resistance to photobleaching, and low toxicity [2, 3]. Herein, up-conversion (UC) describes a nonlinear optical process, in which low-energy photons (usually NIR radiation, i.e., 980 nm) are used to generate high-energy photons (visible and UV light). Remarkably, UCNPs possess further inherent merits, i.e., NIR light penetrates deeper in tissues, and avoids the problem of autofluorescence and a light scattering background [3]. However, up-conversion luminescence relies strictly on high power coherent excitation, e.g., laser sources, and the NIR laser may create a heating effect at high input laser power.

Persistent luminescent materials or phosphors feature long-lasting emission up to several days after the removal of the excitation sources (usually UV and X-rays). Over the past 20 years, persistent phosphors have been widely used in commercial products, including luminous paints, watch dials, fire safety signs, and glow-in-the-dark toys [4]. Recently, there is a growing interest in developing persistent

nanophosphors with near-infrared (NIR) emission for optical imaging in vivo [5]. The persistent luminescence nature of these nanomaterials allows us to achieve real-time imaging without external excitation, rendering low autofluorescence and subsequently high signal-to-noise ratio (SNR). More importantly, the emission range from red to NIR is particularly suitable for bioimaging application because it falls within the well-known “optical transparency window” (700–1100 nm), thus resulting in a significant reduction in the photodamage [6].

In this chapter, the underlying mechanism of luminescence involving photon absorption and emission processes is first described. We then place our emphasis on the discussion of emission features of inorganic persistent phosphors. The influence of defects and impurities on the properties of persistent luminescence is subsequently followed.

When an optical material is irradiated under a light source, five types of optical process could occur, namely light reflection, refraction, scattering, absorption, and emission. In this section, the excitation and emission processes governing the luminescence phenomenon and the transfer of excitation energy within a given phosphor system will be introduced.

### 1.1.1 Absorption

The event of absorption occurs when the energy of incident light matches well with the energy gap of two energy states of the optical materials. During this process, the intensity of incident light will be attenuated, and a fraction of the photons with lower energy could be emitted, giving rise to the occurrence of luminescence. Concurrently, the other portion of the absorbed photons is dissipated through non-radiative processes.

For a simple system with two energy levels, the electron could be excited from the ground state ( $E_1$ ) to an excited state ( $E_2$ ) after absorbing incident photons with appropriate energy. The photon energy and the energy difference between  $E_2$  and  $E_1$  states must obey the following equation:

$$h\nu = E_2 - E_1 \quad (1.1)$$

where  $h$  is the Planck’s constant, and  $\nu$  is the frequency of the photon.

### 1.1.2 Emission

Luminescence is a photodynamic process where the excited electrons return to their ground state along with a spontaneous emission of photons. It can be considered as an inversed process of absorption, despite not being always occurring upon excitation. Luminescence is a kind of cold body radiation that differs from incandescence

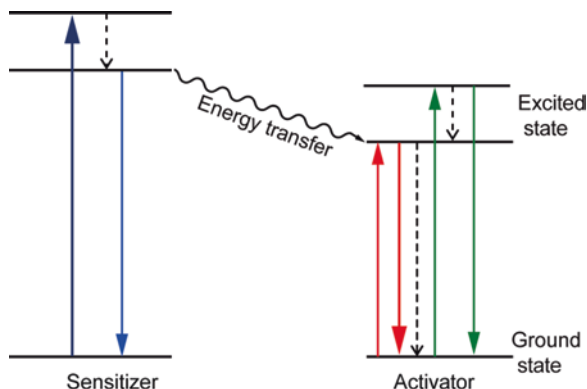
arising from a heat-mediated process. Based on the types of excitation source, luminescence can be divided into several categories such as photoluminescence upon an electromagnetic radiation (usually ultraviolet), cathodoluminescence excited by a beam of energetic electrons, and electroluminescence after stimulation of an electric voltage. It should be noted that thermoluminescence is a re-emission phenomenon, characterized by the release of accumulated energies upon heating, irrespective of the excitation source [7].

Photoluminescence is a light-emitting process from a given luminescent material after the absorption of electromagnetic radiation. Such a photodynamic process is associated with optical transitions of electrons between different electronic energy states. For example, electrons are pumped into higher electronic energy states (excited states) after photon absorption, followed by an emission of photons when the electrons return to lower energy states. Note that the optical transition probability largely depends on the selection rules of quantum mechanics such as Laporte rule. Given the existence of non-radiative decay channels, not all materials have radiative emission on excitation. Specifically, the electrons in the excited electronic states can relax back to their ground states through non-radiative channels where the excitation energy is dissipated by thermal processes instead of being converted into photons. Apparently, to enhance the luminescence efficiency of a given material, the most straightforward strategy is to effectively suppress those non-radiative processes.

### 1.1.2.1 Pure Electronic Transitions

In a given phosphor containing a single emitting center (activator), the photoluminescence efficiency is mainly determined by the distance between two neighboring activators and the absorption cross-section of the activators. Moreover, non-radiative relaxation between electronic states is another important factor that determines the efficiency of the photoluminescence process. In addition to the general factors as described above, there are specific conditions that need to be taken into account. For instance, a minimized energy difference between each excited state and its lower-lying intermediate state could largely facilitate photon absorption and energy transfer during up-conversion photoluminescence processes. However, such singly doped activator usually cannot meet all the requirements, thus leading to the development of multiply doped strategy. The typical photoluminescence processes in the framework of sensitizer–activator pairs can also be depicted schematically in terms of photon absorption, energy transfer, radiative emission, and non-radiative relaxation, as shown in Fig. 1.1. Instead of being excited directly, the activators usually receive the pumping energy transferred from the sensitizers which should have a sufficient absorption cross-section for achieving enhanced photoluminescence efficiency. As an additional benefit, multiply doped approach can also be utilized as an effective tool for the discovery of new types of emitting ions by taking the advantages in the optical transition resonance between the sensitizers and the activators. Förster and Dexter energy transfers are the two main mechanisms underlying the

**Fig. 1.1** Photoluminescence process in a given system containing sensitizer–activator pairs. The upward-solid, downward-solid, downward-dotted, and curved solid arrows represent photon excitation, radiative emission, non-radiative relaxation, and energy transfer processes, respectively



energy transfer process in doped systems. Note that the sensitizers may emit photons upon excitation in some particular cases.

### 1.1.2.2 Franck–Condon Principle

Vibronic transitions involving simultaneous changes in electronic energy states and vibrational energy states of a given molecule can occur when the molecule absorbs or emits photons with appropriate energies. The intensities of the vibronic transitions can be depicted by Franck–Condon principle under which the nuclear configuration of molecule seldom changes during an electronic transition. Given the large mass of the nucleus relative to the electron, it is a general consensus that the electronic transition occurs much faster than the time required for the nucleus to rearrange into a new configuration. The principle also states that the nucleus must vibrate to adopt the new electronic configuration. According to the quantum mechanical perspective of this principle, one can approximately estimate the intensity of a vibronic transition by correlating the square of the overlap integral of vibrational wavefunctions between the two states involved in the transition.

As illustrated in Fig. 1.2, the Franck–Condon principle for vibronic transitions in a molecule can be best described using Morse-like potential energy functions in both the ground and excited electronic states. This diagram shows a correlation between the energy of two electronic states of a vibronic system and the configuration coordinate  $q$ . When the system reaches a particular excited state upon irradiation, the newly formed electron configuration would result in a shift in the equilibrium position of the ground state ( $q_{01}$  as shown in Fig. 1.2). Given the extremely fast electronic transition processes, the molecule could move to a new vibrational state only when it was placed in close proximity to the nuclear and the momentum of the vibrational state is in the original electronic state. The vibronic transition is represented by a vertical arrow because nuclear coordinates are assumed as constant during the transition. Here, the probability of finding the molecule at any particular vibrational energy level is proportional to the square of the vibrational

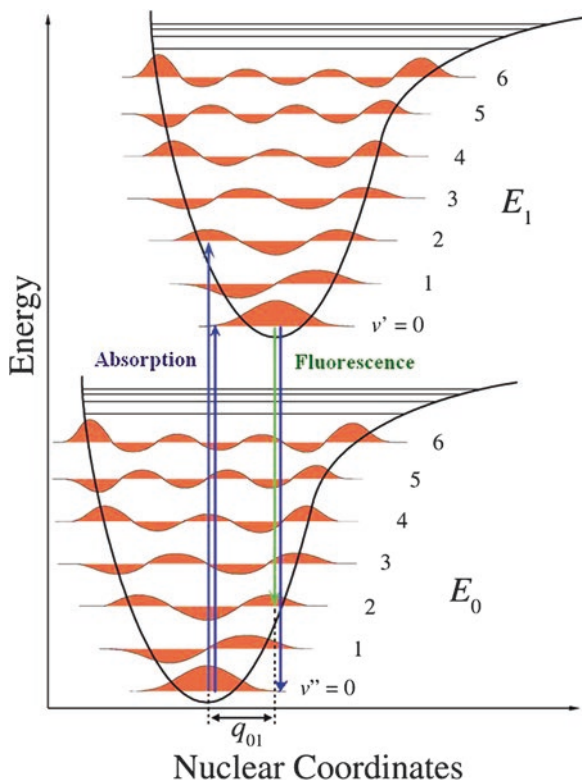


**Fig. 1.2** Franck–Condon principle energy diagram.  $E_0$  and  $E_1$  correspond to the ground-state and excited-state energy, respectively.  $v''$  and  $v'$  represent vibrational levels at the ground and excited states, respectively. The diagram indicates favored vibronic transitions between  $\nu = 0$  and  $\nu = 2$ . Adapted from [https://en.wikipedia.org/wiki/Franck%E2%80%93Condon\\_principle](https://en.wikipedia.org/wiki/Franck%E2%80%93Condon_principle)

wavefunctions overlap between the original and final states. According to Kasha's rule, molecules at the excited state can quickly relax to the lowest vibrational energy level, followed by radiative decay to the lowest electronic level via photon emission. Therefore, the emission generally occurs at a lower energy (longer wavelength) than absorption, and such an energy mismatch is recognized as Stokes shift. Note that electronic transitions to and from the lowest vibrational energy levels are often defined as 0–0 transitions (zero phonon line), featuring the same energies in absorption and emission processes.

For a doped solid phosphor consisting of luminescent centers and an inorganic crystalline host material, a strong coupling between the electrons and the phonons may occur, resulting in continuous vibronic bands. In such situation, optical transitions to higher electronic states can take place by absorbing the pure energies originating from the electronic transition or from the combination of the electronic transition and the phonon-based vibrational transition. In principle, the absorption and emission bands for a particular vibrational mode of the solid lattice are

composed of a series of discrete lines, which are similar to those observed in molecules. Each line corresponds to the generation of a specific number of phonons. However, in practice, the electronic states can couple to many different phonon modes covering a whole range of frequencies, thus giving rise to the spectra in the form of continuous bands [8].

### 1.1.3 Afterglow

Persistent luminescence, also known as long-lasting phosphorescence or afterglow, is a special optical phenomenon characterized by the ability of some materials to emit light even after the end of external light stimulation. This phenomenon could be traced back to ancient Chinese paintings [9] and it was firstly documented for Bologna Stone at the beginning of the seventeenth century [10]. Copper-doped zinc sulfide ( $\text{ZnS}:\text{Cu}^{2+}$ ) has dominated the market as the first commercially available persistent phosphor, including luminous paints and watch dials alongside with glow-in-the-dark toys [4]. Inspired by the pioneering work of Matsuzawa et al. on  $\text{SrAl}_2\text{O}_4:\text{Eu}^{2+}, \text{Dy}^{3+}$ , research interest on long afterglow phosphors has been placed on lanthanide-activated inorganic materials since the end of the twentieth century [11]. In the past few years, NIR-emitting persistent phosphors doped with transition metals have attracted much attention because these materials in the form of nanoparticles have proven effective as luminescent probes for real-time, high sensitivity optical imaging in living animals [5].

Despite the complex mechanisms, it is well known that the process of persistent luminescence involves three key steps, namely ionization, transportation, and liberation (Fig. 1.3). Ionization refers to the process where charge carriers (electrons and holes) are generated upon photon irradiation. The charge carriers can be subsequently trapped at impurity levels, which can be considered as energy reservoirs. Note that the impurity levels could trap free charge carriers either by quantum tunneling or through conduction band-mediated channels. Upon appropriate stimulations, those trapped charge carriers can be gradually released as photons responsible for the observed persistent luminescence.

It is generally accepted that electrons are the main charge carriers. To effectively trap electrons, the most efficient way is to transport the electrons to the trapping center through the conduction band of a host. In principle, the electrons can be transported to the host's conduction band through any of the following channels: (1) directly excited to the conduction band from their ground state upon irradiation, (2) pumped to the emitter's excited states above the conduction band, and (3) energy jumping from the gap states to the conduction band with the assistance of thermal fluctuation [12]. For ultra-long persistent luminescence, the electron trapping is likely due to quantum tunneling. The trapping centers could be in various forms, including codopant, cation or anion vacancy, and antisite defect.

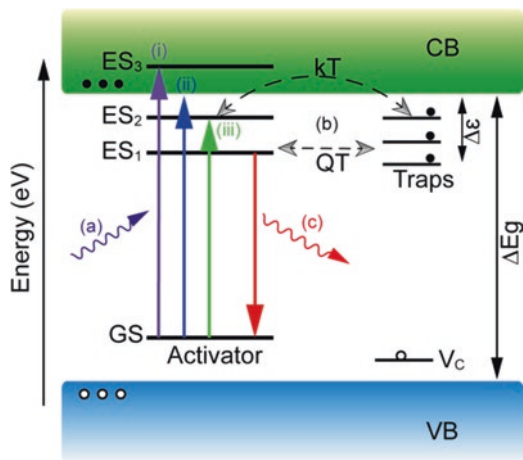


**Fig. 1.3** Schematic diagram of the process of persistent luminescence. CB and VB stand for the conduction band and the valence band of the host, respectively. GS and ES indicate the ground state and excited state of the luminescent system, respectively.  $\Delta E_g$  is the bandgap of the host material,  $\Delta \epsilon$  is the trapping depth of the impurity level,  $T$  is the temperature,  $k$  is the Boltzmann constant, and QT is the abbreviation of Quantum Tunnelling. Steps (a), (b), and (c) represent the absorption, electron trapping, and emission processes. The *upward* and *downward* arrows represent photon excitation and emission processes, respectively

## 1.2 Inorganic Afterglow Phosphors

As mentioned in Sect. 1.1.3, the influence of both host lattices and activators plays an important role in determining the persistent luminescence mechanism or regulating luminescence features. In this section, the band structure of inorganic hosts and the energy levels of typical afterglow emitters as well as the influence of defects and impurities on the persistent luminescence are presented.

### 1.2.1 Band Structure of Inorganic Host

The landscape of main energy levels in a solid is the band structure. Similar to insulators, semiconductors have few electrons that are able to gain enough thermal energy to leap across the bandgap at room temperature. The smaller bandgap of the semiconductors, however, allows for their electrical properties to be tuned by many other means in addition to temperature. When a radiation strikes a piece of semiconductor, it may excite an electron out of its valence band to the conduction band and consequently leave a hole in the valence band. This process is called electron–hole pair generation. Electron–hole pairs are also subject to recombination. The event of recombination is accompanied either by photon radiation or thermal emission in the form of phonons [8].

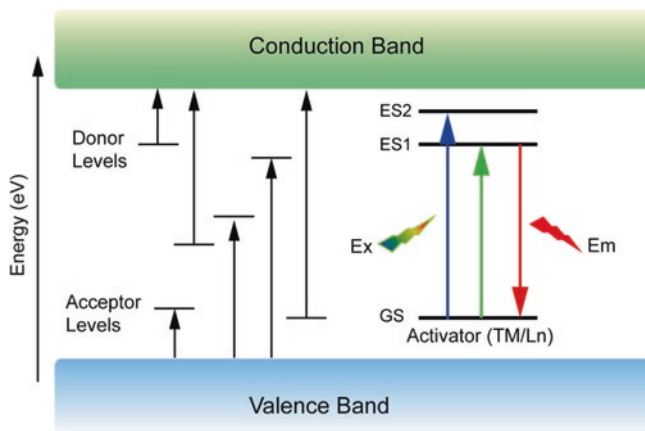


**Fig. 1.4** Proposed electronic transitions in a solid containing defects. The transitions involving transition metal (TM) ions occur within  $d$  orbitals, while the optical transitions based on lanthanide (Ln) dopants proceed within  $f$  orbitals

In practice, the band architecture is rather complex due to the existence of defects. The probability of recombination may be increased by defect-induced carrier traps. Such carrier traps are often purposely added by introducing impurities, in a process known as doping. The amount of the dopant added to an intrinsic semiconductor can modulate the electronic structure of the semiconductor. The defect levels in relation to the dopants within the bandgap could be referred to electron acceptors or donors (Fig. 1.4). A donor atom contributes its weakly bound valence electrons to the material, producing excess carriers with negative charge. The donor atom introduces energy levels under, but very close to the conduction band minimum. Conversely, an acceptor creates a hole, which results in energy states near the valence band maximum. Those energy levels close to the band edges are defined as shallow levels, while those levels located at the center of the bandgap are deep levels.

The electronic transitions may take place directly between the valence and conduction bands, without the involvement of defect levels in the generation and recombination of electron–hole pairs. In addition, the electron may transit between the host band and defect levels, depending on the nature of the levels being deep or shallow. Transitions from shallow energy levels to a nearby host band tend to emit infrared radiation, while transitions involving deep defect levels are likely to generate high-energy emission in the ultraviolet region. Furthermore, transitions can also occur within defect levels without the participation of the valence or conduction bands (Fig. 1.4). For instance, when transition metal ions or lanthanide ions are doped into oxide crystals, they can provide a new set of energy states within the wide bandgap of the oxides (Fig. 1.4). Electron transitions may occur within the  $d$ -manifolds ( $d$ - $d$  transitions) for transition metal dopants or the  $f$ -manifolds ( $f$ - $f$  transitions) for lanthanide dopants.



## 1.2.2 Energy Levels of Isolated Ions in Solids

### 1.2.2.1 Hamiltonian of the Energy State of a Multi-electron Ion

The process of emission or absorption typically occurs when the electrons confined in a solid are able to move from one energy state to another, with the energy difference determined by the units of quantum energy. Different from the energy levels of a free multi-electron ion, the energy states of the ion doped in a solid can be described by the Hamiltonian [13], which mainly consists of two parts, free ion and crystal field. The Hamiltonian of the energy state of an  $N$ -electron ion can be written as

$$H = H_A + H_{CF} \quad (1.2)$$

Here, the  $H_A$  is the free ion part and can be expressed by

$$H_A = H_O + H_C + H_{SO} + \text{other small interactions} \quad (1.3)$$

Generally, the first three terms are the primary terms of the Hamiltonian for an  $N$ -electron ion without the effect from an external field. The first term  $H_O$  represents all relevant interactions except those associated with nonspherically symmetric components of the crystal,  $H_C$  is the inter-electron Coulombic repulsion between the electrons, and  $H_{SO}$  is the spin-orbit interaction of the electrons.

The luminescent centers, either based on transition metal (TM) or lanthanide (Ln) ions, can emit light through intra-configurational  $d-d$  or  $f-f$  transitions besides inter-band  $f-d$  transitions. Considering that the TM's  $d$  electrons are very sensitive to the surrounding environment, the energy levels of such ions may vary substantially when doped in different hosts. In contrast, the behavior of the Ln's  $f$  electrons is quite independent of host materials, because of the shielding effect of the outer layer  $s$  and  $p$  orbitals. However, the coordination environment can still exert a control over the emission of Ln ions by lowering the constraint of the selection rules.

### 1.2.2.2 Term Symbols

Spin-orbit coupling describes a weak magnetic interaction between the particle spin and the motion of this particle. The spin-orbit coupling can lead to hyperfine energy levels of an atomic structure. Two kinds of approximations are proposed to facilitate calculations of this interaction, namely, LS coupling and  $jj$  coupling.

Through LS and  $jj$  coupling, term symbols can be obtained and used to represent the energy states and transitions of the atom. The term symbol has the form of  $^{2S+1}L_J$  where

- $S$  is the total spin quantum number
- $2S + 1$  is the spin multiplicity, i.e., the number of different possible states of  $S$  for a given  $(L, S)$  combination; can be singlet, doublet, or triplet

- $L$  is the total orbital quantum number in spectroscopic notation. Note that  $L$  is usually denoted by a letter  $S, P, D, F, G, H, I$ , etc., corresponding to  $L = 0, 1, 2, 3, 4, 5, 6$ , etc.
- $J$  is the total angular momentum quantum number

For a given electron configuration, by combining  $S, L$ , and  $J$ , the energy states can be described by the term symbol, which has possible microstates of  $(2J + 1)$  associated with this energy level in the corresponding spectral term.

### 1.2.2.3 Energy Levels in Solid State

The effects of the host on the energy levels of an emitter can be described by crystal field theory (CFT) and ligand field theory (LFT). CFT is a classic model typically used to estimate the electronic structure of ligand-stabilized transition metal complexes. In CFT, the metal is treated as a “free ion,” while the ligand is regarded as point charge. It is assumed that there is no overlapping in the orbitals of the metal and the ligand. Consequently, the emission of a complex, take the transition metal complex as example, depends on the involvement of energy levels according to the following factors: (1) the nature of the transition metal ion, particularly the number of d electrons; (2) the spatial arrangement of the ligands around the center metal ion; and (3) the nature of the ligands: the stronger the ligand, the greater the energy difference between the high and low energy state groups.

According to CFT, the five d suborbitals of transition metal ions may be partially filled by a maximum of two electrons in each suborbital. These d orbitals are degenerate when there are no ligands around the metal center. The ligand–metal coordination can induce an inhomogeneous redistribution of the electrons occupying d orbitals of the metal. The redistribution in d-orbital electrons can lead to the orbital splitting. The factor that determines the level of the splitting is the orientation of the ligand with respect to the metal’s d orbitals. In the case of six ligands, the metal complex most likely adopts an octahedral symmetry. As the  $d_{xy}$ ,  $d_{xz}$ , and  $d_{yz}$  orbitals are in a distance farther away from the ligand than the  $d_z^2$  and  $d_{x^2-y^2}$  orbitals, the former group of orbitals has lower energy than the latter. In a tetrahedral crystal field environment, the opposite situation occurs, in that, the low energy levels are occupied by  $d_z^2$  and  $d_{x^2-y^2}$  orbitals. The energy difference between these two groups of d orbitals is given by the symbol  $\Delta$ . The crystal field splitting energy for tetrahedral transition metal complexes (four ligands) is roughly equal to  $4/9$  octahedral  $\Delta$ . Figure 1.5 shows the splitting behavior of d orbitals and their relative  $\Delta$  values in octahedral and tetrahedral complexes.

Quantitative calculations have been made to determine the energy levels of a  $d^n$  system with weak to strong ligand fields. For example, the Tanabe–Sugano diagram can be used to calculate the energy levels of the transition metal ions, as shown in Fig. 1.6. In this diagram, the energies of d orbitals are plotted as the vertical coordinate, and the ligand field strength  $\Delta$  is plotted as the horizontal coordinate. The energy unit is generally taken as the Racah parameter  $B$ . The advantage of this

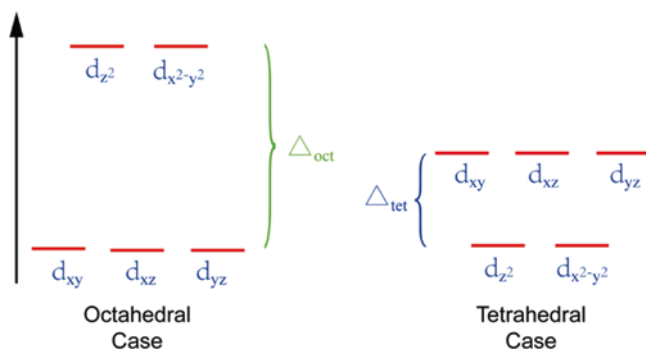
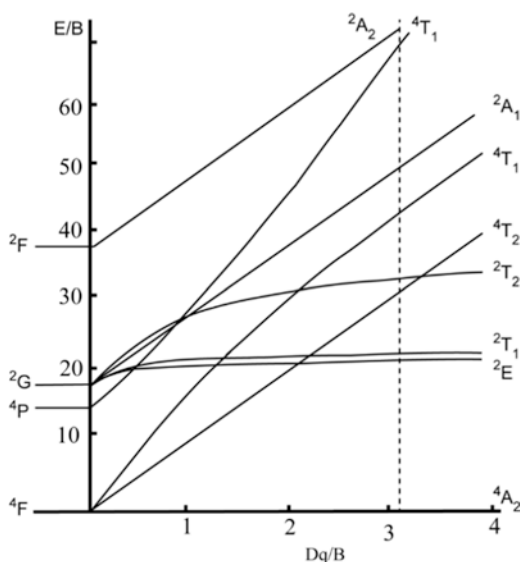


**Fig. 1.5** The splitting behavior of d orbitals and their relative  $\Delta$  value in octahedral and tetrahedral complexes

**Fig. 1.6** Tanabe–Sugano energy-level diagram of a  $3d^3$  system in an octahedral crystal field (calculated for  $C/B = 4.8$ ) [14]



treatment is that the same diagram may be used for those complexes with different  $B$  values. Two parameters  $B$  and  $C$  are required to describe the interelectronic repulsions for a given  $d$ -electron system. The ratio  $C/B$  is given for each diagram, and affects only the relative energies of the excited state having a different spin multiplicity from the ground term. Note that the Tanabe–Sugano diagram has been drawn out primarily for ligand fields with  $O_h$  symmetry. The same diagram may be used for tetrahedral ligand fields (the equivalence  $d^{10-n} = d^n$ ), provided that the  $C/B$  ratio varies with the number of d electrons. The use of this energy-splitting diagram can aid in predicting the optical properties of coordination compounds.

### 1.2.3 Luminescent Centers

#### 1.2.3.1 Trivalent Lanthanide Ions

Trivalent lanthanide ions feature a Xe core electronic configuration with the addition of  $n$   $4f$  electrons, with  $n$  varying from 0 [for La(III)] to 14 [for Lu(III)]. In general, trivalent lanthanide-doped complexes show line emission features as the  $4f^n$  subshell is shielded by the  $5s^2$  and  $5p^6$  subshells. Thus, the most important Hamiltonian to determine the energy level of  $4f$  is the atomic part ( $H_A$ ), and the position pattern of the spectral terms of each lanthanide ion is mainly determined by the spin-orbit interaction ( $H_{SO}$ ) of the electrons. As such, the luminescence properties are similar to those of the free ions. However, when the ion is introduced into a crystal lattice, the crystal field can distort the incompletely filled  $4f$  electron shell to some extent. The multiplets are split and shifted when the localized  $4f$  electrons interact with the electric field of the crystal. The number of energy levels and their energies arising from the  $J$ -term splitting are of major concern in crystal field theory.

In many cases, the influence of the crystal field on the optical properties of lanthanide ions can be regarded as a relatively small perturbation. In other words, the weak environmental effect makes the energy levels of lanthanide ions relatively similar. This enables to compare the energy levels of lanthanide ions doped in different hosts. There are many reviews reporting the luminescence properties and energy levels of lanthanide ions in different hosts [15, 16]. Dieke tabulated empirical data of energy levels for lanthanides doped in anhydrous chlorides and garnets in his monograph [15]. In a separate effort, Morrison and Leavitt presented a collection of spectroscopic data on lanthanide-doped crystals [17]. In their book, they tabulated the experimental energy levels derived from optical absorption and fluorescence spectra for 26 host crystals. The crystal parameters of the host were also provided, revealing the retaining of the crystal structure on lanthanide doping. Thus, this can be applied to predict the energy level of a certain ion in different hosts with the identical environment. Carnall et al. presented a comprehensive energy level diagram of  $\text{LaF}_3:\text{Ln}^{3+}$  by combining free-ion terms with computed crystal field energies [16]. Figure 1.7 shows such a diagram in the energy range of 0–40,000  $\text{cm}^{-1}$ . These energy levels are labeled by  $^{2S+1}L$  and  $J$ , where the dominant character of the levels can be clearly assigned by the term symbol of  $^{2S+1}L_J$ . When the energy becomes higher, the energy levels may overlap with each other and even become continuous. These relative stable energy levels cited in numerous papers can be used as a reference to predict the energy level of lanthanide ions doped in a given host lattice.

Lanthanide ions, for instance,  $\text{Eu}^{3+}$ ,  $\text{Pr}^{3+}$ , and  $\text{Sm}^{3+}$ , are frequently employed as luminescent centers in various hosts, with the commercial representative of  $\text{Y}_2\text{O}_3\text{S}:\text{Eu}^{3+}, \text{Mg}^{2+}, \text{Ti}^{4+}$  [18, 19]. On the other hand, the co-doping of  $\text{Ln}^{3+}$  is the most popular strategy to introduce charge carrier traps for afterglow luminescence [20–22]. For example,  $\text{Dy}^{3+}$  is well applied as codopant in the most famous green afterglow phosphor  $\text{SrAl}_2\text{O}_4:\text{Eu}^{2+}, \text{Dy}^{3+}$  and the blue afterglow phosphor with the chemical formulae of  $\text{Sr}_4\text{Al}_{14}\text{O}_{25}:\text{Eu}^{2+}, \text{Dy}^{3+}$  and  $\text{Sr}_2\text{MgSi}_2\text{O}_7:\text{Eu}^{2+}, \text{Dy}^{3+}$ . Furthermore,

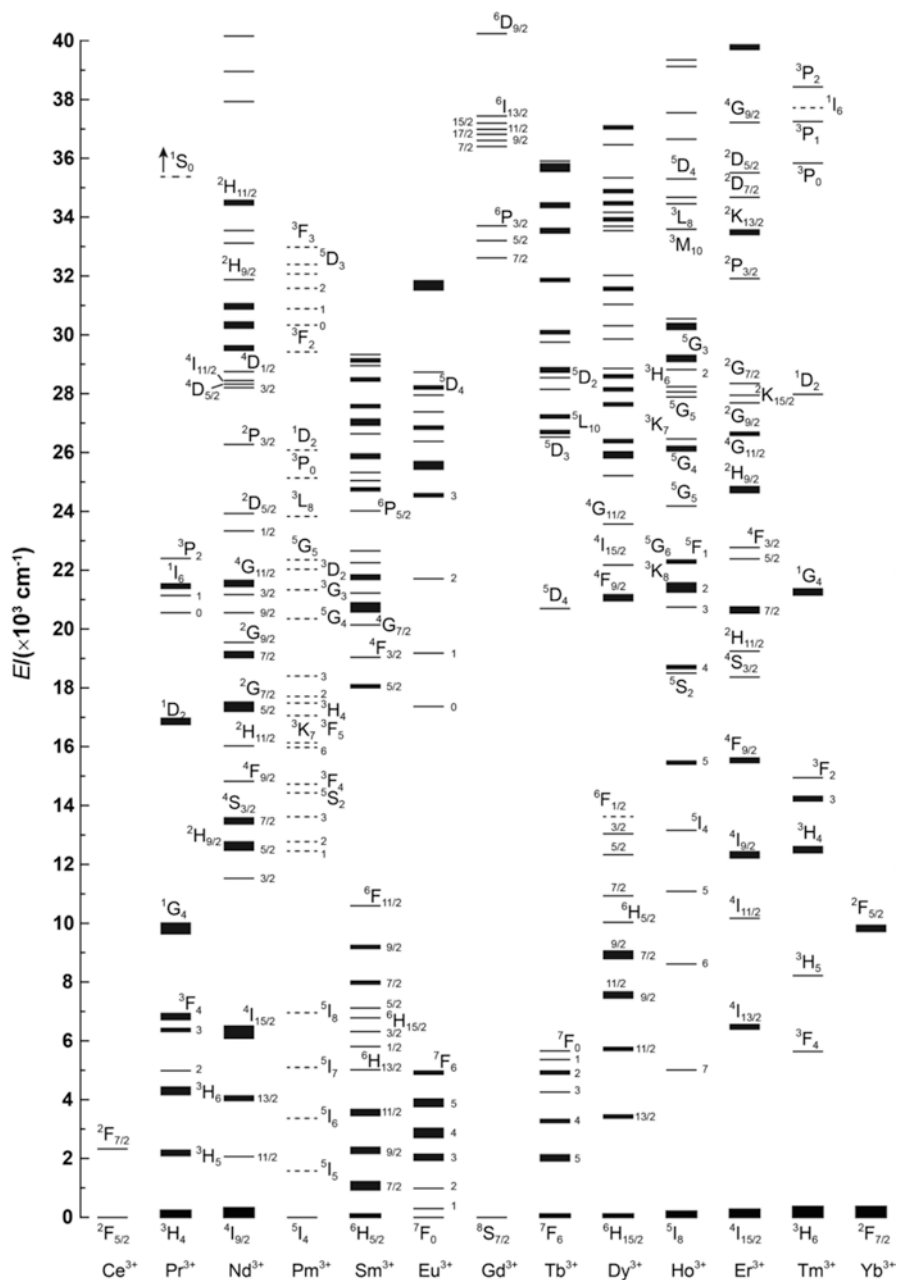
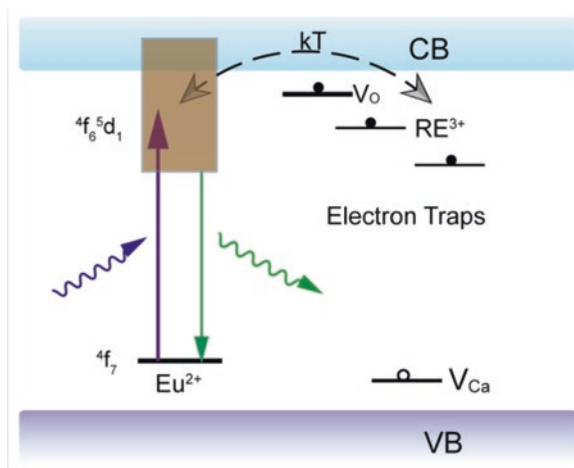


Fig. 1.7 Energy level structure of  $\text{LaF}_3:\text{Ln}^{3+}$  in the range 0–40,000  $\text{cm}^{-1}$  with labels of  $^{2S+1}L$  and/or  $J$ , where the dominant character of the levels can be clearly assigned. Reproduced from [16]

**Fig. 1.8** Schematic showing proposed mechanism for persistent luminescence occurring in  $\text{Eu}^{2+}$ -activated afterglow phosphors



the determination of the energy level of the lanthanide ions within the bandgap could be used as a powerful tool to interpret and predict the process of persistent luminescence. This has been clearly illustrated in the case of  $\text{YPO}_4:\text{Ce}^{3+}, \text{Ln}^{3+}$  phosphor in which  $\text{Ln}^{3+}$  clearly behaves as the electron trap responsible for long-lasting decay time of the phosphor [21].

### 1.2.3.2 Divalent Lanthanide Ions

The luminescence properties of divalent lanthanide ions with  $4f^{n-1}5d$  electronic configurations are strongly influenced by lattice structures, as  $5d$  orbitals are sensitive to the surrounding environment of host lattice. Therefore, the  $4f^n-4f^{n-1}5d$  electronic transitions are very different from  $4f-4f$  transitions. These kinds of transitions via absorption or emission of photons occur likely in divalent lanthanide ions, such as  $\text{Eu}^{2+}$  and  $\text{Yb}^{2+}$  [23]. Over the past decade, divalent lanthanide ions, especially  $\text{Eu}^{2+}$ , are the most studied luminescent centers in persistent luminescent materials, made evident in green-emitting  $\text{SrAl}_2\text{O}_4:\text{Eu}^{2+}, \text{Dy}^{3+}$  and blue-emitting  $\text{Sr}_4\text{Al}_{14}\text{O}_{25}:\text{Eu}^{2+}, \text{Dy}^{3+}$  (or  $\text{Sr}_2\text{MgSi}_2\text{O}_7:\text{Eu}^{2+}, \text{Dy}^{3+}$ ) afterglow phosphors.

Aluminate-based materials, with divalent  $\text{Eu}^{2+}$  ions as emitter and trivalent lanthanide ions as codopant, are the most important persistent phosphors commercially available. Let us take  $\text{SrAl}_2\text{O}_4:\text{Eu}^{2+}, \text{Dy}^{3+}$  [11] as an example, the mechanism of the divalent  $\text{Eu}^{2+}$ -doped phosphor is described as follows: Upon an external irradiation, the excited electrons of  $\text{Eu}^{2+}$  can escape from the mid-gap level to the conduction band. Both oxygen vacancy and trivalent codopant ions may act as electron traps (Fig. 1.8) [24]. The captured electrons can release back to the conduction band due to thermal fluctuation and subsequently recombine with holes resting in the luminescent center. Alternatively, the hole may also migrate as a charge carrier, which may be trapped by cation vacancies or co-doped rare earth ions.

### 1.2.3.3 Transition Metal Ions

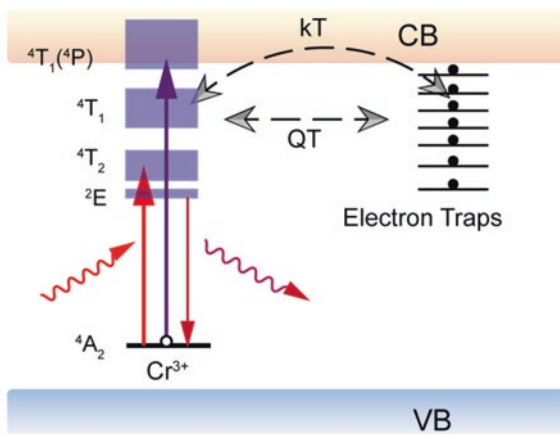
Transition metal ions have the valence electrons residing in the incomplete d shell. Unlike 4f electrons, shielded by the outer shell, d electrons suffer large perturbation from the outer crystal field, much larger than that of spin–orbital interaction. The crystal field from coordination ligands dictates emission profile in a transition metal compound as the ligands can remove the degeneracy of the orbitals and split them into different energy levels.

$\text{Cr}^{3+}$  ion is perhaps one of the most investigated ions for preparing phosphors. The outer layer electron configuration of  $\text{Cr}^{3+}$  is  $3d^3$ . According to the ligand field theory [25] and Fig. 1.6, the spectra terms of  $d^3$  in a strong crystal field will split into  ${}^4\text{A}_{2g}$ ,  ${}^2\text{E}_g$ ,  ${}^2\text{T}_{1g}$ ,  ${}^2\text{T}_{2g}$ , and so on. Energy levels and photoluminescence of  $\text{Cr}^{3+}$  have been investigated in a great number of literature. A doublet energy level  ${}^2\text{E}$  ( $\text{R1} = 687.4 \text{ nm}$  or  $14,548 \text{ cm}^{-1}$ ,  $\text{R2} = 686.5 \text{ nm}$  or  $14,567 \text{ cm}^{-1}$ ) was reported in the luminescence study of  $\text{YAG:Cr}^{3+}$  [26]. Azamatov et al. [27] investigated the spectral parameters of  $\text{Cr}^{3+}$  in single crystals of a series of rare earth garnets  $\text{Re}_3\text{Al}_{4.95}\text{Cr}_{0.05}\text{O}_{12}$  ( $\text{Re} = \text{rare earth atom}$ ). The results showed that the luminescence spectra consist of two intense lines of  ${}^2\text{E}$  ( $\text{Cr}^{3+}$ ) at the same position for all garnets at  $14,401$  and  $14,430 \text{ cm}^{-1}$  at room temperature, and at  $14,420$  and  $14,445 \text{ cm}^{-1}$  at liquid nitrogen temperature.

Whether the  ${}^2\text{E}$  or  ${}^4\text{T}_2$  energy level is the lowest excited states is determined by the strength of the crystal field. Commonly, the emission of  $\text{Cr}^{3+}$  shows characteristic sharp R-line, due to the  ${}^2\text{E} \rightarrow {}^4\text{A}_2$  transition, for instance, the line shapes of  $\text{Cr}^{3+}$  emission in garnet crystals [28]. Meanwhile, the transition of  ${}^4\text{T}_2 \rightarrow {}^4\text{A}_2$  will result in broadband emission. Rasheed et al. [29] found that the crystal field splitting  $\text{D}_q$  varies in the different octahedral sites occupied by  $\text{Cr}^{3+}$  ions. Both  ${}^2\text{E} \rightarrow {}^4\text{A}_2$  (R-line) and  ${}^4\text{T}_{2g} \rightarrow {}^4\text{A}_{2g}$  band are inhomogeneously broadened due to site-to-site disordering.

The study of  $\text{Cr}^{3+}$ -doped afterglow phosphors has recently gained momentum because the NIR persistent luminescence nanoparticles are highly desirable as emerging bioprobe for imaging application. This  $\text{Cr}^{3+}$ -doped phosphor could be activated by low-energy visible light, for instance, orange/red LED, besides the UV light. The generally accepted recombination path through the conduction for the electrons released from traps with the luminescent centers is responsible for the effective activation by ultraviolet light. Meanwhile, another trapping path, quantum tunneling process, may also be involved in the charge carrier trapping and detrapping processes, considering the fact that excitation with low-energy visible light can result in weak but long persistent luminescence. For instance, in  $\text{Zn}_3\text{Ga}_2\text{Ge}_2\text{O}_{10}:0.5\% \text{Cr}^{3+}$ , the electron trapping and detrapping processes were realized through either conduction band or quantum tunneling channels, as shown in Fig. 1.9. Herein, the trap levels were supposed to have a wide range of energies distribution and localize near the  $\text{Cr}^{3+}$  sites. Under UV radiation, the electrons in the ground state of  $\text{Cr}^{3+}$  ions are promoted to the excited energy level and then captured by traps through the conduction band. The recombination between the electrons escaped from shallow traps and the activator  $\text{Cr}^{3+}$  contribute the initial intense NIR afterglow. As for long-term afterglow, the electrons trapped in the deep levels can directly tunnel to the

**Fig. 1.9** Schematic representation of the persistent NIR luminescence mechanism for  $\text{Cr}^{3+}$ -activated afterglow phosphor



nearby  $\text{Cr}^{3+}$  ions and consequently be captured by the matched energy levels of  $\text{Cr}^{3+}$ . This tunneling process proceeds at a slow rate, resulting in the super-long-term persistent luminescence. After low-energy excitation, the deep traps are filled through the quantum tunneling process from the energy-matched  $\text{Cr}^{3+}$  levels and the reverse step gives weak but long persistent luminescence. A similar mechanism is adopted for the NIR phosphor  $\text{LiGa}_5\text{O}_8:\text{Cr}^{3+}$  [30], except that the traps are proposed to be divided into two groups with different depth. Thus, electron transfer through tunneling provides a reasonable explanation for the weak but long afterglow.

### 1.2.4 Influence of Defects and Impurities

As discussed in Sect. 1.1.3, the process of persistent luminescence occurs through a sequence of electron transitions between the energy bands of the host lattice and energy states of dopants, as well as the trapping in intrinsic defects. The emission wavelength of activator strongly depends on the energy levels of the emitter, as well as the influence of surrounding crystal field environment of the host crystal. Whereas, the afterglow intensity and decay time are depended on the traps, including trap type, depth, and density, which are generated by codopants and/or intrinsic lattice defects. These lattice defects can be of various characters, such as anion or cation vacancies, antisites, interstitial ions, and other impurities (intentional or unintentional), which can serve as electrons or holes traps in the material. These traps can be tuned by changing the material composition, impurity type, and dopant concentration [31].

The abovementioned various trap types are illustrated in Fig. 1.10. In an afterglow phosphor, vacancies of cations and anions may occur during crystal growth. The numbers of these anion and cation vacancies must be balanced to preserve electrical neutrality and maintain the composition. These defects, known as Schottky



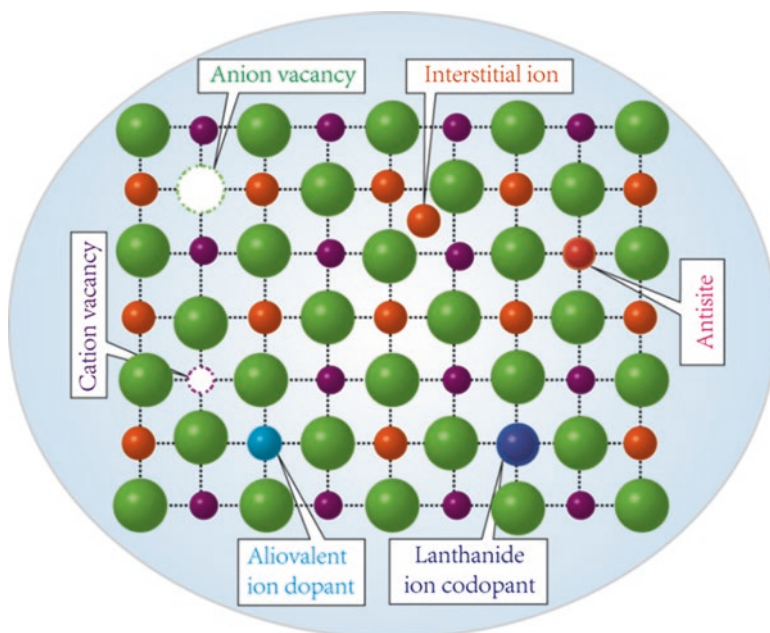


**Fig. 1.10** Schematic illustrations of various trap types. The structural arrangement with ball and stick shows the possible defects in a ternary crystal. Note that the intrinsic lattice defects, i.e., antisite defects, interstitial defects, cation vacancy, and oxygen vacancy may occur spontaneously during crystal growth

defects, are distributed at random throughout the whole crystal structure, instead of being considered to be clustered together. Take  $\text{ZnGa}_2\text{O}_4:\text{Cr}^{3+}$  as an example, vacancies  $\text{Zn}^{2+}$ ,  $\text{Ga}^{3+}$ , and  $\text{O}^{2-}$  are noted as  $V_{\text{Zn}}^{\prime\prime}$ ,  $V_{\text{Ga}}^{\prime\prime\prime}$ , and  $V_{\text{O}}^{\circ\circ}$  (Kröger–Vink notation). Meantime, an ion may move from one sublattice to a normally empty site, producing an interstitial site in the crystal, for instance, cation interstitial defect of  $\text{Zn}^{2+}$  and  $\text{Ga}^{3+}$  ( $\text{Zn}_i^{\circ\circ}$  or  $\text{Ga}_i^{\circ\circ\circ}$ ). These interstitial and vacancy defects are called Frenkel defects. An antisite defect occurs when an atom on a site normally was occupied by a different element, which exists in the materials. These defects are common for the weakly ionic or covalently bonded compounds. In  $\text{ZnGa}_2\text{O}_4:\text{Cr}^{3+}$  structure, a small number of  $\text{Zn}^{2+}$  and  $\text{Al}^{3+}$  cations exchange their sites to form antisite defects ( $\text{Ga}_{\text{Zn}}^{\circ}$  and  $\text{Zn}_{\text{Ga}}^{\prime}$ ). This exchange between octahedral and tetrahedral cations is quite common in  $\text{ZnGa}_2\text{O}_4$ . Impurity defects may be induced by substitution and/or interstitial of different elements. Point defects, such as Schottky, Frenkel, and antisite defects, exist in thermodynamic equilibrium at the temperature above 0 K, which are not possible to be removed by thermal treatments. These intrinsic defects may be produced intentionally by changing the composition of the phosphor and the preparation parameters. However, it is hard to manipulate the defect type and their distribution in a given crystal.

## References

1. Chen, L., Chen, X., Liu, F., Chen, H., Wang, H., Zhao, E., Jiang, Y., Chan, T.S., Wang, C.H., Zhang, W., Wang, Y., Chen, S.: Charge deformation and orbital hybridization: intrinsic mechanisms on tunable chromaticity of  $\text{Y}_3\text{Al}_5\text{O}_{12}:\text{Ce}^{3+}$  luminescence by doping  $\text{Gd}^{3+}$  for warm white LEDs. *Sci. Rep.* **5**, 11514 (2015)
2. Xie, X., Gao, N., Deng, R., Sun, Q., Xu, Q.H., Liu, X.: Mechanistic investigation of photon upconversion in  $\text{Nd}^{3+}$ -sensitized core-shell nanoparticles. *J. Am. Chem. Soc.* **135**, 12608–12611 (2013)
3. Wang, F., Han, Y., Lim, C.S., Lu, Y., Wang, J., Xu, J., Chen, H., Zhang, C., Hong, M., Liu, X.: Simultaneous phase and size control of upconversion nanocrystals through lanthanide doping. *Nature*. **463**, 1061–1065 (2010)
4. Van den Eeckhout, K., Smet, P.F., Poelman, D.: Persistent luminescence in  $\text{Eu}^{2+}$ -doped compounds: a review. *Materials*. **3**, 2536–2566 (2010)
5. de Chermont, Q.L.M., Chanéac, C., Seguin, J., Pellé, F., Maîtrejean, S., Jolivet, J.P., Gourier, D., Bessodes, M., Scherman, D.: Nanoprobes with near-infrared persistent luminescence for in vivo imaging. *Proc. Natl. Acad. Sci. U. S. A.* **104**, 9266–9271 (2007)
6. Chen, G., Qiu, H., Prasad, P.N., Chen, X.: Upconversion nanoparticles: design, nanochemistry, and applications in theranostics. *Chem. Rev.* **114**, 5161–5214 (2014)
7. Xie, R.J., Li, Y.Q., Hirosaki, N., Yamamoto, H.: *Nitride Phosphors and Solid-State Lighting*. CRC Press, England (2011)
8. Fox, M.: *Optical Properties of Solids*. Oxford University Press, Oxford (2002)
9. Cohen, I.B.: A history of luminescence from the earliest times until 1900—Harvey EW. *Am. Hist. Rev.* **63**, 937–939 (1958)
10. Lastusaari, M., Laamanen, T., Malkamäki, M., Eskola, K.O., Kotlov, A., Carlson, S., Welter, E., Brito, H.F., Bettinelli, M., Jungner, H., Hölsä, J.: The bologna stone: history's first persistent luminescent material. *Eur. J. Mineral.* **24**, 885–890 (2012)
11. Matsuzawa, T., Aoki, Y., Takeuchi, N., Murayama, Y.: New long phosphorescent phosphor with high brightness,  $\text{SrAl}_2\text{O}_4:\text{Eu}^{2+}, \text{Dy}^{3+}$ . *J. Electrochem. Soc.* **143**, 2670–2673 (1996)
12. Zhuang, Y., Katayama, Y., Ueda, J., Tanabe, S.: A brief review on red to near-infrared persistent luminescence in transition-metal-activated phosphors. *Opt. Mater.* **36**, 1907–1912 (2014)
13. Liu, G.K., Jacquier, B.: *Spectroscopic Properties of Rare Earths In Optical Materials*. Springer, Berlin (2005)
14. Henderson, B., Imbusch, G.F.: *Optical Spectroscopy of Inorganic Solids*. Oxford, Clarendon (1989)
15. Dieke, G.H.: Spectra and energy levels of rare earth ions in crystal. *Am J Phys.* **38**(3), 399 (1968)
16. Carnall, W.T., Goodman, G.L., Rajnak, K., Rana, R.S.: A systematic analysis of the spectra of the lanthanides doped into single crystal  $\text{LaF}_3$ . *J. Chem. Phys.* **90**, 3443–3457 (1989)
17. Morrison, C.A., Leavitt, R.P.: *Spectroscopic Properties of Triply Ionized Lanthanides in Transparent Host Crystals*. North-Holland Publishing Company, Amsterdam (1982)
18. Wang, X., Zhang, Z., Tang, Z., Lin, Y.: Characterization and properties of a red and Orange  $\text{Y}_2\text{O}_3$ -based long afterglow phosphor. *Mater. Chem. Phys.* **80**, 1–5 (2003)
19. Li, W., Liu, Y., Ai, P.: Synthesis and luminescence properties of red long-lasting phosphor  $\text{Y}_2\text{O}_3:\text{Eu}^{3+}, \text{Mg}^{2+}, \text{Ti}^{4+}$  nanoparticles. *Mater. Chem. Phys.* **119**, 52–56 (2010)
20. Lecointre, A., Bessière, A., Bos, A.J.J., Dorenbos, P., Viana, B., Jacquart, S.: Designing a red persistent luminescence phosphor: the example of  $\text{YPO}_4:\text{Pr}^{3+}, \text{Ln}^{3+}$  ( $\text{Ln} = \text{Nd}, \text{Er}, \text{Ho}, \text{Dy}$ ). *J. Phys. Chem. C*. **115**, 4217–4227 (2011)
21. Bos, A.J.J., Dorenbos, P., Bessière, A., Lecointre, A., Bedu, M., Bettinelli, M., Piccinelli, F.: Study of TL glow curves of  $\text{YPO}_4$  double doped with lanthanide ions. *Radiat. Meas.* **46**, 1410–1416 (2011)

22. Maldiney, T., Lecointre, A., Viana, B., Bessière, A., Bessodes, M., Gourier, D., Richard, C., Scherman, D.: Controlling electron trap depth to enhance optical properties of persistent luminescence nanoparticles for in vivo imaging. *J. Am. Chem. Soc.* **133**, 11810–11815 (2011)
23. Neilo, G.N., Antonyak, O.T., Prokhorov, A.D.: Electron paramagnetic resonance of the  $\text{Eu}^{2+}$  ion in  $\text{SrCl}_2$  at high pressure. *Phys. Solid state.* **43**, 652–654 (2001)
24. Aitasallo, T., Hölsä, J., Jungner, H., Lastusaari, M., Niittykoski, J.: Thermoluminescence study of persistent luminescence materials:  $\text{Eu}^{2+}$ - and  $\text{R}^{3+}$ -doped calcium aluminates,  $\text{CaAl}_2\text{O}_4:\text{Eu}^{2+},\text{R}^{3+}$ . *J. Phys. Chem. B.* **110**, 4589–4598 (2006)
25. Figgis, B.N., Hitchman, M.A.: *Ligand Field Theory and Its Applications*. Wiley-VCH Press, New York (2000)
26. Feofilov, P.P., et al.: On the luminescence of neodymium and chromium in yttrium aluminum garnet. *Opt. Spectrosc.* **19**, 451–452 (1965)
27. Azamatov, Z.T., Arsen'Ev, P.A., Chukichev, M.V.: Spectral parameters of the trivalent chromium ion in crystals of several rare earth garnets. *Sov. Phys. J.* **13**, 1507–1509 (1970)
28. Yamaga, M., Henderson, B., O'Donnell, K.P.: Line shape of the  $\text{Cr}^{3+}$  luminescence in garnet crystals. *Phys. Rev. B Condens. Matter.* **46**, 3273–3282 (1992)
29. Rasheed, F., O'Donnell, K.P., Henderson, B., Hallis, D.B.: Disorder and the optical spectroscopy of  $\text{Cr}^{3+}$ -doped glasses: I. Silicate glasses. *J. Phys. Condens. Matter.* **3**, 1915–1930 (1991)
30. Liu, F., Yan, W., Chuang, Y.J., Zhen, Z., Xie, J., Pan, Z.: Photostimulated near-infrared persistent luminescence as a new optical read-out from  $\text{Cr}^{3+}$ -doped  $\text{LiGa}_5\text{O}_8$ . *Sci. Rep.* **3**, 1554 (2013)
31. Li, Y., Li, Y., Chen, R., Sharafudeen, K., Zhou, S., Gecevicius, M., Wang, H., Dong, G., Wu, Y., Qin, X., Qiu, J.: Tailoring of the trap distribution and crystal field in  $\text{Cr}^{3+}$ -doped non-Gallate phosphors with near-infrared long-persistence phosphorescence. *Npg Asia Mater.* **7**, e180 (2015)

## Chapter 2

# Inorganic Long Persistent Phosphor

### 2.1 Introduction

Upon appropriate stimulation, inorganic long afterglow phosphors can emit light in the range of visible to near-infrared region after the removal of the excitation source. In practice, various excitation sources, including visible light, UV light, X-ray,  $\gamma$ -ray, and electron beam, could be adopted for modulation of the afterglow features of the phosphors. In general, the resulted persistent luminescence can be observable by naked eyes for a period of time ranging from several minutes to tens of hours. When it comes to the mechanism underlying the long afterglow, the consensus is that the excitation energy is partially stored in the form of trapped charge carriers. The capability of preserving energy enables various applications of persistent phosphors in the fields of decoration, instrument display, safety signage, dial displays, security ink, and night-vision surveillance, as well as biological imaging. Particularly, let us consider the newly emerged biological imaging application in an effort to illustrate the advantages of the persistent phosphors compared to traditional biomarkers. As in most tradition biomarker-based studies, the major challenging issue is elimination of tissue autofluorescence when imaging *in vivo*. Given that the persistent luminescence lasts long enough for time-gated imaging, the afterglow emission of the phosphors can be well differentiated from the autofluorescence signals, thus providing significantly enhanced signal-to-noise ratio.

The phenomenon of persistent luminescence was first discovered from ancient luminous pearls containing mineral substances during the Yan and Huang dynasty. It was not until 1602 that the constituent of the luminous pearls was scientifically proven to be barium sulfate. The impurities formed in the barium sulfate have subsequently been proven to be responsible for the observed long-lasting afterglow.

Before 1996, copper- or cobalt-doped zinc sulfide (ZnS) persistent phosphors were widely used for various applications, such as watch dials, luminous paints, and glow-in-the-dark toys [1, 2]. However, the radioactive elements or tritium found in these phosphors largely limit their applications due to the safety concerns. Inspired

by the discovery of  $\text{Eu}^{2+}$ -activated persistent phosphors in 1996, lanthanide-doped phosphors have attracted much attention because of their high luminescence intensity and long-lasting activity. More importantly, these materials are much safer than zinc sulfide-based phosphors. These phosphors with appropriate properties are highly promising for next-generation lighting devices and biomarkers. Nowadays, different types of lanthanide-activated persistent phosphors can be successfully synthesized using various approaches, and key factors for evaluating the phosphor's performance such as luminescence efficiency, emitting color, and chemical stability can be modulated by varying the composition of the materials.

## 2.2 Classification of Inorganic Long Persistent Phosphors

Long-lasting luminescence phenomena have been observed in metal ion-doped aluminates, silicates, phosphates, and oxysulfides since 1996. On the basis of the emission color, the persistent phosphors are generally divided into five groups, namely red, green, blue, white, and near-infrared (NIR) (Tables 2.1, 2.2, 2.3, and 2.4). In addition to the emission color, the commonly used classification criterion is based on the type of the dopant. There are two types of dopants existing in the widely used persistent phosphors, namely lanthanide ions and transition metal ions. In this chapter, we will thoroughly discuss the optical properties of the persistent phosphors that are categorized by the type of the dopant. Tables 2.1, 2.2, and 2.3 enumerate typically used  $\text{Eu}^{2+}$ -based singly and multiply doped persistent phosphors, respectively [3]. Moreover, the phosphors featuring blue-, green-, and red-emitting color are also summarized.

### 2.2.1 Lanthanide-Activated Phosphor

Copper- or cobalt-doped zinc sulfide phosphors have been widely used in markets for centuries. These materials feature a green broadband emission centered at 540 nm, and the resulted luminescence keeps visible for several hours after the excitation has been turned off. However, these materials have shown the following disadvantages: (1) the resulted afterglow is relatively weak, (2) the observed radioactive tritium or promethium raises safety concerns, and (3) the host materials show low resistance against moisture. All the concerns described above have been significantly alleviated since the discovery of  $\text{Eu}^{2+}$ - and  $\text{Dy}^{3+}$ -doped strontium and calcium aluminates in 1996. These lanthanide-doped persistent phosphors exhibit exquisite afterglow properties, including high luminescence intensity and prolonged emission lifetime. The lanthanide-doped persistent phosphors thus became the alternatives of the ZnS-based products to dominate the markets, ranging from display to decoration.

**Table 2.1** Blue-emitting  $\text{Eu}^{2+}$ -activated long persistent phosphors

Host material		Dopants	Maximum emission (nm)	Afterglow duration	References
Aluminate	$\text{CaAl}_2\text{O}_4$	$\text{Eu}^{2+}, \text{Nd}^{3+}$	440	16 h	[7]
	$\text{Sr}_4\text{Al}_{14}\text{O}_{25}$	$\text{Eu}^{2+}, \text{Dy}^{3+}$	490	20 h	[6]
	$\text{SrAl}_4\text{O}_7$	$\text{Eu}^{2+}, \text{Dy}^{3+}$	480	3 h	[33]
	$\text{SrAl}_{12}\text{O}_{19}$	$\text{Eu}^{2+}, \text{Dy}^{3+}$	400	3 h	[34]
	$\text{Ca}_{12}\text{Al}_{14}\text{O}_{33}$	$\text{Eu}^{2+}, \text{Nd}^{3+}$	440	10 min	[35]
	$\text{BaMgAl}_{10}\text{O}_{17}$	$\text{Eu}^{2+}, \text{Co}^{3+}$	450	5 min	[14]
Silicate	$\text{Sr}_2\text{MgSi}_2\text{O}_7$	$\text{Eu}^{2+}, \text{Dy}^{3+}$	465	20 h	[20]
	$\text{Sr}_3\text{MgSi}_2\text{O}_8$	$\text{Eu}^{2+}, \text{Dy}^{3+}$	460	10 h	[24]
	$\text{Ca}_3\text{MgSi}_2\text{O}_8$	$\text{Eu}^{2+}, \text{Dy}^{3+}$	470	5 h	
	$\text{Ba}_3\text{MgSi}_2\text{O}_8$	$\text{Eu}^{2+}, \text{Dy}^{3+}$	440	1 h	
	$\text{CaMgSi}_2\text{O}_6$	$\text{Eu}^{2+}, \text{Dy}^{3+}$	445	4 h	[17]
	$\text{Sr}_3\text{Al}_{10}\text{SiO}_{20}$	$\text{Eu}^{2+}, \text{Ho}^{3+}$	465	6 h	[36]
	$\text{CaAl}_2\text{Si}_2\text{O}_8$	$\text{Eu}^{2+}, \text{Dy}^{3+}$	440	3 h	[37]
	$\text{Sr}_2\text{Al}_2\text{SiO}_7$	$\text{Eu}^{2+}, \text{Dy}^{3+}$	484	2 h	[38]
	$\text{SrMgAl}_2\text{SiO}_7$	$\text{Eu}^{2+}$	421		
	$\text{Sr}_2\text{ZnSi}_2\text{O}_7$	$\text{Eu}^{2+}, \text{Dy}^{3+}$	460	5 min	[39]
Other	$\text{Sr}_2\text{P}_2\text{O}_7$	$\text{Eu}^{2+}, \text{Y}^{3+}$	420	8 h	[30]
	$\text{Ca}_2\text{P}_2\text{O}_7$	$\text{Eu}^{2+}, \text{Y}^{3+}$	416	6 h	[16]
	$\text{SrMg}_2\text{P}_2\text{O}_8$	$\text{Eu}^{2+}, \text{Ce}^{3+}$	400	2 h	[40]
	$\text{CaAl}_2\text{B}_2\text{O}_7$	$\text{Eu}^{2+}$	460	1 h	[41]
	$\text{SrMg}_2(\text{PO}_4)_2$	$\text{Eu}^{2+}, \text{Tb}^{3+}$	411	2 h	[28]
	$\text{BaMg}_2(\text{PO}_4)_2$	$\text{Eu}^{2+}, \text{Gd}^{3+}$	444	2 h	[28]
	$\text{SrB}_2\text{O}_4$	$\text{Eu}^{2+}$	448	Disputed	[26]

**Table 2.2** Green-emitting  $\text{Eu}^{2+}$ -activated long persistent phosphors

Matrix	Host material	Dopants	Maximum emission (nm)	Afterglow duration	References
Aluminate	$\text{SrAl}_2\text{O}_4$	$\text{Eu}^{2+}, \text{Dy}^{3+}$	520	30 h	[4]
	$\text{BaAl}_2\text{O}_4$	$\text{Eu}^{2+}, \text{Dy}^{3+}$	500	2 h	[42]
	$\text{Sr}_3\text{Al}_2\text{O}_6$	$\text{Eu}^{2+}, \text{Dy}^{3+}$	512	Several hours	[43]
	$\text{SrMgAl}_{10}\text{O}_{17}$	$\text{Eu}^{2+}, \text{Dy}^{3+}$	515	3 min	[44]
Silicate	$\text{Ca}_2\text{MgSi}_2\text{O}_7$	$\text{Eu}^{2+}, \text{Dy}^{3+}, \text{Nd}^{3+}$	518	5 h	[18]
	$\text{Sr}_2\text{MgSi}_2\text{O}_7$	$\text{Eu}^{2+}, \text{Tb}^{3+}$	515, 530	Disputed	[45]
	$\text{Ba}_2\text{MgSi}_2\text{O}_7$	$\text{Eu}^{2+}$	500, 515	5 h	[46]
	$\text{Sr}_2\text{SiO}_4$	$\text{Eu}^{2+}, \text{Dy}^{3+}$	480	5 min	[47]
Other	$\text{CaGa}_2\text{S}_4$	$\text{Eu}^{2+}, \text{Ho}^{3+}$ or $\text{Ce}^{3+}$	556 (yellow)	0.5 h	[48]

**Table 2.3** Red-emitting  $\text{Eu}^{2+}$ -activated long persistent phosphors

Host material		Dopants	Afterglow maximum (nm)	Afterglow duration	References
Sulfide	CaS	$\text{Eu}^{2+}, \text{Pr}^{3+}, \text{Li}^+, \text{Sr}^{2+}$	644	1 h	[25]
	$\text{Ca}_2\text{SiS}_4$	$\text{Eu}^{2+}, \text{Nd}^{3+}$	660	0.5 h	[49]
	$\text{Ca}_2\text{SiS}_4$	$\text{Eu}^{2+}$	560, 650	Disputed	[50]
Aluminate	$\text{Sr}_3\text{Al}_2\text{O}_6$	$\text{Eu}^{2+}$	612	Disputed	[15]
Other	$\text{Ca}_2\text{Si}_5\text{N}_8$	$\text{Eu}^{2+}$	605–615 (orange)	1 h	[27]
	$\text{Ca}_2\text{Si}_5\text{N}_8$	$\text{Eu}^{2+}$	609–680		
	$\text{Ca}_2\text{Si}_5\text{N}_8$	$\text{Eu}^{2+}$	570–680		
	$\text{Ga}_2\text{Si}_5\text{N}_8$	$\text{Eu}^{2+}, \text{Tm}^{3+}$	610 (orange)	1 h	[51]
	$\text{La}_2\text{O}_2\text{S}$	$\text{Eu}^{2+}$	590, 614, 627, 710		[52]

**Table 2.4** Blue-emitting non- $\text{Eu}^{2+}$ -activated long persistent phosphors

Host material		Dopants	Maximum emission (nm)	Afterglow duration	References
Aluminate	$\text{BaAl}_2\text{O}_4$	$\text{Ce}^{3+}$	402 + 450	10 h	[73]
	$\text{CaAl}_2\text{O}_4$		400	10 h	[74]
	$\text{SrAl}_2\text{O}_4$		375–385, 427	10 h	[75]
	$\text{CaAl}_2\text{O}_4$	$\text{Ce}^{3+}$	413	10 h	[76]
	$\text{Sr}_4\text{Al}_{14}\text{O}_{25}$	$\text{Ce}^{3+}$	472 + 511 (blue/green)	10 min	[77]
	$\text{Sr}_4\text{Al}_{14}\text{O}_{25}$	$\text{Tb}^{3+}$	380	disputed	[78]
Silicate	$\text{Lu}_2\text{SiO}_5$	$\text{Ce}^{3+}$	410	3 h	[79]
	$\text{Ca}_2\text{Al}_2\text{SiO}_7$	$\text{Ce}^{3+}$	400–417	1 h	[80]
	$\text{Lu}_2\text{SiO}_5$	$\text{Ce}^{3+}$	400 + 430	3 h	[81]
	$\text{SrMgSi}_2\text{O}_6$	$\text{Dy}^{3+}$	455 + 576	5 min	[82]
	$\text{Zn}_3(\text{PO}_4)_2$	$\text{Hf}^{4+}$	470	40 min	[83]

### 2.2.1.1 $\text{Eu}^{2+}$ -Activated Phosphor

Lanthanide ions are widely employed as emitting centers in luminescent materials owing to their abundant energy levels. Given the technological importance,  $\text{Eu}^{2+}$  ions serving as emitting centers of persistent phosphors have received increasing interest during the past two decades. Note that  $\text{Eu}^{2+}$  ions can be doped into different classes of inorganic compounds, including aluminates, silicates, and other oxides. In this section, we begin by discussions of the afterglow features of  $\text{Eu}^{2+}$  ions when doped into different hosts.

*Aluminate-Based Phosphor.* The persistent luminescence of  $\text{Eu}^{2+}$  ions doped into aluminate was first reported by T. Matsuzawa and coworkers in 1996 [4]. As a parallel study, Takasaki et al. observed similar luminescence phenomena in  $\text{Eu}^{2+}$ -doped aluminate at the same time [5]. The  $\text{Eu}^{2+}$ -activated phosphors are characterized by

significantly enhanced emission intensity and a prolonged emission lifetime compared to ZnS:Cu,Co phosphors. For example, green-emitting  $\text{SrAl}_2\text{O}_4:\text{Eu}^{2+},\text{Dy}^{3+}$  is one of the first commercially available phosphors. There has been a steady increase in the exploration of new lanthanide-activated phosphor over the past 20 years, as evidenced by the number of scientific publications. It is noteworthy that most studies concentrated on alkali earth metal aluminate hosts because they can render a suitable coordination environment for emitting centers for achieving excellent luminescent properties. In contrast with the single doping of  $\text{Eu}^{2+}$  ions, the  $\text{Eu}^{2+}$ -doped alkaline earth aluminates present prolonged luminescence time and bright emission when co-doped with additional lanthanides such as  $\text{Dy}^{3+}$  and  $\text{Nd}^{3+}$  [6]. Specifically, these  $\text{Eu}^{2+}$ - and  $\text{Dy}^{3+}/\text{Nd}^{3+}$ -doped alkaline earth aluminate phosphors show visible afterglow for more than 10 h in the dark after exposure to the fluorescent light or sunlight. Typical green- and blue-emitting  $\text{Eu}^{2+}$ -activated aluminate long afterglow phosphors are  $\text{SrAl}_2\text{O}_4:\text{Eu}^{2+},\text{Dy}^{3+}$  [4] and  $\text{CaAl}_2\text{O}_4:\text{Eu}^{2+},\text{Nd}^{3+}$ , [7] respectively, which show an afterglow time over 20 h.

As shown in Fig. 2.1, the toy containing  $\text{SrAl}_2\text{O}_4:\text{Eu}^{2+},\text{Dy}^{3+}$  phosphor emits green light in the dark after sunlight excitation. According to the experimentally collected excitation and emission spectra, it is found that this phosphor could be excited by the light at wavelengths ranging from 200 to 450 nm and be able to produce a broad green emission located at 520 nm. The resulted broadband emission indicates that the underlying optical transition occurred within  $\text{Eu}^{2+}$  ions originates from the electrical dipole allowed  $5d-4f$  transition. Compared to the parity-forbidden intra-configurational transition (f-f transition) of trivalent lanthanide ions, such inter-configurational transitions usually show much higher radiative emission probability.

It should be noted that the afterglow properties of phosphor are usually characterized by the decay curve. The luminescence decay curve of  $\text{SrAl}_2\text{O}_4:\text{Eu}^{2+},\text{Dy}^{3+}$  phosphor in Fig. 2.2a is monitored at 520 nm after irradiation by 365 nm light for 10 min. The diagram represents a correlation of the afterglow emission intensity and time, where the luminescence intensity drops quickly in the first few minutes, followed by a steady decay. To give a direct impression of luminescence lifetime, the experimental data is re-plotted using logarithmic coordinates (Fig. 2.2b) as the

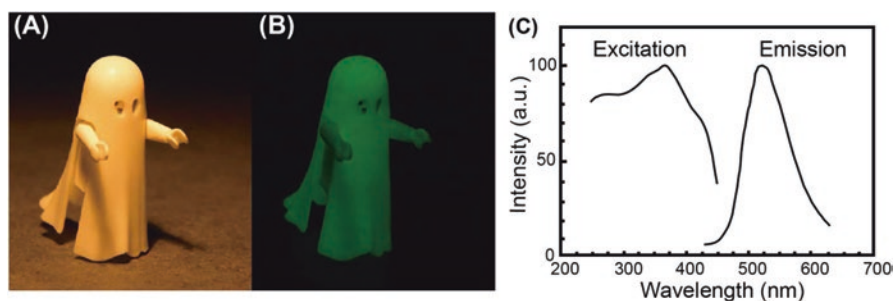
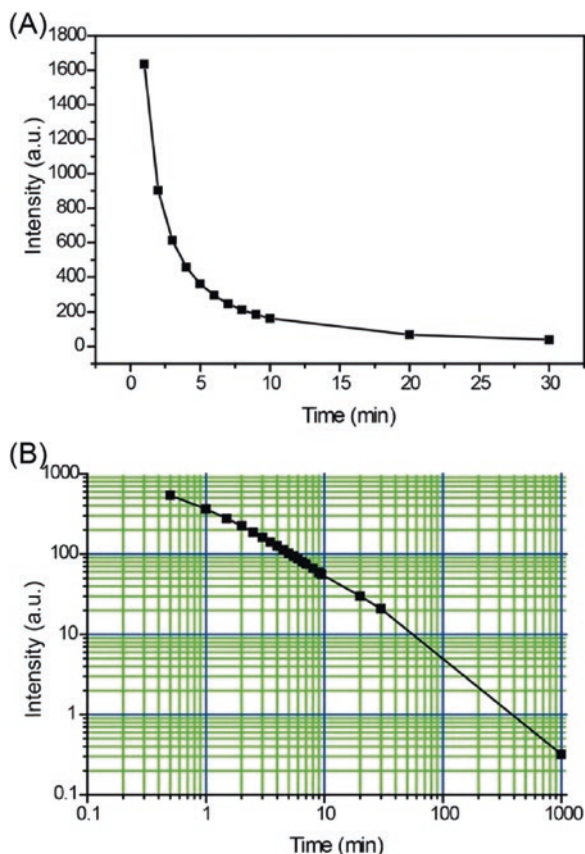


**Fig. 2.1** (a and b) Green persistent luminescence observed in a toy containing green-emitting  $\text{SrAl}_2\text{O}_4:\text{Eu}^{2+},\text{Dy}^{3+}$  phosphors after sunlight excitation. (c) Excitation and emission spectra of  $\text{SrAl}_2\text{O}_4:\text{Eu}^{2+},\text{Dy}^{3+}$  phosphor



**Fig. 2.2** (a) Decay curve of  $\text{Eu}^{2+}$  emission at 520 nm after irradiation for 10 min. The composition of the sample is  $\text{SrAl}_2\text{O}_4:\text{Eu}^{2+},\text{Dy}^{3+}$ . (b) The intensity–time curve is plotted using logarithmic coordinates



slope of the intensity–time curve is recognized as the experimentally determined decay rate. Note that the decay time is defined as the period between the stopping of the excitation and the time at which the emission intensity decreases to 0.32 mcd/m<sup>2</sup>. This value is about 100 times higher than the perceptible limit of the dark-adapted human eye.[8] As shown in Fig. 2.2b, it is clear that the persistent luminescence of this sample can last 1000 min (~16.7 h).

It is generally accepted that the prolonged persistent luminescence of  $\text{MAl}_2\text{O}_4:\text{Eu}^{2+},\text{RE}^{3+}$  ( $\text{M} = \text{Ca}, \text{Sr}$  or  $\text{Ba}$ ,  $\text{RE}^{3+} = \text{Dy}^{3+}$  or  $\text{Nd}^{3+}$ ) is ascribed to codopant  $\text{RE}^{3+}$ -induced defect level. Let us take  $\text{SrAl}_2\text{O}_4:\text{Eu}^{2+},\text{Dy}^{3+}$  and  $\text{CaAl}_2\text{O}_4:\text{Eu}^{2+}, \text{Nd}^{3+}$  for instance,  $\text{Eu}^{2+}$  ions are the emitting center, while  $\text{Dy}^{3+}$  and  $\text{Nd}^{3+}$  ions serve as the trapping centers. When  $\text{Eu}^{2+}$  is irradiated by the ultraviolet source, the ion may return back to its ground state along with radiative emission or capture an electron from the valence band, staying at a metastable state  $^*\text{Eu}^{2+}$ . The resulted hole can either propagate within the valence band or can be captured by codopant-induced traps. Upon appropriate thermal activation, the hole escapes from the traps, returns back to the valence band, and recombines with the excess electron in the  $^*\text{Eu}^{2+}$  center, thus giving rise to the occurrence of the persistent luminescence.

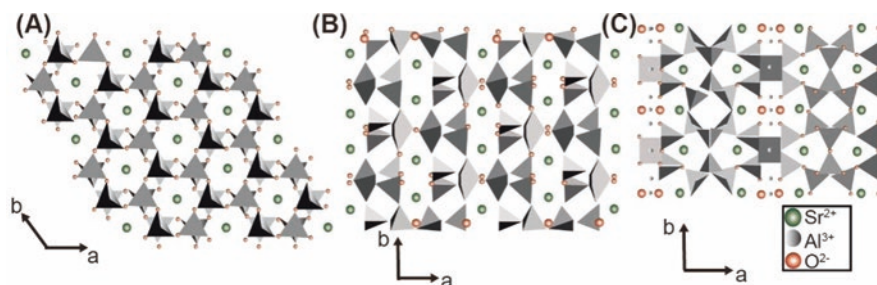


**Fig. 2.3** Three-dimensional crystal structures of (a) hexagonal  $\text{SrAl}_2\text{O}_4$ , (b) monoclinic  $\text{SrAl}_4\text{O}_7$ , and (c) orthorhombic  $\text{Sr}_4\text{Al}_{14}\text{O}_{25}$

The widely used  $\text{SrAl}_2\text{O}_4$  host has two crystallographic forms, namely monoclinic and hexagonal ( $\beta$ - $\text{SrAl}_2\text{O}_4$ ) phase. A reversible transformation between these two counterparts can occur at a temperature of 650 °C [9]. The monoclinic phase is a low-temperature phase characterized by distorted lattice structures, whereas hexagonal phase is considered as a high-temperature hexagonal phase with stuffed tridymite structures [10]. The crystallographic lattice structure of the monoclinic phase (space group  $P2_1$ ,  $a = 8.447 \text{ \AA}$ ,  $b = 8.816 \text{ \AA}$ ,  $c = 5.163 \text{ \AA}$ ,  $\beta = 93.42^\circ$ ) has been established. On the contrary, the lattice structure of the hexagonal one (space group  $P6_322$ ,  $a = 5.140 \text{ \AA}$ ,  $c = 8.462 \text{ \AA}$ ) remains unclear. As sketched in Fig. 2.3, the structure of the  $\beta$ -phase is constructed based on hexagonal rings that composed of six  $\text{Al}_2\text{O}_4$  tetrahedra, and these rings extend on the hexagonal  $aa$ -plane by sharing the three corners of the tetrahedron. The hexagonal rings are stacked layer by layer along the  $c$ -axis by sharing the apical oxygen.  $\text{Sr}^{2+}$  and  $\text{Eu}^{2+}$  ions reside in the interstitial spaces of the hexagonal rings.  $\text{Sr}^{2+}$  has two different crystallographic sites (Wyckoff position 2a), which have the same coordination numbers and similar Sr-O distances. The only difference between these two coordination environments is a slight deformation of their “square planes.” Considering that the  $\text{Sr}^{2+}$  and  $\text{Eu}^{2+}$  ions have very similar ionic size (1.21 and 1.20  $\text{\AA}$ ), the  $\text{Eu}^{2+}$  ions prefer to replace  $\text{Sr}^{2+}$  ions when doped into the  $\text{SrAl}_2\text{O}_4$  host. Given the high similarity in coordination configuration of  $\text{Sr}^{2+}$ ,  $\text{Eu}^{2+}$  ions substitute these two types of  $\text{Sr}^{2+}$  ions without site preference, resulting in a uniform doping. Similarly, the codopant  $\text{Dy}^{3+}$  also intends to occupy the site of  $\text{Sr}^{2+}$  due to a small radius mismatch between  $\text{Sr}^{2+}$  and  $\text{Dy}^{3+}$  ions. Moreover, the large radius mismatch between  $\text{Sr}^{2+}$  (1.21  $\text{\AA}$ ) and  $\text{Eu}^{3+}$  (1.01  $\text{\AA}$ ) explains why the doped  $\text{Eu}^{3+}$  ions can be easily reduced to  $\text{Eu}^{2+}$  ions.

In addition to the hosts of  $\text{SrAl}_2\text{O}_4$  and  $\text{CaAl}_2\text{O}_4$ , other hosts such as  $\text{Sr}_4\text{Al}_{14}\text{O}_{25}$ ,  $\text{SrAl}_4\text{O}_7$ ,  $\text{SrAl}_{12}\text{O}_{19}$ , and  $\text{Sr}_3\text{Al}_2\text{O}_6$  (Tables 2.1, 2.2 and 2.3) have also been investigated. For example,  $\text{Sr}_4\text{Al}_{14}\text{O}_{25}:\text{Eu}^{2+},\text{Dy}^{3+}$  is a representative persistent phosphor featuring a blue emission centered at 490 nm and a persistent time over 20 h [11, 12]. In the case of  $\text{Sr}_3\text{Al}_2\text{O}_6:\text{Eu}^{2+},\text{Dy}^{3+}$  phosphor, the color of the persistent luminescence is still under debate because of inconsistent observation. Chang et al. observed a bright green emission at 510 nm using triboluminescence and photoluminescence measurements.[13] However, the  $\text{Sr}_3\text{Al}_2\text{O}_6:\text{Eu}^{2+},\text{Dy}^{3+}$  samples prepared using microwave and sol-gel processes present red emission centered at 612 nm [14, 15].

Except for the prolonged lifetime and enhanced brightness, aluminate-based phosphors show high chemical stability, as evidenced by the high resistance against UV radiation. Hence these phosphors are suitable for outdoor-associated applications. Unfortunately, these materials have limited stability against moisture, and they usually decompose into nonluminescent substances when encountering water. In addition, the realization of red- and NIR-emitting persistent phosphors using aluminate host remains challenging as all the  $\text{Eu}^{2+}$ -doped aluminate phosphors usually emit blue and green colors (Tables 2.1, 2.2, 2.3, and 2.4).

*Silicate-Based Phosphor.* Silicates-based long afterglow materials have been demonstrated to be suitable alternatives to aluminate-based phosphors because of their high water resistance and good physical and chemical stability [16]. The chemical formula of the lanthanide-activated alkali earth silicate phosphors can be expressed as:



where M and M' represent alkali earth metal, R is flux ( $\text{B}_2\text{O}_3$  and  $\text{P}_2\text{O}_5$ ), Ln stands for lanthanide or transition metal ions, and  $a$ ,  $b$ ,  $c$ ,  $d$ ,  $x$ , and  $y$  are mole ratios ( $0.6 \leq a \leq 6$ ,  $0 \leq b \leq 5$ ,  $1 \leq c \leq 9$ ,  $0 \leq d \leq 0.7$ ,  $0.00001 \leq x \leq 0.2$  and  $0 \leq y \leq 0.3$ ). As summarized in Tables 2.1, 2.2, and 2.3, it is found that the emission spectrum of silicate phosphor is often located in the range of 420–650 nm. Note that the emission peak is usually located between 450 and 580 nm. There are two main types of silicate hosts, namely ternary pyro-silicate and ortho-silicate, which can enable blue and green emission of lanthanide ions. As compiled in Tables 2.1 and 2.2, typical blue- and green-emitting persistent phosphors are  $\text{Sr}_2\text{MgSi}_2\text{O}_7:\text{Eu}^{2+}, \text{Dy}^{3+}$ ,  $\text{Sr}_2\text{MgSi}_2\text{O}_8$  and  $\text{CaMgSi}_2\text{O}_6:\text{Eu}^{2+}, \text{Dy}^{3+}$  [17].

The most well-known silicate-based phosphor featuring long afterglow is  $\text{M}_2\text{MgSi}_2\text{O}_7:\text{Eu}^{2+}, \text{Dy}^{3+}$  (M = Ca, Sr, Ba), which was first demonstrated by Lin et al. in 2001 [17]. By manipulating the types of M cations in silicates, the lanthanide-activated silicates can produce light emissions with different colors, such as the blue-emitting  $\text{Sr}_2\text{MgSi}_2\text{O}_7:\text{Eu}^{2+}, \text{Dy}^{3+}$  (centered at 470 nm) and the  $\text{Ca}_2\text{MgSi}_2\text{O}_7:\text{Eu}^{2+}, \text{Dy}^{3+}, \text{Nd}^{3+}$  (centered at 518 nm) [18]. In general, co-doping of another type of lanthanide ions is the most effective strategy to enhance the optical performance of the persistent phosphors. For instance,  $\text{Dy}^{3+}$  co-doped  $\text{Sr}_2\text{MgSi}_2\text{O}_7:\text{Eu}^{2+}$ , and  $\text{Tm}^{3+}$  co-doped  $\text{Ba}_2\text{MgSi}_2\text{O}_7:\text{Eu}^{2+}$ , phosphors have much brighter emission and longer afterglow time than their singly co-doped counterparts. In stark comparison to the enhancement in the brightness and duration of the afterglow in the aforementioned aluminates and silicates, Hölsä and coworkers observed that the afterglow observed in  $\text{Ca}_2\text{MgSi}_2\text{O}_7:\text{Eu}^{2+}$  was greatly decreased when additional co-doping of trivalent lanthanide ions (except for  $\text{Tb}^{3+}$ ) [19]. These inconsistencies thus stimulate the fundamental investigations on the role of the codopant. In 2007, Shi reported the long afterglow phenomenon in  $\text{Sr}_2\text{MgSi}_2\text{O}_7:\text{Eu}^{2+}, \text{Dy}^{3+}$  phosphor, and pointed out that both  $\text{Eu}^{2+}$  and  $\text{Dy}^{3+}$  ions not only serve as luminescence centers, but also play as trap centers [20]. Compared to the  $\text{Eu}^{2+}$ -induced trap levels, the  $\text{Dy}^{3+}$ -induced trap levels are deeper in energy,

enabling prolonged afterglow lifetime up to 20 h. In studying  $\text{Dy}^{3+}$  singly doped silicates,  $\text{Sr}_2\text{MgSi}_2\text{O}_7:\text{Dy}^{3+}$  has also been reported as a persistent phosphor characterized by long white afterglow. After the excitation of ultraviolet light,  $\text{Sr}_2\text{MgSi}_2\text{O}_7:\text{Dy}^{3+}$  phosphor has a broadband emission centered at 441 nm and three narrow-band emissions centered at 480, 575, and 668 nm, which are generated by the host, the transitions of  ${}^4\text{F}_{9/2}-{}^6\text{H}_{15/2}$ ,  ${}^4\text{F}_{9/2}-{}^6\text{H}_{13/2}$ , and  ${}^4\text{F}_{9/2}-{}^6\text{H}_{11/2}$  within the  $4f^9$  configuration of  $\text{Dy}^{3+}$  emitting ions, respectively.

The emission spectra of  $\text{M}_2\text{MgSi}_2\text{O}_7:\text{Eu}^{2+},\text{Dy}^{3+}$  (M: Ca, Sr, Ba) phosphors at room temperature (Fig. 2.4a) indicate that all the samples show broadband emission, and the main emission peaks are located at 537.5, 475.6, and 500.3 nm, respectively [21]. The absence of particular emission of  $\text{Dy}^{3+}$  and  $\text{Eu}^{3+}$  in the emission spectra suggested that  $\text{Dy}^{3+}$  ions are not emitting centers in the  $\text{M}_2\text{MgSi}_2\text{O}_7$  hosts and  $\text{Eu}^{3+}$  ions are reduced to  $\text{Eu}^{2+}$  completely. Note that the specific positions of the emission peaks are determined by the type of the alkali earth ion. Given that the length of the  $c$ -axis increases from calcium to barium, the orientation of cation's d orbitals becomes energetically less favorable, resulting in shorter emission wavelength [22]. Let us take  $\text{Ca}_2\text{MgSi}_2\text{O}_7:\text{Eu}^{2+},\text{Dy}^{3+}$  phosphor for example, the shortest  $c$ -axis of Ca cation is responsible for the longest emission wavelength compared to Sr and Ba cations. By replacing  $\text{Ca}^{2+}$  with  $\text{Sr}^{2+}$  or  $\text{Ba}^{2+}$ , the emission of  $\text{Eu}^{2+}$  was characterized by short wavelength. However, the main emission wavelength of  $\text{Ba}_2\text{MgSi}_2\text{O}_7:\text{Eu}^{2+},\text{Dy}^{3+}$  is longer than that of  $\text{Sr}_2\text{MgSi}_2\text{O}_7:\text{Eu}^{2+},\text{Dy}^{3+}$  phosphor. Such an abnormality could be ascribed to the severe crystallographic distortion caused by the significant radius mismatch between  $\text{Ba}^{2+}$  (0.134 nm) and  $\text{Eu}^{2+}$  (0.112 nm) ions, which can affect the strength of the crystal field imposed on the  $\text{Eu}^{2+}$  ions and thus the emission spectra.

The luminescent decay curves of different  $\text{M}_2\text{MgSi}_2\text{O}_7:\text{Eu}^{2+},\text{Dy}^{3+}$  phosphors shown in Fig. 2.4b comprise the contributions from a rapid- and a steady decay. Apparently, the initial afterglow intensity and the corresponding decay rate of these samples are different from each other. To obtain the decay time, one can fit the intensity–time curve according to:

$$I = A_1 \exp\left(\frac{-t}{\tau_1}\right) + A_2 \exp\left(\frac{-t}{\tau_2}\right) + A_3 \exp\left(\frac{-t}{\tau_3}\right) \quad (2.1)$$

where  $I$  is the luminescence intensity,  $A_1$ ,  $A_2$ , and  $A_3$  are constants,  $t$  is the time, and  $\tau_1$ ,  $\tau_2$ , and  $\tau_3$  are the decay times related to the exponential components, respectively. The calculated afterglow time of these three samples can reach 5 h.

By examining the crystal structure of  $\text{Ca}_2\text{MgSi}_2\text{O}_7$  host, it is found that the distorted  $(\text{MgSi}_2\text{O}_7)^{4-}$  sheets stack reciprocally with a normal along the (001) direction, while the  $\text{Ca}^{2+}$  cations reside between these layers. Note that there are two different kinds of tetrahedral units existing in the distorted sheets. One is  $\text{MgO}_4$  tetrahedron, where the Mg atoms reside in the cavity of the oxygen-associated tetrahedron. Another one is  $\text{SiO}_4^{4-}$  tetrahedra, which connects each other to form  $\text{Si}_2\text{O}_7^{6-}$  groups through one shared oxygen atom. It is a general consensus that the lanthanide ions, such as  $\text{Eu}^{2+}$ ,  $\text{Dy}^{3+}$ , and  $\text{Nd}^{3+}$ , occupy the  $\text{Ca}^{2+}$  sites in  $\text{Ca}_2\text{MgSi}_2\text{O}_7$

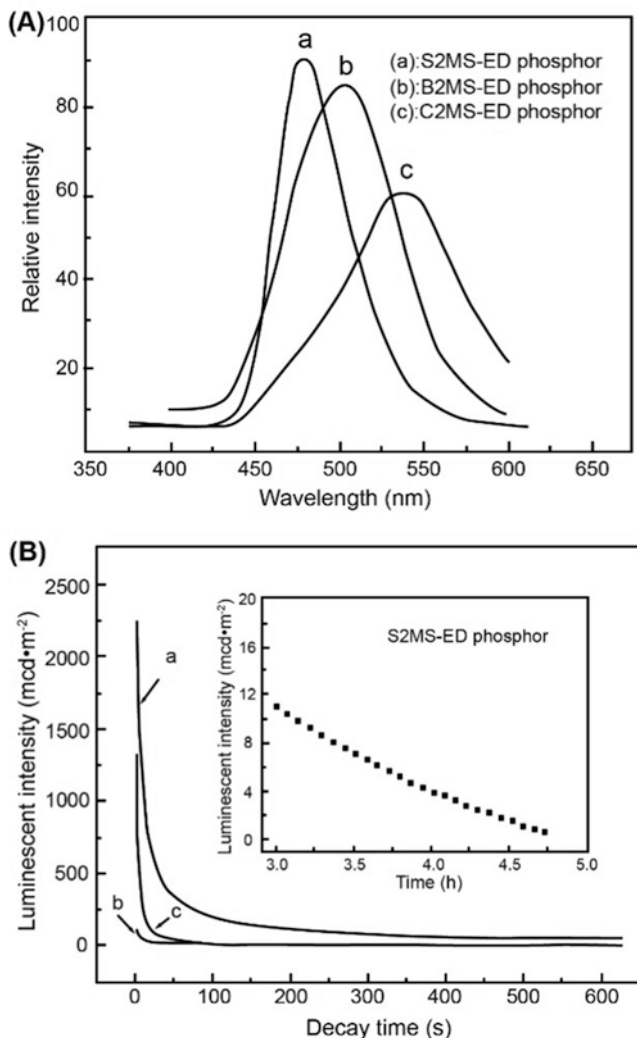
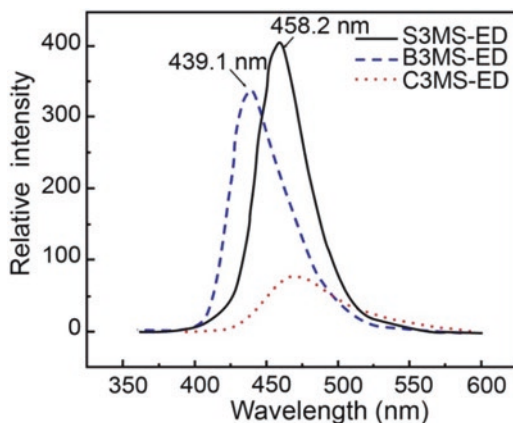


**Fig. 2.4** Emission spectra (a) and decay curves (b) of  $M_2MgSi_2O_7:Eu^{2+},Dy^{3+}$  (M: Ca, Sr, Ba) persistent phosphors (after excitation of 365 nm light).  $Sr_2MgSi_2O_7:Eu^{2+},Dy^{3+}$ ,  $Ba_2MgSi_2O_7:Eu^{2+},Dy^{3+}$ , and  $Ca_2MgSi_2O_7:Eu^{2+},Dy^{3+}$  are marked as S2MS-ED, B2MS-ED and C2MS-ED, respectively

lattice due to the negligible radial mismatch between the  $Ca^{2+}$  (1.12 Å) and  $Eu^{2+}$  (1.12 Å),  $Nd^{3+}$  (1.12 Å) and  $Dy^{3+}$  (1.03 Å). On the other hand, the site for  $Mg^{2+}$  (0.58 Å) or  $Si^{4+}$  (0.26 Å) is too crowded for accommodating lanthanide ions. The lanthanide ions thus are usually observed in  $[CaO_8]$  anion complexes when doped into  $Ca_2MgSi_2O_7$  host [18].

Lin et al. demonstrated that  $Sr_2MgSi_2O_8$  compounds are able to emit blue-colored long afterglow peaking at 476 nm when doped with  $Eu^{2+}$  and  $Dy^{3+}$  ions [23]. Subsequently, the researchers from the same group investigated the persistent lumines-

**Fig. 2.5** Emission spectra of  $R_3MgSi_2O_8:Eu^{2+}, Dy^{3+}$  ( $R = Ca, Sr, Ba$ ). S3MS-ED, B3MS-ED, and C3MS-ED represent  $Sr_3MgSi_2O_8:Eu^{2+}, Dy^{3+}$ ,  $Ba_3MgSi_2O_8:Eu^{2+}, Dy^{3+}$ , and  $Ca_3MgSi_2O_7:Eu^{2+}, Dy^{3+}$ , respectively



cent properties of a collection of  $Eu^{2+}$ - and  $Dy^{3+}$ -co-doped silicates  $R_3MgSi_2O_8$  ( $R = Ca, Sr, Ba$ ), and found all the samples are characterized with long afterglow features [24]. The emission spectra shown in Fig. 2.5 indicate that these phosphors feature with broadband emissions peaked at 471.3, 458.2, and 439.1 nm, respectively, which correspond to the typical 5d-4f optical transitions of the  $Eu^{2+}$  ions. It is noteworthy that the afterglow lifetimes of these phosphors are relatively short.

As summarized in Tables 2.1, 2.2, and 2.3, silicate-based phosphors are usually characterized by bright emission and long afterglow lifetime up to 20 h. Despite these achievements, one challenging issue is related to the precise tuning over emission color since only blue or green emission was observed in these silicate-based phosphors.

*Other Types of Phosphors.* In addition to the aluminate and silicate hosts, other types of hosts, including metal sulfides, metal oxides, borides, nitrides phosphoric oxides, and titanates, have also been demonstrated to the capability of emitting long afterglow (Tables 2.1, 2.2, and 2.3). For example, calcium sulfide (CaS) is a typical metal sulfide host of the persistent phosphors that dominate the consumer markets in 1990s. However, these phosphors are carcinogenic and have limited chemical stability, giving rise to a stringent constraint on the further development of metal sulfide-based persistent phosphors [25].

Lanthanide-doped borate phosphors are of great interest as the synthesis of these phosphors can be achieved at a low temperature. For example, Yoshiyuki Kojima and coworkers reported a green-emitting phosphor  $Sr_2B_2O_5:Eu^{2+}$  [26]. In 2015, the same group of researchers successfully synthesized a blue-emitting  $SrB_2O_4:Eu^{2+}$  phosphor with high color purity. In addition, Li et al. demonstrated that the persistent emission color of  $Eu^{2+}$  ions could vary from yellow to red when doped into different nitridosilicates  $M_2Si_5N_8$  ( $M = Ca, Sr, Ba$ ) with different concentrations [27]. The details of the emission peak positions and afterglow lifetimes associated with these nitridosilicate samples are listed in Table 2.3. Similarly, the stannate host also enables tunability over emission wavelength of phosphors. Note that the long persistent phosphors mentioned in this section are referred to the phosphors that be



able to produce an afterglow with a lifetime of a few seconds. Apart from the aforementioned matrices, sulfur oxide hosts such as  $\text{La}_2\text{O}_2\text{S}$  also render  $\text{Eu}^{2+}$  ions acceptable luminous properties. However, these phosphors show low emission intensity and short afterglow lifetime when compared with the intensity and lifetime of aluminate- and silicate-based persistent phosphors.

Given the high chemical stability, phosphates are usually recognized as promising host candidates for afterglow phosphors. In 2006, Liu et al. reported the first case of phosphate  $\text{SrMg}_2(\text{PO}_4)_2$ , where a long persistent luminescence of doped  $\text{Eu}^{2+}$  was observed [28]. Subsequently, a large number of  $\text{Eu}^{2+}$ -doped phosphates were found to be existing long persistent luminescence, as shown in the last part of Table 2.1. The emission wavelengths of  $\text{Eu}^{2+}$ -doped phosphate persistent phosphors cover a range from approximately 375 to 505 nm. Recently, Pang et al. reported persistent luminescence phenomena in both  $\alpha\text{-Ca}_2\text{P}_2\text{O}_7\text{:Eu}^{2+}, \text{Y}^{3+}$  and  $\alpha\text{-Sr}_2\text{P}_2\text{O}_7\text{:Eu}^{2+}, \text{Y}^{3+}$  phosphors, in which the host lattices have similar orthorhombic pyrophosphate structures [16, 29, 30]. They found that by co-doping with  $\text{Y}^{3+}$  ions, the lifetime of the blue emission could reach 6 and 8 h in  $\text{Ca}_2\text{P}_2\text{O}_7\text{:Eu}^{2+}, \text{Y}^{3+}$  and  $\text{Sr}_2\text{P}_2\text{O}_7\text{:Eu}^{2+}, \text{Y}^{3+}$ , respectively. As listed in Table 2.1, it is found that  $\text{Sr}_2\text{P}_2\text{O}_7\text{:Eu}^{2+}$  phosphors feature with the longest afterglow lifetime among the phosphate phosphors under study. It should be noted that the afterglow lifetime of the phosphate-associated persistent phosphors is still shorter than that of aluminate- and silicate-associated ones.

Alkaline earth nitridosilicates  $\text{M}_2\text{Si}_5\text{N}_8\text{:Eu}^{2+}$  ( $\text{M} = \text{Ca}, \text{Sr}, \text{Ba}$ ) have also been widely studied due to their very broad excitation spectrum and high stability against moisture and heat. In 2009, Van den Eeckhout et al. and Miyamoto et al. independently reported that co-doping of different lanthanide ions can largely enhance the persistent luminescence intensity and prolong the afterglow lifetime of  $\text{Ca}_2\text{Si}_5\text{N}_8\text{:Eu}^{2+}$  phosphors [31]. For instance, a prolonged lifetime over 1 h was observed in the  $\text{Ca}_2\text{Si}_5\text{N}_8\text{:Eu}^{2+}, \text{Tm}^{3+}$  phosphor by co-doping of  $\text{Tm}^{3+}$  ions. Additionally, tunable emission wavelength in  $\text{Ca}_2\text{Si}_5\text{N}_8\text{:Eu}^{2+}$  phosphors can be achieved through the replacement of Ca with Sr ions [32] (Fig. 2.6).

### 2.2.1.2 Lanthanide Ions Other than $\text{Eu}^{2+}$

Given the high sensitivity of  $5d$  orbitals, the  $5d\text{-}4f$  emission wavelength of  $\text{Eu}^{2+}$  ions significantly depends on the host materials mainly through the effect of covalency and ligand polarization and the strength of the crystal field [29]. It is thus believed that tunable emission wavelength could be easily achieved by choosing appropriate host lattice. However, as aforementioned,  $\text{Eu}^{2+}$ -activated persistent phosphors are usually featured with blue and green emissions. The lack of red-emitting persistent phosphors imposes a constraint on the development of new generation illuminating devices and the emerging applications in the field of bioimaging. To overcome such problem, great deals of efforts have been devoted to exploring other lanthanide emitters. Over the past two decades, many different lanthanide ions, including  $\text{Eu}^{3+}$ ,  $\text{Ce}^{3+}$ ,  $\text{Dy}^{3+}$ ,  $\text{Sm}^{3+}$ ,  $\text{Tb}^{3+}$ , and  $\text{Pr}^{3+}$ , have been demonstrated to be able to emit long afterglow when embedded in host lattices, as compiled in Tables 2.4, 2.5, 2.6, and 2.7.

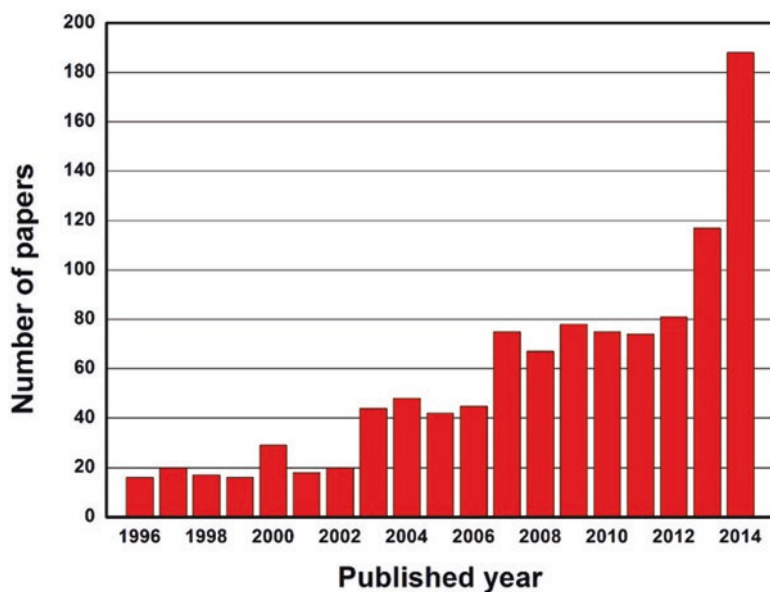


**Fig. 2.6** Number of papers on persistent luminescence published per year since 1996

**Table 2.5** Green-emitting non-Eu<sup>2+</sup>-activated long persistent phosphors

Host material		Dopants	Afterglow maximum (nm)	Afterglow duration	References
Aluminate	CaAl <sub>2</sub> O <sub>4</sub>	Ce <sup>3+</sup> → Tb <sup>3+</sup>	543	10 h	[76]
	CaAl <sub>2</sub> O <sub>4</sub>	Ce <sup>3+</sup> → Mn <sup>2+</sup>	525	10 h	[84]
	SrAl <sub>2</sub> O <sub>4</sub>	Ce <sup>3+</sup> → Mn <sup>2+</sup>	375, 515	5 h	[85]
	MgAl <sub>2</sub> O <sub>4</sub>	defects	520	10 h	[86]
	Y <sub>3</sub> Al <sub>5</sub> O <sub>12</sub>	Ce <sup>3+</sup>	525	2 min	[87]
Silicate	CdSiO <sub>3</sub>	Tb <sup>3+</sup>	540	5 h	[88]
	CdSiO <sub>3</sub>	Pb <sup>2+</sup>	498	2 h	[89]
	Ca <sub>2</sub> Al <sub>2</sub> SiO <sub>7</sub>	Ce <sup>3+</sup> → Mn <sup>2+</sup>	550	10 h	[84]
	Ca <sub>3</sub> SnSi <sub>2</sub> O <sub>9</sub>	Tb <sup>3+</sup>	426, 495 + 542 + 590	10 min	[90]
Phosphate	Ca <sub>9</sub> Tb(PO <sub>4</sub> ) <sub>7</sub>	Tb <sup>3+</sup>	490 + 545	20 min	[91]
Other	Lu <sub>2</sub> O <sub>3</sub>	Tb <sup>3+</sup>	490 + 550	5–7 h	[92]
	Ca <sub>2</sub> SnO <sub>4</sub>	Tb <sup>3+</sup>	483 + 545	3 h	[93]
	CaSnO <sub>3</sub>	Tb <sup>3+</sup>	491 + 545 + 588 + 622	4 h	[94]
	CaZnGe <sub>2</sub> O <sub>6</sub>	Tb <sup>3+</sup>	552	4 h	[95]
	YTbO <sub>4</sub>	Tb <sup>3+</sup>	492 + 543 + 590 + 624	2 h	[96]
	CaWO <sub>4</sub>	Tb <sup>3+</sup>	490 + 546	10 min	[97]



**Table 2.6** Red-emitting non-Eu<sup>2+</sup>-activated long persistent phosphors

Host material		Dopants	Afterglow maximum (nm)	Afterglow duration	References
Titanate	ZnTiO <sub>3</sub>	Pr <sup>3+</sup>	612	20 min	[98]
	SrTiO <sub>3</sub>	Pr <sup>3+</sup> , Al <sup>3+</sup>	614		[3]
	CaTiO <sub>3</sub>	Pr <sup>3+</sup>	614	2 h	[99]
	La <sub>2</sub> Ti <sub>2</sub> O <sub>7</sub>	Pr <sup>3+</sup>	611	1 h	[100]
Silicate	CdSiO <sub>3</sub>	Pr <sup>3+</sup>	402, 600	5 h	[101]
		Eu <sup>3+</sup>	420, 615		
		Sm <sup>3+</sup>	400, 565 + 600 (pink)		
		Tb <sup>3+</sup> , Mn <sup>2+</sup>	486 + 548, 587	1 h	[102]
		Eu <sup>3+</sup> , Mn <sup>2+</sup>	597, 610	1 h	[103]
	Ca <sub>3</sub> SnSi <sub>2</sub> O <sub>9</sub>	Sm <sup>3+</sup>	426, 495 + 542 + 590	10 min	[90]
	BaMg <sub>2</sub> Si <sub>2</sub> O <sub>7</sub>	Ce <sup>3+</sup> , Mn <sup>2+</sup>	408, 680	2 h	[104]
Phosphate	YPO <sub>4</sub>	Pr <sup>3+</sup>	600 + 620	30 min	[105]
Other	Y <sub>2</sub> O <sub>2</sub> S	Eu <sup>3+</sup> , Mg <sup>2+</sup> , Ti <sup>4+</sup>	615/626	3 h	[53]
	Y <sub>2</sub> O <sub>3</sub>	Eu <sup>3+</sup>	612	90 min	[106]
	Lu <sub>2</sub> O <sub>3</sub>	Eu <sup>3+</sup>	611	3 min	[107]
	ZrO <sub>2</sub>	Sm <sup>3+</sup>	570 + 614	15 min	[108]
	SrO	Eu <sup>3+</sup>	594 + 616 (orange)	1 h	[109]
	CaO	Eu <sup>3+</sup>	594, 616	2 h	[110]
	Ba <sub>2</sub> SnO <sub>4</sub>	Sm <sup>3+</sup>	580 + 611 + 623	20 min	[111]
	Sr <sub>2</sub> SnO <sub>4</sub>	Sm <sup>3+</sup>	582 + 624 + 672	1 h	[111]
	Ca <sub>2</sub> SnO <sub>4</sub>	Eu <sup>3+</sup>	585 + 618 + 633	50 min	[112]
		Sm <sup>3+</sup>	566 + 609 + 653	1–7 h	[111]
	Sr <sub>3</sub> Sn <sub>2</sub> O <sub>7</sub>	Sm <sup>3+</sup>	580 + 621 + 665 + 735	1 h	[113]
	Ca <sub>2</sub> Sb <sub>2</sub> O <sub>7</sub>	Sm <sup>3+</sup>	Orange	770 s	
	CaMoO <sub>4</sub>	Eu <sup>3+</sup>	616	5 min	[114]
	CaWO <sub>4</sub>	Eu <sup>3+</sup>	592 + 616	40 min	[55]
		Sm <sup>3+</sup> → Eu <sup>3+</sup>	592 + 616	35 min	[115]
	BaZrO <sub>3</sub>	Eu <sup>3+</sup>	574 + 596 + 614	10 min	[116]
		Ti <sup>4+</sup> → Eu <sup>3+</sup>			

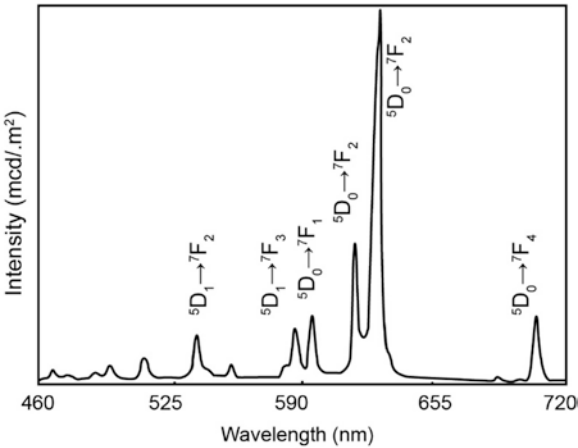
In this section, we will discuss the luminescence features of these non-Eu<sup>2+</sup>-activated persistent phosphors.

**Eu<sup>3+</sup>-Activated Phosphor.** Among red-emitting phosphors under study, **Eu<sup>3+</sup>**-doped sulfur oxide Y<sub>2</sub>O<sub>2</sub>S shows longest afterglow lifetime of 3 h [53]. As indicated in Fig. 2.7, the main emission peaks are originated from the <sup>5</sup>D<sub>J</sub> (*J* = 0, 1) → <sup>7</sup>F<sub>J</sub> (*J* = 0, 1, 2, 3, 4) transition of **Eu<sup>3+</sup>** [54]. In stark comparison with the broad emission spectra of **Eu<sup>2+</sup>** ions, the Y<sub>2</sub>O<sub>2</sub>S:**Eu<sup>3+</sup>** features with several narrow emission bands because the f-f transition usually leads to sharp line-like emission [54]. To achieve red light emission, MWO<sub>4</sub> (M = Ca, Sr, Ba) was also adopted as host to accommodating **Eu<sup>3+</sup>** ions [55]. The resulted afterglow of the optimal sample could last for nearly 40 min.

**Table 2.7** White-emitting non-Eu<sup>2+</sup>-activated long persistent phosphors

Host material		Dopants	Afterglow maximum (nm)	Afterglow duration	References
Silicate	Sr <sub>2</sub> MgSi <sub>2</sub> O <sub>7</sub>	Dy <sup>3+</sup>	470, 575, 678 (white)	0.7 h	[117]
	Sr <sub>2</sub> SiO <sub>4</sub>	Eu <sup>3+</sup> , Dy <sup>3+</sup>	484, 497, 579 (white)	1 h	[118]
	Ca <sub>0.5</sub> Sr <sub>1.5</sub> Al <sub>2</sub> SiO <sub>7</sub>	Ce <sup>3+</sup> → Tb <sup>3+</sup>	386, 483, 542, 591 (white)	1 min	[119]
	CdSiO <sub>3</sub>	Dy <sup>3+</sup>	410, 486 + 580	5 h	[60]
	Sr <sub>2</sub> Al <sub>2</sub> SiO <sub>7</sub>	Ce <sup>3+</sup> → Dy <sup>3+</sup>	408, 491, 573 (white)	1 h	[61]
	CaMgSi <sub>2</sub> O <sub>6</sub>	Dy <sup>3+</sup>	480, 575 (white)	2 h	[62]
	Ca <sub>3</sub> MgSi <sub>2</sub> O <sub>8</sub>	Dy <sup>3+</sup>	480 + 575 + 667	5 min	[62]
	Ca <sub>3</sub> SnSi <sub>2</sub> O <sub>9</sub>	Dy <sup>3+</sup>	426, 484 + 572 + 670	10 min	[90]
	Sr <sub>2</sub> MgSi <sub>2</sub> O <sub>7</sub>	Dy <sup>3+</sup>	441, 480, 575, 668 (white)	0.7 h	[63]
	Ca <sub>0.5</sub> Sr <sub>1.5</sub> Al <sub>2</sub> SiO <sub>7</sub>	Ce <sup>3+</sup>	386, 483, 542, 591 (white)	1 min	[119]
	SrSiO <sub>3</sub>	Dy <sup>3+</sup>	480, 572, 664 (white)	1 h	[59]
	Sr <sub>2</sub> SiO <sub>4</sub>	Dy <sup>3+</sup>	477, 570, 660 (white)	1 h	[64]
	CdSiO <sub>3</sub>	Dy <sup>3+</sup>	420, 486, 580 (white)	5 h	[58]
Others	CaSnO <sub>3</sub>	Pr <sup>3+</sup>	488 + 541 + 620 + 653 (white)	3 h	[94]
	Ca <sub>2</sub> Sb <sub>2</sub> O <sub>7</sub>	Sm <sup>3+</sup>	orange	770 s	

**Fig. 2.7** Emission spectra of Y<sub>2</sub>O<sub>2</sub>S:Eu<sup>3+</sup><sub>0.05</sub>,Ti<sub>0.04</sub>,Mg<sub>0.02</sub> phosphors (λ<sub>ex</sub> = 365 nm)



*Ce<sup>3+</sup>-Activated Phosphor.* It is well known that the luminescence occurring in Ce<sup>3+</sup>-doped solids mainly corresponds to the optical transitions between the lowest 5*d*<sup>1</sup> excited state to the <sup>2</sup>F<sub>5/2</sub> and <sup>2</sup>F<sub>7/2</sub> levels of the 4*f*<sup>1</sup> ground state. Considering that the 5*d* orbital is sensitive to the host environment, the emission from Ce<sup>3+</sup> ions usually shows broadband. Apart from the signature of broadband, the phenomenon of persistent luminescence has also been observed in Ce<sup>3+</sup>-doped phosphors, where the persistent luminescence was determined to be originating from the Ce<sup>3+</sup> ions (Table 2.4).

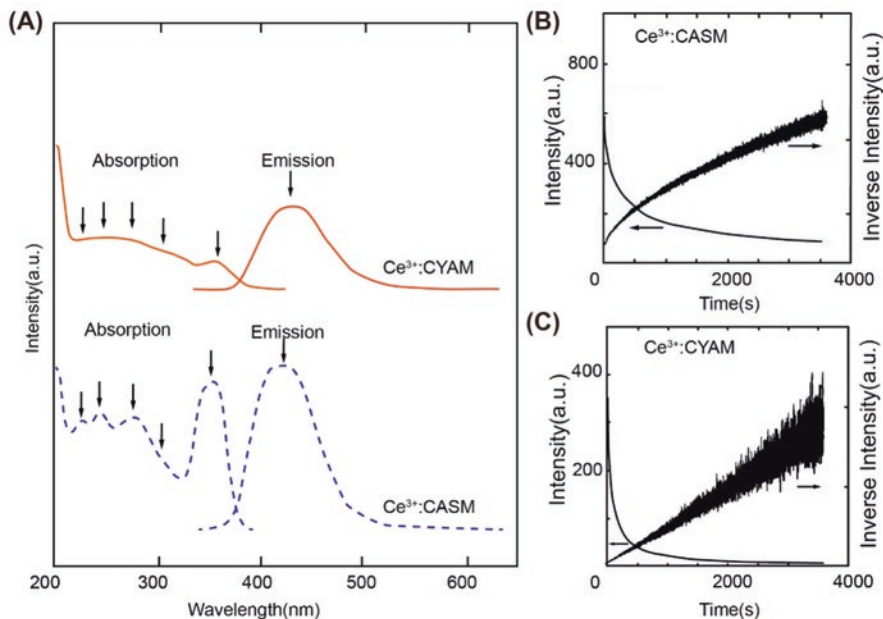


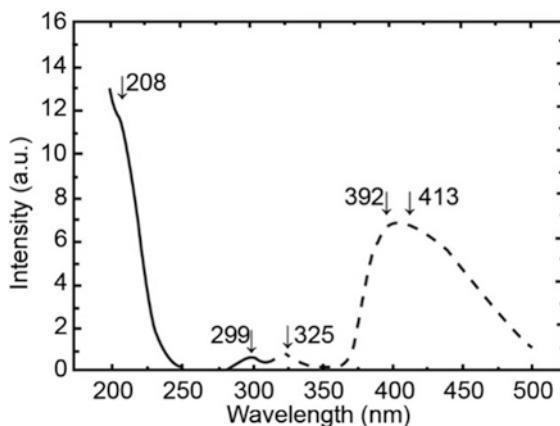
**Fig. 2.8** (a) Absorption spectra of  $\text{Ca}_2\text{Al}_2\text{SiO}_7:\text{Ce}^{3+}$  ( $\text{Ce}^{3+}$ :CASM) and  $\text{CaYAl}_3\text{O}_7:\text{Ce}^{3+}$  ( $\text{Ce}^{3+}$ :CYAM) phosphors and their persistent luminescence spectra after an UV (365 nm) excitation for 300 s. Decay curve and time-dependent inverse afterglow intensity of (b)  $\text{Ca}_2\text{Al}_2\text{SiO}_7:\text{Ce}^{3+}$  (measured at 425 nm) and (c)  $\text{CaYAl}_3\text{O}_7:\text{Ce}^{3+}$  (measured at 417 nm)

In 1999, Nobuhiro Kodama reported the observation of persistent luminescence in  $\text{Ce}^{3+}$ -doped  $\text{Ca}_2\text{Al}_2\text{SiO}_7$  and  $\text{CaYAl}_3\text{O}_7$ . The absorption spectra (Fig. 2.8a) show that these phosphors have five broadbands, which correspond to five energy levels of  $^2\text{D}$  excited state of  $\text{Ce}^{3+}$  ions. Furthermore, it is found that the absorption spectra of  $\text{CaYAl}_3\text{O}_7:\text{Ce}^{3+}$  and  $\text{Ca}_2\text{Al}_2\text{SiO}_7:\text{Ce}^{3+}$  are very similar, only with a slight redshift of absorption spectra in  $\text{CaYAl}_3\text{O}_7:\text{Ce}^{3+}$ . The emission spectra indicate that the emission wavelengths are centered at 417 and 425 nm for  $\text{Ca}_2\text{Al}_2\text{SiO}_7:\text{Ce}^{3+}$  and  $\text{CaYAl}_3\text{O}_7:\text{Ce}^{3+}$ , respectively.

The luminescence decay curves of  $\text{Ca}_2\text{Al}_2\text{SiO}_7:\text{Ce}^{3+}$  at 417 nm and  $\text{CaYAl}_3\text{O}_7:\text{Ce}^{3+}$  at 425 nm are shown in Fig. 2.8b. It is found that both emissions experience a quick decay at the beginning, followed by a slow decay, and the duration times of the persistent luminescence observed in  $\text{Ca}_2\text{Al}_2\text{SiO}_7:\text{Ce}^{3+}$  and  $\text{CaYAl}_3\text{O}_7:\text{Ce}^{3+}$  are over 1 h after the removal of the excitation light. Moreover, the increase in time leads to increased inverse intensity of the persistent luminescence, which is in agreement with the model of electron–hole recombination [56].

One breakthrough in prolonging the afterglow lifetime of  $\text{Ce}^{3+}$  ions was made by Jia et al., who systematically studied the luminescence properties of a collection of  $\text{MAl}_2\text{O}_4:\text{Ce}^{3+}$  ( $\text{M} = \text{Ca}, \text{Sr}, \text{Ba}$ ) phosphors and reported significantly prolonged afterglow durations over 10 h [18, 44–47]. In the case of  $\text{CaAl}_2\text{O}_4:\text{Ce}^{3+}$ , it should be noted that there are three different  $\text{Ca}^{2+}$  sites in  $\text{CaAl}_2\text{O}_4$ , namely 2 six-fold coordinated

**Fig. 2.9** Excitation and emission spectra of  $\text{CaAl}_2\text{O}_4:\text{Ce}^{3+}$  (Excitation spectrum for  $\lambda_{\text{em}} = 325$  nm, emission spectrum for  $\lambda_{\text{ex}} = 299$  nm)



sites and 1 nine-fold coordinated sites. The dopant  $\text{Ce}^{3+}$  ions may substitute any of the aforementioned  $\text{Ca}^{2+}$  sites, thus giving rise to distinct emission and excitation spectra. Let's take the excitation and emission spectra of  $\text{CaAl}_2\text{O}_4:\text{Ce}^{3+}$  for illustration. When the sample is excited by 299 nm UV light, there are three emission bands peaking at 325, 392, and 413 nm, as shown in Fig. 2.9. Considering that six-fold coordination site has shorter lanthanide-anion distance than that of nine-fold site, a larger redshift of lanthanide's  $5d-4f$  emission could be expected when the  $\text{Ce}^{3+}$  replaces six-fold coordinated  $\text{Ca}^{2+}$  ions. Hence, the emission at 325 nm could be ascribed to the nine-fold coordinated  $\text{Ce}^{3+}$  ions, while the emissions at a longer wavelength (392 and 413 nm) could originate from the six-fold coordinated  $\text{Ce}^{3+}$  ions. After removing the UV light,  $\text{CaAl}_2\text{O}_4:\text{Ce}^{3+}$  exhibits a deep blue afterglow, with a lifetime over 10 h.

***Dy<sup>3+</sup>-Activated Phosphor.*** As mentioned in previous chapters,  $\text{Dy}^{3+}$  ions are frequently co-doped into  $\text{Eu}^{2+}$ -activated aluminates and silicates to increase the afterglow lifetime of  $\text{Eu}^{2+}$ . In this section, we will discuss the luminescence properties of  $\text{Dy}^{3+}$ -doped persistent phosphors in which the  $\text{Dy}^{3+}$  ion serves as the emitting center. Given that  $\text{Dy}^{3+}$  ions are capable of emitting blue, green, and red light simultaneously [57], it is believed that  $\text{Dy}^{3+}$ -activated persistent phosphors are highly promising for the realization of white afterglow for the illumination applications (Table 2.7).

Among the hosts under study,  $\text{CdSiO}_3$  lattice renders superior luminescence properties of  $\text{Dy}^{3+}$  ions. For example, Liu et al. reported that  $\text{CdSiO}_3:\text{Dy}^{3+}$  phosphor was able to emit white afterglow, which is generated by mixing three different emissions (420, 486, and 580 nm) rather than producing a monochromatic color [58]. The excitation spectrum shown in Fig. 2.10a indicates that the excitation band centered at 243 nm is ascribed to the host absorption, while the emission spectrum is characterized by strong emission features of  $\text{Dy}^{3+}$  ions, along with the host emission centered at 420 nm indigo blue region. By mixing these different emission light, white light can be achieved (Fig. 2.10b). The afterglow observed in such phosphors can last over 5 h after stopping the UV excitation at 254 nm. In another study, the same group of researchers reported that  $\text{Dy}^{3+}$ -doped  $\text{SrSiO}_3$  was able to produce a

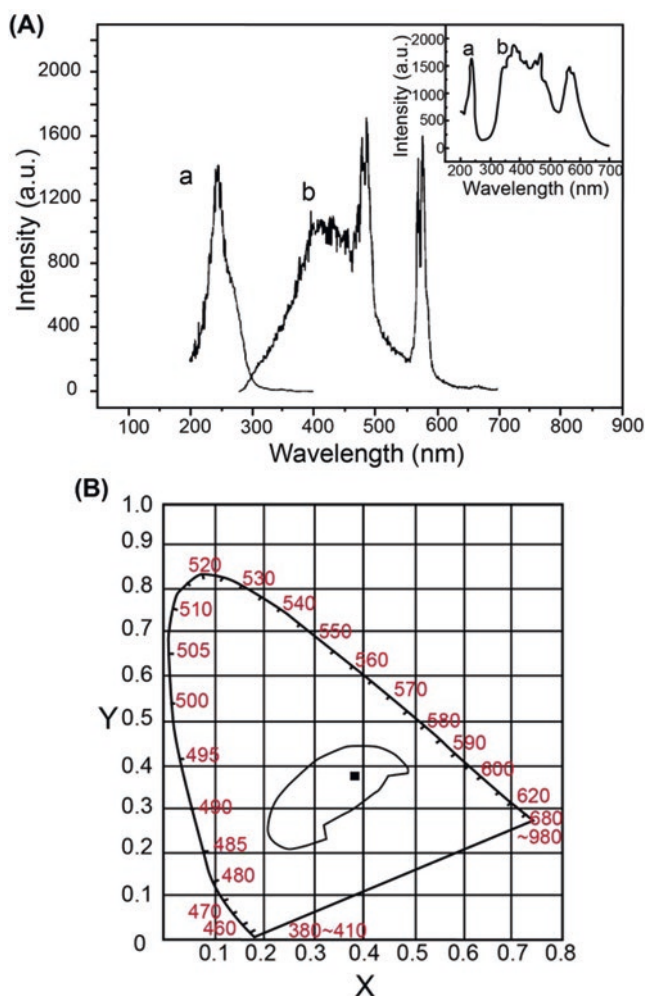
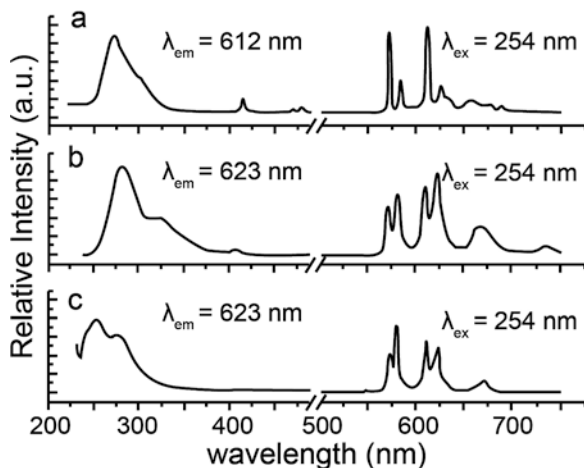


**Fig. 2.10** (a) Excitation (a) and emission spectra (b) of CdSiO<sub>3</sub>:5%Dy. The *inset* shows the luminescence spectra of pure CdSiO<sub>3</sub>. (b) CIE chromaticity coordinates of the emission measured for the synthesized CdSiO<sub>3</sub>:5%Dy

white afterglow, which can last up to 1 h even after irradiating by 254 nm UV for a very short time period (5 min) [59]. Note that the white light observed in CdSiO<sub>3</sub>:Dy<sup>3+</sup> phosphor is a mixture of emissions from both the Dy<sup>3+</sup> ions and the host, whereas the white light in SrSiO<sub>3</sub>:Dy<sup>3+</sup> phosphors is achieved by mixing 480 (<sup>4</sup>F<sub>9/2</sub>-<sup>6</sup>H<sub>15/2</sub>) and 572 nm (<sup>4</sup>F<sub>9/2</sub>-<sup>6</sup>H<sub>13/2</sub>) emissions, which both originate from the Dy<sup>3+</sup> ions. Similarly, such white afterglow could also be obtained in other Dy<sup>3+</sup>-activated phosphors, including CaMgSi<sub>2</sub>O<sub>6</sub>:Dy<sup>3+</sup>, Ca<sub>3</sub>SnSi<sub>2</sub>O<sub>9</sub>:Dy<sup>3+</sup>, Ca<sub>3</sub>MgSi<sub>2</sub>O<sub>8</sub>:Dy<sup>3+</sup>, SrSiO<sub>3</sub>, and Sr<sub>2</sub>SiO<sub>4</sub>:Dy<sup>3+</sup> (Table 2.7) [58–64].

**Fig. 2.11** Excitation (left) and emission (right) spectra of (a)  $\text{Ca}_2\text{SnO}_4\text{:Sm}^{3+}$ , (b)  $\text{Sr}_2\text{SnO}_4\text{:Sm}^{3+}$ , and (c)  $\text{Ba}_2\text{SnO}_4\text{:Sm}^{3+}$



***Sm<sup>3+</sup>-Activated Phosphor.*** **Sm<sup>3+</sup>** ion has been recognized as superior emitters featuring red light emission when incorporated in a given host lattice [65–68]. Over the past few years, considerable efforts have been devoted to the development of **Sm<sup>3+</sup>**-activated phosphors that are able to produce reddish long afterglow (Table 2.6). Among these phosphors under study, hosts of  $\text{M}_2\text{SnO}_4$  ( $\text{M} = \text{Ca}, \text{Sr}, \text{Ba}$ ) enable to achieve reddish-orange afterglow of **Sm<sup>3+</sup>** ions with a lifetime over 7 h (Fig. 2.11) [69]. The excitation spectrum of each sample indicates that the primary emission band of each sample originates from the intrinsic absorption of the host material. Note that different crystal structures and ionic sizes of the alkaline earth ions are responsible for the different shape of the excitation spectra. On the basis of the observed emission spectra, it is found that all the  $\text{M}_2\text{SnO}_4\text{:Sm}^{3+}$  samples have a reddish-orange emission. When it comes to the mechanism underlying the long afterglow, it is believed that the defects in the form of  $\text{V}_{\text{Ca}}$ , **Sn<sup>3+</sup>** and **Sn<sup>2+</sup>** play a crucial role in trapping holes, while the  $\text{Sm}_{\text{Ca}}$  defects are considered as electron traps. Recently, orange afterglow was also reported in **Sm<sup>3+</sup>**-activated  $\text{Ca}_2\text{Sb}_2\text{O}_7$  [70]. However, the afterglow only lasts for 13 min, which is much shorter when compared to the  $\text{M}_2\text{SnO}_4\text{:Sm}^{3+}$  samples.

As compiled in Tables 2.5, 2.6, and 2.7, it is found that the non- $\text{Eu}^{2+}$ -activated aluminates feature the longest afterglow lifetime when compared to other host materials, for example, long-lasting blue emissions up to 10 h were achieved in many  $\text{Ce}^{3+}$ -activated aluminates, such as  $\text{BaAl}_2\text{O}_4$ ,  $\text{CaAl}_2\text{O}_4$ , and  $\text{SrAl}_2\text{O}_4$ . For red-emitting persistent phosphors, silicate hosts are often employed to accommodate the non- $\text{Eu}^{2+}$  emitting centers. In the cases of  $\text{Pr}^{3+}$ -,  $\text{Eu}^{3+}$ -, and  $\text{Sm}^{3+}$ -doped  $\text{CdSiO}_3$ , the lifetime of the red afterglow could reach 5 h.

It should be noted that the abovementioned lanthanide-activated persistent phosphors usually emit light within the visible regime. Despite high brightness and long afterglow lifetime, there are growing demands for persistent phosphors which are able to emit light in the NIR region. Recently, a persistent energy transfer (PET) mechanism has been proposed for explaining the observed NIR emission in  $\text{SrAl}_2\text{O}$

$_4\text{:Eu}^{2+}, \text{Dy}^{3+}, \text{Er}^{3+}$  and  $\text{Ca}_{0.2}\text{Zn}_{0.9}\text{Mg}_{0.9}\text{Si}_2\text{O}_6\text{:Eu}^{2+}, \text{Dy}^{3+}, \text{Mn}^{2+}$  persistent phosphors [71]. The researchers pointed out that the NIR emission originates from the  $\text{Er}^{3+}$  or  $\text{Mn}^{2+}$  ions which are able to absorb the persistently visible emission of the  $\text{Eu}^{2+}$  ions [72]. For instance, Pan et al. reported that an NIR emission centered at 1530 nm can be achieved in the  $\text{SrAl}_2\text{O}_4\text{:Eu}^{2+}, \text{Dy}^{3+}, \text{Er}^{3+}$  persistent phosphors, where the occurrence of persistent NIR emission was ascribed to a continual energy transfer from  $\text{Eu}^{2+}$  ions to  $\text{Er}^{3+}$  ions. Unfortunately, the NIR emission can only last for 10 min due to the limited energy transfer efficiency. More importantly, the inevitable visible persistent luminescence from  $\text{Eu}^{2+}$  ions impedes the further development of such phosphors. To achieve long NIR afterglow, efforts have been devoted in the development of the transition metal-doped materials, which will be discussed in the following parts.

### 2.2.1.3 Summary

In summary, blue, green, red, and white long persistent emission can be realized by adopting particular lanthanide-host combinations. The aluminates and silicates singly doped with lanthanide ions often emit blue or green light, and show excellent persistent luminescence properties, such as high luminescence intensity, long lifetime, and high color purity. On the contrary, the red-emitting persistent phosphors are usually characterized with relatively short decay time and narrow emission bands, which can lead to low color purity.

In an attempt to extend the spectra of the long persistent phosphor to red and NIR regime, co-doping of additional metal ions has been well employed to overcome such problems. Typical red- or NIR-emitting persistent phosphors are usually found to contain co-doped sensitizer–activator pairs, such as  $\text{Eu}^{2+}\text{--Mn}^{2+}$  pair. The  $\text{Eu}^{2+}$  ions not only can participate as an energy source for pumping  $\text{Mn}^{2+}$  emitters through energy transfer, but also can play a crucial role in prolonging the afterglow lifetime. In the case of  $\text{Ca}_9\text{La}(\text{PO}_4)_7\text{:Eu}^{2+}, \text{Mn}^{2+}$ , variation in emission color from green to red can be realized by adjusting the concentration of  $\text{Mn}^{2+}$ , validating the occurrence of energy transfer from  $\text{Eu}^{2+}$  to  $\text{Mn}^{2+}$  [120]. As indicated in Fig. 2.12a, the large degree of spectral overlap between  $\text{Eu}^{2+}$  emission and  $\text{Mn}^{2+}$  excitation leads to efficient energy transfer from  $\text{Eu}^{2+}$  to  $\text{Mn}^{2+}$ . Furthermore, it was found that the emission intensity of  $\text{Mn}^{2+}$  increases with increasing  $\text{Mn}^{2+}$  concentration, while the emission intensity of  $\text{Eu}^{2+}$  indeed decreases with increasing  $\text{Mn}^{2+}$  content (Fig. 2.12b).

The red-emitting long persistent phosphors containing  $\text{Eu}^{2+}\text{--Mn}^{2+}$  pairs are summarized in Table 2.8. Note that most of these phosphors employ silicate and phosphate hosts, and their emission profiles are comprised of several peaks, including the red components centered at 600 nm. The corresponding afterglow lifetimes fall into the range of 0.5–3 h.



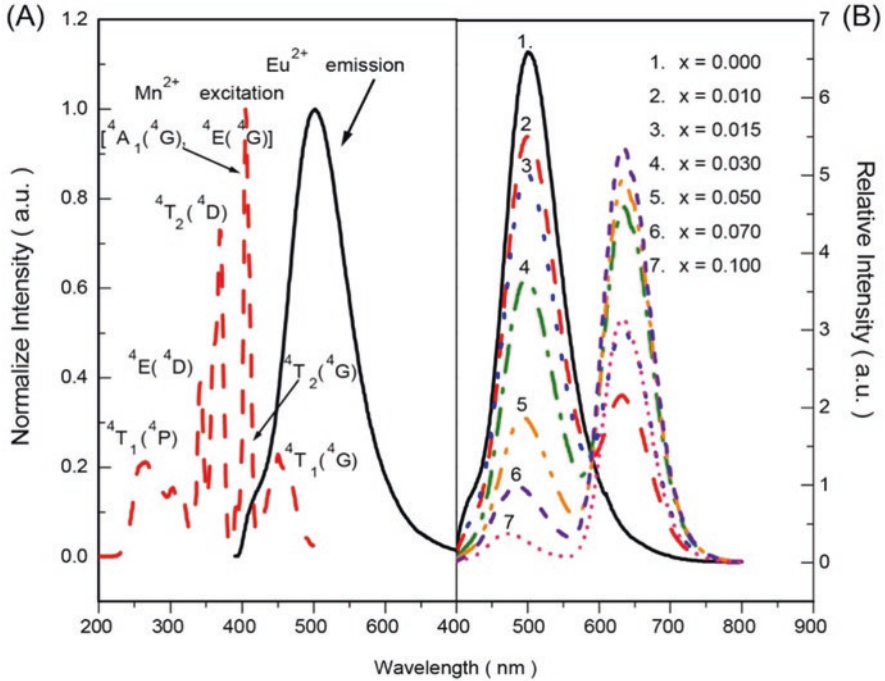


**Fig. 2.12** (a) Emission spectrum of  $\text{Ca}_9\text{La}(\text{PO}_4)_7:\text{Eu}^{2+}$  (solid line) and excitation spectrum of  $\text{Ca}_9\text{La}(\text{PO}_4)_7:\text{Mn}^{2+}$  (dash line), (b) The effect of  $\text{Mn}^{2+}$  concentration on the emission spectra of  $\text{Ca}_9\text{La}(\text{PO}_4)_7:0.005\text{Eu}^{2+}, x\text{Mn}^{2+}$  phosphors [120]

**Table 2.8**  $\text{Eu}^{2+}/\text{Mn}^{2+}$  co-doped phosphors

Host material		Dopants	Maximum emission (nm)	Afterglow duration	References
Phosphate	$\text{Ca}_9\text{La}(\text{PO}_4)_7$	$\text{Eu}^{2+}, \text{Mn}^{2+}$	Disputed		[120]
Silicate	$\text{MgSiO}_3$	$\text{Mn}^{2+}, \text{Eu}^{2+}, \text{Dy}^{3+}$	660	4 h	[121]
	$\text{CaMgSi}_2\text{O}_6$	$\text{Eu}^{2+}, \text{Mn}^{2+}$	450, 580 + 680 (red)	30 min	[122]
	$\text{BaMg}_2\text{Si}_2\text{O}_7$	$\text{Eu}^{2+}, \text{Mn}^{2+}$	400, 630–680 (reddish)	30 min	[123]
	$\text{Sr}_3\text{Mg}_2\text{Si}_2\text{O}_8$	$\text{Eu}^{2+}, \text{Mn}^{2+}$	457, 670	2 h	[124]
	$\text{Ca}_{0.5}\text{Zn}_{0.9}\text{Mg}_{0.9}\text{Si}_2\text{O}_6$	$\text{Eu}^{2+}, \text{Mn}^{2+}$	450, 580 + 680 (near IR)	1 h	[125]
	$\text{CaAl}_2\text{Si}_2\text{O}_8$	$\text{Eu}^{2+}, \text{Mn}^{2+}$	418, 580 (blue)	1 h	[126]
Phosphoric oxide	$\text{SrMg}_2\text{P}_2\text{O}_8$	$\text{Eu}^{2+}, \text{Mn}^{2+}$	678	Disputed	[127]
	$\text{SrMgP}_2\text{O}_7$	$\text{Eu}^{2+}, \text{Mn}^{2+}$	675		
	$\text{Sr}_2\text{Mg}_3\text{P}_4\text{O}_{15}$	$\text{Eu}^{2+}, \text{Mn}^{2+}$	616		
Aluminate	$\text{CaAl}_2\text{O}_4$	$\text{Eu}^{2+}, \text{Mn}^{2+}$	440 (blue)	3 h	[128]



## 2.2.2 Transition Metal-Activated Persistent Phosphor

Similar to lanthanide ions, transition metal ions have also been widely used as emitting centers when embedded in inorganic solids.  $\text{Mn}^{2+}$  ion is the most studied among all transition metal ions. According to the published data,  $\text{Mn}^{2+}$  ion has been successfully doped in hundreds of inorganic hosts, suggesting that the synthesis approaches are well established. These synthetic techniques thus could be transplanted to the preparation of  $\text{Mn}^{2+}$ -activated persistent phosphors.  $\text{Cr}^{3+}$  ion has become to play due to its capability in emitting red and NIR light. In this section, we will focus on the luminescence properties of the long persistent phosphors, in which the  $\text{Mn}^{2+}$  and  $\text{Cr}^{3+}$  ions serve as emission centers.

### 2.2.2.1 $\text{Mn}^{2+}$ -Activated Phosphor

It is well known that  $\text{Mn}^{2+}$ -activated phosphors are generally characterized by high luminescence efficiency and brilliant luminescence color. Moreover, the  $\text{Mn}^{2+}$  emitting ion can be easily excited by various sources, such as X-ray, electron bombardment, UV irradiation, and electric field [129–131]. All these optical characteristics thus make  $\text{Mn}^{2+}$  ion potential contender as an efficient activator of long persistent phosphors. More importantly, by varying the coordination environment,  $\text{Mn}^{2+}$  ion presents a wide optical tunability over emission wavelength. For example,  $\text{Mn}^{2+}$  ion is able to emit green and red light when it is tetrahedrally and octahedrally coordinated, respectively [131, 132]. In the following part, we will discuss the luminescence properties of  $\text{Mn}^{2+}$ -activated persistent phosphors based on the types of the hosts.

*Silicate, Aluminate, and Germinate.* Similar to  $\text{Eu}^{2+}$ -activated long persistent phosphors, silicates and aluminates are also widely used as hosts for  $\text{Mn}^{2+}$ -emitting ions (Table 2.9). Among these hosts, the alkaline earth aluminates and magnesium silicates are of great interest.

*Silicate Aluminate.* Three  $\text{Mn}^{2+}$ -activated persistent phosphors, namely  $\text{Ca}_2\text{Al}_2\text{SiO}_7:\text{Ce}^{3+},\text{Mn}^{2+}$ ,  $\text{CaAl}_2\text{O}_4:\text{Ce}^{3+},\text{Mn}^{2+}$ , and  $\text{MgSiO}_3:\text{Mn}^{2+},\text{Eu}^{2+},\text{Dy}^{3+}$ , were reported by Wang et al. in 2003 [121]. The excitation and emission spectra of these samples indicate that the emissions originate from the  $\text{Mn}^{2+}$  ions that are excited by the energy transferred from the lanthanide ions. By comparing the excitation and emission spectra of  $\text{CaAl}_2\text{O}_4:\text{Ce}^{3+}$  with its co-doped counterpart (Fig. 2.13), it is found that the emission from  $\text{Ce}^{3+}$  ions disappear when  $\text{Mn}^{2+}$  ions exist, thus suggesting an effective energy transfer from  $\text{Ce}^{3+}$  to  $\text{Mn}^{2+}$ .

*Silicate.* In comparison with aluminate-based phosphors, silicate-based phosphors have better resistance against moisture, and are able to render emitting ions with various emission colors. Hence, the development of superior persistent phosphors using silicate hosts has recently become the focus of much research [10, 23, 133–136].

*Cadmium Silicate.* Despite the early usage of  $\text{CdSiO}_3:\text{Mn}^{2+}$  luminescent phosphor in fluorescent lamps, it was not until 2004 that the long persistent luminescence phenomenon was reported by Lei et al. [137]. The researchers demonstrated

**Table 2.9** Mn<sup>2+</sup>-activated long persistent phosphors

Host material		Dopants	Afterglow maximum (nm)	Afterglow duration	References
Silicate	Ca <sub>2</sub> Al <sub>2</sub> SiO <sub>7</sub>	Ce <sup>3+</sup> , Mn <sup>2+</sup>	550 (yellow)	10 h	[121]
	CdSiO <sub>3</sub>	Mn <sup>2+</sup>	575–583 (orange)	1–5 h	[143]
		Eu <sup>3+</sup> , Mn <sup>2+</sup>	587, 610 (orange)	1 h	[103]
		Mn <sup>2+</sup> , Tb <sup>3+</sup>	486 + 548, 587 (orange)	1 h	[102]
	CaMgSi <sub>2</sub> O <sub>6</sub>	Mn <sup>2+</sup>	680	1 h	[140]
	SrMgSi <sub>2</sub> O <sub>6</sub>	Mn <sup>2+</sup>	455, 612 (pink)	15 min	[82]
	BaMg <sub>2</sub> Si <sub>2</sub> O <sub>7</sub>	Mn <sup>2+</sup>	630–680 (red)	30 min	[104]
	Mg <sub>2</sub> SiO <sub>4</sub>	Mn <sup>2+</sup>	650 (red)	20 min	[144]
	MgSiO <sub>3</sub>	Mn <sup>2+</sup> , Eu <sup>2+</sup> , Dy <sup>3+</sup>	660 (red)	4 h	[121]
Aluminate	CaAl <sub>2</sub> O <sub>4</sub>	Ce <sup>3+</sup> , Mn <sup>2+</sup>	520 (green)	10 h	[121]
	CaAl <sub>2</sub> O <sub>4</sub>	Eu <sup>2+</sup> → Mn <sup>2+</sup>	440 (blue)	3 h	[128]
	SrAl <sub>2</sub> O <sub>4</sub>	Ce <sup>3+</sup> , Mn <sup>2+</sup>	375, 515 (green)	5 h	[85]
	Y <sub>3</sub> Al <sub>5</sub> O <sub>12</sub>	Mn <sup>2+</sup>	585 (orange)	18 min	[145]
Phosphate	Zn <sub>3</sub> (PO <sub>4</sub> ) <sub>2</sub>	Mn <sup>2+</sup> , Zr <sup>4+</sup>	616 (red)	3 h	[142]
	Ca <sub>3</sub> (PO <sub>4</sub> ) <sub>2</sub>	Mn <sup>2+</sup>	634–660 (red)	1 h	[146]
	Ca <sub>9</sub> Lu(PO <sub>4</sub> ) <sub>7</sub>	Mn <sup>2+</sup>	660 (red)	20 min	[91]
	Ca <sub>9</sub> Gd(PO <sub>4</sub> ) <sub>7</sub>	Mn <sup>2+</sup>	660 (red)	20 min	[91]
Other	CaZnGe <sub>2</sub> O <sub>6</sub>	Mn <sup>2+</sup>	648 (red)	3 h	[147]
	ZnGa <sub>2</sub> O <sub>4</sub>	Mn <sup>2+</sup>	504 (green)	15 min	[148]
	Zn <sub>2</sub> GaO <sub>4</sub>	Mn <sup>2+</sup>	528 (green)	2 h	[149]
	MgGeO <sub>3</sub>	Mn <sup>2+</sup>	650–670 (red)	30 min	[150]
	Mg/ZnGa <sub>2</sub> O <sub>4</sub>	Mn <sup>2+</sup>	505 (green)	15 min	[148]
	Mg <sub>2</sub> SnO <sub>4</sub>	Mn <sup>2+</sup>	500 (green)	5 h	[151]
	Cd <sub>2</sub> Ge <sub>7</sub> O <sub>16</sub>	Mn <sup>2+</sup>	585 (orange)	3 h	[152]

that the Mn<sup>2+</sup>-activated CdSiO<sub>3</sub> phosphor shows orange persistent luminescence centered at 575 nm after the excitation of UV at 254 nm, and the afterglow can last for 1 h [103]. Furthermore, they also found that the afterglow lifetime of CdSiO<sub>3</sub>:Mn<sup>2+</sup> phosphor can be prolonged by introducing additional lanthanide ions, including Y<sup>3+</sup>, La<sup>3+</sup>, Gd<sup>3+</sup>, and Lu<sup>3+</sup> (Fig. 2.14). The prolonged afterglow lifetime was ascribed to codopant-induced electron traps. As shown in Fig. 2.14, energy transfer from Gd<sup>3+</sup> to Mn<sup>2+</sup> boosts the afterglow of CdSiO<sub>3</sub>:Mn<sup>2+</sup>, Gd<sup>3+</sup> phosphor as evidenced by the changes in the decay rates.

*Alkali Earth Silicate.* Given the efficient energy transfer from Eu<sup>2+</sup> to Mn<sup>2+</sup>, the blue-emitting long persistent phosphors BaMg<sub>2</sub>Si<sub>2</sub>O<sub>7</sub>:Eu<sup>2+</sup>, Dy<sup>3+</sup> and Ca<sub>2</sub>MgSi<sub>2</sub>O<sub>7</sub>:E

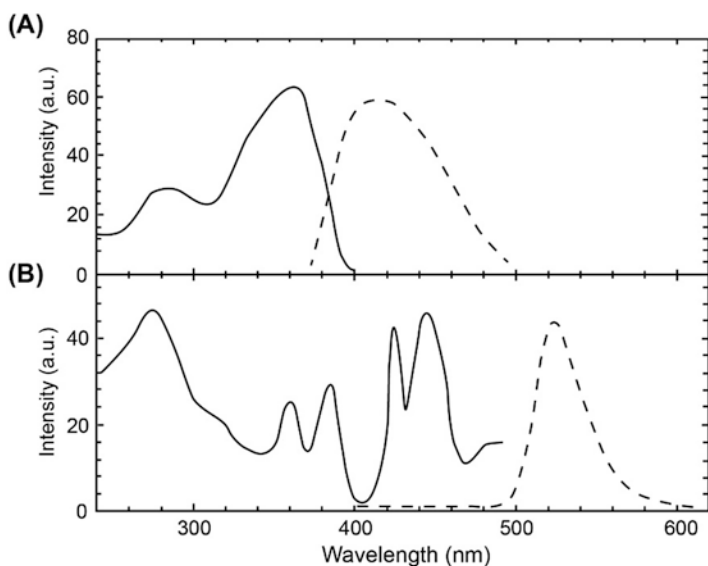


**Fig. 2.13** Emission (dash line) and excitation (solid line) spectra of (a)  $\text{CaAl}_2\text{O}_4:\text{Ce}^{3+}$  and (b)  $\text{CaAl}_2\text{O}_4:\text{Ce}^{3+}, \text{Mn}^{2+}$

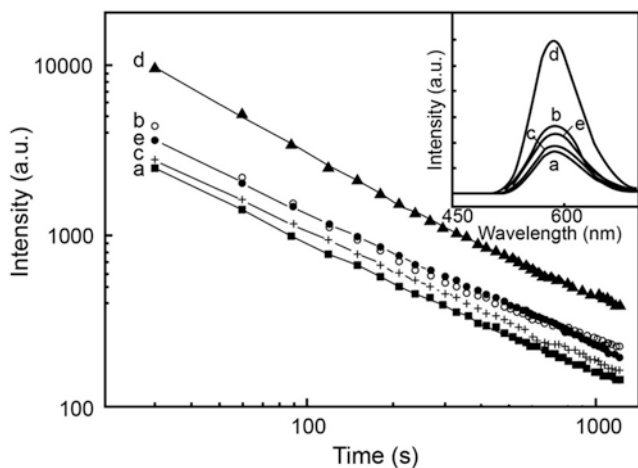


**Fig. 2.14** The persistent luminescence decay curves of  $\text{CdSiO}_3:\text{Mn}^{2+}$  and lanthanide co-doped  $\text{CdSiO}_3:\text{Mn}^{2+}$ . The inset shows the corresponding luminescence spectra after the removal of UV light (a, b, c, and d represent  $\text{CdSiO}_3:\text{Mn}^{2+}$  co-doped with  $\text{Y}^{3+}$ ,  $\text{La}^{3+}$ ,  $\text{Gd}^{3+}$ , and  $\text{Lu}^{3+}$ , respectively)

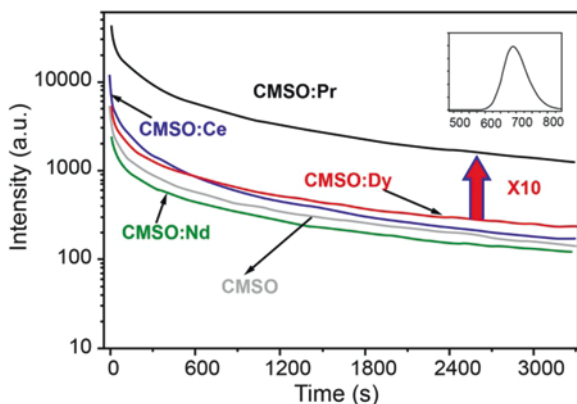
$\text{u}^{2+}, \text{Dy}^{3+}$  can be turned into red-emitting phosphors by introducing  $\text{Mn}^{2+}$  ions. The resulted red afterglow arises from the spin-forbidden transitions within the d-manifold of  $\text{Mn}^{2+}$  ions ( ${}^4\text{T}_1({}^4\text{G}) \rightarrow {}^6\text{A}_1({}^6\text{S})$ ) [23, 136, 138, 139]. Apart from sensitizer  $\text{Eu}^{2+}$  ion,  $\text{Ce}^{3+}$  has also been demonstrated to be capable of serving as a sen-

sitizer in the case of  $\text{BaMg}_2\text{Si}_2\text{O}_7:\text{Mn}^{2+}, \text{Ce}^{3+}$  phosphor. It was found that co-doping of  $\text{Ce}^{3+}$  can prolong the lifetime of  $\text{Mn}^{2+}$ -associated red afterglow over 2 h. Such prolonged emission lifetime benefits from the host structure, in which the  $\text{Mn}^{2+}$  ions can substitute two different  $\text{Mg}^{2+}$  sites, thus leading to two types of traps (trap I and II) with different trap depth. The trap I plays a positive role in prolonging the lifetime of the red afterglow, whereas trap II works negatively.

$\text{Ca}_{0.2}\text{Zn}_{0.9}\text{Mg}_{0.9}\text{Si}_2\text{O}_6$  with the crystalline structure of diopside has also been reported to serve as host of  $\text{Mn}^{2+}$ -activated long persistent phosphor. In 2007, Daniel et al. successfully prepared the diopside-based persistent phosphor  $\text{Ca}_{0.2}\text{Zn}_{0.9}\text{Mg}_{0.9}\text{Si}_2\text{O}_6:\text{Eu}^{2+}, \text{Mn}^{2+}, \text{Dy}^{3+}$  in the form of nanoparticles [71]. In this doped system,  $\text{Eu}^{2+}$ ,  $\text{Mn}^{2+}$ , and  $\text{Dy}^{3+}$  ions serve as sensitizers, emitters, and trapping centers, respectively. In a following paper, the same group of researchers systematically studied the effect of additional trivalent lanthanide ions  $\text{Ln}^{3+}$  ( $\text{Ln} = \text{Dy}, \text{Pr}, \text{Ce}, \text{Nd}$ ) acting as electron traps on the luminescence properties of  $\text{Mn}^{2+}$ -doped diopside persistent phosphors [140]. It was found that in the diopside lattice, incorporation of  $\text{Pr}^{3+}$  dopant can significantly enhance the persistent luminescence of  $\text{Ca}_{0.2}\text{Zn}_{0.9}\text{Mg}_{0.9}\text{Si}_2\text{O}_6:\text{Eu}^{2+}, \text{Mn}^{2+}$ ,  $\text{Pr}^{3+}$  upon X-ray irradiation, which is benefitting from the optimal trap depth for room temperature persistent luminescence (Fig. 2.15). More importantly, after UV light excitation, the emission spectrum of tri-doped  $\text{Ca}_{0.2}\text{Zn}_{0.9}\text{Mg}_{0.9}\text{Si}_2\text{O}_6:\text{Eu}^{2+}, \text{Mn}^{2+}, \text{Pr}^{3+}$  has two emission bands centered at 580 and 685 nm (Fig. 2.16), which originate from two different  $\text{Mn}^{2+}$  sites caused by the substitution of  $\text{Mg}^{2+}$  and  $\text{Ca}^{2+}$  cations. Note that the emission wavelengths fall into the near-infrared optical region, thus allowing for deep tissue penetration. By combining the nature of the long afterglow with the small particle size, this phosphor is highly promising for deep tissue bioimaging without external illumination.

Apart from adopting the aforementioned hosts, afterglow phenomena have also been observed in zinc alumino-silicate ceramic and zinc borosilicate glass when doped with  $\text{Mn}^{2+}$  ions. The former presents long green afterglow, while the latter features long red afterglow. In addition, red afterglow was also observed in

**Fig. 2.15** Decay curves of co-doped  $\text{CaMgSi}_2\text{O}_6:\text{Eu}^{2+}, \text{Mn}^{3+}$  and tri-doped  $\text{CaMgSi}_2\text{O}_6:\text{Eu}^{2+}, \text{Mn}^{3+}, \text{Ln}^{3+}$  ( $\text{Ln} = \text{Dy}, \text{Pr}, \text{Ce}, \text{Nd}$ ) phosphors recorded after 10 min X-ray irradiation. CMSO represents  $\text{CaMgSi}_2\text{O}_6:\text{Eu}^{2+}, \text{Mn}^{3+}$ . The inset shows the emission spectrum



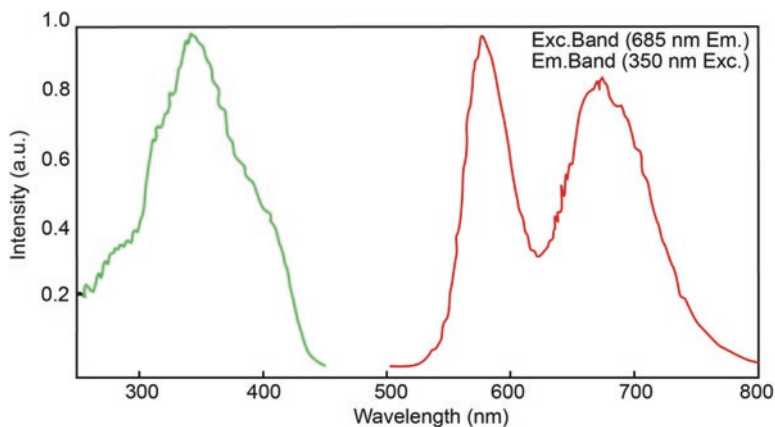


**Fig. 2.16** Excitation (green) and emission (red) spectra of  $\text{Ca}_{0.2}\text{Zn}_{0.9}\text{Mg}_{0.9}\text{Si}_2\text{O}_6:\text{Eu}^{2+},\text{Mn}^{2+},\text{Pr}^{3+}$ . Persistent luminescence spectrum was recorded with a delayed time of 5 ms. The excitation spectrum was recorded corresponding to the emission at 685 nm

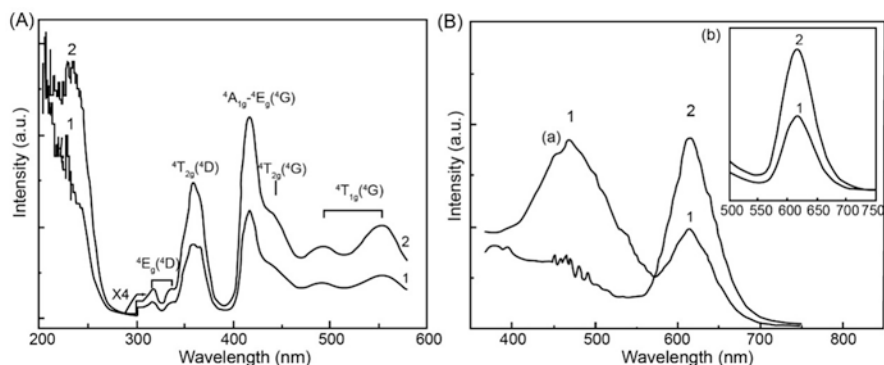


**Fig. 2.17** Excitation (a) and emission (b) spectra of  $\text{Zn}_3(\text{PO}_4)_2:0.05\text{Mn}^{2+},0.03\text{Zr}^{4+}$  (curve 1) and  $\text{Zn}_3(\text{PO}_4)_2:0.05\text{Mn}^{2+}$  (curve 2). The excitation spectra were recorded by measuring the emission at 616 nm, while the emission spectra were recorded after irradiation of 240 nm (a) and 418 nm (b)

$\text{MgGeO}_3:\text{Mn}^{2+},\text{Yb}^{3+}$  and  $\text{MgSiO}_3:\text{Eu}^{2+},\text{Mn}^{2+},\text{Dy}^{3+}$ . Compared with the silicate and silicate aluminate singly doped with  $\text{Mn}^{2+}$ , the counterparts co-doped with additional lanthanide ions show much longer afterglow lifetime up to 10 h.

**Phosphate.** In 2014, long red afterglow phenomenon was first reported in  $\text{Mn}^{2+}$ -doped polycrystalline  $\beta\text{-Zn}_3(\text{PO}_4)_2$  by the group of Su [141]. The resulted red afterglow centered at 616 nm remained visible to human eyes for 2 h after removal of excitation of 418 nm light. By co-doping  $\text{Zr}^{4+}$  ions into  $\beta\text{-Zn}_3(\text{PO}_4)_2$  phosphor, the same group of researchers found that the afterglow with enhanced brightness can last up to 3 h (Fig. 2.17) [142]. However, they also found a blue emission with low intensity ( $\lambda_{\text{em}} = 475 \text{ nm}$ ), which was ascribed to the codopant  $\text{Zr}^{4+}$ .

### 2.2.2.2 Cr<sup>3+</sup>-Activated Phosphor

The past two decades have witnessed a great success in developing long persistent phosphors featuring visible light emission with high brightness and long afterglow lifetime. However, it was not until a few years ago that the researchers discovered the long persistent phosphors with near-infrared (NIR) emission (700–2500 nm) that lasts from several minutes to several hours [71, 72, 153–155]. This is largely due to the lack of trapping systems which can be thermally activated at room temperature. Recently, there has been a steady increase in exploring IR- and NIR-emitting persistent phosphors, principally due to their various applications, including labeling, security, and military utilizations. To extend the long afterglow emission to the IR or NIR regions, selecting appropriate host-emitter pairs are significantly crucial.

Trivalent chromium Cr<sup>3+</sup> ions are found to be able to present NIR long afterglow when doped into inorganic solids. In general, the observed narrow-band emission centered at 700 nm usually results from the spin-forbidden <sup>2</sup>E-<sup>4</sup>A<sub>2</sub> transition, while the broadband emission from 650 to 1600 nm is the consequence of the spin-allowed <sup>4</sup>T<sub>2</sub>-<sup>4</sup>A<sub>2</sub> transition [156, 157]. Among various host materials, gallate hosts have been widely employed to accommodate Cr<sup>3+</sup> ions for achieving red or NIR afterglow as the Cr<sup>3+</sup> has an identical ionic radius of the host Ga<sup>3+</sup> cation. As aforementioned, choosing appropriate emitters is also crucial for the realization of long persistent phosphors with particular emission wavelength. The lanthanide emitters have been demonstrated to be inappropriate for the generation of NIR afterglow because of their high 5d energy levels and inevitable visible emissions [158]. Although the lanthanide ions are not suitable to be used as an emitter, they can serve as trapping centers to prolong the lifetime of NIR afterglows. For example, Jia et al. systematically investigated the luminescence properties of a collection of Cr<sup>3+</sup>-activated persistent phosphors La<sub>3</sub>Ga<sub>5</sub>GeO<sub>14</sub>:Cr<sup>3+</sup>,M (M = Li, Pb<sup>2+</sup>, Zn<sup>2+</sup>, Eu<sup>3+</sup>, Tm<sup>3+</sup>, and Dy<sup>3+</sup>). They found that the Cr<sup>3+</sup>-associated NIR afterglow (700–1100 nm) can last over 8 h by co-doping of Dy<sup>3+</sup> ions. Moreover, both the intensity and the lifetime of the afterglow can be tuned by choosing different codopants. Another suitable host material for Cr<sup>3+</sup> emitter is ZnGa<sub>2</sub>O<sub>4</sub> compound crystallizing in a cubic AB<sub>2</sub>O<sub>4</sub> spinel structure with *Fd* $\bar{3}m$  (O<sub>h</sub><sup>7</sup>) space group. Note that Zn<sup>2+</sup> and Gd<sup>3+</sup> ions occupy the tetrahedral A-sites and the octahedral B-sites, respectively. In 2011, Aurélie Bessière et al. reported that the doped system ZnGa<sub>2</sub>O<sub>4</sub>:Cr<sup>3+</sup> can emit bright red light (650–750 nm) upon UV excitation [155]. The ZnGa<sub>2</sub>O<sub>4</sub>-based phosphor also shows good chemical and thermal stabilities. Interestingly, color-tunable emission can be achieved in the doped ZnGa<sub>2</sub>O<sub>4</sub> by choosing specific transition metal ions [131, 159–165].

Co-doping strategy has also been widely used to enhance the luminescence intensity of Cr<sup>3+</sup>-activated ZnGa<sub>2</sub>O<sub>4</sub> persistent phosphors. For example, both incorporation of oxides In<sub>2</sub>O<sub>3</sub> and co-doping of Li<sup>+</sup> can lead to enhanced emission intensity [166]. Additionally, the emission can also be modified through variation of the ratio of Zn component, as illustrated in the work of Huang et al. and Bessiere et al. where Zn deficiency-reinforced long red afterglow was observed. In addition to

**Table 2.10** Cr<sup>3+</sup>-activated long persistent phosphors

Host material		Dopants	Afterglow maximum (nm)	Afterglow duration	References
Gallate	Zn <sub>3</sub> Ga <sub>2</sub> Sn <sub>1</sub> O <sub>8</sub>	Cr <sup>3+</sup>	600–800 (peaking at 713)	300 h	[173]
	LiGa <sub>5</sub> O <sub>8</sub>	Cr <sup>3+</sup>	716 (NIR)	1000 h	[170]
	La <sub>3</sub> Ga <sub>5</sub> GeO <sub>14</sub>	Cr <sup>3+</sup>	700–1100 (NIR)	8 h	[154]
	ZnGa <sub>2</sub> O <sub>4</sub>	Cr <sup>3+</sup>	650–750		[155]
	Zn <sub>3</sub> Ga <sub>2</sub> Ge <sub>2</sub> O <sub>10</sub>	Cr <sup>3+</sup>	650–1000	360 h	[177]
	SrO	Pb <sup>2+</sup>	390 (UV)	1 h	[109]
Non-gallate	Zn <sub>2</sub> SnO <sub>4</sub>	Cr <sup>3+</sup>	650–1200		

La<sub>3</sub>Ga<sub>5</sub>GeO<sub>14</sub> and ZnGa<sub>2</sub>O<sub>4</sub> hosts, afterglow phenomenon has also been reported in other Cr<sup>3+</sup>-doped gallates, such as La<sub>3</sub>Ga<sub>5</sub>GeO<sub>14</sub>:Cr<sup>3+</sup>, LiGa<sub>5</sub>O<sub>8</sub>:Cr<sup>3+</sup>, Ga<sub>2</sub>O<sub>3</sub>:Cr<sup>3+</sup>, Gd<sub>3</sub>Ga<sub>5</sub>O<sub>12</sub>:Cr<sup>3+</sup>, Zn<sub>3</sub>Ga<sub>2</sub>SnO<sub>8</sub>:Cr<sup>3+</sup>, MgGa<sub>2</sub>O<sub>4</sub>:Cr<sup>3+</sup>, Ca<sub>3</sub>Ga<sub>2</sub>Ge<sub>3</sub>O<sub>12</sub>:Cr<sup>3+</sup>, and SrGa<sub>12</sub>O<sub>19</sub>:Cr<sup>3+</sup> (Table 2.10) [140, 154, 167–176].

Another attractive demonstration is the use of Cr<sup>3+</sup>-doped zinc gallogermanates to achieve incredibly long NIR afterglow (650–1000 nm) over 360 h [177]. These samples have the formula of Zn<sub>x</sub>Ga<sub>y</sub>Ge<sub>z</sub>O<sub>(x+(3y/2)+2z)</sub>:tCr<sup>3+</sup>,mR, where R represents alkaline earth ions, lanthanide ions, or Li<sup>+</sup> ions; x, y, and z are integers ranging from 1 to 5; t is ranging from 0.01 to 5 mol%; and m varies from 0 to 5 mol%. Finding from this study indicates that phosphors with any combination of these variables can exhibit strong NIR emission (650–1000 nm) and long afterglow lifetime. It is noteworthy that these phosphors can be rapidly, effectively, and repeatedly charged through exposure to sunlight under any of the outdoor conditions. After irradiation with sunlight for several seconds or minutes, these phosphors can show persistent NIR light emission over 2 weeks. On the basis of the superior optical properties, these NIR-emitting long persistent phosphors can be potentially applied for light harvesting in solar energy and in vivo bioimaging.

Let us consider the sample Zn<sub>3</sub>Ga<sub>2</sub>Ge<sub>2</sub>O<sub>10</sub>:0.5%Cr<sup>3+</sup>. As shown in Fig. 2.18, under excitation at 400 nm, the doped sample shows a broadened emission from 650 to 1000 nm, peaking at 696 nm. The researchers pointed out that the strong electron-phonon coupling in Cr<sup>3+</sup>-doped zinc gallogermanates is responsible for the broadening of the <sup>2</sup>E-<sup>4</sup>A<sub>2</sub> emission, while the broadening in <sup>4</sup>T<sub>2</sub>-<sup>4</sup>A<sub>2</sub> emission arises from the disordered Cr<sup>3+</sup> sites in the gallogermanate system. By inspecting the excitation spectrum of the phosphor and the spectrum of the solar light, a large degree of overlap between these two spectra from 300 to 650 nm indicates that the Zn<sub>3</sub>Ga<sub>2</sub>Ge<sub>2</sub>O<sub>10</sub>:0.5% Cr<sup>3+</sup> phosphor could be effectively activated through solar radiation.

Apart from the intense and broad NIR emission, another important optical property of Zn<sub>3</sub>Ga<sub>2</sub>Ge<sub>2</sub>O<sub>10</sub>:0.5%Cr<sup>3+</sup> phosphor is the ultra-long afterglow lifetime. Figure 2.19a shows the persistent luminescence decay curve of a Zn<sub>3</sub>Ga<sub>2</sub>Ge<sub>2</sub>O<sub>10</sub>:0.5% Cr<sup>3+</sup> ceramic disc monitored at 713 nm after irradiation by 365 nm light for 5 min. It is found that the afterglow intensity experiences a quick decrease in the first several hours, followed by a slow decrease. Surprisingly, the afterglow intensity is



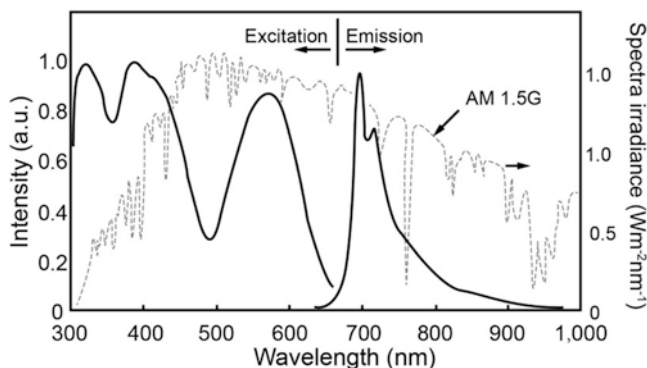


**Fig. 2.18** Normalized excitation and emission spectra of  $\text{Zn}_3\text{Ga}_2\text{Ge}_2\text{O}_{10}:0.5\%\text{Cr}^{3+}$  phosphor. The emission spectrum is collected upon excitation of 400 nm light, and the excitation spectrum is recorded by measuring at 713 nm emission. Note that the gray dashed line depicts the solar spectrum obtained at the Earth's surface at the air mass 1.5 global (AM 1.5G) condition

still greatly higher than the light limit that is perceivable by naked eyes ( $0.32 \text{ mcd/cm}^2$ ) even after 100 h. On the basis of the luminescence spectra recorded at different times (upper inset of Fig. 2.19a), one could infer that the NIR afterglow luminescence originates from the  $\text{Cr}^{3+}$  ions and covers the whole emission band as the shapes of the spectra do not change with decay time. The decay curve plotted in the bottom inset of Fig. 2.19a indicates a good linear relationship between reciprocal afterglow intensity  $I^{-1}$  and time  $t$  at the 20–100 h time period, suggesting that the long persistent NIR luminescence in  $\text{Zn}_3\text{Ga}_2\text{Ge}_2\text{O}_{10}:0.5\% \text{Cr}^{3+}$  phosphor probably arises from tunneling-related processes. Although the emission intensity decreases with increasing decay time (Fig. 2.19b–h), the afterglow remains visible to naked eye even after 360 h. More interestingly, the decayed phosphors can regain their luminescence properties upon heat stimulation (Fig. 2.19i).

Most recently, red emission has also been observed in a new compound  $\text{Zn}_{1+x}\text{Ga}_{2-2x}(\text{Ge},\text{Sn})_x\text{O}_4:\text{Cr}^{3+}$  ( $0 \leq x \leq 0.5$ ), where germanium and tin ions were introduced to partially substitute the host cations. Among all synthesized multi-composition phosphors, the phosphor shows the most intensive red emission and longest afterglow lifetime when the value of  $x$  reaches 0.1 [168].

It is well accepted that lattice defects play a crucial role in the determination of afterglow intensity and duration. The hosts containing particular defects thus potentially allow the realization of ultra-long persistent luminescence. Aside from the gallate,  $\text{Zn}_2\text{SnO}_4$  can also serve as a suitable host lattice for  $\text{Cr}^{3+}$  emitters to achieve ultra-long NIR afterglow. Here, let us consider the defects in  $\text{Zn}_2\text{SnO}_4$  host in an effort to understand how the defect influences the afterglow intensity and lifetime.  $\text{Zn}_2\text{SnO}_4$  possesses a typical inverse spinel crystal structure (Fig. 2.20a, b), where all the  $[\text{Sn}^{\text{VI}}]$  cations and half of the  $[\text{Zn}^{\text{VI}}]$  cations occupy the octahedral sites, and the rest of the  $[\text{Zn}^{\text{IV}}]$  cations occupy the tetrahedral sites. In such structural configuration, it is easy to replace the  $[\text{Sn}^{\text{VI}}]$  or  $[\text{Zn}^{\text{VI}}]$  at octahedral sites with the dopants possessing similar atomic radii, such as aluminum, chromium, gallium, and others.



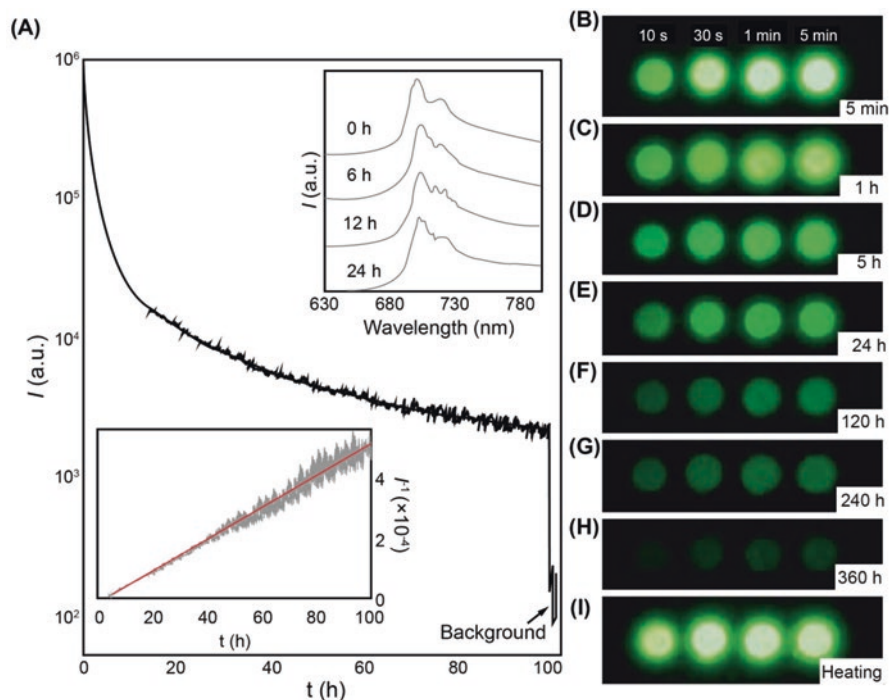


**Fig. 2.19** NIR afterglow decay of  $\text{Zn}_3\text{Ga}_2\text{Ge}_2\text{O}_{10}:0.5\% \text{Cr}^{3+}$  discs excited by a 4 W 365 nm ultra-violet lamp. (a) 713 nm afterglow decay curve of the phosphor after 5 min irradiation. The *inset* located at the *bottom* plots the same data which describe the correlation of reciprocal persistent luminescence intensity ( $I^{-1}$ ) with time ( $t$ ). The *upper inset* displays four afterglow spectra recorded at 0, 6, 12, and 24 h after removal of excitation source. (b–h) NIR images of four phosphor discs taken at different times (5 min to 360 h) after irradiation with 365 nm light for 10 s to 5 min. Note that the discs were placed on a hot plate surface for imaging. Imaging parameters: (b–d) auto/ISO 200/0.3–4 s, (e) manual/ISO 200/30 s, (f–h) manual/ISO 400/30 s. (i) NIR image of the four 360-h-decayed discs upon heating to 400 °C on the hot plate. Imaging parameters: auto/ISO 200/0.3 s

Based on the nature of the host lattice, antisite defects ( $\text{Sn}_{\text{Zn}}$  and  $\text{Zn}_{\text{Sn}}$ ) and substitution defects ( $\text{Sn}_{\text{Cr}}$  and  $\text{Zn}_{\text{Cr}}$ ) are more easily formed compared to the intrinsic Zn vacancies and Zn interstitials. Most recently, Qiu et al. systematically studied the persistent luminescence properties of a series of  $\text{Cr}^{3+}$ -doped  $\text{Zn}_2\text{SnO}_4$  and  $\text{Zn}_{(2-x)}\text{Al}_{2x}\text{Sn}_{(1-x)}\text{O}_4$  [178]. They found that the octahedrally coordinated  $\text{Zn}^{2+}$  and  $\text{Sn}^{4+}$  can be easily substituted by the  $\text{Cr}^{3+}$  dopants, thus giving rise to an NIR afterglow over 35 h. As shown in Fig. 2.20c, d, these phosphors feature broad emission band centered at 800 nm and long afterglow time over 35 h. The corresponding excitation spectra measured at 800 nm emission comprise three bands peaked at 330, 434, and 619 nm, respectively (Fig. 2.20e, f). The researchers argued that the excitation bands centered at 619 and 434 nm are ascribed to the  $d-d$  transitions [ $^4\text{A}_2 \rightarrow ^4\text{T}_2$  ( $t^2e$ )] and [ $^4\text{A}_2 \rightarrow ^4\text{T}_1$  ( $t^2e$ )] of  $\text{Cr}^{3+}$  ions. However, the optical transitions leading to excitation band from 280 to 320 nm still remain unclear.

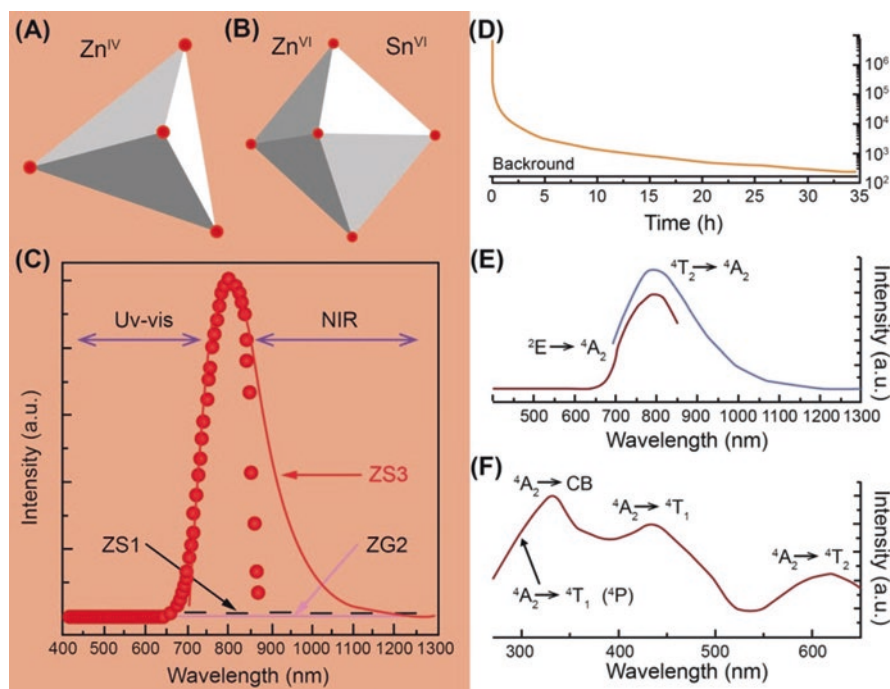


**Fig. 2.20** (a, b) Schematic diagram of octahedral and tetrahedral sites in  $\text{Zn}_2\text{SnO}_4$ . (c) Normalized persistent luminescence spectra of ZS1 ( $\text{Zn}_2\text{SiO}_4:0.2\%\text{Cr}^{3+}$ , black dotted line), ZG2 ( $\text{Zn}_2\text{GeO}_4:0.2\%\text{Cr}^{3+}$ , pink line), and ZS3 ( $\text{Zn}_2\text{SnO}_4:0.2\%\text{Cr}^{3+}$ , red dotted and red solid curve are measured by visible light and NIR detection, respectively) phosphors in the visible and NIR regions after 1 min of the stopping of irradiation. (d) Afterglow decay curve of 800 nm emission. (e, f) Normalized emission spectra in the Vis-NIR regions excited by 330 nm light, and excitation spectra monitored at 800 nm emission of ZS3 sample. Note that the samples were pre-annealed at 600 K before the measurement

### 2.2.3 Summary

As discussed, lanthanide-activated long persistent phosphors are often characterized by bright afterglow in the visible region, especially with regard to blue and green emissions, while transition metal-activated persistent phosphors are capable of emitting light with longer wavelengths ranging from red to NIR region. Most impressive feature of these transition metal-activated phosphors is the ultra-long afterglow time. The afterglow lifetime of some  $\text{Cr}^{3+}$ -activated phosphors can reach several hundreds of hours, enabling the development of new generation bioprobe for bioimaging and bio-detection.

## 2.3 Synthetic Strategies

The preparation of persistent phosphors with controlled crystalline phases, shapes, and sizes not only benefits many technological applications, but also is crucial for the mechanistic investigations. Up to now, many synthetic technologies, such as high-temperature solid-state reaction, sol-gel processing, combustion technique, and hydrothermal treatment, have been widely applied to fabricate high-quality persistent phosphors. In this section, we will focus on a summary of the approaches currently used for synthesizing inorganic persistent phosphors.

### 2.3.1 *High-Temperature Solid-State Reaction*

High-temperature solid-state reaction was first developed for the preparation of inorganic persistent phosphors. This method usually involves two main chemical reactions which are the mixing of solid-state raw materials and the calcination of the mixture at high temperature. The as-synthesized persistent phosphors often have high crystallinity and low surface defects, thus resulting in high emission intensity and long duration. It should be noted that the quality of the final product highly depends on the starting materials, fluxing agents, and reaction atmospheres (reduction, oxidation, or inert gas). Here, we will take the preparation of  $\text{SrAl}_2\text{O}_4:\text{Eu}^{2+}, \text{Dy}^{3+}$  phosphor as an example to illustrate how the high-temperature solid-state reaction works. At the very beginning, starting materials including  $\text{SrCO}_3$ ,  $\text{Al}_2\text{O}_3$ ,  $\text{Eu}_2\text{O}_3$ , and  $\text{Dy}_2\text{O}_3$  are stoichiometrically mixed with proper fluxing agents through ball milling. The mixed materials are subsequently heated at 1200–1400 °C for several hours (2–4 h) under a reductive atmosphere ( $\text{N}_2 + \text{H}_2$ ), followed by a natural cooling process. Finally, the products are crushed and ball-milled into fine powders. Usually, a small amount of fluxing agents is usually added to the mixture to accelerate the chemical reactions. Note that the fluxing agents should have low melting point and no side effect on the final product. When the mixture is heated to a temperature that is higher the melting point of the fluxing agent, the fluxing agent can provide a semi-mobile state, leading to the diffusion and crystallization of the starting materials. Specifically, during the heating process, the mixture undergoes four stages that follow the sequence of diffusion  $\rightarrow$  reaction  $\rightarrow$  nucleation  $\rightarrow$  growing. It is thus believed that the factors including the contacting areas between starting materials, the rate of nucleation, and the diffusion rate of ions potentially affect the reaction rate.

It is important to stress that the solid-state reaction is a typical surface reaction, where the particles of the mixed materials react with each other through surface contact. Therefore, the reactants should be fully ground before the reaction. In addition, many external factors, such as temperature, pressure, additives, and ray emission, also play a crucial role in the determination of the product's quality. As a side note, reaction atmosphere also shows significant influences on the composition of the product, as manifested by the different products obtained by controlling the types of the atmospheres.

The solid-state reaction usually requires high temperature to achieve highly crystalline phases of phosphors, especially with regard to the aluminate- and silicate-based phosphors ( $>1000\text{ }^{\circ}\text{C}$ ). Moreover, the synthetic process also requires long reaction time. Another disadvantage of solid-state reaction is that it may cause inhomogeneous distribution of dopants. In addition, the size of the as-synthesized phosphors is usually characterized to be several tens of micrometers. Hence, a post-grinding process is needed to obtain small particles that are of use to practical applications. However, such grinding process may introduce additional surface defects which are detrimental to the luminescence efficiency of phosphors [179, 180].

### 2.3.2 Sol-Gel Processing

Sol-gel method is a route to prepare solid materials using small molecules as starting materials. The process involves a conversion of small molecules into a colloidal solution (sol) which serves as the precursor for the subsequently formed integrated network (gel). Metal alkoxides are typically used as the precursors. This method has been widely adopted for the fabrication of persistent phosphors because of its ability to control the product's size and morphology. As described in Fig. 2.21, this process comprises the dissolution of starting materials in particular solvent and the subsequent creation of reactive monomer via hydrolysis. The sol can be formed through polymerization of monomers, followed by a condensation reaction with gel formation. Lastly, structural gel is dried and heated according to particular requirements.

Compared to the traditional solid-state reaction, the sol-gel method possesses several advantages. These include relatively low reaction temperature, short reaction time, and high homogeneity. Note that the as-synthesized samples often feature small crystal size. Many phosphors featuring superior luminescence properties have been successfully prepared using this method, such as  $\text{Sr}_3\text{Al}_2\text{O}_6\text{:Eu}^{2+}$ ,  $\text{SrAl}_2\text{O}_4\text{:Eu}^{2+}, \text{Dy}^{3+}$ ,  $\text{SrTiO}_3\text{:Pr}^{3+}, \text{Al}^{3+}$ ,  $\text{CaTiO}_3\text{:Pr}^{3+}$ , and  $\text{CaAl}_2\text{O}_4\text{:Eu}^{2+}, \text{Nd}^{3+}$  [3, 4, 7, 15, 99, 181, 182].

Let us consider the preparation of  $\text{SrAl}_2\text{O}_4\text{:Eu}^{2+}, \text{Dy}^{3+}$  [183]. Here, the starting materials are  $\text{Eu}_2\text{O}_3$  (99.99%),  $\text{Dy}_2\text{O}_3$  (99.9%),  $\text{Sr}(\text{CH}_3\text{CO}_2)_2 \cdot 1/2\text{H}_2\text{O}$  (99%), and  $\text{Al}(\text{i-OC}_3\text{H}_7)_3$  (99%). As illustrated in Fig. 2.22,  $\text{Al}(\text{i-OC}_3\text{H}_7)_3$  is first dissolved in ethylene glycol monoethyl ether at  $80\text{ }^{\circ}\text{C}$ , while the solutions of  $\text{Eu}_2\text{O}_3$  (99.99%) and  $\text{Dy}_2\text{O}_3$  (99.9%) in concentrated nitric acid and  $\text{Sr}(\text{CH}_3\text{CO}_2)_2$  in deionized water are mixed on the basis of the stoichiometry molar ratio. Glycerol is subsequently added to the abovementioned mixture, acting as an additive to avoid the undesirable  $\text{Al}(\text{OH})_3$  precipitation originated from hydrolysis of  $\text{Al}(\text{i-OC}_3\text{H}_7)_3$ . Next, the

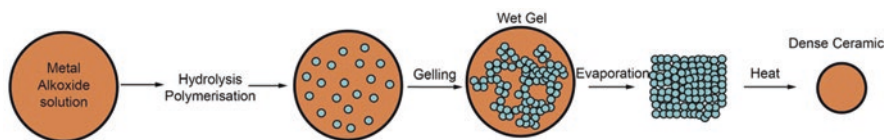
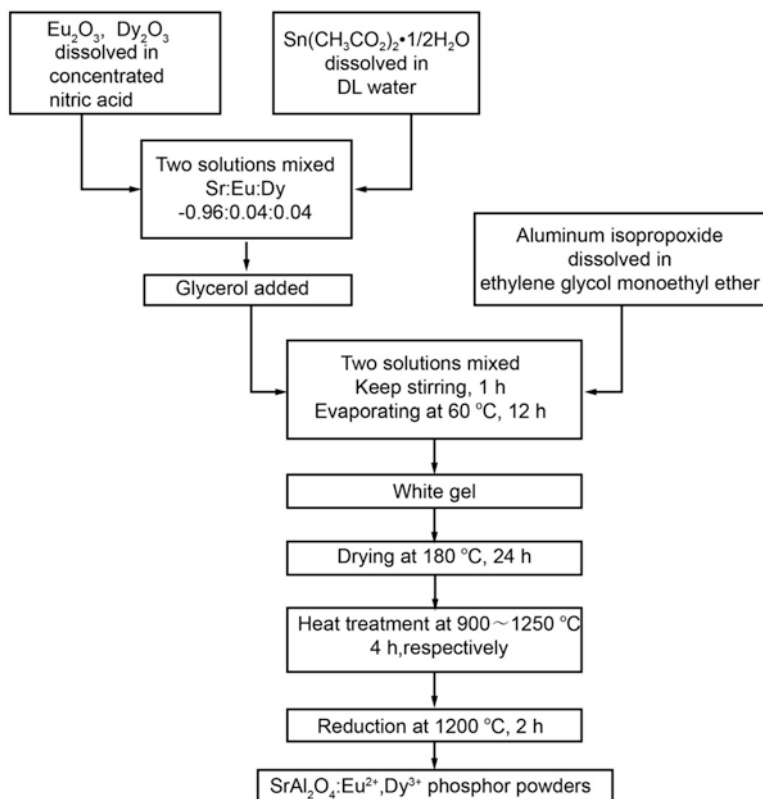


Fig. 2.21 Schematic illustration of sol-gel process

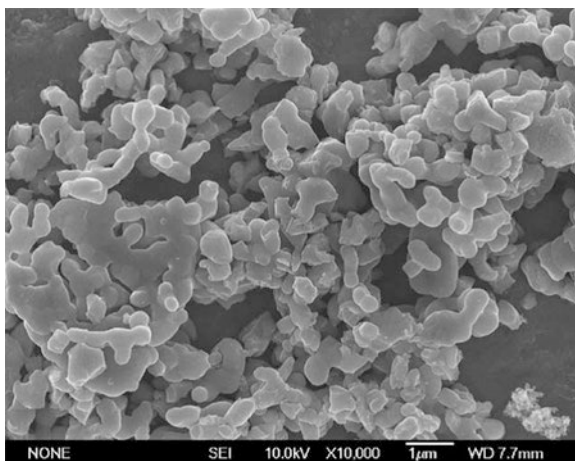


**Fig. 2.22** Schematic illustration of the sol-gel process for the preparation of  $\text{SrAl}_2\text{O}_4:\text{Eu}^{2+}, \text{Dy}^{3+}$

solution of  $\text{Al}(i\text{-OC}_3\text{H}_7)_3$  is added slowly into the same mixture under vigorously stirring at room temperature for 1 h. After hydrolysis and evaporation at  $60^\circ\text{C}$  for 12 h, the resulted white gels are dried at  $180^\circ\text{C}$  for 24 h, followed by a calcination between 900 and  $1250^\circ\text{C}$  for 4 h. Finally, the powders are heated at  $1200^\circ\text{C}$  for 2 h under a reductive atmosphere for the reduction of  $\text{Eu}^{3+}$  to  $\text{Eu}^{2+}$  in the sample. According to the FESEM imaging shown in Fig. 2.23, the final products have a smaller particle size with narrower size distribution when compared to the samples prepared using solid-state reaction.

Phosphors prepared by solid-state method are hardly used for in vivo applications because of their large crystallite size up to micrometers. By comparison, phosphors synthesized using sol-gel approach are usually characterized by small particle size [71, 140]. For example,  $\text{CaMgSi}_2\text{O}_6:\text{Eu}^{2+}, \text{Mn}^{2+}, \text{Pr}^{3+}$  and  $\text{CaZnMgSi}_2\text{O}_6:\text{Eu}^{2+}, \text{Mn}^{2+}, \text{Dy}^{3+}$  nanoparticles have been successfully prepared using sol-gel method and applied for in vivo imaging. In the case of  $\text{CaZnMgSi}_2\text{O}_6:\text{Eu}^{2+}, \text{Dy}^{3+}, \text{Mn}^{2+}$  preparation, raw materials, including  $\text{Mg}(\text{NO}_3)_2$ ,  $\text{ZnCl}_2$ ,  $\text{CaCl}_2$ ,  $\text{EuCl}_3$ ,  $\text{Dy}(\text{NO}_3)_3$ , and  $\text{MnCl}_2$ , were dissolved in deionized water containing a certain amount of nitric acid. Tetraethoxysilane

**Fig. 2.23** FESEM image of  $\text{SrAl}_2\text{O}_4:\text{Eu}^{2+},\text{Dy}^{3+}$  phosphor prepared by sol-gel method (calcinated at 1250 °C)



was subsequently added to the mixture solution rapidly, and the solution was kept stirring vigorously at room temperature for a period of time until the solution became limpid. Then the solution was heated at 70 °C until the sol transformed into gel (~ 2 h). The resulted wet gel was then dried at 110 °C for 20 h to obtain opaque gel, and the gel was calcined in a weak reductive atmosphere at 1050 °C for 10 h. In addition, post-grinding was conducted to achieve a further decrease in nanoparticle size. Electronic microscopy analysis of the as-synthesized  $\text{CaZnMgSi}_2\text{O}_6:\text{Eu}^{2+},\text{Dy}^{3+},\text{Mn}^{2+}$  shows that the nanoparticles obtained using this method have a particle diameter of 50–100 nm with a narrow size distribution [71] (Fig. 2.24).

### 2.3.3 Combustion Technique

Combustion technique, also known as Self-propagation High-temperature Synthesis (SHS), usually makes use of the energies released from self-sustaining chemical reactions [135, 184]. Generally, the exothermic combustion reaction is triggered at the ignition temperature of starting materials, enabling generation of heat. The high combustion temperature (1000–1650 K) produced in this process is able to volatilize impurities with low boiling point, thus making the product purer than that of prepared by conventional solid-state high-temperature method. Typically, metal nitrate and urea are used as oxidizing reactant and reductive reactant in such combustion process, respectively. This technique offers a number of advantages, including simple equipment, short reaction time, small sample size, and high sample purity.

Given these advantages, combustion technique has been intensively applied to the synthesis of nanoscale materials [134, 135]. Let us take the preparation of  $\text{SrAl}_2\text{O}_4:\text{Eu}^{2+},\text{Dy}^{3+}$  phosphor for illustration. Starting materials including  $\text{Sr}(\text{NO}_3)_2$ ,  $\text{Al}(\text{NO}_3)_3 \cdot 9\text{H}_2\text{O}$ ,  $\text{Dy}(\text{NO}_3)_3$ ,  $\text{Eu}(\text{NO}_3)_3$ , and glycine were dissolved in distilled water. Then the solution was introduced into a muffle furnace maintained at 500 °C. The



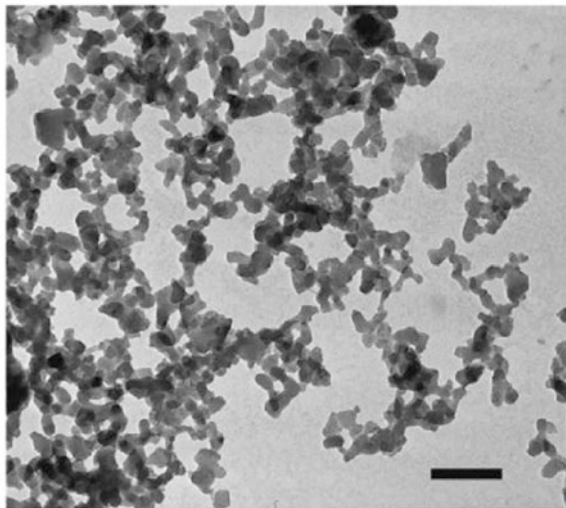


**Fig. 2.24** TEM image of  $\text{CaZnMgSi}_2\text{O}_6:\text{Eu}^{2+}, \text{Dy}^{3+}, \text{Mn}^{2+}$  nanoparticles (Scale bar: 200 nm)

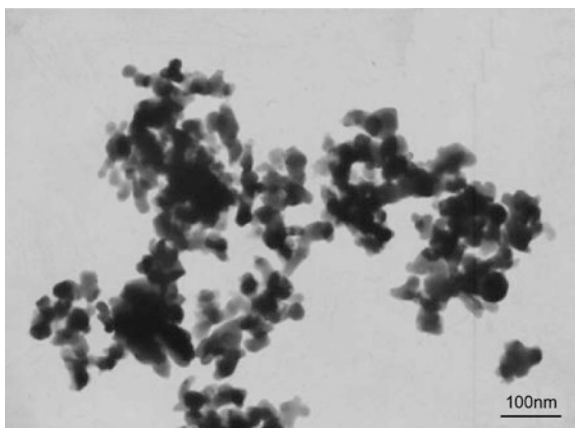
solution firstly boiled, and experienced dehydration and decomposition, thus releasing large amounts of gases. Subsequently, spontaneous ignition and combustion occurred accompanied by the formation of swelling, white foamy and voluminous  $\text{SrAl}_2\text{O}_4:\text{Eu}^{2+}, \text{Dy}^{3+}$  which can be easily milled to produce fine precursor powder of the phosphor. After annealing the precursor powder at 1100 °C for 2 h in a reductive atmosphere, the  $\text{SrAl}_2\text{O}_4:\text{Eu}, \text{Dy}$  phosphors in the form of nanoparticle were finally obtained. As shown in Fig. 2.25, the as-synthesized phosphors have a size of 15–45 nm, which is greatly smaller than that of the phosphors prepared using solid-state method [135].

By taking advantages of both sol-gel and combustion method, researchers have developed an advanced synthetic approach, namely sol-gel-combustion process [180, 185, 187]. The reactions involved in this chemical synthesis usually occurred at a relatively low temperature. In general, citric acid is used in the synthesis to chelate metal cations. The citric acid possessing polymerization capability not only can be utilized for the generation of sol, but also can perform as a fuel to facilitate the exothermic combustion reaction when the dried gel is calcinated to certain temperature. Compared to the phosphors prepared by solid-state reaction, the phosphors synthesized using sol-gel-combustion approach are often characterized by small size, along with homogeneous distribution of dopants.

### 2.3.4 Hydrothermal Treatment

Hydrothermal treatment is a typical wet-chemistry strategy in which starting materials are partially dissolved in vaporous or liquid water at high pressure (10–100 MPa) and high temperature (100–1000 °C). This method makes use of water as

**Fig. 2.25** TEM image of  $\text{SrAl}_2\text{O}_4\text{:Eu}^{2+},\text{Dy}^{3+}$  phosphor prepared using combustion technique [135]



pressure-transferring medium. The main differences between hydrothermal treatment and solid-state reaction are the phase of starting materials and the reaction mechanism. In the case of solid-state reaction, starting materials are in solid phase, and the reactions comprise diffusions across two-phase boundary. Unlike in solid-state reaction, reactions occurred in hydrothermal treatment are classic liquid-phase reactions. Hydrothermal treatment has been widely adopted for preparing crystals with controlled size and morphology. The first preparation of ultrafine powders using hydrothermal treatment could be dated back to 1982. This method has several advantages, such as low treatment temperature, mild synthetic conditions, high sample uniformity, and high stability.

$\text{Sr}_3\text{Al}_2\text{O}_6\text{:Eu}^{2+}(\text{Eu}^{3+}),\text{Dy}^{3+}$  phosphors have been successfully synthesized using hydrothermal treatment, followed by a post-annealing process. The raw materials including aqueous solution of  $\text{Sr}(\text{NO}_3)_2$ ,  $\text{Al}(\text{NO}_3)_3 \cdot 9\text{H}_2\text{O}$ ,  $\text{CO}(\text{NH}_2)_2$ ,  $\text{Eu}(\text{NO}_3)_3$ , and  $\text{Dy}(\text{NO}_3)_3$  are filled into a Teflon-lined autoclave, and the autoclave is then sealed, heated to 120 °C, and kept for 12 h. Subsequently, the resulting precipitate is filtered, washed with distilled water and absolute ethanol for several times, and dried. After that, the obtained precursors are post-annealed at 1200 °C for 3 h in a reductive atmosphere to produce  $\text{Sr}_3\text{Al}_2\text{O}_6\text{:Eu}^{2+},\text{Dy}^{3+}$  phosphors. As shown in Fig. 2.26a, the precursors obtained by hydrothermal treatment are in the form of regular nanorods. After the post-annealing treatment, the final products present an averaged grain size of 1  $\mu\text{m}$  (Fig. 2.26b) which is much smaller than that of products synthesized by solid-state method [186].

In 2009, Wang et al. successfully prepared  $\text{CaTiO}_3\text{:Pr}^{3+},\text{Al}^{3+}$  using hydrothermal method [187]. The starting materials were calcium chloride ( $\text{CaCl}_2$ ), titanium tetrachloride ( $\text{TiCl}_4$ ), aluminium nitrate ( $\text{Al}(\text{NO}_3)_3$ ), and praseodymium chloride ( $\text{PrCl}_3$ ). At the very beginning, the solution containing these four compounds was sealed in a high-pressure autoclave, and the autoclave was subsequently kept in an oven at 200 °C. After reaction for a period of time, the produced sediment was separated, washed, and dried. The phosphor was finally obtained by calcining the resulting sediment under a reductive atmosphere.



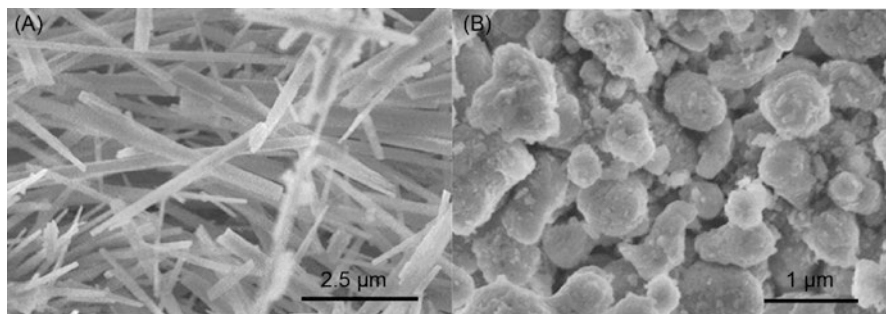


**Fig. 2.26** (a) FESEM image of  $\text{Sr}_3\text{Al}_2\text{O}_6:\text{Eu}^{2+},\text{Dy}^{3+}$  prepared using hydrothermal treatment. (b) FESEM image of  $\text{Sr}_3\text{Al}_2\text{O}_6:\text{Eu}^{2+},\text{Dy}^{3+}$  prepared by calcinating the precursor at 1200 °C for 3 h under a reductive atmosphere

Compared to liquid water, organic solvents often possess a number of particular properties, such as various viscosities, large-scale boiling points, and abundant functional groups. Moreover, subcritical organic solvents may initiate novel reactions, offering the resulting products with metastable state and good dispersity. Taken together, it is believed that persistent phosphors with intriguing optical properties could be achieved by replacing liquid water with organic solvents when hydrothermal treatment is applied.

### 2.3.5 Other Emerging Methods

To enhance the overall performance of persistent phosphors, the most straightforward strategy is to effectively modify the synthetic methods. Indeed, the development of advanced techniques for the preparation of persistent phosphors has attracted much research interest over the past few decades. In this section, a particular emphasis will be placed on two emerging approaches, namely co-precipitation and laser-heated pedestal-grown method.

It is well known that traditional aluminate-based phosphors show excellent luminescence properties, such as high afterglow intensity and long afterglow lifetime. However, their low resistance against moisture largely limits themselves from the use in practical applications. To improve moisture resistance, encapsulation strategy can be adopted. In the work of Chen and coworkers [42], triethanolamine layer was used to encapsulate the  $\text{MAl}_2\text{O}_4:\text{Eu}^{2+},\text{Dy}^{3+}$  ( $\text{M} = \text{Sr}, \text{Ca}, \text{Ba}$ ) phosphors thoroughly by precipitation, which could be considered as the prototype of the co-precipitation method. Particles prepared by co-precipitation method are usually characterized by smaller size and better luminous properties compared to the ones prepared by conventional approaches. Here, let us consider the synthesis of  $\text{SrAl}_2\text{O}_4:\text{Eu}^{2+},\text{Dy}^{3+}$  phosphor. At the very beginning of the synthesis,  $\text{Na}_2\text{C}_2\text{O}_4$  and 8-hydroxyquinoline were poured into solution of  $\text{Sr}(\text{NO}_3)_2$ ,  $\text{Al}(\text{NO}_3)_3 \cdot 9\text{H}_2\text{O}$ ,  $\text{Eu}(\text{NO}_3)_3$ , and  $\text{Dy}(\text{NO}_3)_3$ . The precipitates obtained by filtering, washing, and drying were further post-annealed in a furnace

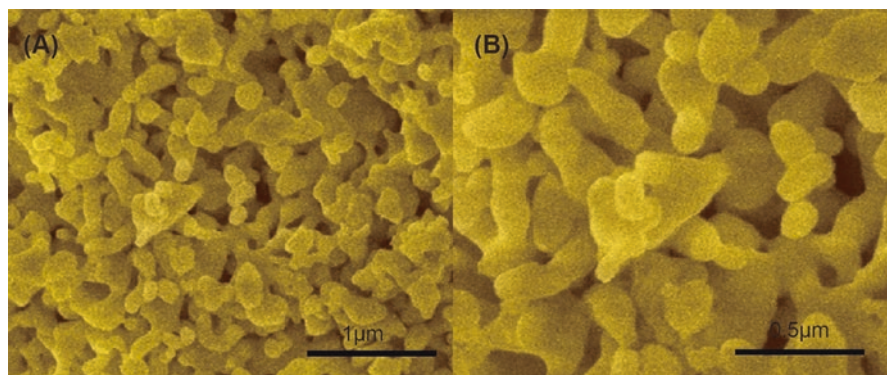
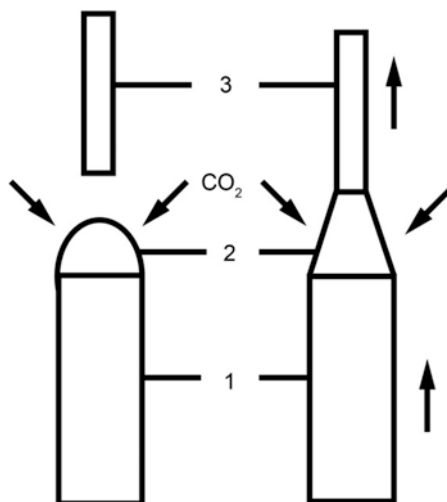


**Fig. 2.27** SEM of  $\text{SrAl}_2\text{O}_4:\text{Eu}^{2+}, \text{Dy}^{3+}$  prepared using co-precipitation approach

**Fig. 2.28** Schematic diagram of LHPG (1—Feed rod, 2—Melting zone, and 3—Seed rod)



under a reductive atmosphere at 1100 °C for 3 h. After that,  $\text{SrAl}_2\text{O}_4:\text{Eu}^{2+}, \text{Dy}^{3+}$  phosphor was finally obtained (Fig. 2.27).

Compared with conventional methods, the most attractive feature of the co-precipitation method is that the size, structure, and purity of the products could be facilely manipulated by varying the experimental condition. Moreover, co-precipitation procedures for the synthesis of persistent phosphors are highly repeatable. As a side note, co-precipitation process may introduce a small amount of residual precipitant reagents into the final products.

Laser-heated pedestal-grown (LHPG) method is considered as a fast, inexpensive and environmentally friendly way to prepare persistent phosphors (Fig. 2.28) [188]. LHPG is a modified Czochralski method in which a laser is used as heating source, enabling the formation of fibrous single-crystal without crucible. The LHPG is also called “crystal growth by zone melting method” because of partial melting.

The persistent phosphors synthesized by LHPG methods are usually found to have a high crystallinity.

Typical persistent phosphors prepared by LHPG method are  $\text{SrAl}_2\text{O}_4:\text{Ce}^{3+}$  and  $\text{CaAl}_2\text{O}_4:\text{Tb}^{3+}, \text{Ce}^{3+}$ . In the work of Meltzer and coworkers [76],  $\text{CaAl}_2\text{O}_4:\text{Tb}^{3+}, \text{Ce}^{3+}$  phosphor synthesized using LHPG method presents green-violet afterglow. At the beginning of the preparation, starting materials, including  $\text{CaCO}_3$  and  $\text{Al}_2\text{O}_3$ , were mixed with the addition of  $\text{Ce}^{3+}$  and  $\text{Tb}^{3+}$  ions, followed by a sintering process in air at  $1350^\circ\text{C}$  for 5 h. After that, the obtained ceramic pellets were cut into bars which were used as feeds. The fibers were pulled into the air using a typical LHPG fiber pulling system, and subsequently calcined at  $1300^\circ\text{C}$  under a flowing reductive atmosphere. Finally, the resulting fibers were found to be transparent with an average diameter of 0.8 mm.

### 2.3.6 Summary

In summary, a number of advanced synthetic techniques have been developed for the preparation of long persistent phosphors. Among them, high-temperature solid-state method is the most commonly used method, and the as-prepared products often show high emission intensity and long afterglow lifetime due to the high crystallinity benefitting from high-temperature treatment. However, the particle size is relatively large up to several tens of micrometers, which is the major obstacle to their application in field of biology. Other methods, such as sol-gel, combustion, and hydrothermal method, are suitable for the preparation of phosphors with particle size at nanoscale. Note that a post-annealing treatment is necessary to achieve long afterglow. Compared to the phosphors prepared by the solid-state reaction, these phosphors often show shorter afterglow lifetime. Hence, up to now, phosphors featuring ultra-long afterglow, such as  $\text{Cr}^{3+}$ -activated NIR-emitting phosphors, are usually synthesized using high-temperature solid-state method.

## 2.4 Optical Properties

The past few decades have witnessed a steady progress in the development of inorganic persistent phosphors. Nowadays, green- and blue-emitting persistent phosphors have been widely used in various applications due to their superior luminescence properties, including high emission intensity and long luminescence duration. Currently,  $\text{SrAl}_2\text{O}_4:\text{Eu}^{2+}, \text{Dy}^{3+}$  and  $\text{CaAl}_2\text{O}_4:\text{Eu}^{2+}, \text{Nd}^{3+}$  phosphors are the most studied green- and blue-emitting phosphors among all lanthanide-activated long persistent phosphors. Compared to the phosphors with green or blue emission, phosphors featuring red and NIR emission are still at an early stage of development. Furthermore, these red- and NIR-emitting phosphors usually show low emission intensity and short afterglow time. Apparently, precise controlling over emission wavelength and enhancement of luminescence intensity and lifetime remain

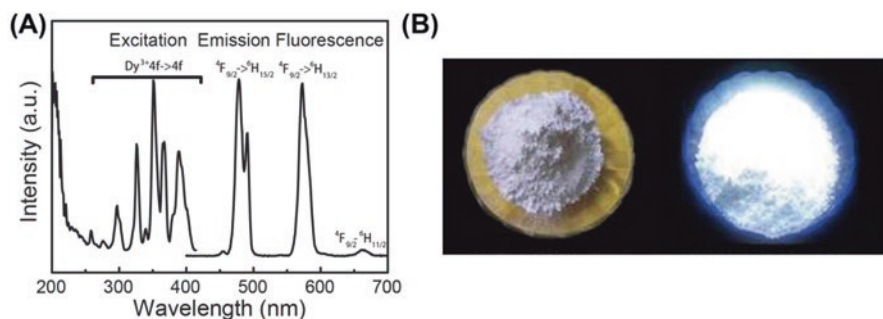


**Fig. 2.29** (a) Emission ( $\lambda_{\text{ex}} = 350$  nm) and excitation ( $\lambda_{\text{em}} = 572$  nm) spectra of white-emitting phosphor  $\text{SrSiO}_3:\text{Dy}^{3+}$ . (b) Photograph of white persistent powder

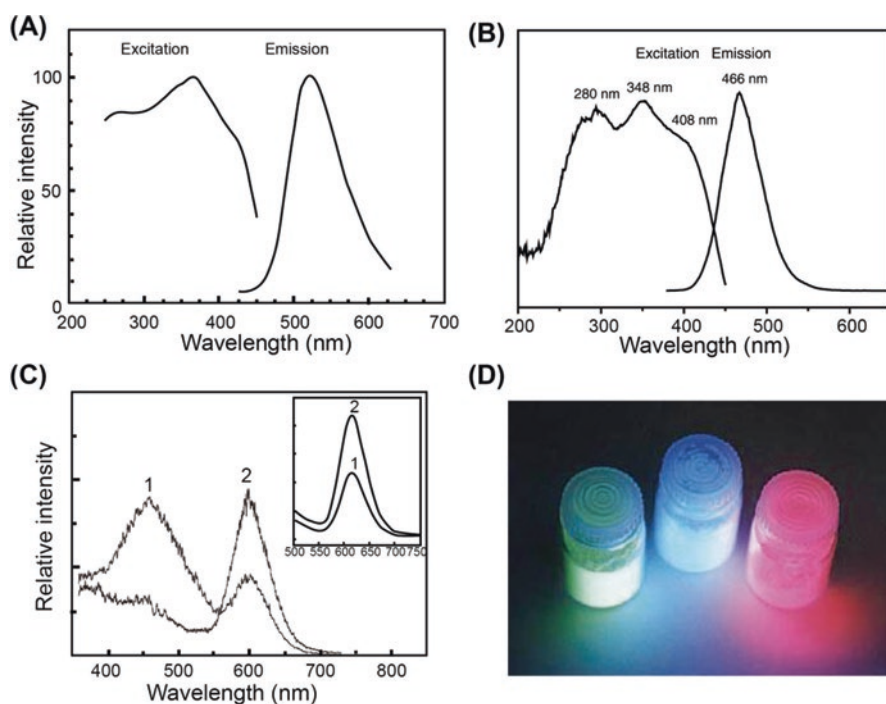


**Fig. 2.30** Excitation and emission spectra of (a) green-emitting  $\text{SrAl}_2\text{O}_4:\text{Eu}^{2+},\text{Dy}^{3+}$ , and (b) blue-emitting  $\text{Sr}_3\text{Al}_{10}\text{SiO}_{20}:\text{Eu}^{2+},\text{Ho}^{3+}$  phosphors. (c) Emission spectra of  $\text{Zn}_3(\text{PO}_4)_2:0.05\text{Mn}^{2+},0.03\text{Zr}^{4+}$  (curve 1) and  $\text{Zn}_3(\text{PO}_4)_2:0.05\text{Mn}^{2+}$  (curve 2) under the excitation at 240 and 418 nm, respectively. The insert shows the corresponding excitation spectra. (d) The photographs of green, blue and red emitting phosphors.

challenging. Figures 2.29 and 2.30 show the excitation and emission spectra of several widely used persistent phosphors, including  $\text{SrSiO}_3:\text{Dy}^{3+}$  (white),  $\text{SrAl}_2\text{O}_4:\text{Eu}^{2+},\text{Dy}^{3+}$  (green),  $\text{Sr}_3\text{Al}_{10}\text{SiO}_{20}:\text{Eu}^{2+},\text{Ho}^{3+}$  (blue), and  $\text{Zn}_3(\text{PO}_4)_2:0.05\text{Mn}^{2+}$  (red). Note that the photographs of these phosphors are also presented.

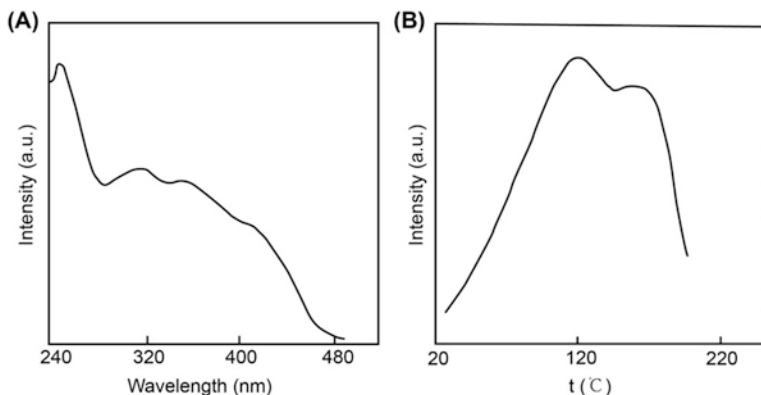


**Fig. 2.31** Excitation spectrum (a) and thermoluminescence spectrum (b) of  $\text{SrAl}_2\text{O}_4:\text{Eu}^{2+}$

It should be noted that persistent phosphors can be excited either optically, thermally, or mechanically. Here, we consider the case of  $\text{SrAl}_2\text{O}_4:\text{Eu}^{2+}$  which can be thermally activated. As shown in Fig. 2.31a, it is found that excitation bands are centered at 248, 316, 360, and 408 nm, which are in agreement with the excitation profile of  $\text{Eu}^{2+}$  ion [189]. It means that  $\text{SrAl}_2\text{O}_4:\text{Eu}^{2+}$  can be effectively activated upon ultraviolet and blue light irradiation. Figure 2.31b shows the thermoluminescence spectrum of  $\text{SrAl}_2\text{O}_4:\text{Eu}^{2+}$  phosphor. It is found that two peaks appear when the samples are heated over 80 °C, indicating two trapping levels existed in  $\text{SrAl}_2\text{O}_4:\text{Eu}^{2+}$ . In general, phosphor requiring a thermal excitation at high temperature usually contains deep trapping level from which the trapped carriers need to overcome a large energy barrier to escape. The duration of afterglow can be verified indirectly by analyzing the thermoluminescence spectra.

Another attractive optical property of persistent phosphors is that they are able to convert high-energy X-rays into a plenty of photons in the UV-visible range. Such optical property endows them with great ability to detect X-rays which are widely used in the fields of medical radiology and X-ray computed tomography (CT) [190]. Despite different mechanisms underlying various applications, the general requirements on the phosphors are efficient absorption of X-ray and intensive emission ranging from 500 to 800 nm (Fig. 2.32).

## 2.5 Commercially Available Long Persistent Phosphor

Until early 1990s, commercially available long persistent phosphors are still limited to sulfide-based phosphors, which were used in the fields of safety indication, luminous paint, and optical memory devices. However, their poor chemical and physical stability and unsatisfied afterglow brightness significantly hinder the further

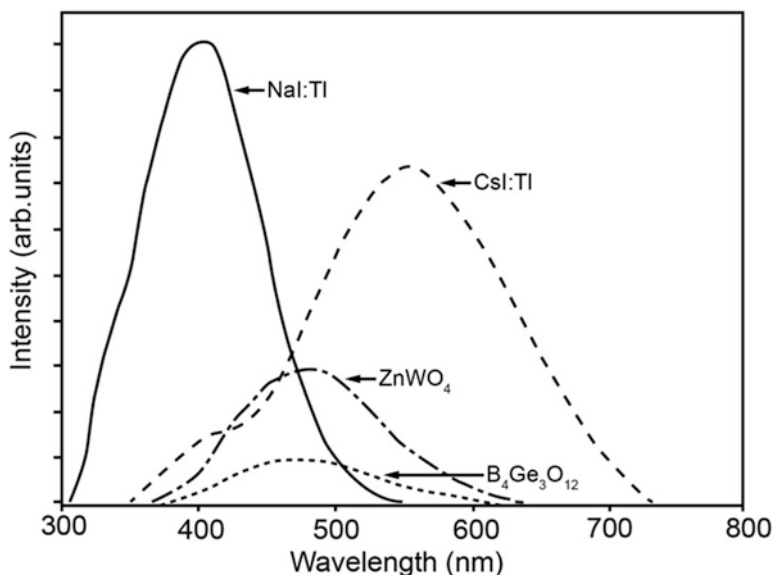


**Fig. 2.32** Emission spectra of NaI:Tl, CsI:Tl, ZnWO<sub>4</sub>, and B<sub>4</sub>Ge<sub>3</sub>O<sub>12</sub> phosphors upon excitation of X-ray

development of sulfide-based phosphors, thus stimulating the search for new persistent phosphors with high emission intensity and stability [191].

Over the past decade, Eu<sup>2+</sup>-doped aluminates have been demonstrated to be superior persistent phosphors featuring high emission intensity and long afterglow lifetime. Compared to the traditional ZnS-based persistent phosphor, emission intensity and afterglow duration observed in Eu<sup>2+</sup>-activated aluminate are largely enhanced, thus enabling the overall performance of the phosphor-based devices used in various applications. The currently commercially available persistent phosphors are listed in Table 2.11. It is found that green-emitting SrAl<sub>2</sub>O<sub>4</sub>:Eu<sup>2+</sup>, Dy<sup>3+</sup> and Sr<sub>4</sub>Al<sub>14</sub>O<sub>25</sub>:Eu<sup>2+</sup>, Dy<sup>3+</sup> present the longest afterglow lifetime, along with relatively high emission intensity. As a side note, high-temperature solid-state method is the commercially employed technique for phosphor preparation largely due to the advantages of mature technology, simple equipment, and high crystallinity of the resulting sample.

To meet market demands, the performance evaluation of long persistent phosphors should not solely rely on the afterglow duration. For particular applications, there may be specific requirements that need to be satisfied. For instance, the light level is as important as afterglow duration when phosphors are designed for outdoor safety signage, while emission within NIR region would be appreciated for achieving deep tissue penetration depth in bioimaging applications.

**Table 2.11** Commercially available long persistent phosphors [192, 193]

Host material	Dopants	Afterglow maximum (nm)	Afterglow duration
MeO·xAl <sub>2</sub> O <sub>3</sub> (Me = Ca, Mg, Sr; x = 0.5–2.0)	Eu <sup>2+</sup>	520	12 h
		490	12 h
		440	6 h
MeO·xAl <sub>2</sub> O <sub>3</sub> ·ySiO <sub>2</sub> (Me = Ca, Mg, Sr, Ba; x = 0.5–2.0, y = 0.01–0.5)	Eu <sup>2+</sup>	520	10 h
MeO·xSiO <sub>2</sub> (Me = Ca, Sr, Mg, Ba; x = 0.5–1.5)	Eu <sup>2+</sup>	470	12 h
(Ca <sub>1-x</sub> Sr <sub>x</sub> )S (x = 0–1.0)	Eu <sup>2+</sup>	650	1 h
		630	1 h
Re <sub>2</sub> O <sub>2</sub> S (Re: lanthanides)	Eu <sup>2+</sup>	650	2 h
SrAl <sub>2</sub> O <sub>4</sub>	Eu <sup>2+</sup> , Dy <sup>3+</sup>	520	66 h
Sr <sub>4</sub> Al <sub>14</sub> O <sub>25</sub>	Eu <sup>2+</sup> , Dy <sup>3+</sup>	490	66 h
Sr <sub>2</sub> CaMgSi <sub>2</sub> O <sub>7</sub>	Eu <sup>2+</sup> , Dy <sup>3+</sup>	510	16 h
Sr <sub>2</sub> MgSi <sub>2</sub> O <sub>7</sub>	Eu <sup>2+</sup> , Dy <sup>3+</sup>	469	33 h
CaAl <sub>2</sub> O <sub>4</sub>	Eu <sup>2+</sup> , Nd <sup>3+</sup>	440	16 h
Y <sub>2</sub> O <sub>2</sub> S	Eu <sup>2+</sup> , Mg <sup>2+</sup> , Ti <sup>4+</sup>	593	5 h

## 2.6 Factors Affecting Afterglow Properties

Despite the ambiguous mechanisms underlying persistent luminescence, it is well accepted that the presence of charge carrier traps endows phosphors with persistent luminescence by gradually releasing these charge carriers upon external stimulations. These charge carriers are subsequently transferred to emitting centers, generating long persistent luminescence. It is important to stress that the occurrence and duration of afterglow largely depend on the depth of the trap levels within bandgap. Specifically, phosphors containing shallow traps often feature with short afterglow lifetime. On the contrary, deep traps usually enable long persistent luminescence. However, the afterglow phenomenon would not occur if the trap depth is too deep for charge carriers to escape. Apparently, the trap depth plays a crucial role in the determination of afterglow duration in a given phosphor. It should be noted that there are a number of factors that affect the distribution of trapping levels, including the type of dopant and host, doping concentration, and preparation conditions. In this section, an emphasis will be placed on the parameters that affect the persistent luminescence properties.

### 2.6.1 Emitting ion

*Type of emitting ion.* As already mentioned in Sect. 2.2.2, lanthanide and transition metal ions act as emitting centers of a given persistent phosphors. In view of the difference in electronic nature between lanthanide and transition metal ions,



different optical transitions will occur when appropriate excitation applies, thus giving rise to distinct emission profiles. For instance,  $5d \rightarrow 4f$  transition of  $\text{Eu}^{2+}$  ions results in broadband emission centered at 520 nm when doped in  $\text{SrAl}_2\text{O}_4$ . Whereas,  $4f \rightarrow 4f$  transition of  $\text{Eu}^{3+}$  ions generates narrow-band emission with the wavelengths of 610–620 nm. Given the shielding effect, the f orbitals of lanthanide ions are hardly affected by the coordination environment. It means that each lanthanide ions emit particular color when the emission originates from  $4f \rightarrow 4f$  transition, irrespective of the host used. On the contrary, emissions involving  $d \rightarrow f$  or  $d \rightarrow d$  transition greatly depend on the crystal field owing to the susceptible d orbitals. For example, the emission spectrum of tri-doped  $\text{Ca}_{0.7}\text{Zn}_{0.9}\text{Mg}_{0.9}\text{Si}_2\text{O}_6:\text{Eu}^{2+}, \text{Mn}^{2+}, \text{Pr}^{3+}$  comprises two emission bands centered at 580 and 685 nm, which originate from the same  ${}^4\text{T}_1-{}^6\text{A}_1$  transition of  $\text{Mn}^{2+}$  sitting at two different cation sites.  $\text{Mn}^{2+}$  ions sitting at  $\text{Mg}^{2+}$  site lead to the emission band at 685 nm, while  $\text{Mn}^{2+}$  ions replacing  $\text{Ca}^{2+}$  generate the emission band at 580 nm.

**Doping concentration.** The concentration of emitting ions can directly affect the afterglow properties of phosphors. In general, the emission intensity and duration increase with the increasing concentration of emitting ions. Unfortunately, when the concentration of emitting ions reaches a certain value, further increase in concentration could cause quenching effect due to the very short distance between two emitting ions. Such a phenomenon is also known as concentration quenching. To achieve long afterglow duration and high emission intensity, the most effective strategy is to optimize the doping concentration of both emitting ions and the codopant. The optimal doping concentration varies depending on the host-dopant combination [194]. In the case of  $\text{Eu}^{2+}$ -doped  $\text{SrAl}_2\text{O}_4$ , it is found that emission at 415 nm decreases with the increasing of  $\text{Eu}^{2+}$  concentration (Fig. 2.33). However, only the emission at 516 nm can be observed when the  $\text{Eu}^{2+}$  concentration reached 2.4%.

### 2.6.2 Host

It is well accepted that the host affects the emission features of emitting ions by providing different coordination environments. For instance, the luminescence of  $\text{Eu}^{2+}$ -doped aluminate phosphors originates from the  $4f^65d \rightarrow 4f^7$  optical transitions. Given the high sensitivity of d orbital to the environment, crystal field shows significant impacts on the luminescence profile of  $\text{Eu}^{2+}$  ions. Unlike the d orbital, crystal field has small effect on the luminescence properties of  $\text{Eu}^{3+}$  ions involving  $f \rightarrow f$  transition because the f orbitals are well shielded from the external interference. By altering the coordination surroundings, emission with a particular wavelength can be achieved in doped phosphors. The most straightforward way to vary coordination environment is to use different host lattices. Let us consider the structural configurations of  $\text{MAl}_2\text{O}_4$  for illustration. Here, M represents different host metal cations. Despite the same type of hosts, different M ions can result in different crystal structures. The geometrical structures of these host lattices are listed in Table 2.12, along with the corresponding luminescence properties of



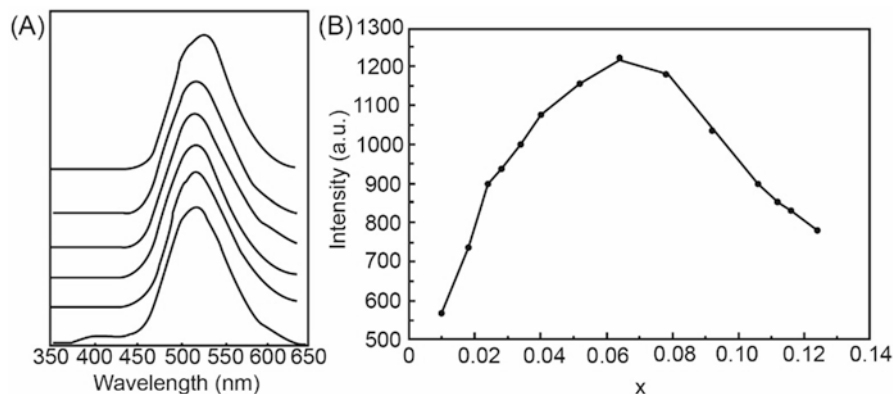


**Fig. 2.33** (a) Emission spectra of  $(\text{Sr}_{1-x}\text{Eu}_x)\text{O} \cdot \text{Al}_2\text{O}_3$  ( $x = 0.01, 0.018, 0.024, 0.052, 0.064, 0.106$ , from bottom to top). (b) Dependence of emission intensity on  $\text{Eu}^{2+}$  concentration ( $x$ ) for  $(\text{Sr}_{1-x}\text{Eu}_x)\text{O} \cdot \text{Al}_2\text{O}_3$  ( $\lambda_{\text{ex}} = 254 \text{ nm}$ )

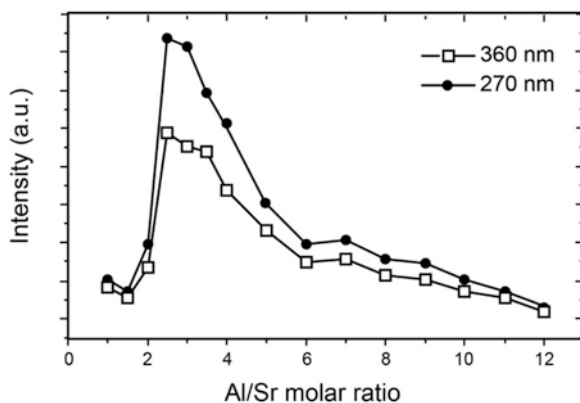
**Table 2.12** Crystal structures and persistent luminescence properties of  $\text{MAl}_2\text{O}_4:\text{Eu}^{2+}, \text{RE}^{3+}$  phosphor

Matrix	Crystal system	Dopants	Afterglow maximum (nm)	Excitation wavelength (nm)
$\text{SrAl}_2\text{O}_4$	Monoclinic	$\text{Eu}^{2+}, \text{RE}^{3+}$	516	263
$\text{MgAl}_2\text{O}_4$	Cube		480	335
$\text{CaAl}_2\text{O}_4$	Monoclinic		440	323
$\text{BaAl}_2\text{O}_4$	Hexagonal		500	348

$\text{MAl}_2\text{O}_4:\text{Eu}^{2+}, \text{RE}^{3+}$ . If the radius of  $\text{RE}^{3+}$  is larger than that of M ion, replacing M with  $\text{RE}^{3+}$  would lead to lattice expansion. Simultaneously, the lattice would resist such an expansion through oppressing the electron cloud of  $\text{RE}^{3+}$  ions, thus leading to the changes in the energy gap between the excited 5d levels and the ground-state 4f levels [195]. Consequently, different emission peaks could be expected in these phosphors.

In addition, the component of the host material also affects the afterglow properties. For instance, an overdose of Ba in  $\text{BaAl}_2\text{O}_4:\text{Eu}^{2+}$  phosphor can lead to a quench of persistent luminescence. If the dose of Ba is at the stoichiometric point or slightly less, the observed afterglow can last up to 2 h. Chen et al. investigated the effect of Al/Sr ratios on the afterglow properties of  $\text{SrAl}_2\text{O}_4:\text{Eu}^{2+}, \text{Dy}^{3+}$  phosphors. They found that the initial emission intensities of these products vary with the ratios of Al/Sr (Fig. 2.34) [196]. The strongest emission intensity can be achieved in the product in which the ratio of Al/Sr reached 2. Note that the main phase at such Al/Sr ratio is  $\text{SrAl}_2\text{O}_4$ . On the contrary, the afterglow duration is shortest when Al/Sr ratio is 1, where  $\text{Sr}_3\text{Al}_2\text{O}_6$  phase dominates.

**Fig. 2.34** Dependence of initial emission intensity on Al/Sr ratio in  $\text{SrAl}_2\text{O}_4:\text{Eu}^{2+},\text{Dy}^{3+}$  phosphor under irradiation of 360 and 270 nm



### 2.6.3 Codopant

*Type of codopant.* On the basis of persistent luminescence mechanisms, it is promising to improve the performance of persistent phosphor through control over the trap depth. Thomas Maldiney et al. reported that co-doping of additional lanthanide ions  $\text{Ln}^{3+}$  ( $\text{Ln} = \text{Dy}, \text{Pr}, \text{Ce}, \text{Nd}$ ) into  $\text{CaMgSi}_2\text{O}_6:\text{Mn}^{2+}$  nanoparticles can prolong the afterglow duration and enhance the emission intensity [140]. A novel composition of  $\text{CaMgSi}_2\text{O}_6:\text{Eu}^{2+},\text{Mn}^{2+},\text{Pr}^{3+}$  was demonstrated to be suitable for in vivo imaging. They ascribed the achievement to the presence of codopant which serves as charge carrier traps. By adopting different codopants, the resulting trap depth varies, subsequently giving rise to different emission intensities and lifetimes.

The proposed mechanism of persistent luminescence observed in  $\text{CaMgSi}_2\text{O}_6:\text{Mn}^{2+},\text{Ln}^{3+}$  is schematically shown in Fig. 2.35. Under excitation,  $\text{Mn}^{2+}$  ions sitting at  $\text{Mg}^{2+}$  sites may trap holes from VB to form  $\text{Mn}^{3+}$  ions, while oxygen vacancies ( $\text{V}_\text{O}$ ) and  $\text{Ln}^{3+}$  ions could trap electrons wandering in CB. After the stopping of excitation source, the trapped electrons will be thermally released and captured by  $\text{Mn}^{3+}$  ions, leading to  ${}^4\text{T}_1 \rightarrow {}^6\text{A}_1$  emission. The depth of electron trap  $E$ , defined as the energy difference between the trapping level and the CBM, can be roughly estimated through the simple equation of  $E \approx 0.002\text{TM}$ , where TM is the temperature at which the emission intensity is the strongest when measuring the thermally activated luminescence spectra [197]. As shown in Fig. 2.36, the trap depths are found to be around 0.45, 0.7, 0.92, and 0.96 eV when co-doping of  $\text{Ce}^{3+}$ ,  $\text{Pr}^{3+}$ ,  $\text{Nd}^{3+}$ , and  $\text{Dy}^{3+}$ , respectively. Note that  $\text{Pr}^{3+}$ -induced trap depth (0.7 eV) is the most suitable energy barrier which can be effectively overcome at room temperature.

*Codopant concentration.* Apart from being emitting centers, trivalent lanthanide ions can also act as trapping centers to achieve prolonged afterglow when co-doped into the host lattice [198]. Considering that the interactions between dopants can largely influence the position of the trapping levels within the bandgap, codopant

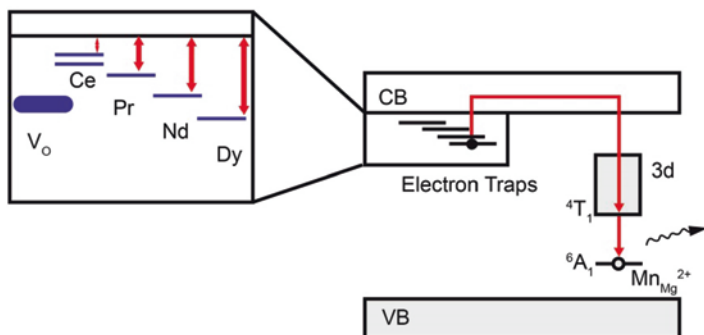


**Fig. 2.35** Schematic energy level diagram of  $\text{CaMgSi}_2\text{O}_6:\text{Mn}^{2+}, \text{Ln}^{3+}$ . Note that  $\text{Mn}^{2+}$  sitting at  $\text{Mg}^{2+}$  site acts as hole traps, while oxygen vacancies ( $\text{V}_\text{O}$ ) and  $\text{Ln}^{3+}$  ions act as electron traps

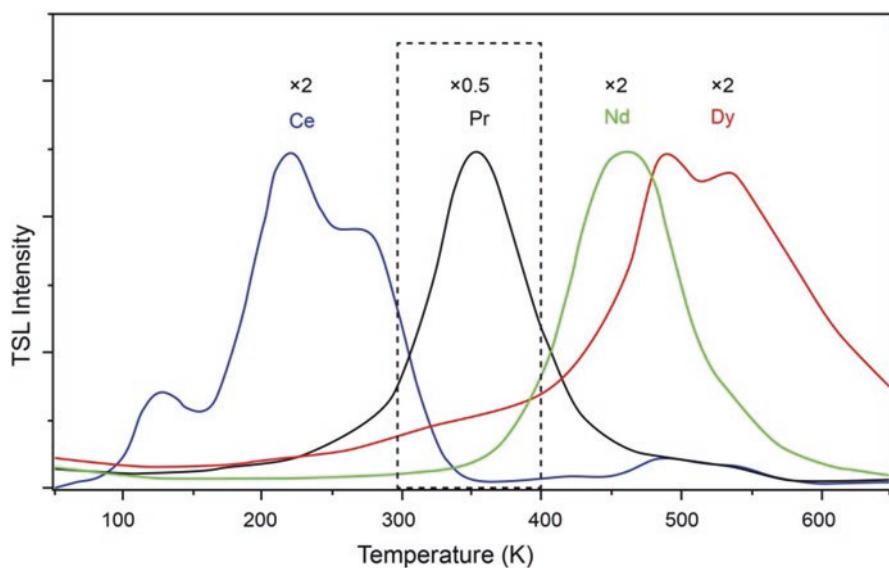
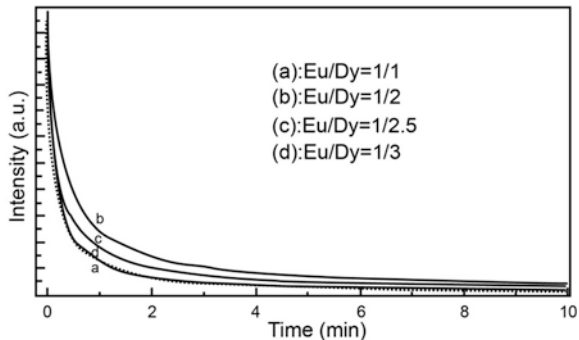


**Fig. 2.36** Normalized luminescence intensity at 685 nm of  $\text{CaMgSi}_2\text{O}_6:\text{Mn}^{2+}, \text{Ln}^{3+}$  ( $\text{Ln} = \text{Ce}^{3+}, \text{Nd}^{3+}, \text{Dy}^{3+}$ , and  $\text{Pr}^{3+}$ ), measured after 10 min X-ray excitation. Note that the concentration of the codopant is 1%

concentration needs to be well controlled in order to provide the trapping levels with appropriate trap depths. For example, the afterglow duration of  $\text{Sr}_4\text{Al}_{14}\text{O}_{25}:\text{Eu}^{2+}$  phosphor can be significantly prolonged when additional  $\text{Dy}^{3+}$  ions are co-doped into the system [11]. Among these samples,  $\text{Sr}_4\text{Al}_{14}\text{O}_{25}:\text{Eu}^{2+}, \text{Dy}^{3+}$  phosphor in which the ratio of  $\text{Eu}/\text{Dy}$  is 1/2 shows the longest afterglow time (Fig. 2.37).

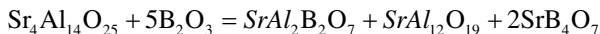
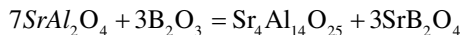
**Fig. 2.37** Decay curves of  $\text{Sr}_4\text{Al}_{14}\text{O}_{25}:\text{Eu}^{2+},\text{Dy}^{3+}$  samples with different contents of co-doped  $\text{Dy}^{3+}$



### 2.6.4 Fluxing Agent

The use of fluxing agent during the preparation of phosphors can also affect the persistent luminescence. Considering that the fluxing agent is often used to accelerate chemical reaction, we here take the solid-state reaction for example to illustrate how the fluxing agent influences the luminescence properties of the final products.

The effect of borate ( $\text{B}_2\text{O}_3$ ) on luminescence properties has been studied in  $\text{SrAl}_2\text{O}_4:\text{Eu}^{2+},\text{Dy}^{3+}$  system [4, 34]. In the preparation of  $\text{SrAl}_2\text{O}_4:\text{Eu}^{2+},\text{Dy}^{3+}$  phosphor,  $\text{B}_2\text{O}_3$  was used as one of the starting materials. It should be noted that  $\text{B}_2\text{O}_3$  not only can destroy the  $\text{AlO}_4$  framework by distorting the crystal structures of  $\text{SrAlO}_4$  and  $\text{BO}_4$ , but also can contribute to the formation of superstructure units by forming Al–O–B bonds. The reaction processes can be described as:



Consequently, borate can be part of the final product when its concentration reaches a certain value. One may expect significant changes in luminescence profile due to the presence of by-products. On the other hand, the  $\text{B}_2\text{O}_3$  can still affect the afterglow properties through the manipulation of trap depth even within a reasonable range of concentration. According to the thermoluminescence shown in Fig. 2.38, the final product without  $\text{Dy}^{3+}$  does not show persistent luminescence upon heating. The co-doping of  $\text{Dy}^{3+}$  ions enables the occurrence of afterglow in  $\text{SAEDB}_0$  at high temperature, indicating the presence of deep traps. Given the large value of trap depth, this phosphor does not show afterglow at room temperature as the trapped electrons are not able to escape from the trapping centers to the conduction band at room temperature. By increasing the concentration of  $\text{B}_2\text{O}_3$ ,  $\text{SAEDB}_{0.05}$  and  $\text{SAEDB}_{0.4}$  are found to be able to produce persistent luminescence when heated to 50 °C, indicating a trap depth around 0.63 eV. Taken together,  $\text{B}_2\text{O}_3$  indeed plays an important role in the determination of the product's composition and the manipulation of the codopant-associated trap depth.

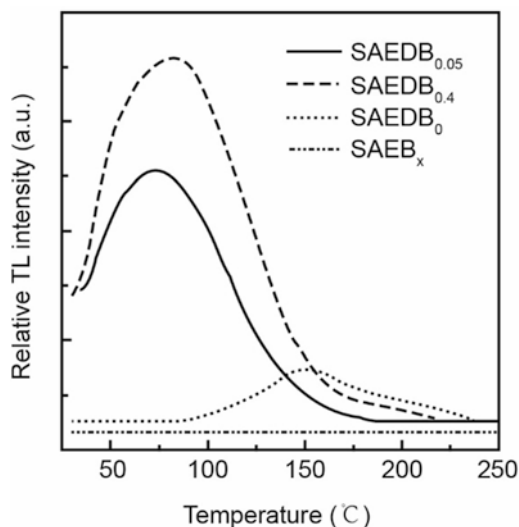


**Fig. 2.38** Thermoluminescence glow curves of  $\text{SAEDB}_x$  ( $\text{S} = \text{Sr}$ ,  $\text{A} = \text{Al}$ ,  $\text{E} = \text{Eu}$ ,  $\text{D} = \text{Dy}$ ,  $\text{B} = \text{B}_2\text{O}_3$ ). Note that  $x$  represents the percentage of  $\text{B}_2\text{O}_3$  component

### 2.6.5 Preparation Condition

It is well accepted that the composition of the final product largely depends on the preparation condition. For instance, the as-synthesized  $\text{SrAl}_2\text{O}_4$  can have very different amounts of by-product  $\text{Sr}_3\text{Al}_2\text{O}_6$  content depending on the preparation condition [199]. Such unexpected by-product can deteriorate the luminescence intensity of the  $\text{SrAl}_2\text{O}_4:\text{Eu}^{2+}, \text{Dy}^{3+}$  persistent phosphor. Generally, the phase composition of the  $\text{SrAl}_2\text{O}_4$  and  $\text{Sr}_3\text{Al}_2\text{O}_6$  is evaluated by the ratio of the  $P_{124}/(P_{124} + P_{326})$ . In the study of Xu and coworkers [200], the ratio of the  $P_{124}/(P_{124} + P_{326})$  was found to be about 53% at 750 °C, 92% at 1000 °C, and 97% at 1300 °C, respectively (Fig. 2.39). Apparently, a gradual conversion from  $\text{Sr}_3\text{Al}_2\text{O}_6$  phase to  $\text{SrAl}_2\text{O}_4$  phase can be achieved with increasing calcination temperature. A complete transformation occurs at 1400 °C, which is in line with the dramatically increased luminescence intensity at 519 nm, as illustrated in Fig. 2.39a. Moreover, the recorded afterglow decay curves shown in Fig. 2.39b indicate that the afterglow lifetime increases slightly with increasing calcination temperature.

## 2.7 Surface Modification

Surface modification has been considered as an effective strategy to increase the stability and the compatibility of phosphors for particular applications. As discussed, aluminate- and sulfide-based persistent phosphors often show limited

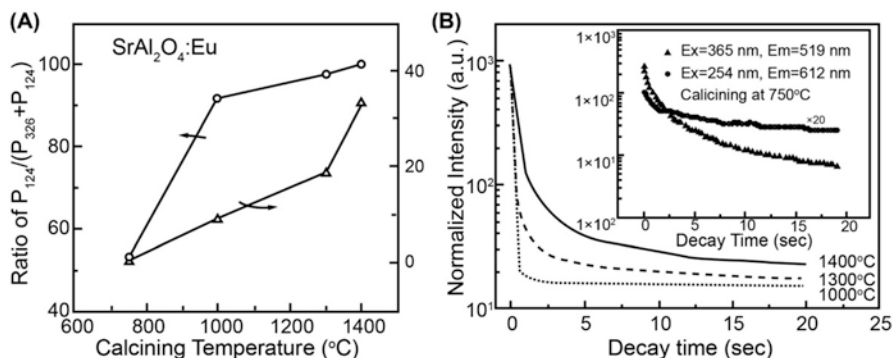


**Fig. 2.39** (a) Dependence of phase composition and luminescence intensity on calcining temperature. (b) Afterglow decay curves of  $\text{SrAl}_2\text{O}_4:\text{Eu}^{2+},\text{Dy}^{3+}$  phosphors prepared at different temperatures

stability against moisture. When exposed to the atmosphere, these phosphors may decompose, along with the vanished luminescence. On the other hand, these phosphors have poor organic miscibility owing to their inorganic nature. Therefore, it is very difficult to disperse these inorganic phosphors in the organic solvent or macro-molecule fluid, which are necessary working conditions for some particular applications. Such problems can be largely mitigated through surface modification. Apart from enhancing water resistance and organic miscibility of phosphors, surface modification can also improve the luminescence performance by eliminating the surface defects [201].

Surface modification is usually divided into three categories depending on the types of the modifier, namely inorganic modification, small molecule modification, and polymer modification. In general, linking small organic molecule to the phosphor and grafting polymer onto phosphor are the convenient and effective ways to achieve a surface modification. There are three main criteria when choosing surface modifiers [202]. One is that the phosphors should be dispersed in the selected modification material. The second is that the modifier must be transparent to keep the luminescent properties intact. The last is that the modified phosphors should meet the requirements of specific applications. In this section, we will summarize the approaches currently used for surface modification, along with the discussion on the effect of the modification on the luminescence properties of phosphors.

### 2.7.1 Inorganic Coating

Inorganic coating technique makes use of chemically stable inorganic material to form a thin film onto the surface of phosphors. It is usually achieved through either physical or chemical reaction. Physical vapor deposition melting, steam coating, and sol-gel coating are the typical coating methods in which the modifier and the

phosphors are simply mixed. On the contrary, chemical reactions occur during chemical coating, such as chemical vapor deposition and chemical deposition. Silica and alumina have been widely adopted for surface modification due to their high chemical stability and low production cost. Huang et al. successfully coated  $\text{SrAl}_2\text{O}_4:\text{Eu}^{2+},\text{Dy}^{3+}$  phosphor with a thin layer of  $\text{SiO}_2$  or  $\text{Al}_2\text{O}_3$  through neutralization deposition [203]. At the beginning of the coating process,  $\text{SrAl}_2\text{O}_4:\text{Eu}^{2+},\text{Dy}^{3+}$  phosphors were dispersed in water or other solvents and stirred. After that, the vitriol and sodium silicate or sodium aluminate were dropwise added into the aforementioned mixture under stirring for several hours. Eventually, the final product was collected, washed, and dried. Compared with the bare phosphor, the coated phosphor shows improved heat and water resistances. For example, the coated phosphor can maintain its superior luminous performance upon heating. This is likely because silicon or aluminum film can protect the  $\text{Eu}^{2+}$  ions from being oxidized. As a side note, this inorganic coating could barely improve the organic miscibility.

### 2.7.2 Small Molecule Modification

Small molecule modification can also protect phosphor from oxygen and moisture. Lu et al. reported that the silane coupling agent can be used to introduce methyl methacrylate to form an organic film on the surface of  $\text{SrAl}_2\text{O}_4:\text{Eu}^{2+},\text{Dy}^{3+}$  phosphor [204]. Figure 2.40a shows the time-dependent variation in pH of the solution containing encapsulated and nonencapsulated phosphors. It is found that the pH of the solution containing nonencapsulated phosphors increases dramatically due to the decomposition of the phosphor. In contrast, the pH of the solution containing encapsulated phosphors remains constant, indicating high stability against moisture. However, the encapsulated phosphors show a slight decrease in both excitation and emission intensities, as shown in Fig. 2.40b.

Small molecule-based organic compound can also be used as a modifier for surface modification. In general, the organic compound adheres to the surface of phosphor by reacting with the hydroxyl group sitting on the particle's surface. However, the presence of hydroxyl group on the surface of phosphor would deteriorate its luminescent performance under water or base condition [205]. An alternative route towards surface modification is to utilize active metal sites on the surface of phosphor, such as  $\text{Sr}^{2+}$ ,  $\text{Al}^{3+}$ ,  $\text{Eu}^{2+}$ , and  $\text{Dy}^{3+}$ . Given that organic compound with coordinative groups can coordinate with metal ions [206], Zhang and coworkers have successfully coated  $\text{SrAl}_2\text{O}_4:\text{Eu}^{2+},\text{Dy}^{3+}$  with five different ligands, including 8-hydroxyquinoline, acetylacetone, tartaric acid and citric acid, which were excellent ligands [205]. Note that the charge transfer from oxygen atoms to their coordinated metal ions is responsible for the formation of the conjugated rings, as schematically shown in Fig. 2.41. They pointed out that the modified phosphors show enhanced water resistance and organic miscibility, along with high brightness and slightly prolonged afterglow lifetime.

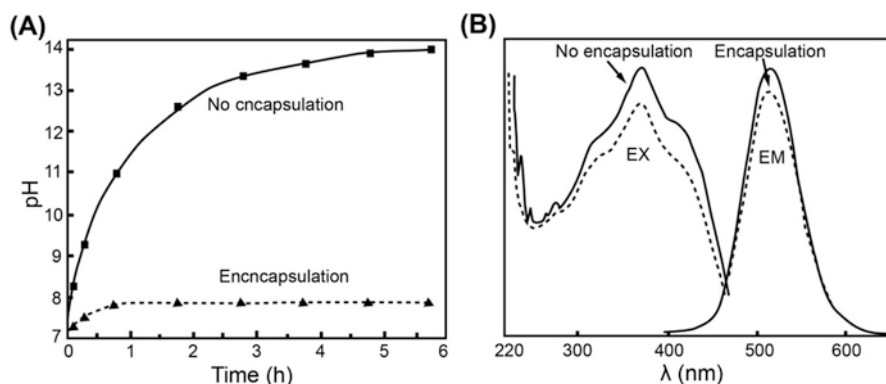
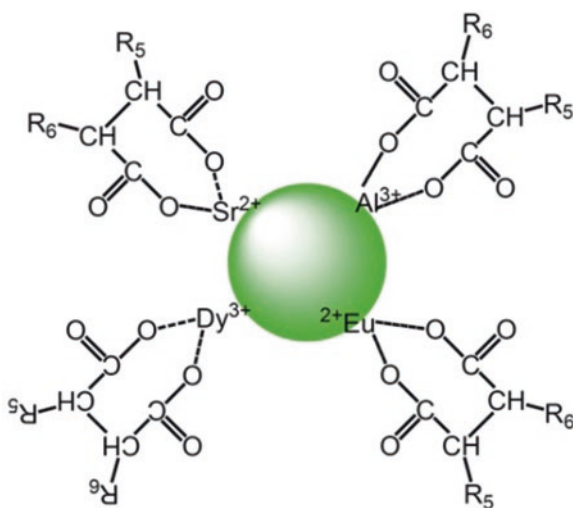


**Fig. 2.40** (a) Water resistance of  $\text{SrAl}_2\text{O}_4:\text{Eu}^{2+}, \text{Dy}^{3+}$  particles before and after encapsulation. (b) Excitation and emission spectra of  $\text{SrAl}_2\text{O}_4:\text{Eu}^{2+}, \text{Dy}^{3+}$  particles before and after encapsulation

**Fig. 2.41** Schematic illustration of ligand coordinated  $\text{SrAl}_2\text{O}_4:\text{Eu}^{2+}, \text{Dy}^{3+}$



Apart from enhancing water resistance and organic miscibility, surface modification can also be conducted to improve the biocompatibility of the phosphors that are widely used for biomedical applications. In the work of de Chermont, Scherman and coworkers, three types of  $\text{Ca}_{0.2}\text{Zn}_{0.9}\text{Mg}_{0.9}\text{Si}_2\text{O}_6:\text{Eu}^{2+}, \text{Dy}^{3+}, \text{Mn}^{2+}$  particles featuring different surface charges were successfully achieved through particular surface modifications (Fig. 2.42) [71]. The resulting persistent phosphors show superior biocompatibility, as manifested by their uniform *in vivo* distribution. Furthermore, these surface modifications were found to be effective in achieving lung or liver targeting and long-lasting bold circulation.

Another demonstration was shown in  $\text{Zn}_{2.94}\text{Ga}_{1.96}\text{Ge}_2\text{O}_{10}:\text{Cr}^{3+}, \text{Pr}^{3+}$  persistent phosphor in which greatly enhanced biocompatibility and water solubility were achieved through PEGylation-based surface modification (Fig. 2.43) [169]. By further conjugating



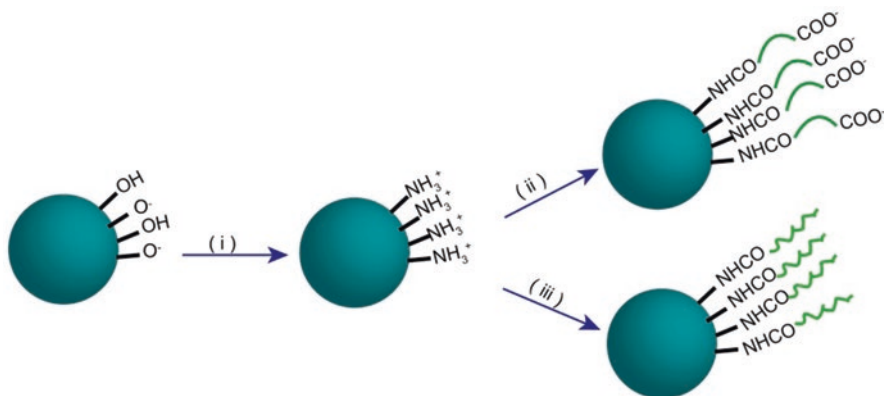


**Fig. 2.42** Schematic representation of  $\text{Ca}_{0.2}\text{Zn}_{0.9}\text{Mg}_{0.9}\text{Si}_2\text{O}_6:\text{Eu}^{2+},\text{Dy}^{3+},\text{Mn}^{2+}$  nanophosphor with surface modification. (i) Amino-nanoparticles were obtained through reaction of phosphor nanoparticles with 3-aminopropyl-triethoxysilane. (ii) Carboxyl-nanoparticles were obtained through reaction of amino-nanoparticles with diglycolic anhydride. (iii) PEG-nanoparticles were synthesized by coupling amino-nanoparticles with  $\text{PEG}_{5000}\text{COOH}$  through a peptide

with c(RGDyK) peptide, the phosphor was demonstrated to be a promising candidate for in vivo targeted tumor imaging with low toxicity.

### 2.7.3 Polymer Modification

Polymer-coated phosphors have several advantages over pure inorganic phosphors. These include high chemical stability and good compatibility with both organic solutions and polymers. Polymer modification is usually achieved through either physical or chemical adsorption. In this section, we will discuss the physical and chemical approaches for surface coating, along with the effect of the modifier on the phosphor's optical properties.

#### 2.7.3.1 Physical Coating

In 1995, Dutta and Dullea reported a physical coating method to improve the organic miscibility of phosphors.[207]. The coating method comprises three main procedures: (1) the phosphor powders were mixed with polymer solution at a concentration of 2.5%, (2) particular surfactant was added to the solution under stirring for 30 min, and (3) the final product was collected and dried at 140 °C. As summarized in Table 2.13, polymer used for surface modification needs to be carefully selected to meet the performance requirements on the phosphor for particular applications.

Another widely used physical coating method is monomer polymerization. In a typical in situ polymerization process, phosphor and initiators are firstly added into

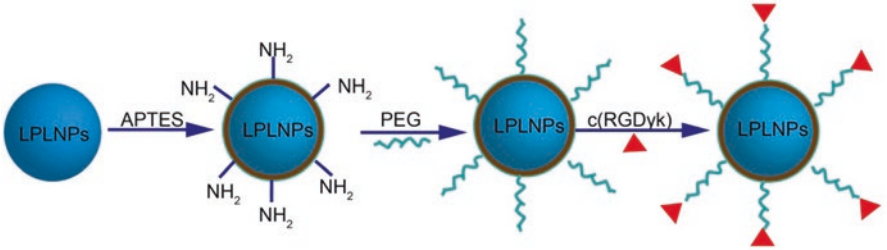


**Fig. 2.43** Schematic representation of  $\text{Zn}_{2.94}\text{Ga}_{1.96}\text{Ge}_2\text{O}_{10}:\text{Cr}^{3+},\text{Pr}^{3+}$  long persistent luminescent nanoparticles (LPLNPs) with surface modification. APTES is reacted with the particles via a condensation reaction between the silanol groups in APTES and hydroxyl groups on surface of LPLNPs. PEG is subsequently covalently linked to the amino groups. An RGD peptide  $\alpha(\text{RGDyK})$  is subsequently conjugated with the PEG-LPLNPs for tumor-targeted imaging application

**Table 2.13** Comparison of reported physical coating strategies using polymer modifier

Procedure	Polymer	Influence	Derivation
Mix polyester with phosphor in solvent under stirring	polyester, nitrocellulose, and polyalkyl acrylate	Increase the resistance against moisture	US4863826
Add phosphor into the solution of polymer, followed by an addition of surfactant	polymethacrylic, polyethylene pyrimidine and it's derivatives, polyethylenimine, etc.	Increase the affinity to organic compound	US5441774
Disperse phosphor in solution of polymer	light-sensitive resin containing carboxylic groups	Increase the stability of phosphor especially the photoresistance	JP09125056

a flask, and monomers are subsequently added into the reaction system under rapid stirring. Gases are expelled from the suspension through a nitrogen flux. After reaction for 4–8 h, the reaction system is cooled down to 25 °C. The phosphors are collected through filtration and washed using dried hexane, and then dried at 60 °C for 12 h. The in situ polymerization leads to a continuous film of polymer that covers the entire powder surface. Given a weak binding between polymer and phosphor, the phosphor may face the problems of phase separation and conglomeration.

**2.7.3.2 Chemical Coating**

Compared to the physical adsorption of polymer on the particle’s surface, chemical coating usually leads to a stronger interaction between phosphor and polymer, as manifested by the formation of chemical bonds. There are general strategies for chemical coating, namely direct bonding and mediated adsorption. Considering that

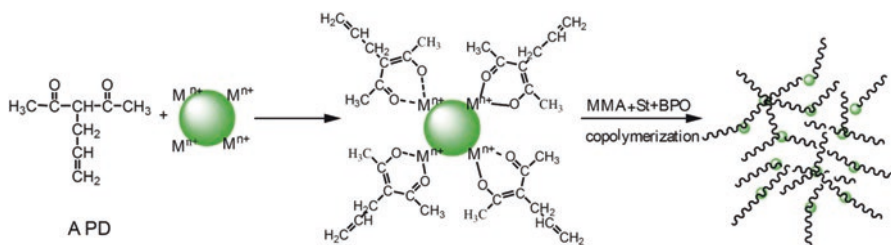


**Fig. 2.44** Schematic synthesis process of polymer-grafted SAO-ED

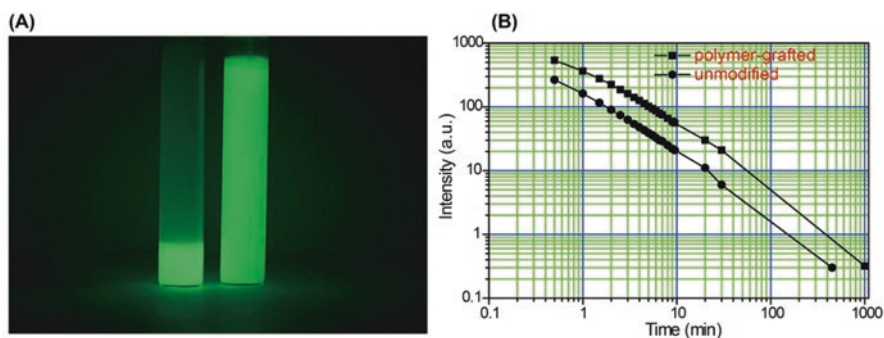


**Fig. 2.45** (a) Digital photographs of the ethanol solution containing unmodified  $\text{SrAl}_2\text{O}_4:\text{Eu}^{2+}, \text{Dy}^{3+}$  (left) and polymer-grafted  $\text{SrAl}_2\text{O}_4:\text{Eu}^{2+}, \text{Dy}^{3+}$  (right) in darkness. (b) Decay curves of polymer-grafted  $\text{SrAl}_2\text{O}_4:\text{Eu}^{2+}, \text{Dy}^{3+}$  and unmodified  $\text{SrAl}_2\text{O}_4:\text{Eu}^{2+}, \text{Dy}^{3+}$

there are unsaturated metal ions or hydroxyl groups on the surface of the luminescent nanoparticles, the polymers can directly adhere to the particles via covalent bonds or coordinate bonds. In the case of mediated adsorption, particular small organic molecule is firstly attached to the particle's surface, followed by a further attachment of polymer.

A demonstration of chemical coating based on mediated adsorption was shown in the case of  $\text{SrAl}_2\text{O}_4:\text{Eu}^{2+}, \text{Dy}^{3+}$  phosphor in which high water resistance and high organic miscible were achieved [208]. The researchers linked a polymer to the phosphor through a bifunctional ligand, namely 3-allyl-2, 4-pentanedione (APD), as shown in Fig. 2.44. The APD was firstly attached on the surface of the phosphor through the coordinate bond, and the coordinated phosphor was subsequently mixed with methyl methacrylate, benzoyl peroxide, and styrene. After a copolymerization reaction at 80–90 °C for 4–8 h, polymer-grafted  $\text{SrAl}_2\text{O}_4:\text{Eu}^{2+}, \text{Dy}^{3+}$  can be collected through filtration and drying treatments. As shown in Fig. 2.45a, the products can be uniformly dispersed in ethanol without precipitate, indicating high water resistance and high organic miscibility. In addition, it was found that the emission intensity of the polymer-grafted  $\text{SrAl}_2\text{O}_4:\text{Eu}^{2+}, \text{Dy}^{3+}$  phosphor was higher than that of the unmodified one (Fig. 2.45b), which was ascribed to the decreased surface defects.

## References

1. Hoogenstraaten, W., Klasens, H.A.: Some properties of zinc sulfide activated with copper and cobalt. *J. Electrochem. Soc.* **100**, 366–375 (1953)
2. Yen, W.M., Yamamoto, H.: *Phosphor Handbook*. CRC Press, Boca Raton (2006)
3. He, X., Dong, W., Zheng, F., Fang, L., Shen, M.: Effect of tartaric acid on the microstructure and photoluminescence of  $\text{SrTiO}_3\text{:Pr}^{3+}$  phosphors prepared by a sol–gel method. *Mater. Chem. Phys.* **123**, 284–288 (2010)
4. Matsuzawa, T., Aoki, Y., Takeuchi, N., Murayama, Y.: A new long phosphorescent phosphor with high brightness,  $\text{SrAl}_2\text{O}_4\text{:Eu}^{2+},\text{Dy}^{3+}$ . *J. Electrochem. Soc.* **143**, 2670–2673 (1996)
5. Takasaki, H., Tanabe, S., Hanada, T.: Long-lasting afterglow characteristics of Eu, Dy codoped  $\text{SrO-Al}_2\text{O}_3$  phosphor. *J. Ceram. Soc. Jpn.* **104**, 322–326 (1996)
6. Suriyamurthy, N., Panigrahi, B.S.: Effects of non-stoichiometry and substitution on photoluminescence and afterglow luminescence of  $\text{Sr}_4\text{Al}_{14}\text{O}_{25}\text{:Eu}^{2+},\text{Dy}^{3+}$  phosphor. *J. Lumin.* **128**, 1809–1814 (2008)
7. Zhang, X., Jiang, W., Liu, X., Lu, L., Wang, X., Bai, Z., Liu, Q., Cao, Z.: Preparation and characterization of  $\text{CaAl}_2\text{O}_4\text{:Eu}^{2+},\text{Nd}^{3+}$  nanoparticles. *Spectrosc. Spectr. Anal.* **25**, 1560–1563 (2006)
8. Poelman, D., Avci, N., Smet, P.F.: Measured luminance and visual appearance of multi-color persistent phosphors. *Opt. Express.* **17**, 358–364 (2009)
9. Ito, S., Banno, S., Suzuki, K., Inagaki, M.: Phase transition in  $\text{SrAl}_2\text{O}_4$ . *Z. Phys. Chem.* **105**, 173 (1977)
10. Clabau, F., Rocquefelte, X., Jolic, S., Deniard, P., Whangbo, M.-H., Garcia, A., Le Mercier, T.: Mechanism of phosphorescence appropriate for the long-lasting phosphors  $\text{Eu}^{2+}$ -doped  $\text{SrAl}_2\text{O}_4$  with codopants  $\text{Dy}^{3+}$  and  $\text{B}^{3+}$ . *Chem. Mater.* **17**, 3904–3912 (2005)
11. Lin, Y., Tang, Z., Zhang, Z.: Preparation of long-afterglow  $\text{Sr}_4\text{Al}_{14}\text{O}_{25}$ -based luminescent material and its optical properties. *Mater. Lett.* **51**, 14–18 (2001)
12. Lin, Y., Tang, Z., Zhang, Z., Nan, C.W.: Anomalous luminescence in  $\text{Sr}_4\text{Al}_{14}\text{O}_{25}\text{:Eu,Dy}$  Phosphors. *Appl. Phys. Lett.* **81**, 996–998 (2002)
13. Akiyama, M., Xu, C.-N., Nonaka, K., Watanabe, T.: Intense visible light emission from  $\text{Sr}_3\text{Al}_2\text{O}_6\text{:Eu,Dy}$ . *Appl. Phys. Lett.* **73**, 3046 (1998)
14. Zhang, P., Xu, M., Zheng, Z., Sun, B., Zhang, Y.: Rapid formation of red long afterglow phosphor  $\text{Sr}_3\text{Al}_2\text{O}_6\text{:Eu}^{2+},\text{Dy}^{3+}$  by microwave irradiation. *Mater. Sci. Eng. B.* **136**, 159–164 (2007)
15. Zhang, P., Li, L., Xu, M., Liu, L.: The new red luminescent  $\text{Sr}_3\text{Al}_2\text{O}_6\text{:Eu}^{2+}$  phosphor powders synthesized via sol–gel route by microwave-assisted. *J. Alloys Compd.* **456**, 216–219 (2008)
16. Pang, R., Li, C., Zhang, S., Su, Q.: Luminescent properties of a new blue long-lasting phosphor  $\text{Ca}_2\text{P}_3\text{O}_7\text{:Eu}^{2+},\text{Y}^{3+}$ . *Mater. Chem. Phys.* **113**, 215–218 (2009)
17. Jiang, L., Chang, C., Mao, D., Feng, C.: Luminescent properties of  $\text{CaMgSi}_2\text{O}_6$ -based phosphors co-doped with different rare earth ions. *J. Alloys Compd.* **377**, 211–215 (2004)
18. Jiang, L., Chang, C., Mao, D., Feng, C.: Luminescent properties of  $\text{Ca}_2\text{MgSi}_2\text{O}_7$  phosphor activated by  $\text{Eu}^{2+}$ ,  $\text{Dy}^{3+}$  and  $\text{Nd}^{3+}$ . *Opt. Mater.* **27**, 51–55 (2004)
19. Aitasalo, T., Hölsä, J., Kirm, M., Laamanen, T., Lastusaari, M., Niittykoski, J., Raud, J., Valtanen, R.: Persistent luminescence and synchrotron radiation study of the  $\text{Ca}_2\text{MgSi}_2\text{O}_7\text{:Eu}^{2+},\text{L R}^{3+}$  materials. *Radiat. Meas.* **42**, 644–647 (2007)
20. Shi, C., Fu, Y., Liu, B., Zhang, G., Chen, Y., Qi, Z., Luo, X.: The roles of  $\text{Eu}^{2+}$  and  $\text{Dy}^{3+}$  in the blue long-lasting phosphor  $\text{Sr}_2\text{MgSi}_2\text{O}_7\text{:Eu}^{2+},\text{Dy}^{3+}$ . *J. Lumin.* **122–123**, 11–13 (2007)
21. Lin, Y., Nan, C.-W., Zhou, X., Wu, J., Wang, H., Chen, D., Xu, S.: Preparation and characterization of long afterglow  $\text{M}_2\text{MgSi}_2\text{O}_7$ -based (M: Ca, Sr, Ba) photoluminescent phosphors. *Mater. Chem. Phys.* **82**, 860–863 (2003)
22. Poort, S.H.M., Reijnhoudt, H.M., van der Kuip, H.O.T., Blasse, G.: Luminescence of  $\text{Eu}^{2+}$  in silicate host lattices with alkaline earth ions in a row. *J. Alloys Compd.* **241**, 75–81 (1996)
23. Lin, Y., Tang, Z., Zhang, Z., Wang, X., Zhang, J.: Preparation of a new long afterglow blue-emitting  $\text{Sr}_2\text{MgSi}_2\text{O}_7$ -based photoluminescent phosphor. *J. Mater. Sci. Lett.* **20**, 1505–1506 (2001)

24. Lin, Y., Tang, Z., Zhang, Z., Nan, C.W.: Luminescence of  $\text{Eu}^{2+}$  and  $\text{Dy}^{3+}$  activated  $\text{R}_3\text{MgSi}_2\text{O}_8$ -based ( $\text{R} = \text{Ca, Sr, Ba}$ ) phosphors. *J. Alloys Compd.* **348**, 76–79 (2003)
25. Kojima, Y., Toyama, T.: Effect of strontium and lithium ions on afterglow time of red-emitting  $\text{CaS:Eu}^{2+}, \text{Pr}^{3+}$  phosphor upon visible-light irradiation. *J. Alloys Compd.* **475**, 524–528 (2009)
26. Zheng, J., Ying, L., Cheng, Q., Guo, Z., Cai, L., Lu, Y., Chen, C.: Blue-emitting  $\text{SrB}_2\text{O}_4:\text{Eu}^{2+}$  phosphor with high color purity for near-UV white light-emitting diodes. *Mater. Res. Bull.* **64**, 51–54 (2015)
27. Li, Y.Q., van Steen, J.E.J., van Krevel, J.W.H., Botty, G., Delsing, A.C.A., DiSalvo, F.J., de With, G., Hintzen, H.T.: Luminescence properties of red-emitting  $\text{M}_2\text{Si}_5\text{N}_8:\text{Eu}^{2+}$  ( $\text{M} = \text{Ca, Sr, Ba}$ ) LED conversion phosphors. *J. Alloys Compd.* **417**, 273–279 (2006)
28. Liu, L., Li, C., Wang, S., Su, Q.: Redshift phenomenon of the excitation light of long life emission phosphor. *Appl. Phys. Lett.* **88**, 1107 (2006)
29. Dorenbos, P.: Energy of the first  $4f^7 \rightarrow 4f^65d$  transition of  $\text{Eu}^{2+}$  in inorganic compounds. *J. Lumin.* **104**, 239–260 (2003)
30. Pang, R., Li, C., Shi, L., Su, Q.: A novel blue-emitting long-lasting prophyosphate phosphor  $\text{Sr}_2\text{P}_2\text{O}_7:\text{Eu}^{2+}, \text{Y}^{3+}$ . *J. Phys. Chem. Solids.* **70**, 303–306 (2009)
31. Van den Eeckhout, K., Smet, P.F., Poelman, D.: Persistent luminescence in rare-earth codoped  $\text{Ca}_2\text{Si}_5\text{N}_8:\text{Eu}^{2+}$ . *J. Lumin.* **129**, 1140–1143 (2009)
32. Miyamoto, Y., Kato, H., Honna, Y., Yamamoto, H., Ohmi, K.: An orange-emitting, long-persistent phosphor,  $\text{Ca}_2\text{Si}_5\text{N}_8:\text{Eu}^{2+}, \text{Tm}^{3+}$ . *J. Electrochem. Soc.* **156**, J235–J241 (2009)
33. Jianhui, Y., Honghui, Y., Jihua, Z.: Synthesis of blue long afterglow phosphors  $\text{SrAl}_2\text{O}_7:\text{Eu}^{2+}, \text{Dy}^{3+}$  and its luminescent properties. *J. Optoelectron. Laser.* **17**, 444–449 (2006)
34. Nag, A., Kutty, T.R.N.: Role of  $\text{B}_2\text{O}_3$  on the phase stability and long phosphorescence of  $\text{SrAl}_2\text{O}_4:\text{Eu, Dy}$ . *J. Alloys Compd.* **354**, 221–231 (2003)
35. Zhang, J., Zhang, Z., Wang, T., Hao, W.: Preparation and characterization of a new long afterglow indigo phosphor  $\text{Ca}_{12}\text{Al}_{14}\text{O}_{33}:\text{Nd, Eu}$ . *Mater. Lett.* **57**, 4315–4318 (2003)
36. Kuang, J., Liu, Y., Zhang, J., Huang, L., Rong, J., Yuan, D.: Blue-emitting long-lasting phosphor,  $\text{Sr}_3\text{Al}_{10}\text{SiO}_{20}:\text{Eu}^{2+}, \text{Ho}^{3+}$ . *Solid State Commun.* **136**, 6–10 (2005)
37. Wang, Y., Wang, Z., Zhang, P., Hong, Z., Fan, X., Qian, G.: Preparation of  $\text{Eu}^{2+}$  and  $\text{Dy}^{3+}$  co-activated  $\text{CaAl}_2\text{Si}_2\text{O}_8$ -based phosphor and its optical properties. *Mater. Lett.* **58**, 3308–3311 (2004)
38. Ding, Y., Zhang, Y., Wang, Z., Li, W., Mao, D., Han, H., Chang, C.: Photoluminescence of Eu single doped and Eu/Dy codoped  $\text{Sr}_2\text{Al}_2\text{SiO}_7$  phosphors with long persistence. *J. Lumin.* **129**, 294–299 (2009)
39. Jiang, L., Chang, C., Mao, D., Zhang, B.: A new long persistent blue-emitting  $\text{Sr}_2\text{ZnSi}_2\text{O}_7:\text{Eu}^{2+}, \text{Dy}^{3+}$  prepared by sol–gel method. *Mater. Lett.* **58**, 1825–1829 (2004)
40. Liu, L., Li, C., Wang, S., Qiang, S.: Redshift phenomenon of the excitation light of long life emission phosphor. *Appl. Phys. Lett.* **88**, 241107–241107-3 (2006)
41. Zheng, Y., Chen, D., Li, W.: A study on the luminescence properties of  $\text{CaAl}_2\text{B}_2\text{O}_7:\text{Eu}^{2+}$  phosphor. *Phys. B Condens. Matter.* **406**, 996–999 (2011)
42. Ji, P.T., Chen, X.Y., Wu, Y.Q.: Encapsulating  $\text{MAl}_2\text{O}_4:\text{Eu}^{2+}, \text{Dy}^{3+}$  ( $\text{M} = \text{Sr, Ca, Ba}$ ) phosphors with triethanolamine to enhance water resistance. *Appl. Surf. Sci.* **258**, 1888–1893 (2011)
43. Chang, C., Li, W., Huang, X., Wang, Z., Chen, X., Qian, X., Guo, R., Ding, Y., Mao, D.: Photoluminescence and afterglow behavior of  $\text{Eu}^{2+}, \text{Dy}^{3+}$  and  $\text{Eu}^{3+}, \text{Dy}^{3+}$  in  $\text{Sr}_3\text{Al}_2\text{O}_6$  matrix. *J. Lumin.* **130**, 347–350 (2010)
44. Tang, W., Chen, D., Wu, M., Tang, W., Chen, D., Wu, M.: Luminescence studies on  $\text{SrMgAl}_{10}\text{O}_{17}:\text{Eu, Dy}$  phosphor crystals. *Opt. Laser Technol.* **41**, 81–84 (2009)
45. Li, B., Yang, J., Wang, J., Wu, M.: Two-color emitting of  $\text{Eu}^{2+}$  and  $\text{Tb}^{3+}$  co-doped  $\text{Sr}_2\text{MgSi}_2\text{O}_7$  for UV LEDs. *Opt. Mater.* **36**, 1649–1654 (2014)
46. Tam, T.T.H., Du, N.V., Kien, N.D.T., Thang, C.X., Cuong, N.D., Huy, P.T., Chien, N.D., Nguyen, D.H.: Co-precipitation synthesis and optical properties of green-emitting  $\text{Ba}_2\text{MgSi}_2\text{O}_7:\text{Eu}^{2+}$  phosphor. *J. Lumin.* **147**, 358–362 (2014)
47. Lakshminarasimhan, N., Varadaraju, U.V.: Luminescence and afterglow in  $\text{Sr}_2\text{SiO}_4:\text{Eu}^{2+}, \text{RE}^{3+}$  [ $\text{RE} = \text{Ce, Nd, Sm and Dy}$ ] phosphors—role of co-dopants in search for afterglow. *Mater. Res. Bull.* **43**, 2946–2953 (2008)

48. Guo, C., Tang, Q., Huang, D., Zhang, C., Su, Q.: Influence of co-doping different rare earth ions on  $\text{CaGa}_2\text{S}_4\text{:Eu}^{2+}, \text{RE}^{3+} (\text{RE}=\text{Ln})$  phosphors. *J. Phys. Chem. Solids*. **68**, 217–223 (2007)
49. Smet, P., Avci, N., Poelman, D.: Red persistent luminescence in  $\text{Ca}_2\text{SiS}_4\text{:Eu,Nd}$ . *J. Electrochem. Soc.* **156**, H243–H248 (2009)
50. Nanai, Y., Sakamoto, Y., Okuno, T.: Luminescence properties of rare-earth-doped thiosilicate phosphors on silicon substrate. *Jpn. J. Appl. Phys.* **52**, 04CG15 (2013)
51. Miyamoto, Y., Kato, H., Honna, Y., Yamamoto, H., Ohmi, K.: An orange-emitting, long-persistent phosphor,  $\text{Ca}_2\text{Si}_5\text{N}_8\text{:Eu}^{2+}, \text{Tm}^{3+}$ . *J. Electrochem. Soc.* **156**, (2009)
52. Song, C.-Y., Lei, B.-F., Liu, Y.-L., Shi, C.-S., Zhang, J.-X., Huang, L.-H., Yuan, D.-S.: The long afterglow of  $\text{Eu}^{2+}$ -activated  $\text{La}_2\text{O}_2\text{S}$ . *Chin. J. Inorg. Chem.* **20**, 89–93 (2004)
53. Wang, Y., Wang, Z.: Characterization of  $\text{Y}_2\text{O}_2\text{S:Eu}^{3+}, \text{Mg}^{2+}, \text{Ti}^{4+}$  long-lasting phosphor synthesized by flux method. *J. Rare Earths*. **24**, 25–28 (2006)
54. Wang, X., Zhang, Z., Tang, Z., Lin, Y.: Characterization and properties of a red and orange  $\text{Y}_2\text{O}_2\text{S}$ -based long afterglow phosphor. *Mater. Chem. Phys.* **80**, 1–5 (2003)
55. Kang, F., Hu, Y., Chen, L., Wang, X., Mu, Z., Wu, H., Ju, G.:  $\text{Eu}^{3+}$  doped  $\text{CaWO}_4$ —a potential red long afterglow phosphor. *Appl. Phys. B*. **107**, 833–837 (2012)
56. Delbecq, C.J., Toyozawa, Y., Yuster, P.: Tunneling recombination of trapped electrons and holes in KCl: AgCl and KCl: TiCl. *Phys. Rev. B*. **9**, 4497 (1974)
57. Van den Eeckhout, K., Poelman, D., Smet, P.: Persistent luminescence in non- $\text{Eu}^{2+}$ -doped compounds: a review. *Materials*. **6**, 2789–2818 (2013)
58. Liu, Y., Lei, B., Shi, C.: Luminescent properties of a white afterglow phosphor  $\text{CdSiO}_3\text{:Dy}^{3+}$ . *Chem. Mater.* **17**, 2108–2113 (2005)
59. Kuang, J., Liu, Y., Zhang, J.: White-light-emitting long-lasting phosphorescence in  $\text{Dy}^{3+}$ -doped  $\text{SrSiO}_3$ . *J. Solid State Chem.* **179**, 266–269 (2006)
60. Fu, L., Liang, L., Ren, Y.: A novel white light emitting long-lasting phosphor. *Chin. Chem. Lett.* **15**, 335–338 (2004)
61. Gong, Y., Wang, Y., Li, Y., Xu, X.:  $\text{Ce}^{3+}$ ,  $\text{Dy}^{3+}$  co-doped white-light long-lasting phosphor:  $\text{Sr}_2\text{Al}_2\text{SiO}_7$  through energy transfer. *J. Electrochem. Soc.* **157**, J208–J211 (2010)
62. Chen, Y., Cheng, X., Liu, M., Qi, Z., Shi, C.: Comparison study of the luminescent properties of the white-light long afterglow phosphors:  $\text{Ca}_x\text{MgSi}_2\text{O}_{5+x}\text{:Dy}^{3+}$  ( $x = 1, 2, 3$ ). *J. Lumin.* **129**, 531–535 (2009)
63. Liu, B., Kong, L., Shi, C.: White-light long-lasting phosphor  $\text{Sr}_2\text{MgSi}_2\text{O}_7\text{:Dy}^{3+}$ . *J. Lumin.* **122–123**, 121–124 (2007)
64. Zhang, L., Han, P., Wang, K., Lu, Z., Wang, L., Zhu, Y., Zhang, Q.: Enhanced luminescence of  $\text{Sr}_2\text{SiO}_4\text{:Dy}^{3+}$  by sensitization ( $\text{Ce}^{3+}/\text{Bi}^{3+}$ ) and its composition-induced phase transition. *J. Alloys Compd.* **541**, 54–59 (2012)
65. Zhao, W., An, S., Fan, B., Li, S.: Luminescence properties of  $\text{Na}_3\text{YSi}_3\text{O}_9\text{:M}^{3+} (\text{M}=\text{Sm, Tb, tm})$  glass ceramics. *J. Alloys Compd.* **566**, 142–146 (2013)
66. Zhang, Y., Zhu, Z., Zhang, W., Qiao, Y.: Photoluminescence properties of  $\text{Sm}^{3+}$  ions doped oxyfluoride calcium borosilicate glasses. *J. Alloys Compd.* **566**, 164–167 (2013)
67. Sobczyk, M., Szymański, D.: A study of optical properties of  $\text{Sm}^{3+}$  ions in  $\alpha\text{-Na}_3\text{Y}(\text{VO}_4)_2$  single crystals. *J. Lumin.* **142**, 96–102 (2013)
68. Arunkumar, S., Marimuthu, K.: Concentration effect of  $\text{Sm}^{3+}$  ions in  $\text{B}_2\text{O}_3\text{--PbO--PbF}_2\text{--Bi}_2\text{O}_3\text{--ZnO}$  glasses—structural and luminescence investigations. *J. Alloys Compd.* **565**, 104–114 (2013)
69. Ju, Z., Wei, R., Zheng, J., Gao, X., Zhang, S., Liu, W.: Synthesis and Phosphorescence mechanism of a reddish orange emissive long afterglow phosphor  $\text{Sm}^{3+}$ -doped  $\text{Ca}_2\text{SnO}_4$ . *Appl. Phys. Lett.* **98**, 121906 (2011)
70. Shi, L., Zhang, J., Li, H., Feng, P., Liu, X., Fu, Z., Wang, Y.: Afterglow luminescence properties and mechanism of novel orange afterglow phosphor:  $\text{Ca}_2\text{Sb}_2\text{O}_7\text{:Sm}^{3+}$ . *J. Alloys Compd.* **579**, 82–85 (2013)
71. de Chermont, Q.M., Chanéac, C., Seguin, J., Pellé, F., Maîtrejean, S., Jolivet, J.-P., Gourier, D., Bessodes, M., Scherman, D.: Nanoprobes with near-infrared persistent luminescence for in vivo imaging. *Proc. Natl. Acad. Sci.* **104**, 9266–9271 (2007)



72. Yu, N., Liu, F., Li, X., Pan, Z.: Near infrared long-persistent phosphorescence in  $\text{SrAl}_2\text{O}_4:\text{Eu}^{2+}, \text{Dy}^{3+}, \text{Er}^{3+}$  phosphors based on persistent energy transfer. *Appl. Phys. Lett.* **95**, 1110 (2009)
73. Jia, D., Wang, X.-J., Van der Kolk, E., Yen, W.: Site dependent thermoluminescence of long persistent phosphorescence of  $\text{BaAl}_2\text{O}_4:\text{Ce}^{3+}$ . *Opt. Commun.* **204**, 247–251 (2002)
74. Jia, D., Yen, W.: Trapping mechanism associated with electron delocalization and tunneling of  $\text{CaAl}_2\text{O}_4:\text{Ce}^{3+}$ , a persistent phosphor. *J. Electrochem. Soc.* **150**, H61–H65 (2003)
75. Jia, D., Wang, X.-J., Jia, W., Yen, W.: Trapping processes of 5d electrons in  $\text{Ce}^{3+}$  doped  $\text{SrAl}_2\text{O}_4$ . *J. Lumin.* **122**, 311–314 (2007)
76. Jia, D., Meltzer, R.S., Yen, W.M., Jia, W., Wang, X.: Green phosphorescence of  $\text{CaAl}_2\text{O}_4:\text{Tb}^{3+}, \text{Ce}^{3+}$  through persistence energy transfer. *Appl. Phys. Lett.* **80**, 1535–1537 (2002)
77. Sharma, S., Pitale, S., Manzarmalik, M., Dubey, R., Qureshi, M.: Luminescence studies on the blue–green emitting  $\text{Sr}_4\text{Al}_{14}\text{O}_{25}:\text{Ce}^{3+}$  phosphor synthesized through solution combustion route. *J. Lumin.* **129**, 140–147 (2009)
78. Su, Z., Ran, P., Li, C., Qiang, S.: Green photoluminescence, but blue afterglow of  $\text{Tb}^{3+}$  activated  $\text{Sr}_4\text{Al}_{14}\text{O}_{25}$ . *J. Lumin.* **130**, 2223–2225 (2010)
79. Gartia, R.K., Singh, T.T., Singh, T.B.: Optically Stimulated luminescence (OSL) of  $\text{Lu}_2\text{SiO}_5:\text{Ce}$  powder: a preliminary study. *Nucl. Instrum. Methods Phys. Res., Sect. B.* **269**, 30–33 (2011)
80. Kodama, N., Takahashi, T., Yamaga, M., Tanii, Y., Qiu, J., Hirao, K.: Long-lasting phosphorescence in  $\text{Ce}^{3+}$ -doped  $\text{Ca}_2\text{Al}_2\text{SiO}_7$  and  $\text{CaYAl}_3\text{O}_7$  crystals. *Appl. Phys. Lett.* **75**, 1715–1717 (1999)
81. Dorenbos, P., Eijk, C.W.E.V., Bos, A.J.J., Melcher, C.L.: Afterglow and thermoluminescence properties of  $\text{Lu}_2\text{SiO}_5:\text{Ce}$  scintillation crystals. *J. Phys. Condens. Matter.* **6**, 4167–4180(14) (1994)
82. He, Z., Wang, X.J., Yen, W.M.: Behavior of  $\text{Mn}^{2+}$  Ions in the trapping process of  $\text{SrMg}(\text{SiO}_3)_2:\text{Mn}, \text{Dy}$ . *J. Lumin.* **122**, 381–384 (2007)
83. Peng, Z., Xu, Z., Luo, C., Yu, J., Zhang, G.: Synthesis and luminescent properties of a novel bluish-white afterglow phosphor,  $\beta\text{-Zn}_3(\text{PO}_4)_2:\text{Hf}^{4+}$ . *Lumin. J. Biol. Chem. Lumin.* **23**, 14–16 (2008)
84. Wang, X.:  $\text{Mn}^{2+}$  activated green, yellow, and red long persistent phosphors. *J. Lumin.* **102–103**, 34–37 (2003)
85. Xu, X., Wang, Y., Yu, X., Li, Y., Gong, Y.: Investigation of Ce–Mn energy transfer in  $\text{SrAl}_2\text{O}_4:\text{Ce}^{3+}, \text{Mn}^{2+}$ . *J. Am. Ceram. Soc.* **94**, 160–163 (2011)
86. Jia, D., Yen, W.M.: Enhanced  $\text{VK}^{3+}$  center afterglow in  $\text{MgAl}_2\text{O}_4$  by doping with  $\text{Ce}^{3+}$ . *J. Lumin.* **101**, 115–121 (2003)
87. Zhong-Fei, M., Yin-Hai, W., Yi-Hua, H.: The afterglow and thermoluminescence properties of  $\text{Y}_3\text{Al}_5\text{O}_{12}:\text{Ce}^{3+}$ . *Acta Phys. Sin.* **60**, 013201–012110 (2011)
88. Rodrigues, L.C., Brito, H.F., Hölsä, J., Lastusaari, M.: Persistent luminescence behavior of materials doped with  $\text{Eu}^{2+}$  and  $\text{Tb}^{3+}$ . *Opt. Mater. Express.* **2**, 382–390 (2012)
89. Kuang, J., Liu, Y.: Luminescence properties of a  $\text{Pb}^{2+}$  activated long-afterglow phosphor. *J. Electrochem. Soc.* **153**, G245–G247 (2005)
90. Xu, X., Wang, Y., Zeng, W., Gong, Y., Liu, B.: Luminescent properties of the multicolor afterglow phosphors  $\text{Ca}_3\text{SnSi}_2\text{O}_9:\text{re}^{3+}$  ( $\text{Re} = \text{Pr}, \text{Tb}, \text{Sm}$ ). *J. Am. Ceram. Soc.* **94**, 3632–3635 (2011)
91. Bessière, A., Benhamou, R.A.T., Wallez, G., Lecointre, A., Viana, B.: Site occupancy and mechanisms of thermally Stimulated luminescence in  $\text{Ca}_9\text{Ln}(\text{PO}_4)_7$  ( $\text{Ln} = \text{lanthanide}$ ). *Acta Mater.* **60**, 6641–6649 (2012)
92. Trojan-Piegza, J., Zych, E., Hölsä, J., Niittykoski, J.: Spectroscopic properties of persistent luminescence phosphors:  $\text{Lu}_2\text{O}_3:\text{Tb}^{3+}, \text{M}^{2+}$  ( $\text{M} = \text{Ca}, \text{Sr}, \text{Ba}$ ). *J. Phys. Chem. C.* **113**, 20493–20498 (2009)
93. Jin, Y., Hu, Y., Chen, L., Wang, X., Ju, G., Mu, Z.: Luminescent properties of  $\text{Tb}^{3+}$ -doped  $\text{Ca}_2\text{SnO}_4$  phosphor. *J. Lumin.* **138**, 83–88 (2013)

94. Lei, B.F., Li, B., Zhang, H.R., Zhang, L.M., Cong, Y., Li, W.L.: Synthesis and luminescence properties of cube-structured  $\text{CaSnO}_3/\text{RE}^{3+}$  ( $\text{RE}=\text{Pr}, \text{Tb}$ ) long-lasting phosphors. *J. Electrochem. Soc.* **154**, (2007)
95. Liu, C., Che, G., Xu, Z., Wang, Q.: Luminescence properties of a  $\text{Tb}^{3+}$  activated long-afterglow phosphor. *J. Alloys Compd.* **474**, 250–253 (2009)
96. Takayama, T., Katsumata, T., Komuro, S., Morikawa, T.: Growth and characteristics of a new long afterglow Phosphorescent yttrium tantalate crystal. *J. Cryst. Growth.* **275**, e2013–e2017 (2005)
97. Wu, H., Hu, Y., Kang, F., Chen, L., Wang, X., Ju, G., Mu, Z.: Observation on long afterglow of  $\text{Tb}^{3+}$  in  $\text{CaWO}_4$ . *Mater. Res. Bull.* **46**, 2489–2493 (2011)
98. Haranath, D., Khan, A.F., Chander, H.: Bright red luminescence and energy transfer of  $\text{Pr}^{3+}$ -doped  $(\text{Ca}, \text{Zn})\text{TiO}_3$  phosphor for long decay applications. *J. Phys. D: Appl. Phys.* **39**, 4956–4960(5) (2006)
99. Haranath, D., Khan, A.F., Chander, H.: Luminescence enhancement of  $(\text{Ca}, \text{Zn})\text{TiO}_3:\text{Pr}^{3+}$  phosphor using nanosized silica powder. *Appl. Phys. Lett.* **89**, 091903 (2006)
100. Minghui, C., Dapeng, J., Chengjiu, Z., Bin, L.: Long-lasting phosphorescence properties of Pyrochlore  $\text{La}_2\text{Ti}_2\text{O}_7:\text{Pr}^{3+}$  phosphor. *Chin. Phys. Lett.* **27**, 208–211 (2004)
101. Jia, W., Yuan, H., Lu, L., Liu, H., Yen, W.M.: Crystal growth and characterization of  $\text{Eu}^{2+}, \text{Dy}^{3+}:\text{SrAl}_2\text{O}_4$  and  $\text{Eu}^{2+}, \text{Nd}^{3+}:\text{CaAl}_2\text{O}_4$  by the LHPG method. *J. Cryst. Growth.* **200**, 179–184 (1999)
102. Qu, X., Cao, L., Liu, W., Su, G.: Preparation and properties of  $\text{CdSiO}_3:\text{Mn}^{2+}, \text{Tb}^{3+}$  phosphor. *Ceram. Int.* **38**, 1765–1769 (2012)
103. Kuang, J., Liu, Y., Lei, B.: Effect of  $\text{RE}^{3+}$  as a co-dopant in long-lasting phosphorescence  $\text{CdSiO}_3:\text{Mn}^{2+}$  ( $\text{RE}=\text{Y}, \text{La}, \text{Gd}, \text{Lu}$ ). *J. Lumin.* **118**, 33–38 (2006)
104. Gong, Y., Xu, X., Zeng, W., Wu, C., Wang, Y.:  $\text{Ce}^{3+}, \text{Mn}^{2+}$  co-doped red–light long–lasting phosphor:  $\text{BaMg}_2\text{Si}_2\text{O}_7$  through energy transfer. *Phys. Procedia.* **29**, 86–90 (2012)
105. Lecointre, A., Bessière, A., Bos, A.J.J., Dorenbos, P., Viana, B., Jacquart, S.: Designing a red persistent luminescence phosphor: the example of  $\text{YPO}_4:\text{Pr}^{3+}, \text{Ln}^{3+}$  ( $\text{Ln} = \text{Nd}, \text{Er}, \text{Ho}, \text{Dy}$ ). *J. Phys. Chem. C.* **115**, 4217–4227 (2011)
106. Lin, Y., Nan, C.W., Cai, N., Zhou, X., Wang, H., Chen, D.: Anomalous afterglow from  $\text{Y}_2\text{O}_3$ -based phosphor. *J. Alloys Compd.* **361**, 92–95 (2003)
107. Zych, E., Trojan-Piegius, J.: Anomalous activity of  $\text{Eu}^{3+}$  in S6 site of  $\text{Lu}_2\text{O}_3$  in persistent luminescence. *J. Lumin.* **122**, 335–338 (2007)
108. Zhao, Z., Wang, Y.: The synthesis and afterglow luminescence properties of a novel red afterglow phosphor:  $\text{ZrO}_2:\text{Sm}^{3+}, \text{Sn}^{4+}$ . *J. Lumin.* **132**, 2842–2846 (2012)
109. Fu, J.: ChemInform abstract: orange and violet-emitting long-lasting phosphors. *Cheminform.* **33**(14), 255–257 (2002)
110. Fu, J.: Orange and red emitting long-lasting phosphors  $\text{MO}:\text{Eu}^{3+}$  ( $\text{M} = \text{Ca}, \text{Sr}, \text{Ba}$ ). *Electrochem. Solid-State Lett.* **3**, 350–351 (2000)
111. Xu, X., Wang, Y., Wei, Z., Yu, G.: Luminescence and storage properties of sm-doped alkaline-earth atannates. *J. Electrochem. Soc.* **158**, J305–J309 (2011)
112. Gao, X., Zhang, Z., Wang, C., et al.: The persistent energy transfer and effect of oxygen vacancies on red long-persistent phosphorescence phosphors  $\text{Ca}_2\text{SnO}_4:\text{Gd}^{3+}, \text{Eu}^{3+}$ . *J. Electrochem. Soc.* **158**, J405–J408 (2011)
113. Lei, B., Man, S.Q., Liu, Y., Yue, S.: Luminescence properties of  $\text{Sm}^{3+}$ -doped  $\text{Sr}_3\text{Sn}_2\text{O}_7$  phosphor. *Mater. Chem. Phys.* **124**, 912–915 (2010)
114. Feng-Wen, K., Yi-Hua, H., Hao-Yi, W., Gui-Fang, J.: Red afterglow properties of  $\text{Eu}^{3+}$  in  $\text{CaMoO}_4$  phosphor. *Chin. Phys. Lett.* **28**, 107201–107204(4) (2011)
115. Kang, F., Hu, Y., Wu, H., Mu, Z., Ju, G., Fu, C., Li, N.: Luminescence and red long afterglow investigation of  $\text{Eu}^{3+}-\text{Sm}^{3+}$  co-doped  $\text{CaWO}_4$  phosphor. *J. Lumin.* **132**, 887–894 (2012)
116. Sun, D., Li, D., Zhu, Z., Xiao, J., Tao, Z., Liu, W.: Photoluminescence properties of europium and titanium Co-doped  $\text{BaZrO}_3$  phosphors powders synthesized by the solid-state reaction method. *Opt. Mater.* **34**, 1890–1896 (2012)
117. Sahu, I.P., Bisen, D.P., Brahme, N.: Dysprosium doped di-strontium magnesium di-silicate white light emitting phosphor by solid state reaction method. *Displays.* **35**, 279–286 (2014)



118. Yang, G., Yongsheng, W., Dawei, H., Ming, F., Yujing, Z., Yue, L., Feng, M.: Synthesis and luminescence properties of  $\text{Sr}_2\text{SiO}_4\text{:Eu}^{3+},\text{Dy}^{3+}$  phosphors for white light LEDs. *Rare Metal Mater. Eng.* **2**, (2011)
119. Ito, Y., Komeno, A., Uematsu, K., Toda, K., Sato, M.: Luminescence properties of long-persistence silicate phosphors. *J. Alloys Compd.* **408–412**, 907–910 (2006)
120. Huang, C.H., Chen, T.M.:  $\text{Ca}_9\text{La}(\text{PO}_4)_7\text{:Eu}^{2+},\text{Mn}^{2+}$ : an emission-tunable phosphor through efficient energy transfer for white light-emitting diodes. *Opt. Express.* **18**, 5089–5099 (2010)
121. Wang, X.-J., Jia, D., Yen, W.M.:  $\text{Mn}^{2+}$  activated green, yellow, and red long persistent phosphors. *J. Lumin.* **102**, 34–37 (2003)
122. Lecointre, A., Bessière, A., Viana, B., Gourier, D.: Red persistent luminescent silicate nanoparticles. *Radiat. Meas.* **45**, 497–499 (2010)
123. Abe, S., Uematsu, K., Toda, K., Sato, M.: Luminescent properties of red long persistence phosphors,  $\text{BaMg}_2\text{Si}_2\text{O}_7\text{:Eu}^{2+},\text{Mn}^{2+}$ . *J. Alloys Compd.* **408**, 911–914 (2006)
124. Gong, Y., Wang, Y., Xu, X., Li, Y., Xin, S., Shi, L.: The persistent energy transfer of  $\text{Eu}^{2+}$  and  $\text{Mn}^{2+}$  and the thermoluminescence properties of long-lasting phosphor  $\text{Sr}_3\text{MgSi}_2\text{O}_8\text{:Eu}^{2+},\text{Mn}^{2+},\text{Dy}^{3+}$ . *Opt. Mater.* **33**, 1781–1785 (2011)
125. Lecointre, A., Viana, B., LeMasne, Q., Bessière, A., Chanéac, C., Gourier, D.: Red long-lasting luminescence in clinoenstatite. *J. Lumin.* **129**, 1527–1530 (2009)
126. Zhang, J., Chen, B., Sun, J., Li, X., Cheng, L., Zhong, H.: White long-lasting phosphorescence generation in a  $\text{CaAl}_2\text{Si}_2\text{O}_8\text{:Eu}^{2+},\text{Mn}^{2+},\text{Dy}^{3+}$  system through persistent energy transfer. *J. Phys. D: Appl. Phys.* **45**, 1418–1420 (2012)
127. Yun, Y.J., Lim, H.J., Park, J.S., Wu, M., Jung, H.K., Choi, S.: Temperature variable luminescence and color tuning of  $\text{Eu}^{2+}/\text{Mn}^{2+}$ -codoped strontium magnesium phosphates as promising red-emitting phosphors for light emitting diodes. *Dalton Trans.* **44**, 338–344 (2015)
128. Xu, X., Wang, Y., Li, Y., Gong, Y.: Energy transfer between  $\text{Eu}^{2+}$  and  $\text{Mn}^{2+}$  in long-afterglow phosphor  $\text{CaAl}_2\text{O}_4\text{:Eu}^{2+},\text{Nd}^{3+}$ , and  $\text{Mn}^{2+}$ . *J. Appl. Phys.* **105**, 083502–083502-4 (2009)
129. Smith, B.A., Zhang, J.Z., Joly, A., Liu, J.: Luminescence decay kinetics of  $\text{Mn}^{2+}$ -doped  $\text{ZnS}$  nanoclusters grown in reverse micelles. *Phys. Rev. B.* **62**, 2021 (2000)
130. Minami, T., Maeno, T., Kuroi, Y., Takata, S.: High-luminance green-emitting thin-film electroluminescent devices using  $\text{ZnGa}_2\text{O}_4\text{:Mn}$  phosphor. *Jpn. J. Appl. Phys.* **34**, L684 (1995)
131. Shea, L., Datta, R., Brown, J.: Photoluminescence of  $\text{Mn}^{2+}$ -activated  $\text{ZnGa}_2\text{O}_4$ . *J. Electrochem. Soc.* **141**, 1950–1954 (1994)
132. Parke, S.: Effect of temperature on the fluorescence of divalent manganese in glasses. *J. Phys. Chem. Solids.* **32**, 669–675 (1971)
133. Fu, Z., Zhou, S., Zhang, S.: Study on optical properties of rare-earth ions in nanocrystalline monoclinic  $\text{SrAl}_2\text{O}_4\text{:Ln}$  ( $\text{Ln} = \text{Ce}^{3+}, \text{Pr}^{3+}, \text{Tb}^{3+}$ ). *J. Phys. Chem. B.* **109**, 14396–14400 (2005)
134. Yu, X., Zhou, C., He, X., Peng, Z., Yang, S.-P.: The influence of some processing conditions on luminescence of  $\text{SrAl}_2\text{O}_4\text{:Eu}^{2+}$  nanoparticles produced by combustion method. *Mater. Lett.* **58**, 1087–1091 (2004)
135. Peng, T., Yang, H., Pu, X., Hu, B., Jiang, Z., Yan, C.: Combustion synthesis and photoluminescence of  $\text{SrAl}_2\text{O}_4\text{:Eu, Dy}$  phosphor nanoparticles. *Mater. Lett.* **58**(3), 352–356 (2004)
136. Toda, K., Imanari, Y.-I., Nonogawa, T., Miyoshi, J., Uematsu, K., Sato, M.: Synthesis and characterization of new long persistent phosphor. *J. Ceram. Soc. Jpn.* **110**, 283–288 (2002)
137. Lei, B., Liu, Y., Ye, Z., Shi, C.: Luminescence properties of  $\text{CdSiO}_3\text{:Mn}^{2+}$  phosphor. *J. Lumin.* **109**, 215–219 (2004)
138. Ye, S., Zhang, J., Zhang, X., Lu, S., Ren, X., Wang, X.-J.:  $\text{Mn}^{2+}$  activated red phosphorescence in  $\text{BaMg}_2\text{Si}_2\text{O}_7\text{:Mn}^{2+},\text{Eu}^{2+},\text{Dy}^{3+}$  through persistent energy transfer. *J. Appl. Phys.* **101**, 063545 (2007)
139. Ye, S., Zhang, J., Zhang, X., Wang, X.:  $\text{Mn}^{2+}$  activated red long persistent phosphors in  $\text{BaMg}_2\text{Si}_2\text{O}_7$ . *J. Lumin.* **122**, 914–916 (2007)
140. Maldiney, T., Lecointre, A., Viana, B., Bessière, A.L., Bessodes, M., Gourier, D., Richard, C., Scherman, D.: Controlling electron trap depth to enhance optical properties of persistent luminescence nanoparticles for in vivo imaging. *J. Am. Chem. Soc.* **133**, 11810–11815 (2011)

141. Wang, J., Wang, S., Su, Q.: The role of excess  $\text{Zn}^{2+}$  ions in improvement of red long lasting phosphorescence (LLP) performance of  $\beta\text{-Zn}_3(\text{PO}_4)_2\text{:Mn}$  phosphor. *J. Solid State Chem.* **177**, 895–900 (2004)
142. Wang, J., Su, Q., Wang, S.: Blue and red long lasting phosphorescence (LLP) in  $\beta\text{-Zn}_3(\text{PO}_4)_2\text{:Mn}^{2+}, \text{Zr}^{4+}$ . *J. Phys. Chem. Solids.* **66**, 1171–1176 (2005)
143. Qu, X., Cao, L., Liu, W., Su, G., Wang, P.: Luminescence properties of  $\text{CdSiO}_3\text{:Mn}^{2+}, \text{RE}^{3+}$  (RE = Sm, Dy, Eu) phosphors. *J. Alloys Compd.* **487**, 387–390 (2009)
144. Lin, L., Yin, M., Shi, C., Zhang, W.: Luminescence properties of a new red long-lasting phosphor:  $\text{Mg}_2\text{SiO}_4\text{:Dy}^{3+}, \text{Mn}^{2+}$ . *J. Alloys Compd.* **455**, 327–330 (2008)
145. Mu, Z., Hu, Y., Wang, Y., Wu, H., Fu, C., Kang, F.: The structure and luminescence properties of long afterglow phosphor  $\text{Y}_{3-x}\text{Mn}_x\text{Al}_{5-x}\text{Si}_x\text{O}_{12}$ . *J. Lumin.* **131**, 676–681 (2011)
146. Bessière, A., Lécointre, A., Benhamou, R.A.T., Suard, E., Wallez, G., Viana, B.: how to induce red persistent luminescence in biocompatible  $\text{Ca}_3(\text{PO}_4)_2$ . *J. Mater. Chem. C.* **1**, 1252–1259 (2013)
147. Che, G., Liu, C., Li, X., Xu, Z., Liu, Y., Wang, H.: Luminescence properties of a new  $\text{Mn}^{2+}$ -activated red long-afterglow phosphor. *J. Phys. Chem. Solids.* **69**, 2091–2095 (2008)
148. Uheda, K., Maruyama, T., Takizawa, H., Endo, T.: Synthesis and long-period phosphorescence of  $\text{ZnGa}_2\text{O}_4\text{:Mn}^{2+}$  spinel. *J. Alloys Compd.* **262**, 60–64 (1997)
149. Sun, Z.X.: Enhanced green-light-emitting afterglow in  $\text{Zn}_2\text{GeO}_4\text{:Mn}^{2+}$  phosphor by  $\text{Yb}^{3+}$  codoping. *Chinese J. Inorg. Chem.* **28**, 1229–1233 (2012)
150. Yan, C., Li, B., Yue, S., Zhang, L., Li, W., Wang, X.J.: Enhanced red Phosphorescence in  $\text{MgGeO}_3\text{:Mn}^{2+}$  by addition of  $\text{Yb}^{3+}$  ions. *J. Electrochem. Soc.* **156**, H272–H275 (2009)
151. Lei, B., Li, B., Wang, X., Li, W.: Green emitting long lasting phosphorescence (LLP) properties of  $\text{Mg}_2\text{SnO}_4\text{:Mn}^{2+}$  phosphor. *J. Lumin.* **118**, 173–178 (2006)
152. Che, G., Li, X., Liu, C., Wang, H., Liu, Y., Xu, Z.: Long-lasting phosphorescence properties of  $\text{Mn}^{2+}$ -doped  $\text{Cd}_2\text{Ge}_7\text{O}_{16}$  orange light-emitting phosphor. *Phys. Status Solidi A.* **205**, 194–198 (2008)
153. Yan, W., Liu, F., Lu, Y.-Y., Wang, X.-J., Yin, M., Pan, Z.: Near infrared long-persistent phosphorescence in  $\text{La}_3\text{Ga}_5\text{GeO}_{14}\text{:Cr}^{3+}$  phosphor. *Opt. Express.* **18**, 20215–20221 (2010)
154. Jia, D., Lewis, L.A., Wang, X.-J.:  $\text{Cr}^{3+}$ -doped lanthanum gallogermanate phosphors with long persistent IR emission. *Electrochem. Solid-State Lett.* **13**, J32–J34 (2010)
155. Bessière, A., Jacquart, S., Priolkar, K., Lécointre, A., Viana, B., Gourier, D.:  $\text{ZnGa}_2\text{O}_4\text{:Cr}^{3+}$ : a new red long-lasting phosphor with high brightness. *Opt. Express.* **19**, 10131–10137 (2011)
156. Struve, B., Huber, G.: The effect of the crystal field strength on the optical spectra of  $\text{Cr}^{3+}$  in gallium garnet laser crystals. *Appl. Phys. B.* **36**, 195–201 (1985)
157. Forster, L.S.: The photophysics of chromium (III) complexes. *Chem. Rev.* **90**, 331–353 (1990)
158. Shannon, R.T.: Revised effective ionic radii and systematic studies of interatomic distances in halides and chalcogenides. *Acta Cryst. A.* **32**, 751–767 (1976)
159. Minami, T., Kuroi, Y., Miyata, T., Yamada, H., Takata, S.:  $\text{ZnGa}_2\text{O}_4$  as host material for multicolor-emitting phosphor layer of electroluminescent devices. *J. Lumin.* **72**, 997–998 (1997)
160. Jeong, I.-K., Park, H.L., Mho, S.-I.: Two self-activated optical centers of blue emission in zinc Gallate. *Solid State Commun.* **105**, 179–183 (1998)
161. Sampath, S.K., Cordaro, J.F.: Optical properties of zinc aluminate, zinc gallate, and zinc aluminogallate spinels. *J. Am. Ceram. Soc.* **81**, 649–654 (1998)
162. Kim, J., Park, H., Chon, C., Moon, H., Kim, T.: The origin of emission color of reduced and oxidized  $\text{ZnGa}_2\text{O}_4$  phosphors. *Solid State Commun.* **129**, 163–167 (2004)
163. Dhak, P., Kundu, A., Pramanik, K., Pramanik, P., Dhak, D.: Dielectric diffuseness and conductivity behavior of  $\text{Ba}_{1-x}\text{Cu}_x\text{Ti}_{1-x}(\text{AlK})_x\text{O}_3$  nanoceramics prepared by chemical route. *Adv. Mater. Lett.* **6**(6), 492–500 (2015)
164. Kahan, H., Macfarlane, R.: Optical and microwave spectra of  $\text{Cr}^{3+}$  in the spinel  $\text{ZnGa}_2\text{O}_4$ . *J. Chem. Phys.* **54**, 5197–5205 (1971)

165. Hornstra, J., Keulen, E.: The oxygen parameter of the spinel  $\text{ZnGa}_2\text{O}_4$ . *Philips Res. Rep.* **27**, 76 (1972)
166. Moon, J.-W., Moon, H.-S., Oh, E., Kang, H., Kim, J., Park, H., Kim, T.: Dependence of the structural and the optical properties of  $\text{ZnGa}_2\text{O}_4$  phosphors on the mixture molar ratio of  $\text{ZnO}$  and  $\text{Ga}_2\text{O}_3$ . *Int. J. Inorg. Mater.* **3**, 575–578 (2001)
167. Bessière, A.I., Sharma, S.K., Basavaraju, N., Priolkar, K.R., Binet, L., Viana, B., Bos, A.J., Maldiney, T., Richard, C., Scherman, D.: Storage of visible light for long-lasting phosphorescence in chromium-doped zinc gallate. *Chem. Mater.* **26**, 1365–1373 (2014)
168. Allix, M., Chenu, S.b., Véron, E., Poumeyrol, T., Kouadri-Boudjelthia, E.A., Alahache, S., Porcher, F., Massiot, D., Fayon, F.: Considerable improvement of long-persistent luminescence in germanium and tin substituted  $\text{ZnGa}_2\text{O}_4$ . *Chem. Mater.* **25**, 1600–1606 (2013)
169. Abdukayum, A., Chen, J.-T., Zhao, Q., Yan, X.-P.: Functional near infrared-emitting  $\text{Cr}^{3+}/\text{Pr}^{3+}$  co-doped zinc Gallogermanate persistent luminescent nanoparticles with superlong afterglow for in vivo targeted bioimaging. *J. Am. Chem. Soc.* **135**, 14125–14133 (2013)
170. Liu, F., Yan, W., Chuang, Y.-J., Zhen, Z., Xie, J., Pan, Z.: Photostimulated near-infrared persistent luminescence as a new optical read-out from  $\text{Cr}^{3+}$ -doped  $\text{LiGa}_5\text{O}_8$ . *Sci. Rep.* **3**, 1554 (2013)
171. Li, Y., Zhou, S., Dong, G., Peng, M., Wondraczek, L., Qiu, J.: Anti-stokes fluorescent probe with incoherent excitation. *Sci. Rep.* **4**, 4059 (2014)
172. Zhuang, Y., Ueda, J., Tanabe, S.: Tunable trap depth in  $\text{Zn}(\text{Ga}_{1-x}\text{Al}_x)_2\text{O}_4:\text{Cr},\text{Bi}$  red persistent phosphors: considerations of high-temperature persistent luminescence and photostimulated persistent luminescence. *J. Mater. Chem. C*, **1**, 7849–7855 (2013)
173. Li, Y., Zhou, S., Li, Y., Sharafudeen, K., Ma, Z., Dong, G., Peng, M., Qiu, J.: Long persistent and photo-Stimulated luminescence in  $\text{Cr}^{3+}$ -doped  $\text{Zn-Ga-Sn-O}$  phosphors for deep and reproducible tissue imaging. *J. Mater. Chem. C*, **2**, 2657–2663 (2014)
174. Chen, D., Chen, Y., Lu, H., Ji, Z.: A bifunctional  $\text{Cr}/\text{Yb}/\text{tm}:\text{Ca}_3\text{Ga}_2\text{Ge}_3\text{O}_{12}$  phosphor with near-infrared long-lasting phosphorescence and upconversion luminescence. *Inorg. Chem.* **53**, 8638–8645 (2014)
175. Ueda, J., Kuroishi, K., Tanabe, S.: Bright persistent ceramic phosphors of  $\text{Ce}^{3+}$ - $\text{Cr}^{3+}$ -codoped garnet able to store by blue light. *Appl. Phys. Lett.* **104**, 101904 (2014)
176. Sharma, S., Gourier, D., Viana, B., Maldiney, T., Teston, E., Scherman, D., Richard, C.: Persistent luminescence of  $\text{AB}_2\text{O}_4:\text{Cr}^{3+}$  ( $\text{A} = \text{Zn, mg, B} = \text{Ga, al}$ ) spinels: new biomarkers for in vivo imaging. *Opt. Mater.* **36**, 1901–1906 (2014)
177. Pan, Z., Lu, Y.-Y., Liu, F.: Sunlight-activated long-persistent luminescence in the near-infrared from  $\text{Cr}^{3+}$ -doped zinc gallogermanates. *Nat. Mater.* **11**, 58–63 (2012)
178. Li, Y., Li, Y., Chen, R., Sharafudeen, K., Zhou, S., Gecevicius, M., Wang, H., Dong, G., Wu, Y., Qin, X.: Tailoring of the trap distribution and crystal field in  $\text{Cr}^{3+}$ -doped non-gallate phosphors with near-infrared long-persistence phosphorescence. *NPG Asia Mater.* **7**, e180 (2015)
179. Rao, R.P.: Preparation and characterization of fine-grain yttrium-based phosphors by sol-gel process. *J. Electrochem. Soc.* **143**, 189–197 (1996)
180. Huang, P., Cui, C.-E., Wang, S.: Influence of calcination temperature on luminescent properties of  $\text{Sr}_3\text{Al}_2\text{O}_6:\text{Eu}^{2+},\text{Dy}^{3+}$  phosphors prepared by sol-gel-combustion processing. *Opt. Mater.* **32**, 184–189 (2009)
181. Zhang, P., Xu, M., Zheng, Z., Liu, L., Li, L.: Synthesis and characterization of europium-doped  $\text{Sr}_3\text{Al}_2\text{O}_6$  phosphors by sol-gel technique. *J. Sol-Gel Sci. Technol.* **43**, 59–64 (2007)
182. Zhang, P., Xu, M., Liu, L., Li, L.: Luminescent properties of  $\text{Sr}_3\text{Al}_2\text{O}_6$ : Eu, Pr prepared by sol-gel method. *J. Sol-Gel Sci. Technol.* **50**, 267–270 (2009)
183. Lu, Y., Li, Y., Xiong, Y., Wang, D., Yin, Q.:  $\text{SrAl}_2\text{O}_4:\text{Eu}^{2+},\text{Dy}^{3+}$  phosphors derived from a new sol-gel route. *Microelectron. J.* **35**, 379–382 (2004)
184. Young, K., Fetcenko, M., Li, F., Ouchi, T., Koch, J.: Effect of vanadium substitution in C14 laves phase Alloys for NiMH battery application. *J. Alloys Compd.* **468**, 482–492 (2009)
185. Zhang, R., Han, G., Zhang, L., Yang, B.: Gel combustion synthesis and luminescence properties of nanoparticles of monoclinic  $\text{SrAl}_2\text{O}_4:\text{Eu}^{2+},\text{Dy}^{3+}$ . *Mater. Chem. Phys.* **113**, 255–259 (2009)

186. Chen, X.Y., Bao, S.P., Wu, Y.C.: Controlled synthesis and luminescent properties of  $\text{Eu}^{2+}(\text{Eu}^{3+})$ ,  $\text{Dy}^{3+}$ -doped  $\text{Sr}_3\text{Al}_2\text{O}_6$  phosphors by hydrothermal treatment and postannealing approach. *J. Solid State Chem.* **183**, 2004–2011 (2010)
187. Rong, W., Jianxin, M.: Hydrothermal preparation and characterization of long-afterglow phosphors  $\text{CaTiO}_3\text{:Pr,Al}$ . *J. Chin. Rare Earth Soc.* **27**, 349–352 (2009)
188. Linhua, Y., Jianshe, Y., Jiqin, C.: Growth of  $\text{YVO}_4$  Crystal fiber using LHPG technique. *J. Synth. Cryst.* **25**, 118–121 (1996)
189. Mingdao, T., Changkuan, L., Zhiwu, G.: The study on long persistence of  $\text{SrAl}_2\text{O}_4\text{:Eu}^{2+}$ . *Chin. J. Lumin.* **1**, 51–56 (1995)
190. Rossner, W., Grabmaier, B.C.: Phosphors for X-ray detectors in computed tomography. *J. Lumin.* **48–49**, 29–36 (1991)
191. Kuang, J., Liu, Y.: Observation of energy transfer from host to Rare earth ions in  $\text{Pr}^{3+}$ -doped  $\text{CdSiO}_3$  long-lasting phosphor. *Chem. Phys. Lett.* **424**, 58–62 (2006)
192. LUMING Technology Group Co., L. <http://www.luminglight.com/product/index.asp>
193. <http://detail.1688.com/offer/37070647373.html?spm=0.0.0.0.dVdMpx>
194. Dong, W., Yin, Q., Li, Y., Wang, M.: Concentration quenching of  $\text{Eu}^{2+}$  in  $\text{SrOAl}_2\text{O}_3\text{:Eu}^{2+}$  phosphor. *J. Lumin.* **97**, 1–6 (2002)
195. Yongjie, C., Yanbin, S.: Studies on superlong afterglow luminescence materials. *Chin. Rare Earths.* **23**, 50–53 (2002)
196. Chen, I., Chen, T.-M.: Effect of host compositions on the afterglow properties of phosphorescent strontium aluminate phosphors derived from the sol-gel method. *J. Mater. Res.* **16**, 1293–1300 (2001)
197. Randall, J., Wilkins, M.: Phosphorescence and electron traps. I. The study of trap distributions. *Proc. R. Soc. Lond. A: Math. Phys. Eng. Sci.* **184**, 365–389 (1945)
198. Katsumata, T., Sakai, R., Komuro, S., Morikawa, T., Kimura, H.: Growth and characteristics of long duration phosphor crystals. *J. Cryst. Growth.* **198**, 869–871 (1999)
199. Song, Y., Choi, S., Moon, H., Kim, T., Mho, S.-I., Park, H.: Phase studies of  $\text{SrOAl}_2\text{O}_3$  by emission signatures of  $\text{Eu}^{2+}$  and  $\text{Eu}^{3+}$ . *Mater. Res. Bull.* **32**, 337–341 (1997)
200. Liu, Y., Xu, C.-N.: Influence of calcining temperature on photoluminescence and triboluminescence of europium-doped strontium aluminate particles prepared by sol-gel process. *J. Phys. Chem. B.* **107**, 3991–3995 (2003)
201. Hongtao, C., Yaowen, Z., Guangyan, H.: the surface coating technology of phosphor. *J. Funct. Mater.* **32**, 2000209206 (2001)
202. Qiu, G., Sun, Y., Chen, Y., Zhang, M.: Studies on self-luminous material and coating with long persistent yellow-green afterglow. *J. Rare Earths.* **21**, 533 (2003)
203. Shiyan, H., Huaihua, Z., Huimin, H.: Inorganic encapsulation of strontium aluminate phosphors. *Chin. Rare Earths.* **29**, 39–44 (2008)
204. Lu, X.D., Shu, W.Y.: Organic encapsulation on  $\text{SrAl}_2\text{O}_4\text{:Eu}^{2+}, \text{Dy}^{3+}$  phosphors and its characterization. *Chin. J. Appl. Chem.* **22**, 638–642 (2005)
205. Wu, S., Zhang, S., Liu, Y., Yang, J.: The organic ligands coordinated long afterglow phosphor. *Mater. Lett.* **61**, 3185–3188 (2007)
206. Guo, B., Xu, J., Cao, X.Z.: Surface modification of long afterglow phosphors by different saturated fatty acid based al-Zr coupling agent. *Paint Coatings Ind.* **41**, 9–13 (2011)
207. Dutta, A., Dullea, L.V.: Method of coating phosphors of fluorescent lamp glass. Google Patents, (1995)
208. Wu, S., Zhang, S., Yang, J.: Highly water-resistant and organic miscible inorganic/polymer composite luminescent material. *Mater. Lett.* **63**, 1172–1174 (2009)
209. Pham-Thi, M., Morell, A.: Process optimization and characterization of the red no-mill phosphor  $\text{Y}_2\text{O}_3\text{:Eu}$ . *J. Electrochem. Soc.* **138**, 1100–1103 (1991)
210. Ma, Q.-L., Zhai, B.-G., Huang, Y.M.: Effect of sol-gel combustion temperature on the luminescent properties of trivalent Dy doped  $\text{SrAl}_2\text{O}_4$ . *Ceram. Int.* **41**, 5830–5835 (2015)

## Chapter 3

# Material Characterizations

### 3.1 Optical Properties

Due to their diversified electronic configurations or bandgap features, luminescent phosphors have unique optical characteristics. In this section, we discuss the optical properties of luminescent phosphors, with a particular emphasis on basic optical properties of luminescent phosphors, as well as thermoluminescence and luminescence decay in long persistent luminescent materials. We begin by describing basic optical characteristics of luminescent phosphors, including excitation, emission, absorption, and reflection. Next, we discuss thermoluminescence phenomenon in long persistent luminescent materials. Selected examples will be presented in this section. Finally, the luminescence decay will be also introduced.

#### 3.1.1 *Excitation and Emission*

Emission is an optical process that a substance releases energy by electromagnetic radiation form. In principle, phosphors can be excited by light at any wavelength which can be absorbed. As a matter of fact, the optimal wavelength for excitation often differs from the maximum absorption wavelength. Excitation spectrum reflects the correlation between luminescence intensity of phosphors and excitation wavelength, allowing us to identify the optimal wavelength of excitation light for maximum emission intensity. The excitation spectrum is recorded by monitoring emission at the wavelength of maximum intensity while the phosphor is excited by a light source with a group of continuous wavelengths. Emission spectrum shows the emission intensity at a series of wavelengths when phosphor is under the irradiation of a particular excitation source, such as light, electron beam, heat, or X-ray. By employing a monochromator equipped with a suitable light detector, the excitation and emission spectrum can be recorded. The emission spectra can typically be

**Fig. 3.1** (a) Emission and (b) excitation spectra of  $\text{SrAl}_2\text{O}_4:\text{Eu}^{2+}$

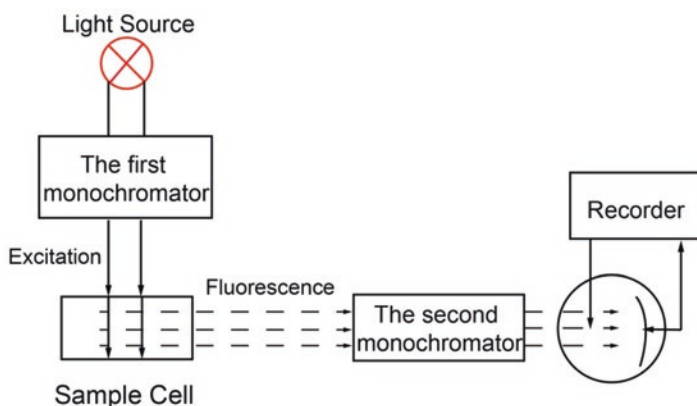
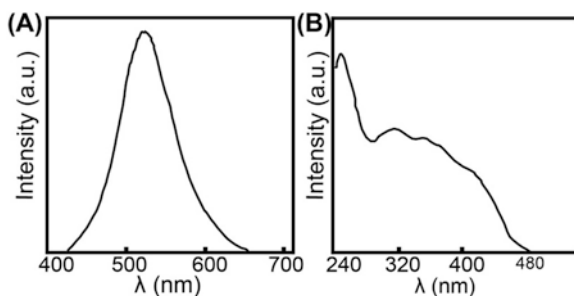


**Fig. 3.2** Schematic diagram of instrument used for fluorescence measurement

characterized by lines, bands, or continuous radiations, which is mainly determined by phosphors and excitation. Figure 3.1 shows typical excitation and emission spectra of  $\text{SrAl}_2\text{O}_4:\text{Eu}^{2+}$  phosphor, offering a broadband (240–480 nm) and a narrow-band (450–600 nm) features, respectively.

A typical spectrometer for luminescence measurement consists of a light source, two monochromators, a sample cell, and a recorder, as shown in Fig. 3.2. When the light source turns on, excitation beam goes through the first monochromator, releases light with a certain wavelength and excites the sample. The excited sample emits light with a certain wavelength. Subsequently, the emission passes through the second monochromator, and is finally collected by the recorder.

### 3.1.2 Reflection and Absorption

The interaction between electromagnetic wave (light) and matter is mainly classified into three ways: reflection, absorption, and transmission. Reflection is an optical process by which electromagnetic radiation is returned after interaction with matter. Transmission is the process that electromagnetic radiation passes through a

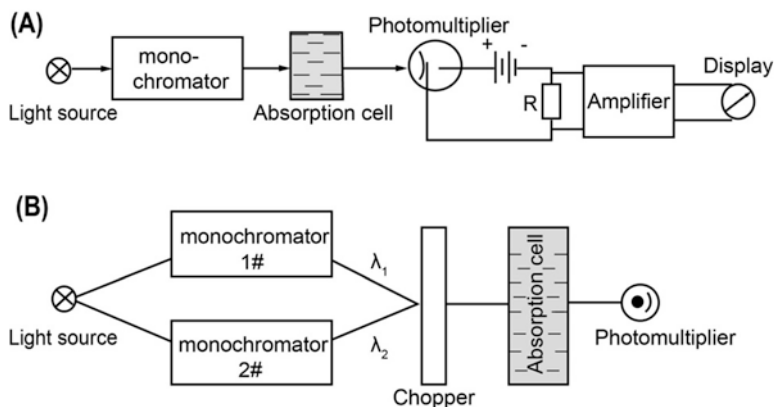


**Fig. 3.3** Schematic illustrations of (a) single beam spectrophotometer and (b) double beam spectrophotometer

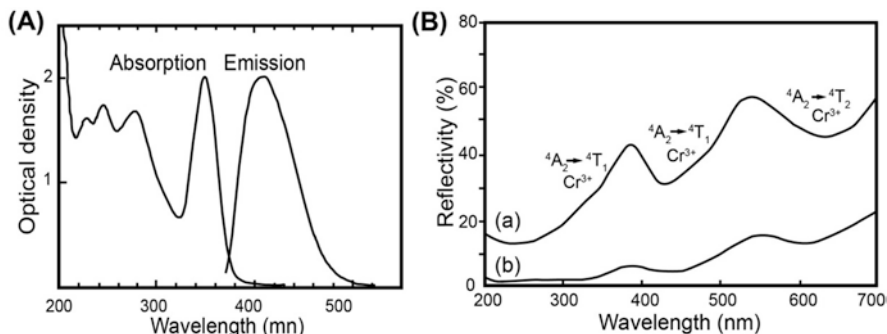


**Fig. 3.4** (a) Absorption and emission spectra of  $\text{Ca}_2\text{Al}_2\text{SiO}_7:\text{Ce}^{3+}$  measured at room temperature. (b) Diffuse reflection spectra of  $\text{Gd}_3\text{Ga}_5\text{O}_{12}:\text{Cr}^{3+},\text{Ce}^{4+}$  (a) and  $\text{Gd}_3\text{Ga}_5\text{O}_{12}:\text{Cr}^{3+},\text{Ce}^{3+}$  (b)

medium. Absorption is accompanied by the transformation of incident light to another type of energy.

UV-vis spectrophotometer is generally used for measuring the absorption spectroscopy. There are usually two types of spectrophotometers—single beam and double beam spectrophotometers and the schematic diagrams are shown in Fig. 3.3.

Reflection and absorption spectra reveal the relationship between wavelength and the intensity of light absorbed by the sample at the sample surface and in the interior of the sample, respectively. The energy bands of the material and the impurity levels in the material can be obtained from the absorption spectrum. The absorption intensity varies with the wavelength of incident light (Fig. 3.4a) [1].

The refraction index and extinction coefficient are two important parameters for the refraction and absorption of a given material, respectively. The extinction coefficient is usually used to quantify the absorbance. According to the Kramers–Kronig relation, the extinction coefficient is also quantitatively related to refractive index



coefficients. Thus, by using simplified assumptions or models, the approximated absorbance can be deduced from a scattering or reflection spectrum (Fig. 3.4b).

3.1.3 Thermoluminescence

As discussed in above chapters, charge carrier traps play an important role in afterglow luminescence. The duration of afterglow luminescence is strongly determined by the “depth” and “distribution” of these traps. The information of trap depth can be obtained by measuring thermoluminescence of the phosphors.

The thermoluminescence process is dominantly classified to three stages: irradiation, storage, and escaping. In the first stage, upon the high energy irradiation, free charge carriers are yielded in crystalline materials. Subsequently, the electrons are trapped and stored in the trap center. Finally, with the increase of temperature, the trapped electrons interact with phonons, escape from the trap center, and then recombine with holes, eventually yielding afterglow emission. With the increase of temperature, emission intensity will increase and then gradually attenuates due to the decreased number of trapped electrons. The change in luminescence intensity as a function of temperature is depicted by a glow curve. Generally, thermoluminescence spectrum shows multiple peaks, which is attributable to multiple traps or trap distributions. Therefore, the information on the depths and distributions of those traps can be obtained by analyzing the shape and wavelength of the different peaks. Table 3.1 shows trap depth(s) values of a variety of well-known long afterglow phosphors.

Half-peak width method was commonly used to calculate trap state energy level. The full width at half maximum intensity ( $\delta$ ) can be described as follows:

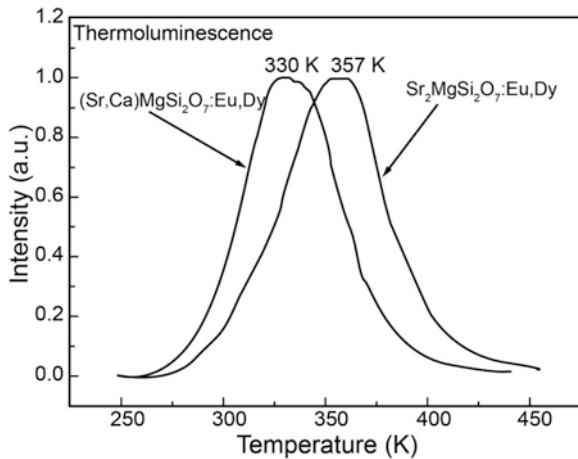
$$\delta = T_2 - T_m$$

**Table 3.1** Estimated trap depth(s) of persistent phosphors

Phosphor	Trap depths (eV)	Reference
SrAl <sub>2</sub> O <sub>4</sub> :Eu <sup>2+</sup> ,Dy <sup>3+</sup>	1.1	[3]
CaAl <sub>2</sub> O <sub>4</sub> :Eu <sup>2+</sup> ,Dy <sup>3+</sup>	0.56/0.65	[4]
CaAl <sub>2</sub> O <sub>4</sub> :Eu <sup>2+</sup> ,Dy <sup>3+</sup> ,Nd <sup>3+</sup>	0.76	[5]
CaAl <sub>2</sub> O <sub>4</sub> :Eu <sup>2+</sup> ,Dy <sup>3+</sup> ,La <sup>3+</sup>	0.80	
Sr <sub>4</sub> Al <sub>14</sub> O <sub>25</sub> :Eu <sup>2+</sup> ,Dy <sup>3+</sup>	0.91	[6]
(Sr,Ca)MgSi <sub>2</sub> O <sub>7</sub> :Eu <sup>2+</sup> ,Dy <sup>3+</sup>	0.66	[2]
Sr <sub>2</sub> MgSi <sub>2</sub> O <sub>7</sub> :Eu <sup>2+</sup> ,Nd <sup>3+</sup>	0.08/0.18/0.29/0.23	[7]
Ca <sub>2</sub> MgSi <sub>2</sub> O <sub>7</sub> :Eu <sup>2+</sup> ,Tm <sup>3+</sup>	0.56	[8]
Y <sub>2</sub> O <sub>2</sub> S:Eu <sup>3+</sup> ,Mg <sup>2+</sup> ,Ti <sup>4+</sup>	0.43	[9]
Zn <sub>3</sub> (PO <sub>4</sub> ) <sub>2</sub> :Mn <sup>2+</sup>	0.38	[10]
Sr <sub>3</sub> Al <sub>10</sub> SiO <sub>20</sub> :Eu <sup>2+</sup> ,Ho <sup>3+</sup>	0.46	[11]



**Fig. 3.5** Thermoluminescence spectra of  $\text{Sr}_2\text{MgSi}_2\text{O}_7:\text{Eu}^{2+},\text{Dy}^{3+}$  and  $(\text{Sr,Ca})\text{MgSi}_2\text{O}_7:\text{Eu}^{2+},\text{Dy}^{3+}$



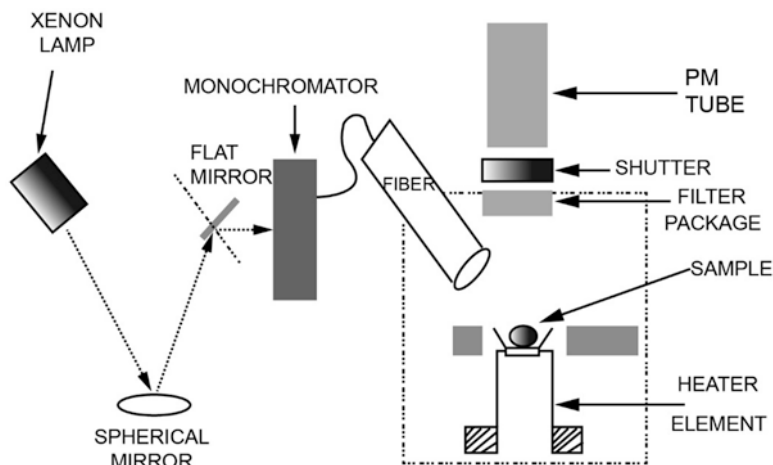
where  $T_m$  and  $T_2$  are the temperature at the peak point and half maximum intensity, respectively. The trap state ( $E$ ) can be expressed by

$$E = \frac{2kT_m^2}{\delta}$$

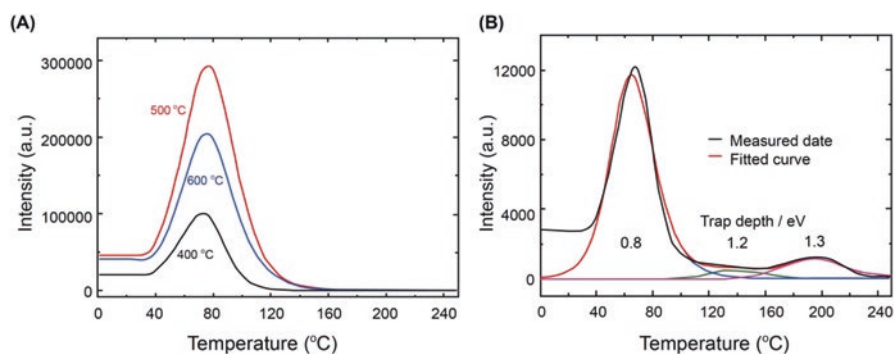
where  $k$  is Boltzmann's constant. By simplifying the equation, the related energy level is calculated to be  $E = T_m/500$ . Therefore, the maximum emission intensity from higher energy level or deeper traps is often observed at a higher temperature.

Figure 3.5 shows typical thermoluminescence spectra of  $\text{Sr}_2\text{MgSi}_2\text{O}_7:\text{Eu}^{2+},\text{Dy}^{3+}$  and  $(\text{Sr,Ca})\text{MgSi}_2\text{O}_7:\text{Eu}^{2+},\text{Dy}^{3+}$  phosphors. The glow curve suggests a strong dependence of emission intensity on the temperature ranging from 250 to 450 K. The maximum emission intensity occurs at 357 K and 330 K for  $\text{Sr}_2\text{MgSi}_2\text{O}_7:\text{Eu}^{2+},\text{Dy}^{3+}$  and  $(\text{Sr,Ca})\text{MgSi}_2\text{O}_7:\text{Eu}^{2+},\text{Dy}^{3+}$ , respectively [2]. By using the simplified equation, the depth of trap for  $(\text{Sr,Ca})\text{MgSi}_2\text{O}_7:\text{Eu}^{2+},\text{Dy}^{3+}$  is calculated to be 0.66 eV, which is in good accordance with the previously reported results calculated by the second order kinetics equation.

Figure 3.6 displays schematic illustration of a typical spectrometer for measurement of thermoluminescence spectra. The optical component arrangement is mainly divided into three parts: an optical input for excitation, a temperature controller for sample heating, and optical output for signal recording [12]. The thermoluminescence measurement system was first developed in the early years of the twentieth century. Before thermoluminescence measurement, the sample should be kept in the dark for enough time or heating to release all the electrons from the traps. Then, the sample is cooled by liquid nitrogen or helium and sufficiently irradiated by a white light source. After removal of the light source, the sample is heated by a temperature-programmed controller with a constant heating rate. At the same time, the emission of the sample is recorded and plotted as a function of temperature.



**Fig. 3.6** Schematic diagram of instrument used for thermoluminescence measurement



**Fig. 3.7** (a) Afterglow curve of  $\text{BaAl}_2\text{O}_4:\text{Eu}^{2+}, \text{Dy}^{3+}$  obtained by combustion method at different temperatures. (b) Experimentally detected and fitted afterglow curve of  $\text{BaAl}_2\text{O}_4:\text{Eu}^{2+}, \text{Dy}^{3+}$  prepared by solid-state method at 1500 °C

The thermoluminescence behavior of the phosphors is strongly dependent on the synthetic approach. Different experimental parameters yield the long persistent phosphors with different traps depths and numbers, which determine optical properties (e.g., lifetime, emission intensity, and afterglow duration) of phosphors. As shown in Fig. 3.7a,  $\text{BaAl}_2\text{O}_4:\text{Eu}^{2+}, \text{Dy}^{3+}$  phosphors obtained by combustion method at different temperatures show different maximum emission intensity at the same temperature, suggesting that the resulting phosphors have different trap numbers and similar trap depth [13]. By comparison, the glow curve of the  $\text{BaAl}_2\text{O}_4:\text{Eu}^{2+}, \text{Dy}^{3+}$  phosphors obtained by solid-state method at 1500 °C exhibits three traps characteristics, suggesting that high reaction temperature facilitates the formation of traps.

The thermoluminescence of phosphors is also strongly affected by excitation wavelength. The trap depth varies over excitation wavelength. Figure 3.8 shows

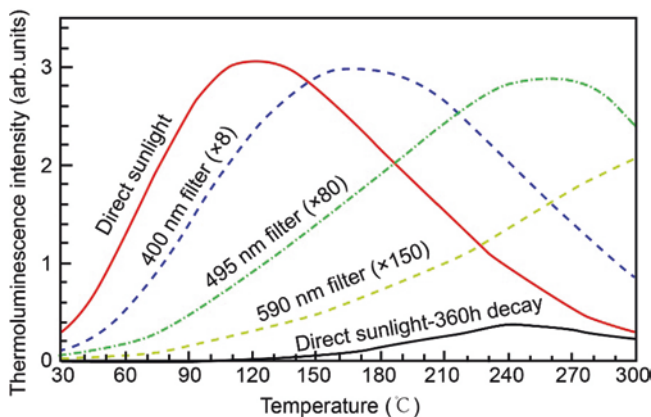


**Fig. 3.8** Thermoluminescence curves of  $\text{Zn}_3\text{Ga}_2\text{Ge}_2\text{O}_{10}:0.5\%\text{Cr}^{3+}$  phosphor irradiated by entire sunlight (solid lines) and partial sunlight with particular spectra ranges for 5 min (monitored at 713 nm). The curves are recorded after the stopping of irradiation for 2 min and 360 h

afterglow curves of  $\text{Zn}_3\text{Ga}_2\text{Ge}_2\text{O}_{10}:0.5\%\text{Cr}^{3+}$  phosphor excited by sunlight with different wavelength ranges. When irradiated by direct sunlight, an asymmetric broad-band curve range from 30 to  $\sim 300^\circ\text{C}$  can be observed with a delay time of 2 min (red line). As the excitation moves to the long-wavelength solar spectral region, peak positions shift to the higher temperature region, indicating that traps with different depths are produced by different excitation energies. In addition, upon the irradiation of direct sunlight for 360 h (black solid line), emission intensity of phosphors at low-temperature range (30 to  $\sim 120^\circ\text{C}$ ) attenuates to be nearly zero and peak position appears at high-temperature range ( $\sim 120$  to  $\sim 300^\circ\text{C}$ ), suggesting that the electrons trapped in shallow traps can be released earlier than that in deep traps.

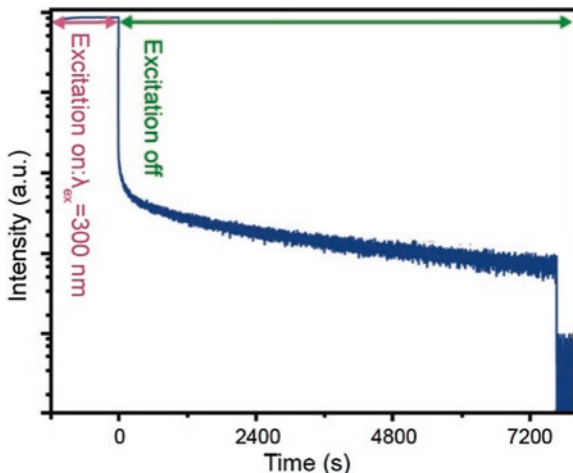
### 3.1.4 Luminescence Decay

Upon shutting down the excitation source, luminescence from phosphors lasts for some time. And the emission intensity gradually decreases and eventually disappears. This process is called luminescence decay. This luminescence decay process can be monitored by time-resolved luminescence spectrum. The instantaneous luminescence intensity  $I(\lambda, t)$  on a given time  $t$  and wavelength  $\lambda$  can be expressed as:

$$I(\lambda) = \int_{-\infty}^0 I(\lambda, t) dt$$

The luminescence decay is typically characterized by a rapid decrease in the initial several seconds followed by a slow decay [14]. The decay time of afterglow

**Fig. 3.9** Long afterglow decay curve of  $\text{Cr}^{3+}_{0.001}:\text{SrGa}_{0.999}\text{O}$  phosphor after excited by 300 nm light for 10 min (monitored at 750 nm)



luminescence is defined by the time after which the emission intensity decreases to a brightness value ( $<0.32 \text{ mcd/m}^2$ ) that the human eye cannot identify. As shown in Fig. 3.9, after a rapid decay, the afterglow luminescence of  $\text{Cr}^{3+}_{0.001}:\text{SrGa}_{0.999}\text{O}$  phosphor could last for more than 7200 s.

All photoluminescent materials have an afterglow characteristic. Compared with the long persistent (light-storage) phosphors, luminescence from non-storage materials has a fast decay and a short twilight. The luminous intensity is decayed exponentially after shutting down the excitation source. The emission intensity can be described by:

$$I = I_0 e^{-\alpha t} = I_0 e^{-t/\tau}$$

where  $I$  is the luminous intensity at  $t$  after stopping excitation,  $I_0$  is the luminous intensity at  $t_0$  when the excitation is stopped,  $\alpha$  is the probability for electrons jumping to the ground state,  $t$  is time, and  $\tau$  is equal to  $1/\alpha$ , which is the average luminescent lifetime or life of electrons in the excited state. By comparison, the decay process of long persistent luminescence is more complex, which can be expressed by the following equation.

$$I = At^{-n}$$

where  $n$  is decay constant. The longer the afterglow time is, the smaller the decay constant is.

Luminance meter is usually used to evaluate luminous intensity. Figure 3.10 shows the schematic illustration of a typical luminance meter. By monitoring the emission intensity over time, lifetime and afterglow duration can be obtained (Fig. 3.11).

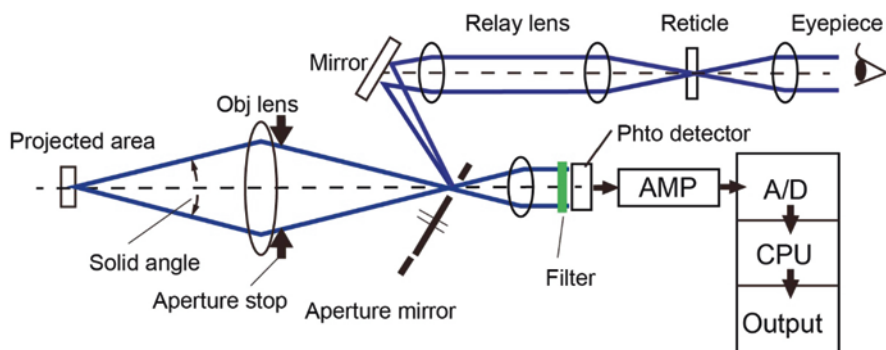


Fig. 3.10 Schematic diagram of luminance meter

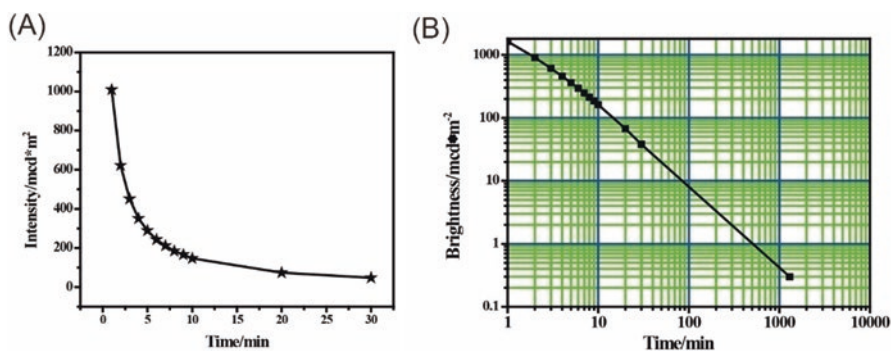


Fig. 3.11 (a) Afterglow decay curve of  $\text{SrAl}_2\text{O}_4:\text{Eu}^{2+}, \text{Dy}^{3+}$  long persistent phosphor. (b) The same data plotted as  $\log I$  vs. time

## 3.2 Structural Characteristics

### 3.2.1 Size and Morphology

Precise control of size and morphology of persistent phosphors has attracted considerable research interests in practical applications. For example, when the long persistent phosphors are used in luminescent coating, the particle size should be in the range of 1–50  $\mu\text{m}$  to ensure coating appearance uniformly. Likewise, the nanoscale size and spherical morphology of phosphors are particularly useful for cell uptake in biological applications,

Scanning electron microscopy (SEM) and transmission electron microscopy (TEM) are two kinds of most commonly used techniques for size and morphology characterization. Figure 3.12 illustrates the schematic diagram of a SEM microscope. High-resolution SEM imaging provides detailed information of the sample surface by scanning a focused electron beam on the sample and recording secondary or backscattered electron signal. In addition, the corresponding quantitative

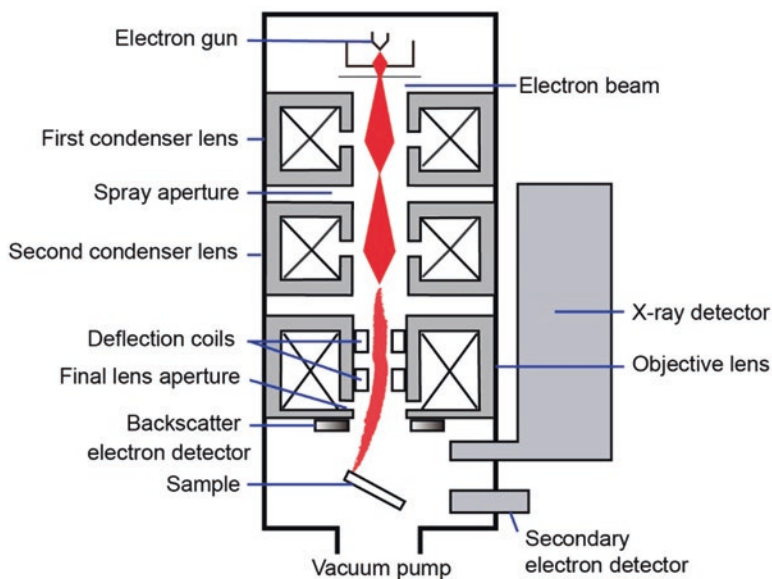


**Fig. 3.12** Schematic diagram of a scanning electron microscope (SEM)

compositional information can be obtained by an Energy Dispersive X-Ray (EDX) measurement.

Different from SEM, TEM detects electrons that transmit through the sample. Therefore, SEM provides the information of the sample surface, while TEM shows the details of the sample. The TEM image is obtained by amplified signal of the electrons transmitted through the thin specimens (tissue sections, molecules, etc.).

The long persistent phosphors obtained by current synthetic approaches (e.g., sol-gel, combustion, solvothermal, and solid-state reaction) usually have an irregular shape and broad size distribution. The particle size-cumulative quality curve of the phosphor is used to evaluate particle size distribution of phosphors. In the curve, the abscissa represents particle size and the ordinate is cumulative mass fraction. Particle Size Distribution D50, the value of the particle diameter at 50% in the cumulative distribution, is an important parameter for particle size characterization.

Particle size analyzer is a useful analytical instrument to evaluate the size distribution. The schematic of particle size analyzer is shown in Fig. 3.13. Upon interaction with laser, particles with different sizes take on different speeds. The fluctuation of particles in the certain direction is recorded using photon correlation spectroscopic theory.

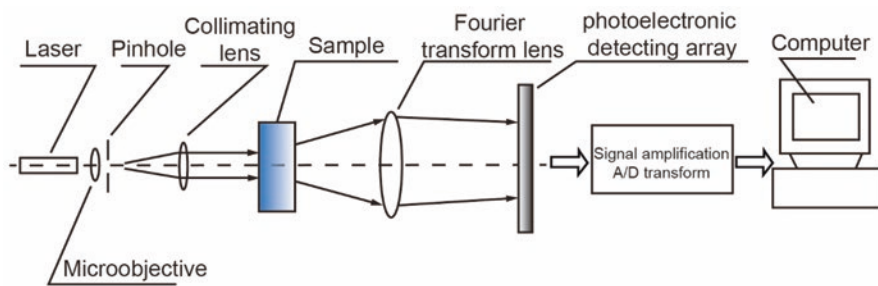


Fig. 3.13 Schematic diagram of a laser particle size analyzer

### 3.2.2 Crystal Structure

In inorganic phosphors, a trace amount of impurities (e.g., activators, crystal defects, and dislocations) in the crystal structure lead to lattice irregularities. As well, these inhomogeneities in the crystals can generate new energy levels, which strongly affect the optical properties such as prolonging luminescence decay and emission wavelength shift. Therefore, it is of importance to know the detail information of crystals structure or defect for mechanistic investigation of luminescence. X-ray powder diffraction (XRD) has proven a promising analytical technique to reveal detailed crystal information such as phase identification and unit cell dimensions.

In 1912, Max von Laue demonstrated that crystalline materials can serve as three-dimensional diffraction gratings for X-ray wavelengths, just as the spacing of planes in a crystal lattice. The nature of XRD is the constructive interference between monochromatic X-rays and a crystalline sample. In the measuring instrument, the X-rays created by a cathode ray tube are firstly filtered to generate monochromatic X-rays, calibrated to concentrate, and then directed to irradiate the sample. When the conditions satisfy Bragg's Law ( $n\lambda = 2d \sin \theta$ ), the interplay between the incident X-rays and the sample generates constructive interference (and a diffracted ray), where  $\lambda$  represents the wavelength of incident X-ray, and  $n$  is the order of diffraction. Then the diffracted X-rays are detected, processed and counted. Upon scanning the sample over a range of  $2\theta$  angles, diffractions in any possible directions of the lattice will be obtained because of the random orientation of the powdered sample. As shown in Fig. 3.14, the different diffraction from different orders laps each other, therefore, scattered X-ray will enhance or weak. Thus, different crystal structure has different and specific peaks of XRD patterns. In addition, the diffraction peaks can be converted to  $d$ -spacings, which can be used to identify the mineral by comparing the measured  $d$ -spacings with standard reference patterns.

XRD measuring instrument is made up of high voltage generator, X-ray light tube, light filter, collimator, slit detector, amplifier, and recorder (Fig. 3.15). The electrons are accelerated by the X-rays generated in a cathode ray tube, and directed to bombarding the target material. It is worth to note that the X-rays generated in a

**Fig. 3.14** Schematic diagram showing X-ray diffraction mechanism

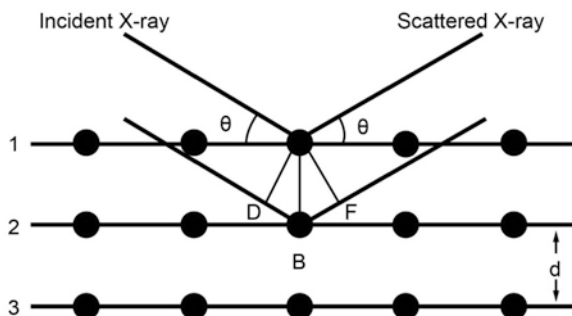
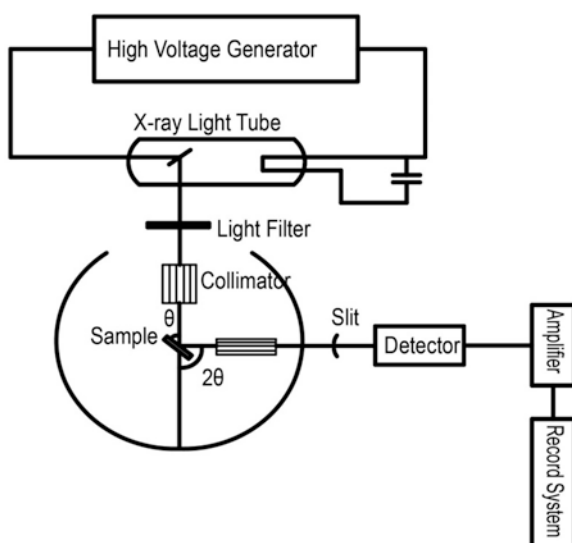


**Fig. 3.15** Schematic diagram of an X-ray diffraction instrument



cathode ray tube need to be filtered by foils or crystal monochromators to create monochromatic X-rays before they are directed to irradiate the sample. The most commonly used target material is copper for single-crystal diffraction, which has  $\text{CuK}_\alpha$  radiation of  $1.5418 \text{ \AA}$ . If the energy of electrons is high enough to make the inner shell electrons of the target jump out, characteristic X-ray signal will be generated. The X-ray signals are recorded and processed by a detector, and then converted to a count rate. Finally, the data are output to an equipment such as a printer or a computer monitor.

For example, as an important host of long afterglow phosphor,  $\text{CaMgSi}_2\text{O}_6$  pyroxene (diopside) is a major mineral of peridotites and basalts [15]. In order to detect crystal structure, X-Ray Diffraction (XRD) is an efficient method. Figure 3.16 illustrates the XRD patterns of different rare earth ions doped  $\text{CaMgSi}_2\text{O}_6$  phosphors. All of the XRD patterns can be assigned to the phase of  $\text{CaMgSi}_2\text{O}_6$  (pyroxene structure, as shown in Fig. 3.16b), which suggest that no new phases are formed



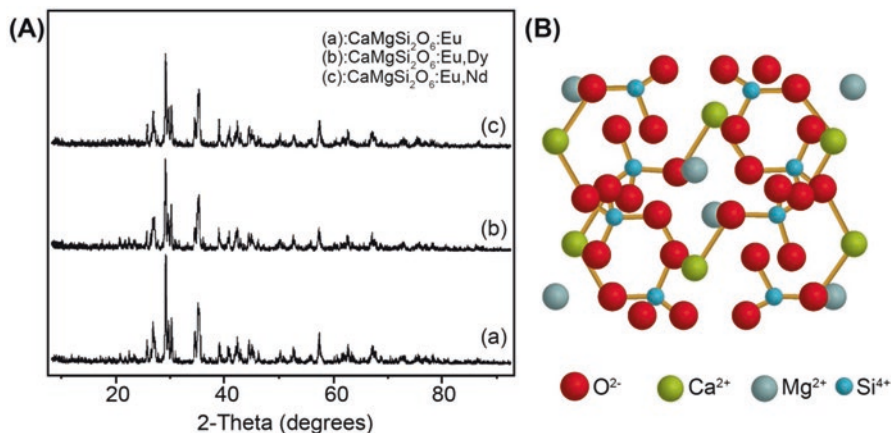


**Fig. 3.16** (a) XRD patterns of  $\text{CaMgSi}_2\text{O}_6$ -based phosphors doped with different lanthanide ions. (b) Structure map of  $\text{CaMgSi}_2\text{O}_6$  along (010) direction

by doping  $\text{Eu}^{2+}$ ,  $\text{Dy}^{3+}$  and  $\text{Nd}^{3+}$ . Although there are few small changes in lattice parameters, it shows that the doping ions could not cause the big lattice distortion.

In addition, according to Debye–Scherrer equation, the average size of crystallite particles can be estimated by the following equation.

$$D = \frac{K\gamma}{B \cos \theta}$$

where  $K$  is Scherrer constant. If  $B$  represents width at half maximum intensity of diffraction peak,  $K$  will be 0.89, while, if  $B$  is integration area of diffraction peak,  $K$  will be 1.  $D$  represents the average size of particles, which are perpendicular to one face of the lattice.  $\theta$  is the diffraction angle of the peak.  $\lambda$  is the wavelength of X-rays (0.154 nm). Because of inconsistent particle size,  $D$  might only get the average size. Then for nonspherical particles,  $D$  changes with  $\theta$ , so we can get different  $D$  values for different diffraction peaks. For that reason, the particle shape can be estimated by different  $D$  values. Furthermore, with the decrease in particle size, the diffraction rings are broadened. The method is suitable to calculate the particle size with a diameter ranging from 1.0 to 0.01  $\mu\text{m}$  in the premise that the particles have a good crystallinity.

## References

1. Kodama, N., Tanii, Y., Yamaga, M.: Optical properties of long-lasting phosphorescent crystals  $\text{Ce}^{3+}$ -doped  $\text{Ca}_2\text{Al}_2\text{SiO}_7$  and  $\text{CaYAl}_3\text{O}_7$ . *J. Lumin.* **87–89**, 1076–1078 (2000)
2. Liu, B., Shi, C., Yin, M., Dong, L., Xiao, Z.: The trap states in the  $\text{Sr}_2\text{MgSi}_2\text{O}_7$  and  $(\text{Sr},\text{Ca})\text{MgSi}_2\text{O}_7$  long afterglow phosphor activated by  $\text{Eu}^{2+}$  and  $\text{Dy}^{3+}$ . *J. Alloys Compd.* **387**, 65–69 (2005)

3. Nakazawa, E., Mochida, T.: Traps in  $\text{SrAl}_2\text{O}_4\text{:Eu}^{2+}$  phosphor with rare-earth ion doping. *J. Lumin.* **72**, 236–237 (1997)
4. Tuomas, A., Jorma, H.L., Hogne, J., Mika, L., Janne, N.: Thermoluminescence study of persistent luminescence materials:  $\text{Eu}^{2+}$ - and  $\text{R}^{3+}$ -doped calcium aluminates,  $\text{CaAl}_2\text{O}_4\text{:Eu}^{2+},\text{R}^{3+}$ . *J. Phys. Chem. B.* **110**, 4589–4598 (2006)
5. Xiaoming, T., Weidong, Z., Huaqiang, H.: Influence of  $\text{La}^{3+}$  and  $\text{Dy}^{3+}$  on the properties of the long afterglow phosphor  $\text{CaAl}_2\text{O}_4\text{:Eu}^{2+},\text{Nd}^{3+}$ . *Rare Metals.* **27**, 335–339 (2008)
6. Nakazawa, E., Murazaki, Y., Saito, S.: Mechanism of the persistent phosphorescence in  $\text{Sr}_4\text{Al}_{14}\text{O}_{25}\text{:Eu}$  and  $\text{SrAl}_2\text{O}_4\text{:Eu}$  codoped with rare earth ions. *J. Appl. Phys.* **100**, 113113–113113-7 (2006)
7. Jia, D., Jia, W., Jia, Y.: Long persistent alkali-earth silicate phosphors doped with  $\text{Eu}^{2+},\text{Nd}^{3+}$ . *J. Appl. Phys.* **101**, 023520 (2007)
8. Aitasalo, T., Hölsä, J., Kirm, M., Laamanen, T., Lastusaari, M., Niittykoski, J., Raud, J., Valtonen, R.: Persistent luminescence and synchrotron radiation study of the  $\text{Ca}_2\text{MgSi}_2\text{O}_7\text{:Eu}^{2+},\text{R}^{3+}$  materials. *Radiat. Meas.* **42**, 644–647 (2007)
9. Wang, Y., Wang, Z.: Characterization of  $\text{Y}_2\text{O}_3\text{:Eu}^{3+},\text{Mg}^{2+},\text{Ti}^{4+}$  long-lasting phosphor synthesized by flux method. *J. Rare Earths.* **24**, 25–28 (2006)
10. Wang, J., Su, Q., Wang, S.: Blue and red long lasting phosphorescence (LLP) in  $\beta\text{-Zn}_3(\text{PO}_4)_2\text{:Mn}^{2+},\text{Zr}^{4+}$ . *J. Phys. Chem. Solids.* **66**, 1171–1176 (2005)
11. Kuang, J., Liu, Y., Zhang, J., Huang, L., Rong, J., Yuan, D.: Blue-emitting long-lasting phosphor,  $\text{Sr}_3\text{Al}_{10}\text{SiO}_{20}\text{:Eu}^{2+},\text{Ho}^{3+}$ . *Solid State Commun.* **136**, 6–10 (2005)
12. Bos, A.J.J., van Duijvenvoorde, R.M., van der Kolk, E., Drozdowski, W., Dorenbos, P.: Thermoluminescence excitation spectroscopy: a versatile technique to study persistent luminescence phosphors. *J. Lumin.* **131**, 1465–1471 (2011)
13. Rodrigues, L., Stefani, R., Brito, H., Felinto, M., Hölsä, J., Lastusaari, M., Laamanen, T., Malkamäki, M.: Thermoluminescence and synchrotron radiation studies on the persistent luminescence of  $\text{BaAl}_2\text{O}_4\text{:Eu}^{2+},\text{Dy}^{3+}$ . *J. Solid State Chem.* **183**, 2365–2371 (2010)
14. Xu, J., Chen, D., Yu, Y., Zhu, W., Zhou, J., Wang, Y.:  $\text{Cr}^{3+}\text{:SrGa}_2\text{O}_9$ : a broadband near-infrared long-persistent phosphor. *Chem. Asian J.* **9**, 1020–1025 (2014)
15. Jiang, L., Chang, C., Mao, D., Feng, C.: Luminescent properties of  $\text{CaMgSi}_2\text{O}_6$ -based phosphors co-doped with different rare earth ions. *J. Alloys Compd.* **377**, 211–215 (2004)

## Chapter 4

# Applications of Inorganic Afterglow Phosphors

Long persistent phosphor is considered as one kind of miraculous materials with unique luminescent properties that trigger attractive attention. Many natural ores with long afterglow are used to produce various artworks, such as “legendary luminous pearl” (Fig. 4.1a), “luminous wine cup” (Fig. 4.1b), and “phosphorescent bird” (Fig. 4.1c). Common use of long afterglow materials includes glow-in-the-dark toys, paint, and clock dials. The applications of persistent luminescent materials as luminous paint could be dated back to twentieth century, which was based on the development of sulfide materials, i.e.,  $\text{ZnS}:\text{Cu}^{2+}$  [1]. The modern persistent luminescent materials appeared in the commercial market since alkaline earth aluminate phosphor ( $\text{SrAl}_2\text{O}_4:\text{Eu}^{2+},\text{Dy}^{3+}$ ) was reported in 1995 [2].

Three commercially available persistent phosphors, namely  $\text{Sr}_2\text{MgSi}_2\text{O}_7:\text{Eu}^{2+},\text{Dy}^{3+}$  (blue),  $\text{SrAl}_2\text{O}_4:\text{Eu}^{2+},\text{Dy}^{3+}$  (green), and  $\text{Y}_2\text{O}_3:\text{Eu}^{3+},\text{Mg}^{2+},\text{Ti}^{4+}$  (red), are widely used for practical applications [3]. The emission spectra of these phosphors are shown in Fig. 4.2a. It provides a strategy to white-emitting persistent light that could be obtained by combining these three primary colors emitting phosphors. Figure 4.2b shows photograph images containing these three phosphors in daylight, under UV irradiation, and in dark after UV excitation.

Persistent luminescence phosphors can be dispersed in various medium and then be used for manufacturing specific products, for example, luminous paint, luminous ink, luminous plastic, luminous fiber, luminous pottery, porcelain, and so on. Among them, luminous paints are presently the main commercial application of persistent luminescent phosphors. The products containing long persistent phosphors can be applied in the field of architecture decoration, safety signs, and lighting source. Additionally, the use of persistent luminescence nanomaterials as highly sensitive luminescent probes for real-time bioimaging attracts much attention since 2007 [4]. In this chapter, we will briefly introduce industrial applications of persistent luminescence in safety signs, luminous fiber, artwork, as well as the rising use as bio-probe in bioimaging and molecular sensing.



**Fig. 4.1** Artworks made from natural ores with long afterglow. (a) Legendary luminous pearl (<http://baike.sogou.com/v266358.htm?jsessionid=DB584C3535A1E5B018AA5233116742D6>). (b) Luminous wine cup ([http://www.gs.xinhuanet.com/history/2009-08/26/content\\_17505774.htm](http://www.gs.xinhuanet.com/history/2009-08/26/content_17505774.htm)). (c) Phosphorescent bird (<https://en.wikipedia.org/wiki/Phosphorescence>)

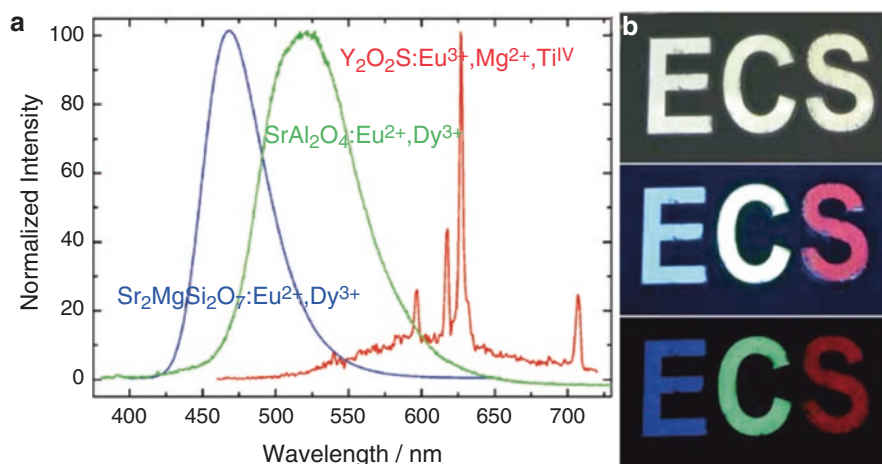


**Fig. 4.2** (a) The luminescence spectra of the blue-emitting  $\text{Sr}_2\text{MgSi}_2\text{O}_7:\text{Eu}^{2+},\text{Dy}^{3+}$ , green-emitting  $\text{SrAl}_2\text{O}_4:\text{Eu}^{2+},\text{Dy}^{3+}$ , and red-emitting  $\text{Y}_2\text{O}_2\text{S}:\text{Eu}^{3+},\text{Mg}^{2+},\text{Ti}^{4+}$  phosphors after UV excitation. (b) The persistent luminescence behavior of the blue-emitting  $\text{Sr}_2\text{MgSi}_2\text{O}_7:\text{Eu}^{2+},\text{Dy}^{3+}$ . (E) Green-emitting  $\text{SrAl}_2\text{O}_4:\text{Eu}^{2+},\text{Dy}^{3+}$ . (C) Red-emitting  $\text{Y}_2\text{O}_2\text{S}:\text{Eu}^{3+},\text{Mg}^{2+},\text{Ti}^{4+}$  (S) phosphors in daylight, under UV excitation, and in dark [3]

## 4.1 Display and Lighting

Persistent luminescent materials are capable of absorbing radiation energy from light sources and making an afterglow. These radiation sources include UV lamp, fluorescent lamp, halogen lamp and incandescent lamp, as well as the direct sunlight. In general, the phosphor releases its stored energy gradually and shows a long afterglow. Commercially persistent luminescence phosphors such as strontium aluminate ( $\text{SrAl}_2\text{O}_4:\text{Eu}^{2+},\text{Dy}^{3+}$ ) and strontium silicate ( $\text{Sr}_2\text{MgSi}_2\text{O}_7:\text{Eu}^{2+},\text{Dy}^{3+}$ ) are

widely used for emergency “way-finding” applications. These products generally maintain long service life because of the advantages of rechargeable excitation and stable emission. At present,  $\text{SrAl}_2\text{O}_4:\text{Eu}^{2+}, \text{Dy}^{3+}$  phosphors with the size of 10–65  $\mu\text{m}$  is the most widely applied phosphor. It shows yellow-green emission centered at 520 nm under the UV light excitation (200–450 nm). The initial luminance value more than 2000 mcd/m<sup>2</sup> and the afterglow can last more than 12 h.

### 4.1.1 Fire Safety Signs

Persistent phosphor is popularly used as safety and exit marking with a most common form of “FIRE EXIT” signage (Fig. 4.3). At present, the fire safety signs have been applied in many areas, such as construction, airport, and metro.

Performance criteria were stipulated by international standards and guidelines for the industry. In the 1980s, The International Organization for Standardization also released a number of safety standards for safety signs, providing accurate graphic symbols to express the security information. Most countries have passed the corresponding legislation to regulate the use of these environmentally friendly products. In 1987, Japan developed the Z JIS 9100 Standard, which provides the performance requirements for the luminous evacuation signs. In 1994, Germany also promulgated the National Standard 67510-3 DIN, which has been adopted by European countries. Luminous evacuation signs are more and more popular in public and civil construction, even though the electrically driven evacuation signs are still necessary in many cases. In general, the luminous evacuation signs should have the following common characteristics:

- (A) Good performance of light absorption, energy storage, and automatically continuous emission in the dark. In detail, after absorption of daylight, lamplight, or other visible light for ca. 20 min, the stored energy can support automatically and continuously emission more than 12 h in the dark.

**Fig. 4.3** Photographs of a “Fire exit” signage taken in the day (*top*) and in the dark (*down*) (<http://teleganpressedproducts.com/telglow-photoluminescent-2/>)



- (B) The system is electric power free, nontoxic, nonradioactive, chemically stable, energy-saving, and environmentally friendly.
- (C) The manufacturing cost is low and daily maintenance is not necessary. The luminous evacuation signs can absorb and emit light repeatedly and have long service life.
- (D) Products can be customized on demands and be easily installed at different sites, such as wall, ground, and stairs.
- (E) Good resistant properties to aging, corrosion, heat, wear, and scratch.

### 4.1.2 Road Traffic Signs

Persistent phosphor is widely used in road traffic signs, for instance, directional signs, warning signs, as well as tourist signs. These signs can store the energy of sunlight during the day and are utilized as emitting sources at night. It is a kind of intelligent energy-saving light-emitting materials without electrical driven or manual operation. Road traffic sign generally consists of a graphic symbol and/or character, delivering legal information and warning to drivers and pedestrians. It is useful to control and direct the traffic, which plays an important role in the modern highway transportation management. There is a luminous road in Netherlands, which was built of luminous paint (Fig. 4.4). The persistent phosphors in paint absorb the sunshine during the day and act as lighting sources at night. By setting up road traffic signs, traffic capacity could be improved and traffic accidents could be reduced.

### 4.1.3 Luminous Watch

It is hard to read the time of a watch in the dark and the aid of other light source is often required. Hence, the luminous material was fabricated on the pointers and dial (Fig. 4.5). Zinc sulfide is the first persistent material employed in the luminous

**Fig. 4.4** Luminous road  
(<https://www.asme.org/engineering-topics/articles/energy/glowing-the-roads>)

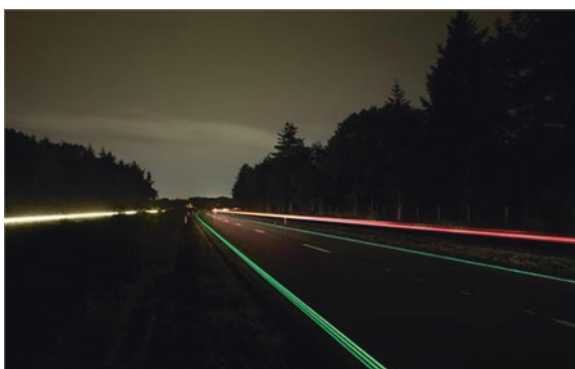


**Fig. 4.5** Luminous watch  
([http://www.bladehq.com/  
item--Lum-Tec-B17-  
Combat-Super-  
Precision--17777](http://www.bladehq.com/item--Lum-Tec-B17-Combat-Super-Precision--17777))



watch. However, this kind of materials could only continue to produce afterglow for a short period of time. To improve the endurance of afterglow, radioactive elements are adopted. Radium was the first element to be used, subsequently replaced by a less harmful but still radioactive element, tritium. However, radioactive elements can undermine luminescent materials. Consequently, the afterglow is only enhanced at an initial time and finally weakened. More importantly, radioactive elements do harm to human body. Therefore, the radioactive tritium strategy was also discarded in the early 1990s. An attractive approach was developed by a Japanese company named Nemoto, in which a nonradioactive substitute, rare earth doped alkaline earth aluminate, was firstly used. This new long persistent phosphor is essentially different from the traditional zinc sulfide and possesses more stable chemical properties, higher brightness, and longer afterglow.

#### **4.1.4 Luminous Fibers**

Luminous fiber, also known as noctilucent fibers, is a new environmental friendly luminescent material. By using spinning raw materials as a substrate, the fiber is made of rare earth doped luminescent materials with long afterglow (commonly aluminate and silicate). Noctilucent fibers can continuously shine more than 10 h in the dark after absorbing visible light for 10 min. In the light, luminous fibers containing different kinds of persistent materials present a variety of colors, for instance, red, yellow, green, and blue (Fig. 4.6). These luminous fibers are widely used in clothing textiles, trademark, pattern, etc. In comparison with traditional textiles, products made of noctilucent fibers do not need dyeing and are environmentally friendly.



**Fig. 4.6** Luminous fiber  
(<http://www.hzkzy.com/>)



## 4.2 Biological Applications

### 4.2.1 *In Vivo* Imaging

As typical bioprobes, organic dyes, quantum dots, and up-conversion nanocrystals have been widely used for bioimaging [5–12]. Nevertheless, a further application is hampered by their intrinsic disadvantages. For instance, fluorescent dyes suffer from photobleaching and photostability. The biosafety issues of quantum dots need to be addressed for *in vivo* study. Up-conversion nanocrystals often require high excitation power density to obtain bright emission to penetrate biotissues, resulting from their inherently extremely low up-converting efficiency [13–18]. Recently, persistent luminescence nanoparticles (PLNPs) have received considerable attention in biological application because of their distinctive optical features [19–22]. Firstly, PLNPs endow optical irradiation before injection and their *in vivo* behaviors can be directly detected without any additional excitation sources [4, 21]. Secondly, the absence of *in situ* excitation can efficiently reduce photodamage effect by laser irradiation and lower autofluorescence from biotissues, leading to an ultrahigh signal-to-noise ratio [20, 23]. Therefore, PLNPs with near-infrared (NIR) emissions are particularly suitable for deep tissue imaging as a result of low optical absorption of water and hemoglobin in this region [24].

Scherman and coworkers demonstrated *in vivo* small animal imaging by PLNPs ( $\text{Ca}_{0.2}\text{Zn}_{0.9}\text{Mg}_{0.9}\text{Si}_2\text{O}_6:\text{Eu}^{2+},\text{Dy}^{3+},\text{Mn}^{2+}$ ) [4]. The fabricating procedures of the PLNPs included synthesis of precursor by a sol-gel method, annealing at a high temperature, and wet grinding. Slightly aggregated PLNPs (50–100 nm) with relatively narrow size distribution were obtained after elimination of large particles by selective



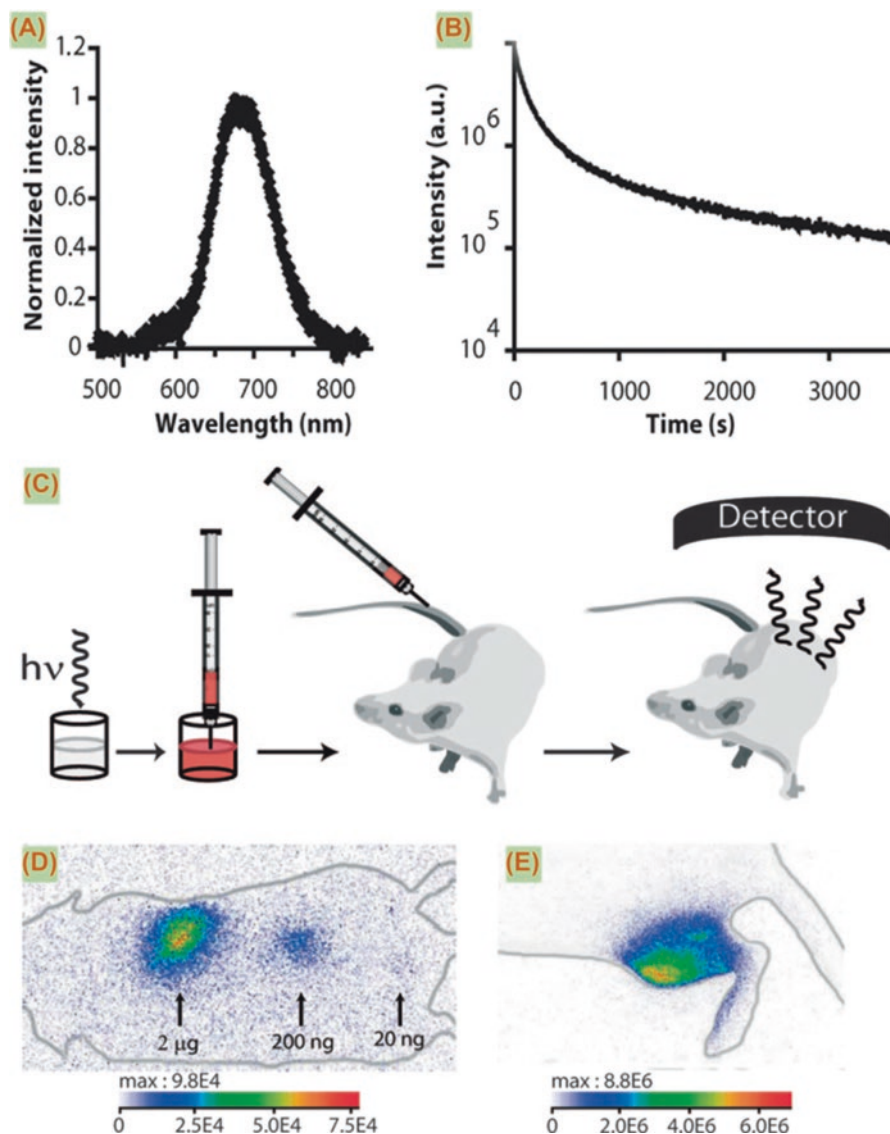


**Fig. 4.7** In vivo small animal imaging by PLNPs. (a) Afterglow emission spectrum. (b) Time dependence of luminescence intensity. (c) Principle of in vivo imaging. A solution containing PLNPs is illuminated by UV lamp and is directly injected into mice for signal acquisition. (d) In vivo image after subcutaneous injection of different amounts of PLNPs (2  $\mu$ g, 200 ng, 20 ng) at different sites. (e) An image after intramuscular injection of PLNPs. Reproduced with permission from [4]. Copyright 2007 National Academy of Science, USA

sedimentation and centrifugation. The as-synthesized PLNPs present red afterglow emission with a long lifetime (Fig. 4.7a, b). Image acquisition after subcutaneous and intratumoral administration (Fig. 4.7d, e) shows the feasibility of PLNPs for in vivo studies based on whole-body blood circulation. PLNPs with different

surface coating were then used for real-time tracking and in vivo biodistribution studies (Fig. 4.7c). The results indicate that in vivo behaviors for these three types of nanoparticles with different surface charges were different. Amino-modified NPs (positive charged) are likely to be trapped in the lungs, while carboxyl-modified NPs (negative charged) and PEGylated NPs (neutral) were preferred to distribute in the liver. More interestingly, PEG-coated NPs could avoid fast clearance from blood and increase circulating time because of the PEG shielding effect [4]. A systematical investigation on biodistribution of PLNPs in mice was followed by considering the effect of surface coating, core diameter, and PEG chain length [25]. In vivo biodistribution of PLNPs was found to be highly dependent on core diameter and surface modification.

However, the long-lasting afterglow of PLNPs is low in intensity and is not suitable for long-term tracking in vivo, which needs to be conquered in practical bioapplication. Furthermore, high calcination temperature exceeding 1000 °C is usually required for intensity improvement of afterglow emission [26–28]. To this end, inevitable agglomeration and big particles with the size of sub- to super-micron and with irregular morphologies are usually obtained, instead of monodispersed PLNPs with a narrow size distribution, which seriously hinders their widespread use in in vivo bioimaging [19, 29]. Therefore, many efforts are made on the synthesis of PLNPs with high morphological uniformity and bright/long afterglow [4, 21, 23, 25]. Various PLNPs by different synthesis methods such as  $\text{Sr}_2\text{MgSi}_2\text{O}_7\text{:Eu}^{2+}, \text{Dy}^{3+}$  [30],  $\text{Ca}_{1.86}\text{Mg}_{0.14}\text{ZnSi}_2\text{O}_7\text{:Eu}^{2+}, \text{Dy}^{3+}$  [31] and  $\text{Zn}_{2.94}\text{Ga}_{1.96}\text{Ge}_2\text{O}_{10}\text{:Cr}^{3+}, \text{Pr}^{3+}$  [23] by sol-gel method,  $\text{SrMgSi}_2\text{O}_6\text{:0.01Eu}^{2+}, 0.02\text{Dy}^{3+}$  [32] and  $\text{ZnGa}_2\text{O}_4\text{:Cr}^{3+}$  by templating method [33], and  $\text{ZnGa}_2\text{O}_4\text{:Cr}^{3+}$  by hydrothermal method [21, 34, 35] were prepared for bioimaging investigation.

The NIR-emitting PLNPs ( $\text{Zn}_{2.94}\text{Ga}_{1.96}\text{Ge}_2\text{O}_{10}\text{:Cr}^{3+}, \text{Pr}^{3+}$ ) reported by Yan and coworkers were demonstrated for in vivo targeted tumor imaging [23]. The PLNP powder exhibits an intense NIR emission with a long afterglow time of over 15 days. The luminescence of the colloidal solution at the PLNPs concentration of  $1 \text{ mg mL}^{-1}$  remains detectable till 24 h after ceasing UV excitation. PEGylation on PLNPs (PEG-PLNPs) was carried out for a better biocompatibility and longer circulation time of nanoparticles. Further c(RGDyK) peptide bioconjugation on PLNPs (RGD-PLNPs) was on the purpose of tumor-specific targeting of PLNPs. In vivo imaging results show that both PEG-PLNPs and RGD-PLNPs were rapidly circulated all over mice body within 9 min (Fig. 4.8a, b). Luminescence signals from RGD-PLNPs were detectable at the tumor site (Fig. 4.8b), in contrast to the images of normal mice (Fig. 4.8c, d). The accumulation of PLNPs in the tumor site can also be supported by corresponding ex vivo luminescence image and semi-quantification analysis of a tumor (Fig. 4.8e, f). This PLNP was then combined with gadolinium complexes as a multifunctional nanoprobe for in vivo NIR luminescence and magnetic resonance imaging (MRI) by the same group [36]. PLNPs with Gd-functionalization not only provide excellent NIR persistent luminescence in optical imaging but also give a high contrast effect in MRI.

A new generation of PLNPs ( $\text{ZnGa}_2\text{O}_4\text{:Cr}^{3+}$ , labeled as n-ZGO) was exploited by Maldiney et al., whose persistent luminescence can be re-charged in vivo by an

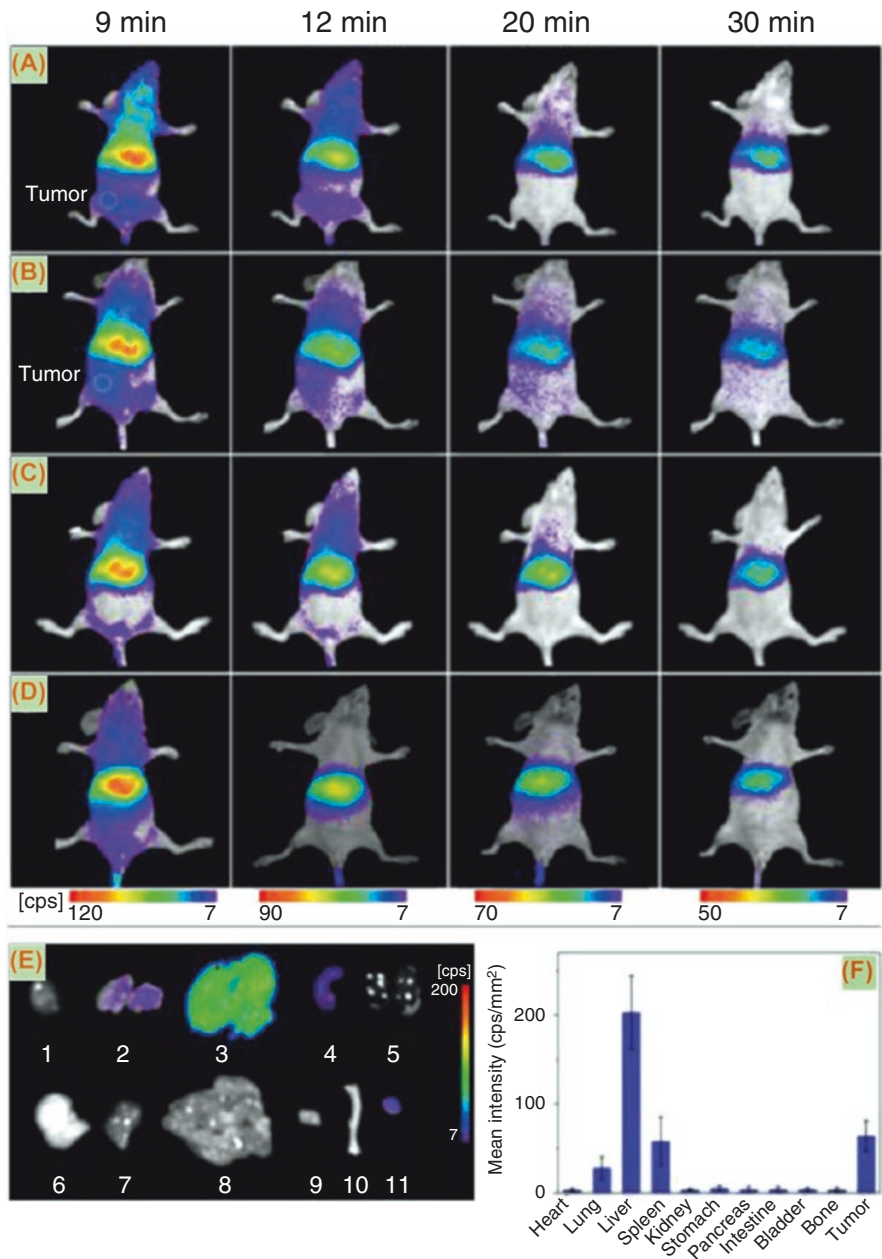


**Fig. 4.8** In vivo images of PEG-PLNPs (a, c) and RGD-PLNPs (b, d) in U87MG tumor-bearing mice (a, b) and normal mice (c, d). Images are captured after intravenous injection of nanoparticles with the dose of 0.4 mg and with 10 min UV excitation in advance. Tumor sites are marked with white circles in a and b. Ex vivo images (e) and semi-quantification of emission intensity (f) of isolated organs and tumor during 6 h after intravenous injection of RGD-PLNPs. The signs 1–11 in e represent heart, lung, liver, spleen, kidney, stomach, pancreas, intestine, bladder, bone, and tumor, respectively [23]

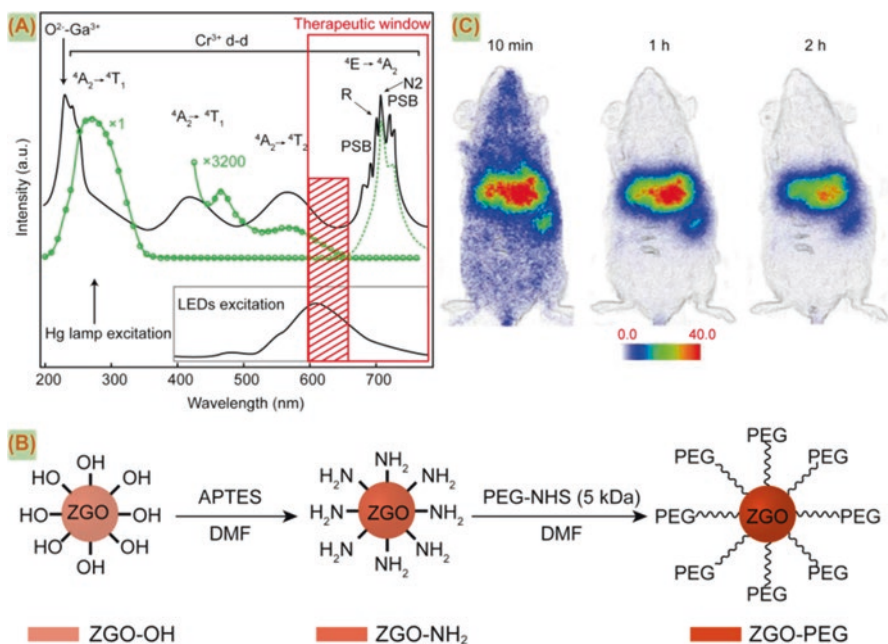


**Fig. 4.9** In vivo activation of PLNPs for optical imaging. (a) Persistent luminescence excitation (black solid line) and emission (black dotted line) spectra, compared with TSL excitation (green open points) and emission (green dotted lines) spectra of Cr<sup>3+</sup>-doped n-ZGO. (b) A schematic representation of surface functionalization for ZGO-OH nanoparticles. (c) Images of persistent luminescence by real-time monitoring. The acquisition was performed during 10 min, 1 h, and 2 h after subcutaneous injection of ZGO-OH nanoparticles in healthy mouse. Reproduced with permission from [21]

orange/red light-emitting diodes [21]. The NIR persistent luminescence under orange/red light activation could be explained by a thermally stimulated luminescence (TSL) excitation spectrum (Fig. 4.9a). The TSL excitation curve is composed of an intense broadband located at 260 nm resulting from the host bandgap transition and *d-d* transitions of Cr<sup>3+</sup>. Other excitation bands centered at 465 and 570 nm attribute to <sup>4</sup>A<sub>2</sub> (<sup>4</sup>F) → <sup>4</sup>T<sub>1</sub> (<sup>4</sup>F) and <sup>4</sup>A<sub>2</sub> (<sup>4</sup>F) → <sup>4</sup>T<sub>2</sub> (<sup>4</sup>F) transitions of Cr<sup>3+</sup>, respectively. These bands red-shift slightly when compared with those of the photoluminescence excitation spectrum. These results show that the PLNPs can be excited not only by cross-bandgap irradiation but also by lower energy photons (with orange/red light). In addition, the PLNPs show an intense afterglow centered on 695 nm and remain strong intensity after several red-LED re-excitation cycles. For in vivo imaging application, the ZGO-OH nanoparticles were surface functionalized by PEG (Fig. 4.9b), which can prolong the circulating time of nanoparticles in living model. After intravenous injection of ZGO-OH nanoparticles, the persistent luminescence signal is still detectable 2 h after the end of UV excitation (Fig. 4.9c). An identical persistent luminescence can be obtained by the reactivation with an orange/red LED source after complete extinction of emission. The red-excitable persistent

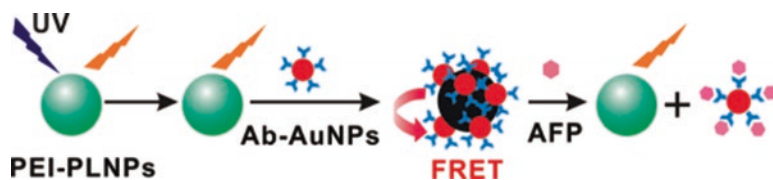
luminescence makes this PLNP a promising candidate for long-term tracking in vivo optical imaging.

### 4.2.2 Molecular Sensing

PLNPs can be ideal probes for molecular sensing by taking advantages of low background autofluorescence and high detection sensitivity over conventional fluorescent probes. In this section, we briefly introduce the persistent luminescence nanomaterials as efficient optical probes for detection of biomolecules and tumor biomarkers in vitro.

#### 4.2.2.1 Homogeneous FRET Assay

A pioneer work of homogeneous fluorescence resonance energy transfer (FRET) assay based on PLNPs was demonstrated by Yan's group [31], where biocompatible polyethyleneimine functionalized  $\text{Ca}_{1.86}\text{Mg}_{0.14}\text{ZnSi}_2\text{O}_7\text{:Eu}^{2+}, \text{Dy}^{3+}$  PLNPs (labeled as PEI-PLNPs) were proposed as FRET probes for detection of R-fetoprotein (AFP). In this case, a FRET-based inhibition assay was designed by combination with PEI-PLNPs and AFP-antibody-gold nanoparticle conjugates (Ab-AuNPs). The FRET efficiency can be modulated by AFP via inhibition of the electrostatic interactions between Ab-AuNPs and PEI-PLNPs (Scheme 4.1). The FRET efficiency is fulfilled by spectral overlap between the emission band of PEI-PLNPs and the absorption band of Ab-AuNPs (Fig. 4.10a). The luminescence quenching of PEI-PLNPs occurs due to the formation of PEI-PLNPs/Ab-AuNPs conjugates with FRET inhibition characteristic (Fig. 4.10b), which is due to the electrostatic interaction between PEI-PLNPs and AuNPs. The recovery of the persistent luminescence of PEI-PLNPs can be obtained by the presence of AFP. AFP is a destructor for the conjugation structure of Ab-AuNPs and PEI-PLNPs, due to the strong and specific affinity of AFP to the antibody, leading to desorption of Ab-AuNPs from PEI-PLNPs (Scheme 4.1 and Fig. 4.10c). A good linear relationship occurs when the enhanced luminescence intensity ( $\Delta P$ ) of the PLNPs is against the AFP concentration (Fig. 4.10d). Owing to the specific affinity of Ab-AuNPs to AFP, the inhibition probe exhibits high selectivity to AFP (Fig. 4.10e), indicating that this probe is suitable for in vitro detection



**Scheme 4.1** Schematic diagram of the FRET inhibition assay for AFP on the basis of luminescence quenching effect of PEI-PLNPs by Ab-AuNPs [31]



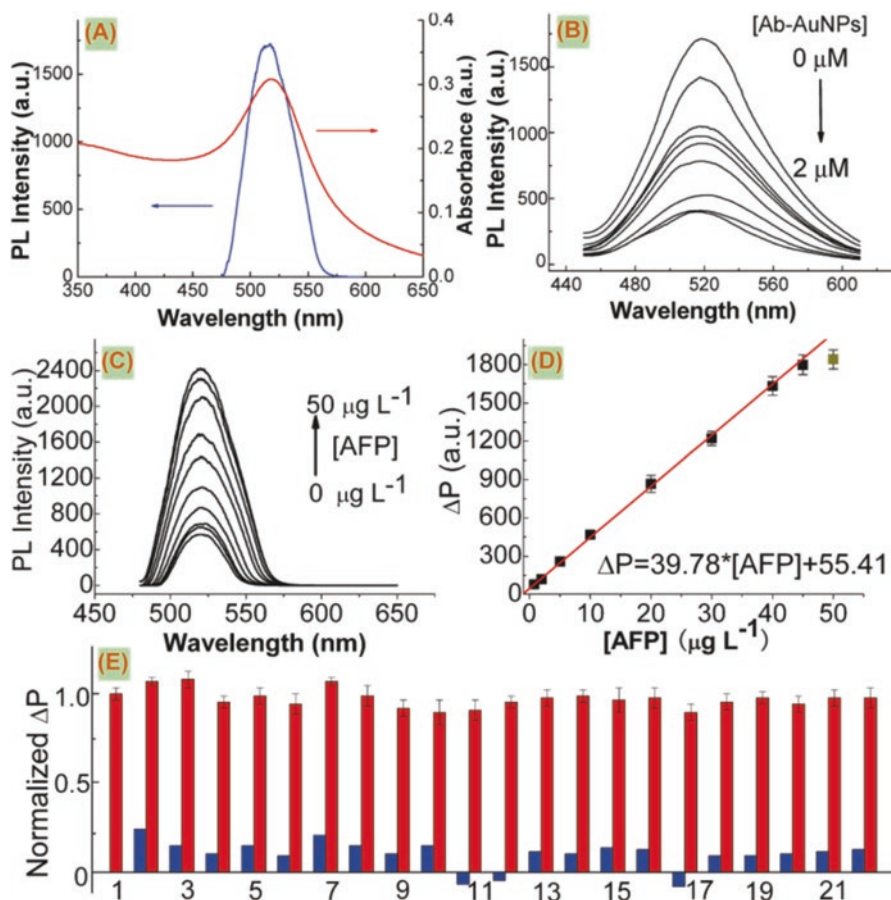
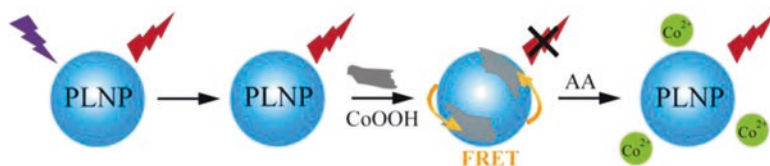


**Fig. 4.10** (a) Emission spectrum (blue curve) of PEI-PLNPs and absorption spectrum (red curve) of Ab-AuNPs. (b) Persistent luminescence quenching effect of PEI-PLNPs by Ab-AuNPs. (c) Emission recovery of PEI-PLNPs/Ab-AuNPs by the addition of AFP. (d) The linear relationship between enhanced emission intensity ( $\Delta P$ ) and AFP concentration. (e) Emission responses of diverse analytes to PEI-PLNPs/Ab-AuNPs in PBS buffer (pH 7.4) [31]

of AFP in human serum samples. The background autofluorescence and scattering light are effectively eliminated for the long-lasting luminescence nature of PLNPs, facilitating the detection sensitivity and accuracy without external excitation. Subsequently, this FRET assay method was extended to detect prostate-specific antigen (PSA), a kind of most sensitive biomarker of prostate cancer [37].



**Scheme 4.2** Schematic diagram of AA detection using CoOOH-modified PLNPs

#### 4.2.2.2 Homogeneous Reaction Assay

Tang and coworkers [38] developed a bioprobe based on the chemical reaction between cobalt oxyhydroxide (CoOOH) and  $\text{Sr}_2\text{MgSi}_2\text{O}_7:0.01\text{Eu}^{2+},0.02\text{Dy}^{3+}$  PLNPs for detection of ascorbic acid (AA) from cell extracts. When CoOOH nanoflakes were modified on the surface of the PLNPs, the persistent luminescence of the PLNPs was efficiently quenched by CoOOH through FRET. In the presence of AA, the luminescence of PLNPs was restored as a result of the reduction of CoOOH to  $\text{Co}^{2+}$  (Scheme 4.2). AA was oxidized to dehydroascorbic acid during the redox reaction. The nanoprobe exhibited high selectivity and quick response to the presence of AA with the detection range of 2.5–100  $\mu\text{M}$  in the cell extracts and with limit of detection of 2.20  $\mu\text{M}$ . This nanoprobe was also further developed to apply in *in vivo* detection and imaging of AA in living cells and mouse model.

#### 4.2.3 Lateral Flow Assay

Lateral flow assay (LFA) is one of the most promising assay formats for point-of-care diagnostics, which is widely known in pregnancy tests [39]. Photoluminescent labels, such as conventional gold nanoparticles, fluorescent nanoparticles and quantum dots, have been used in LFAs [40]. Andrew S. Paterson and coworkers developed a LFA reporter based on commercial  $\text{SrAl}_2\text{O}_4:\text{Eu}^{2+},\text{Dy}^{3+}$  PLNPs with surface modification [41]. These functionalizations enable proteins covalently attaching upon the PLNPs. NeutrAvidin PLNPs were demonstrated as reporters in LFAs with biotinylated hen egg lysozyme (bHEL) as a model analyte and with monoclonal anti-lysozyme HyHEL-5 antibodies at the test line. In this case, bovine serum albumin was biotinylated and adsorbed on the nitrocellulose to serve as a control line. The binding of a NeutrAvidin phosphor to bHEL captured by antibodies at the test line is depicted in Fig. 4.11a. The comparison between LFAs run with NeutrAvidin PLNPs and streptavidin gold nanoparticles as reporters shows that the detection limit for LFAs run with PLNPs is more sensitive than the streptavidin gold nanoparticles (Fig. 4.11b). This developed FLA with PLNPs as reporters shows a promising application in sensitive point-of-care tests.

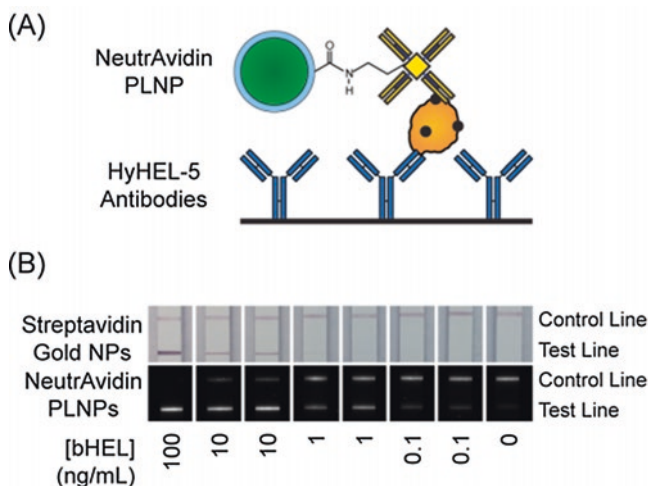


**Fig. 4.11** (a) Schematic of test line showing NeutrAvidin phosphor bound to bHEL captured by anti-HEL antibodies. (b) LFA strips showing bHEL serial dilutions with duplicates and detection with streptavidin gold nanoparticles (*top*) and NeutrAvidin PLNPs (*bottom*)

## References

- Hölsä, J., Laamanen, T., Lastusaari, M., Malkamäki, M., Novák, P.: Persistent luminescence- Quo vadis. *J. Lumin.* **129**, 1606–1609 (2009)
- Matsuzawa, T., Aoki, N., Takeuchi, N., Murayama, Y.: New long phosphorescent phosphor with high brightness,  $\text{SrAl}_2\text{O}_4:\text{Eu}^{2+}, \text{Dy}^{3+}$ . *J. Electrochem. Soc.* **143**, 2670–2673 (1996)
- Hölsä, J., Hölsä, J.: Persistent luminescence beats the afterglow-400 hundred years of persistent luminescence. *Electrochem. Soc. Interface.* **18**, 42–45 (2009)
- de Chermont, Q.L.M., Chanéac, C., Seguin, J., Pellé, F., Maîtrejean, S., Jolivet, J.P., Gourier, D., Bessodes, M., Scherman, D.: Nanoprobes with near-infrared persistent luminescence for in vivo imaging. *Proc. Natl. Acad. Sci. U. S. A.* **104**, 9266–9271 (2007)
- Chan, J., Dodani, S.C., Chang, C.J.: Reaction-based small-molecule fluorescent probes for chemoselective bioimaging. *Nat. Chem.* **4**, 973–984 (2012)
- Guo, Z., Park, S., Yoon, J., Shin, I.: Recent progress in the development of near-infrared fluorescent probes for bioimaging applications. *Chem. Soc. Rev.* **43**, 16–29 (2014)
- Wu, P., Yan, X.P.: Doped Quantum dots for chemo/biosensing and bioimaging. *Chem. Soc. Rev.* **42**, 5489–5521 (2013)
- Li, J., Zhu, J.J.: Quantum dots for fluorescent biosensing and bio-imaging applications. *Analyst.* **138**, 2506–2515 (2013)
- Deng, D., Chen, Y., Cao, J., Tian, J., Qiang, Z., Achilefu, S., Gu, Y.: High-quality  $\text{CuInS}_2/\text{ZnS}$  quantum dots for in vitro and in vivo bioimaging. *Chem. Mater.* **24**, 3029–3037 (2012)
- Wang, F., Banerjee, D., Liu, Y., Chen, X., Liu, X.: Upconversion nanoparticles in biological labeling, imaging, and therapy. *Analyst.* **135**, 1839–1854 (2010)
- Shen, J., Zhao, L., Han, G.: Lanthanide-doped upconverting luminescent nanoparticle platforms for optical imaging-guided drug delivery and therapy. *Adv. Drug Deliv. Rev.* **65**, 744–755 (2013)
- Ang, L.Y., Lim, M.E., Ong, L.C., Zhang, Y.: Applications of upconversion nanoparticles in imaging, detection and therapy. *Nanomedicine.* **6**, 1273–1288 (2011)



13. Liu, Q., Yang, T., Feng, W., Li, F.: Blue-emissive upconversion nanoparticles for low-power-excited bioimaging in vivo. *J. Am. Chem. Soc.* **134**, 5390–5397 (2012)
14. Arunkumar, E., Fu, N., Smith, B.D.: Squaraine-derived rotaxanes: highly stable, fluorescent near-ir dyes. *Chem. Eur. J.* **12**, 4684–4690 (2006)
15. Yoon, H.K., Ray, A., Lee, Y.E.K., Kim, G., Wang, X., Kopelman, R.: Polymer–protein hydrogel nanomatrix for stabilization of indocyanine green towards targeted fluorescence and photoacoustic bio-imaging. *J. Mater. Chem. B*, **1**, 5611–5619 (2013)
16. Nirmal, M., Dabbousi, B.O., Bawendi, M.G., Macklin, J.J., Trautman, J.K., Harris, T.D., Brus, L.E.: Fluorescence intermittency in single cadmium selenide nanocrystals. *Nature*, **383**, 802–804 (1996)
17. Derfus, A.M., Chan, W.C., Bhatia, S.N.: Probing the cytotoxicity of semiconductor quantum dots. *Nano Lett.* **4**, 11–18 (2004)
18. Boyer, J.-C., van Veggel, F.C.J.M.: Absolute quantum yield measurements of colloidal  $\text{NaYF}_4:\text{Er}^{3+}, \text{Yb}^{3+}$  upconverting nanoparticles. *Nanoscale*, **2**, 1417–1419 (2010)
19. Pan, Z., Lu, Y.Y., Liu, F.: Sunlight-activated long-persistent luminescence in the near-infrared from  $\text{Cr}^{3+}$ -doped zinc gallogermanates. *Nat. Mater.* **11**, 58–63 (2012)
20. Maldiney, T., Kaikkonen, M.U., Seguin, J., le Masne de Chermont, Q., Bessodes, M., Airenne, K.J., Ylä-Herttua, S., Scherman, D., Richard, C.: In vitro targeting of avidin-expressing glioma cells with biotinylated persistent luminescence nanoparticles. *Bioconjug. Chem.* **23**, 472–478 (2012)
21. Maldiney, T., Bessière, A., Seguin, J., Teston, E., Sharma, S.K., Viana, B., Bos, A.J.J., Dorenbos, P., Bessodes, M., Gourier, D., Scherman, D., Richard, C.: The in vivo activation of persistent nanophosphors for optical imaging of vascularization, tumours and grafted cells. *Nat. Mater.* **13**, 418–426 (2014)
22. Li, Y., Zhou, S., Li, Y., Sharafudeen, K., Ma, Z., Dong, G., Peng, M., Qiu, J.: Long persistent and photo-stimulated luminescence in  $\text{Cr}^{3+}$ -doped  $\text{Zn-Ga-Sn-O}$  phosphors for deep and reproducible tissue imaging. *J. Mater. Chem. C*, **2**, 2657–2663 (2014)
23. Abdukayum, A., Chen, J.T., Zhao, Q., Yan, X.P.: Functional near-infrared-emitting  $\text{Cr}^{3+}/\text{Pr}^{3+}$  Co-doped zinc gallogermanate persistent luminescent nanoparticles with superlong afterglow for in vivo targeted bioimaging. *J. Am. Chem. Soc.* **135**, 14125–14133 (2013)
24. Weissleder, R.: A clearer vision for in vivo imaging. *Nat. Biotechnol.* **19**, 316–316 (2001)
25. Maldiney, T., Richard, C., Seguin, J., Wattier, N., Bessodes, M., Scherman, D.: Effect of core diameter, surface coating, and PEG chain length on the biodistribution of persistent luminescence nanoparticles in mice. *ACS Nano*, **5**, 854–862 (2011)
26. Gruzintsev, A.: Two-photon excitation of anti-stokes photoluminescence in  $\text{Y}_{1.80}\text{Er}_{0.10}\text{Yb}_{0.10}\text{O}_2\text{S}$ . *Inorg. Mater.* **50**, 821–825 (2014)
27. Georgobiani, A.N., Gruzintsev, A.N., Barthou, C., Benalloul, P.: Infrared luminescence of  $\text{Y}_2\text{O}_2\text{S}:\text{Er}^{3+}$  and  $\text{Y}_2\text{O}_3:\text{Er}^{3+}$ . *Inorg. Mater.* **40**, 840–844 (2004)
28. Lin, Y., Tang, Z., Zhang, Z., Wang, X., Zhang, J.: Preparation of a new long afterglow blue-emitting  $\text{Sr}_2\text{MgSi}_2\text{O}_7$ -based photoluminescent phosphor. *J. Mater. Sci. Lett.* **20**, 1505–1506 (2001)
29. Maldiney, T., Lecointre, A., Viana, B., Bessière, A., Bessodes, M., Gourier, D., Richard, C., Scherman, D.: Controlling electron trap depth to enhance optical properties of persistent luminescence nanoparticles for in vivo imaging. *J. Am. Chem. Soc.* **133**, 11810–11815 (2011)
30. Li, N., Li, Y., Han, Y., Pan, W., Zhang, T., Tang, B.: A highly selective and instantaneous nanoprobe for detection and imaging of ascorbic acid in living cells and in vivo. *Anal. Chem.* **86**, 3924–3930 (2014)
31. Wu, B.Y., Wang, H.F., Chen, J.T., Yan, X.P.: Fluorescence resonance energy transfer inhibition assay for  $\alpha$ -fetoprotein excreted during cancer cell growth using functionalized persistent luminescence nanoparticles. *J. Am. Chem. Soc.* **133**, 686–688 (2010)
32. Li, Z.J., Zhang, H.W., Sun, M., Shen, J.S., Fu, H.X.: A facile and effective method to prepare long-persistent phosphorescent nanospheres and its potential application for in vivo imaging. *J. Mater. Chem.* **22**, 24713–24720 (2012)

33. Li, Z., Zhang, Y., Wu, X., Wu, X., Maudgal, R., Zhang, H., Han, G.: In vivo repeatedly charging near-infrared-emitting mesoporous  $\text{SiO}_2/\text{ZnGa}_2\text{O}_4:\text{Cr}^{3+}$  persistent luminescence nanocomposites. *Adv. Sci.* **2**, (2015)
34. Srivastava, B.B., Kuang, A., Mao, Y.: Persistent luminescent sub-10 nm Cr-doped  $\text{ZnGa}_2\text{O}_4$  nanoparticles by a biphasic synthesis route. *Chem. Commun.* **51**, 7372–7375 (2015)
35. Li, Z., Zhang, Y., Wu, X., Huang, L., Li, D., Fan, W., Han, G.: Direct aqueous-phase synthesis of sub-10 nm “Luminous Pearls” with enhanced in vivo renewable near-infrared persistent luminescence. *J. Am. Chem. Soc.* **137**, 5304–5307 (2015)
36. Abdukayum, A., et al.: Gadolinium complexes functionalized persistent luminescent nanoparticles as a multimodal probe for near-infrared luminescence and magnetic resonance imaging in vivo. *Anal. Chem.* **86**, 4096–4101 (2014)
37. Wu, B.Y., Yan, X.P.: Bioconjugated persistent luminescence nanoparticles for Förster resonance energy transfer immunoassay of prostate specific antigen in serum and cell extracts without in situ excitation. *Chem. Commun.* **51**, 3903–3906 (2015)
38. Na, L., Wang, H., Xue, M., Chang, C., Chen, Z., Zhuo, L., Tang, B.: A highly selective and sensitive nanoprobe for detection and imaging of the superoxide anion radical in living cells. *Chem. Commun.* **48**, 2507–2509 (2012)
39. Posthuma-Trumpie, G.A., Korf, J., van Amerongen, A.: Lateral flow (immuno) assay: its strengths, weaknesses, opportunities and threats. a literature survey. *Anal. Bioanal. Chem.* **393**, 569–582 (2009)
40. Lee, L.G., et al.: A low-cost, high-performance system for fluorescence lateral flow assays. *Biosensors*. **3**, 360–373 (2013)
41. Paterson, A.S., Raja, B., Garvey, G., Kolhatkar, A., Hagström, A.E.V., Kourentzi, K., Lee, T.R., Willson, R.C.: Persistent luminescence strontium aluminate nanoparticles as reporters in lateral flow assays. *Anal. Chem.* **86**, 9481–9488 (2014)

## Chapter 5

# Organic Afterglow Phosphors

Compared to inorganic materials, organic optoelectronic counterparts of carbon-based small molecules or polymers prepared by various organic and polymeric synthetic methods hold important and advisable features including reduced manufacturing costs, versatility of molecular structures and properties, and compatibility with a vast range of substrates from transparent glass to flexible polymeric materials [1, 2].

The recent several decades have witnessed the intensive studies and rapid development of a large variety of organic semiconductors with diversified optoelectronic properties for various applications, ranging from low-power display, energy-saving lighting, smart window, solar cell, transistor, chemo/biosensors, etc. [3–5]. However, organic materials capable of persistent luminescence for afterglow emission with a lifetime longer than 0.1 s are rather rare. This is because the excited states of organic molecules are highly active, which can be deactivated radiatively or non-radiatively in many ways with very fast deactivation rates [6–8]. Thanks to continuous efforts on understanding and manipulating excited states both experimentally and theoretically, basic molecular design principles have been proposed to take advantages of the high molecular structure versatility of organic materials. Especially, a significant breakthrough in excited state lifetime tuning of organic materials has been achieved recently [9]. The purely organic molecules can be designed to show an ultra-long-lived excited state under ambient conditions with luminescence lifetime over 1.85 s [10]; the multicomponent material systems can be set to exhibit a long-lived photoluminescence with a lifetime up to 22.4 s [11]. These extraordinary long lifetimes, that are several orders of magnitude longer than that of traditional organic fluorophores (~ns) and phosphors (~ms) at room temperature, qualify them as organic afterglow materials [12].

The newly emerged organic afterglow materials with ultra-long room-temperature phosphorescence have renovated the conventional understandings of organic phosphors; their investigations may initiate new directions for research and exhibit profound impacts on many disciplines [13]. In this chapter, we summarized the recent research progress of organic afterglow materials and applications, from basic

theoretical insights on the luminescence mechanism, molecular design of organic afterglow phosphors, the photophysical properties and characterizations, to the amazing and diversified optoelectronic applications.

## 5.1 Principle of Organic Luminescence

Organic luminescence, which is different from the f/d-electron mediated radiative transitions of the rare earth metals in inorganic luminescence [14], relates closely to the excited state deactivations of organic molecules. According to the spin state of the excited state, two basic forms of organic luminescence can be classified into fluorescence and phosphorescence, respectively [15]. Fluorescence refers to the emitting of light due to radiative relaxation between two energy states of the same spin multiplicity, while phosphorescence is caused by the deactivation between the states with different multiplicity [16]. Generally, the ground states ( $S_0$ ) of organic materials are singlet. By absorbing light or other electromagnetic radiation, the molecule will be excited to high singlet excited states ( $S_n$ ,  $n \geq 1$ ) from  $S_0$  following Franck–Condon principle. The high-lying  $S_n$  then relaxes quickly to the lowest singlet excited state ( $S_1$ ) via rapid internal conversion. From  $S_1$ , the molecule can be radiatively deactivated to  $S_0$  by emitting fluorescence. The  $S_1$  can also transform to the triplet excited states ( $T_n$ ) when the intersystem crossing (ISC) is efficient enough. Through rapid internal conversion from  $T_n$ , the lowest triplet excited state ( $T_1$ ) will be finally generated. The radiative decay of  $T_1$  to  $S_0$  produces phosphorescence. However, the actual luminescent behaviors of organic materials are much more complicated due to their rich and highly flexible excited state structures.

### 5.1.1 Fluorescence

Fluorescence, which is the irradiative deactivation from singlet excited state to the ground state, belongs substantially to a kind of down-conversion luminescence with a lower energy than the absorbed radiation and therefore a red-shifted spectrum known as Stokes shift. The lifetime of fluorescence is generally short in a range of  $10^{-8}$  to  $10^{-9}$  s. Thus, the short-lived luminescence of fluorescence would disappear immediately just after removing the excitation source [17].

Mechanically, fluorescence occurs when an orbital electron of a molecule relaxes irradiatively to its ground state ( $S_0$ ) by emitting a photon from an excited singlet state, in most cases, from  $S_1$  as expressed in Eq. (5.1) and Fig. 5.1a.



where  $h\nu_{\text{em}}$  is a generic term for fluorescence with Plank's constant ( $h$ ) and emission frequency ( $\nu_{\text{em}}$ ). Non-radiative relaxations, which compete with the radiative relaxations, produce heat (vibrations) during excitation energy dissipation of the excited molecule in  $S_1$  [18].

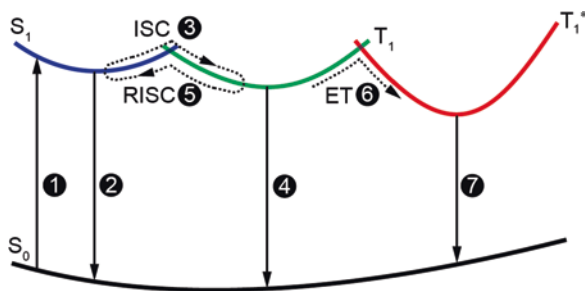


**Fig. 5.1** Various luminescent behaviors of organic materials after photoexcitation [13]. (a) Fluorescence due to radiative deactivation from  $S_1$  to  $S_0$  (① and ②); (b) Phosphorescence due to the emissive decay of  $T_1$  formed by intersystem crossing (ISC) from  $S_1$  (①, ③, and ④); (c) TADF due to delayed fluorescence after reverse intersystem crossing (RISC) from  $T_1$  (①, ③, ⑤, and ②); (d) Organic ultra-long room-temperature phosphorescence (OURTP) due to the slow emissive decay of the stabilized  $T_1$  ( $T_1^*$ ) formed through a tandem stabilization process of ISC and energy trapping (ET) (①, ③, ⑥, and ⑦)

The fluorescence quantum yield ( $\Phi$ ), defined as the ratio of the number of emitted photons to the number of absorbed photons, can be related to the decay rates of the excited state (Eq. (5.2)).

$$\Phi = \frac{k_f}{\sum_i k_i} \quad (5.2)$$

where  $k_f$  is the rate constant of fluorescence and  $k_i$  is the rate of various decay pathways of excited states including both radiative and non-radiative decays [19]. Fluorescence lifetime ( $\tau$ ), referred to the average time the molecule stays on its excited state before emitting a photon, can be figured out from the time-resolved decay curve of fluorescence intensity (Eq. (5.3)).

$$I(t) = I_0 e^{-t/\tau} \quad (5.3)$$

where  $I_0$  is the initial fluorescence strength at starting time ( $t = 0$ ). For conventional fluorescent compounds, typical fluorescence lifetime is within the range of 0.5–20 ns [17, 20].

### 5.1.2 Phosphorescence

Unlike fluorescence, which is a fast luminescence with a short lifetime in the order of  $\sim 10$  ns due to the allowed transition between the available energy states, phosphorescence is associated with a “forbidden” process in quantum mechanics, ascribed to the spin flip during deactivation from the excited state to the ground

state. Consequently, a phosphorescent material does not immediately re-emit the radiation it absorbs but re-emits at a much lower intensity with a much longer emissive lifetime in the range of  $10^{-6}$  to  $10^0$  s [21].

To emit phosphorescence upon photoexcitation through radiative deactivation of the triplet excited state, two intersystem crossing (ISC) processes are needed. Firstly, the  $T_1$  should be populated by ISC from  $S_1$  to  $T_1$ . Secondly, another ISC occurs from  $T_1$  to  $S_0$  for radiative decay of phosphorescence emission and non-radiative relaxation. Due to the classically forbidden transition feature of ISC, the rate of ISC process is at significantly slower time scales (Eq. (5.4) and Fig. 5.1b).

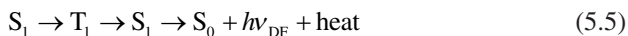


Compared to the slow kinetically unfavored radiative ISC of  $T_1$  for phosphorescence, the non-radiative relaxation may dominate the main relaxation processes of  $T_1$ , leading to very low phosphorescent quantum yield. To facilitate the radiative “forbidden” transition ISC rates for intense phosphorescence, heavy atoms or lone-pair electron containing atoms should be incorporated into the materials to promote the spin-orbital coupling and facilitate  $T_1 \rightarrow S_0$  radiative transition for phosphorescence luminescence. Traditionally, heavy metals such as Iridium (Ir) and Platinum (Pt) are highly effective in enhancing the ISC processes for highly efficient organic phosphorescence [22–24].

### 5.1.3 Thermally Activated Delayed Fluorescence (TADF)

In sharp contrast to fluorescence and phosphorescence, thermally activated delayed fluorescence (TADF) is rather complicated. By careful molecular design and sophisticated control of both singlet and triplet excited states to make them as close as possible in energy levels with very small singlet-triplet splitting ( $<0.3$  eV), the excited state can be transferred between  $S_1$  and  $T_1$  back and forth efficiently with the aid of thermal energy via both facile ISC and reverse intersystem crossing (RISC) processes that are generally “forbidden” in common organic molecules. In addition, the  $T_1$  is non-emissive and highly stable without  $T_1 \rightarrow S_0$  for phosphorescence and non-radiative relaxations, while the  $S_1$  is highly emissive for strong fluorescence [25–27].

Upon photoexcitation, TADF molecules are excited to  $S_1$ , from which either immediate radiative decay occurs for the promote fluorescence (PF), or  $T_1$  forms via ISC process; the stable  $T_1$  will return back to  $S_1$  via RISC process in next step and decayed radiatively to generate delayed fluorescence (DF) as illustrated in Eq. (5.5) and Fig. 5.1c.

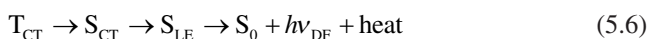


The prompt component of TADF has the same properties of the common fluorescence with a lifetime of several ns, while its delayed component shows significantly elongated emission lifetime of several microseconds due to the additional forward and reverse ISC processes that slow down the DF emission. Considering the rapid internal transitions between  $S_1$  and  $T_1$  states and the only radiative relaxation outlet is the spin-allowed  $S_1 \rightarrow S_0$  for fluorescence, the TADF can harvest both singlet and triplet excitons with high TADF quantum efficiency [28].

Despite its short history, TADF represents a highly active area of recent researches in organic optoelectronics. Various TADF molecules designed by involving metal (Cu(I), Ag(I), Au(I), and Sn(IV))-organic complexes, D-A molecule systems, and fullerenes have been developed. TADF-based devices such as organic light-emitting diodes (OLEDs), oxygen and temperature sensors show significantly improved device performance that is comparable to the traditional rare-metal complexes [29].

#### 5.1.4 Hybridized Local and Charge Transfer

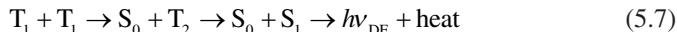
Organic luminescence via hybridized local and charge transfer (HLCT) is even more complicated than TADF. The HLCT state combines both local excited (LE) and charge transfer (CT) states together to afford a large transition moment from the LE state (cold exciton) for high-efficient fluorescence and a weakly bound exciton from the CT state (hot exciton) for efficient RISC ( $T_{CT} \rightarrow S_{CT}$ ) [30, 31]. When the internal conversion (IC) from  $T_{CT}$  to  $T_{LE}$  is blocked with a very large energy gap, 100% non-luminescent triplet excitons can be transferred to singlet exciton via RISC through CT state that has a small singlet-triplet splitting, leading to increased  $S_{CT}$  and eventually high  $S_{LE}$  (after IC process) for enhanced fluorescence. These processes can be illustrated in Eq. (5.6).



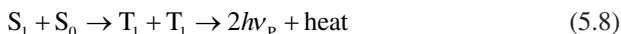
According to Kasha's rule, the blocking of the internal conversion process in organic materials is rather difficult, and the majority of the excitons tend to be in the lowest  $S_1$  or  $T_1$  state instead of the high-lying  $S_{CT}$  or  $T_{CT}$  excited state. Consequently, the molecular design and synthesis of such molecular system with an efficient HLCT excited state structure is a great challenge.

#### 5.1.5 Triplet-Triplet Annihilation and Singlet Fission

Triplet-triplet annihilation (TTA) is a photon up-conversion process in which the two triplet excitons lead to one high energy singlet exciton with delayed fluorescent lifetime that is much longer than traditional fluorescence (Eq. (5.7)) [32, 33].



In contrast, singlet fission (SF) is an apparently inverse process of triplet-triplet annihilation, in which a singlet exciton shares its excitation energy with another chromophore in ground state and both of them convert into two triplet excitons with maximum quantum efficiency up to 200% (Eq. (5.8)).



### 5.1.6 Organic Ultra-long Room-Temperature Phosphorescence (OURTP)

Very recently, significant progress in manipulating excited states of organic materials has been made under ambient conditions at room temperature with emission lifetime up to seconds, which are several orders of magnitude longer than those of conventional fluorescence ( $\sim$ ns), phosphorescence ( $\mu$ s  $\sim$  ms), and TADF ( $\sim$  $\mu$ s) [13]. This breakthrough in lifetime control of the highly active excited states represents a huge scientific advance in expanding the scope of purely organic luminescent materials for optoelectronic applications. Nevertheless, almost all the reported organic luminescent mechanisms are not applicable to support the emission of the excited states for such a long lifetime.

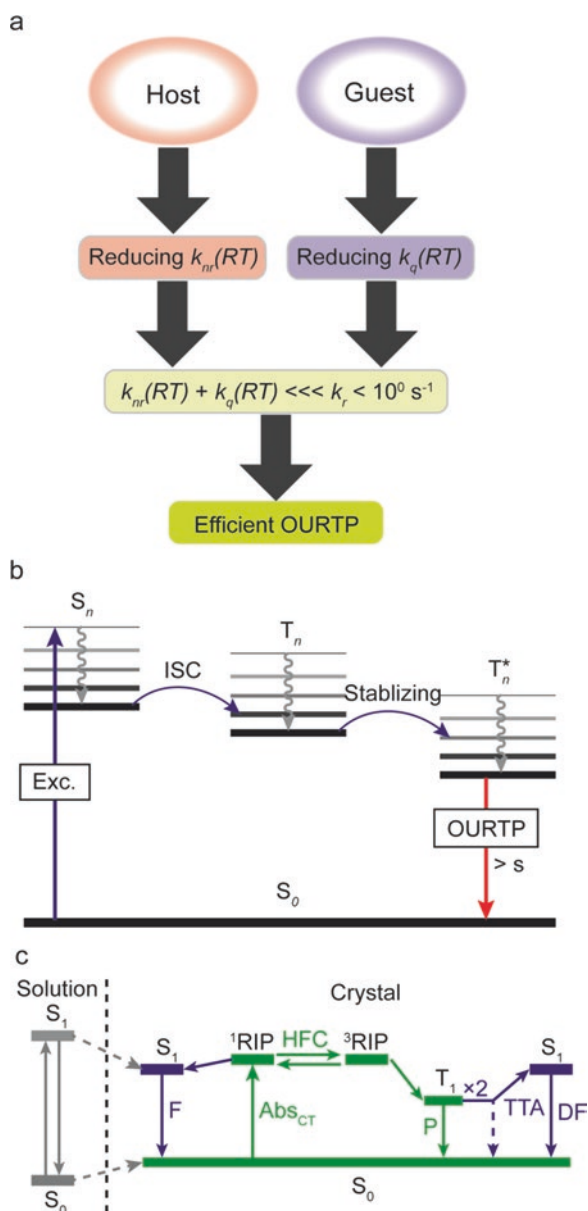
The long-lived luminescence, named as organic ultra-long room-temperature phosphorescence (OURTP), was essentially the phosphorescence due to radiative decay of triplet excited states. Therefore, the most conventional way in realizing long-lived OURTP for afterglow is to minimize the non-radiative decay and exciton quenching effects according to Eq. (5.9).

$$\tau_p = \frac{1}{k_r + k_{nr} + k_q} \quad (5.9)$$

where  $\tau_p$  is the lifetime of phosphorescence,  $k_r$  and  $k_{nr}$  are the rate constants for radiative and non-radiative deactivations from the triplet states to the ground states, respectively;  $k_q$  is the rate constant referring to quenching of the triplet excitons by interaction with the surrounding substance such as moisture and oxygen. For organic hydrocarbon molecules, typical  $k_r$  values are around  $10^{-1}$  to  $10^2$  s $^{-1}$ , due to the spin-orbital forbidden feature of the phosphorescence from triplet excited states to the singlet ground states. Therefore, it is rational to expect the purely organic afterglow materials with suitable  $k_r$  values ( $\sim 10^{-1}$ ) to give OURTP (up to 10 s) if non-radiative decay and exciton quenching were strictly impeded. With these basic considerations, various material design strategies can be conceived.



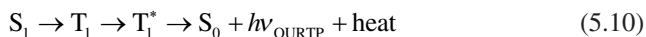
**Fig. 5.2** Typical mechanisms to realize organic afterglow in (a) multicomponent host-guest systems [34] and single-component materials by (b) stabilization of intersystem crossed triplet exciton [12] and (c) radical-ion-pair (RIP) mediated processes [35]



For the multicomponent OURTP materials as illustrated in Fig. 5.2a, the phosphor emitter has been deuterated to restrict the non-radiative deactivation pathways such as C-H stretching vibration, and highly rigid host matrices are used to protect the long-lived exciton from the quenching by humidity and oxygen and by themselves [34]. Following this strategy, various host and guest materials developed and

the longest lifetime of OURTP was reported to be up to 22.4 s in a multicomponent host–guest material system.

To achieve single-component purely organic afterglow materials, a mechanism including four key steps has been proposed and demonstrated in Fig. 5.2b [12]. In the first step,  $S_1$  is generated upon excitation with a lifetime of several nanoseconds (ns) (step 1). Then,  $S_1$  is transformed to  $T_1$  via ISC (step 2). In the third step, the trap or stabilization of  $T_1$  (step 3) leads to the formation of a stabilized triplet excited state ( $T_1^*$ ) (step 4). In the final step, OURTP is resulted from the radiative decay of  $T_1^*$ ; the exciton-protecting and transition “forbidden” features result in low radiative decay rate and even lower non-radiative decay rate, which are responsible for lifetime up to seconds.



It should be noted that the aggregated structures for accommodating  $T_1^*$  influence OURTP significantly. Generally, H-aggregation is applauding by providing lower energy levels to stabilize the triplet excitons to induce OURTP efficiently. Besides, crystal-induced phosphorescence (CIP) with aggregation-enhanced emission properties is also effective in realizing OURTP for organic afterglow at room temperature.

A radical-ion-pair (RIP) mechanism for the single-component phosphorescence was also proposed [35]. In crystals, the raise of  $S_0$  level and drop of  $S_1$  level caused by HOMO–HOMO and LUMO–LUMO interactions, respectively, lead to smaller bandgaps and red-shifted luminescence. The  $\pi$ – $\pi$  molecular stacking enables dimer formation for CT absorption and radical ion pairs upon photoexcitation. The energy level of singlet RIP ( $^1\text{RIP}$ ) should be very close to that of triplet RIP ( $^3\text{RIP}$ ) when two electrons spin over two molecules with weak spin coupling. Therefore, the spin exchange for singlet-to-triplet conversion is facilitated and promoted by hyperfine coupling (HFC), a nuclear spin magnetism-assisted spin conversion ( $^1\text{RIP}$ – $^3\text{RIP}$ ), to generate emissive triplet excitons for phosphorescence efficiently.

## 5.2 Materials for Organic Afterglow

Efficient room-temperature organic phosphorescence is traditionally confined to organometallic complexes containing heavy metals to promote the ISC processes in generating triplet excitons and enhancing the radiative decay of triplet excited state. However, metal complexes generally have luminescent lifetimes of several microseconds ( $\mu\text{s}$ ), which is too short to produce organic afterglow. To further elongate the lifetime of organometallic complex to several seconds at room temperature is extremely difficult or even impossible, because of the significantly facilitated IC and radiative  $T_1 \rightarrow S_0$  transition for phosphorescence with high relaxation rate constant ( $\sim 10^6 \text{ s}^{-1}$ ) when heavy metals participate.

Metal-free organic materials, on the other hand, usually have very weak phosphorescence due to the spin-forbidden transitions between singlet and triplet states which dramatically suppress the triplet radiative deactivation. To overcome the typically dark triplet states in organic luminogens by promoting transitions between singlet and triplet states, lone-pair electron containing moieties such as carbonyl and sulfuryl groups or heteroatoms has been introduced into the  $\pi$ -conjugated molecular systems to facilitate  $n\text{-}\pi^*$  transitions. Thus promoted luminescence of phosphorescence still belongs the typical organic phosphorescence, showing triplet exciton lifetime lower than 20 ms at room temperature.

In the aim to further extend the luminescence lifetime to the scope of seconds at room temperature, additional means should be taken, focusing on suppressing adversary factors towards the existence of triplet excitons. Abundant molecular interactions and limited atom motions will contribute to restricting non-radiative decay processes of triplet excitons, while moderate spin-orbit coupling will be helpful in extending lifetime of radiative processes. Furthermore, solid states either crystal or uniform film are essential for further stabilizing the triplet exciton or to prevent the triplet luminogens from contacting with quenchers.

Several strategies have been developed to design organic afterglow materials. For single-component OURTP molecules, not only groups capable of promoting  $n\text{-}\pi^*$  transitions to populate triplet excited states, but also H-aggregation structure in solid state to further stabilize and protect the generated triplet exciton are essentially required; felicitous using of intermolecular interactions in crystals can also suppress non-radiative deactivation processes to gain efficient organic afterglow. For multi-component organic afterglow material systems, enhanced and elongated OURTP from organic phosphorescent molecules can be observed by being dispersed in a suitable host which has a rigid solid-state condition to minimize the non-radiative deactivation and quenching process. Polymers are also possible to show OURTP for organic afterglow emission; the widely used fluorescent semiconducting polymer of poly [2-methoxy-5-(2'-ethylhexyloxy)-*p*-phenylene vinylene] (MEH-PPV) was found to have persistent luminescence in nanoparticles with a size range of 20–50 nm, although the fundamental reason for the afterglow is unclear [36]. Furthermore, carbon dots and metal-organic frameworks (MOFs) were also found to be able to emit long-lived phosphorescence with a lifetime up to sub-second order in ambient condition upon UV excitation [37, 38].

### 5.2.1 Single-Component Small Molecules

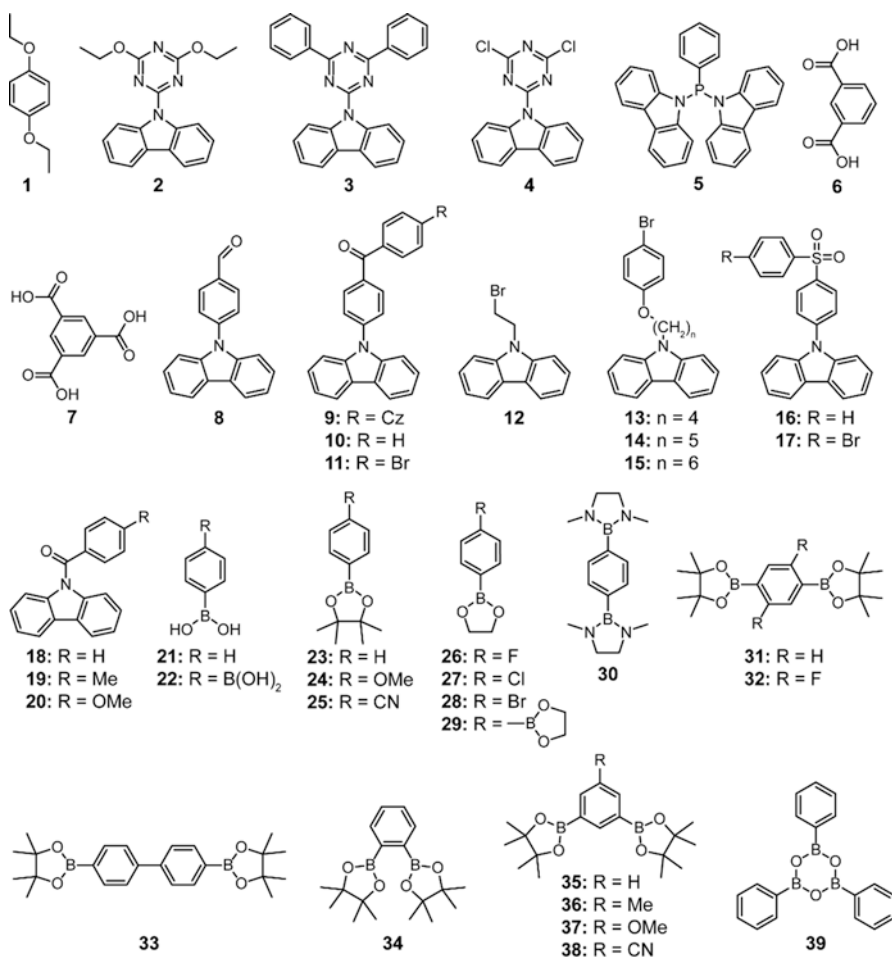
Single-component organic molecules with intrinsic afterglow properties are highly attractive for both mechanism studies and device applications [12]. According to the organic afterglow mechanism, the featured afterglow emission peaks are generally weak with low quantum efficiency ( $\sim 1\%$ ) and red-shifted in comparison with that of the fluorescent and phosphorescent peaks, indicating a lower excited state for organic afterglow emission. Organic afterglow molecules usually exhibit

temperature-sensitive feature with longer luminescent lifetime at a lower temperature. Rigidity of these materials in crystal protects them from contacting with oxygen and moisture, thus reduces sensitivity to these quenchers. Their afterglow emission can be switched on and off reversibly through phase transition achieved by a repeat of heating, fuming, or grinding procedures.

Following the basic principles in realizing organic afterglow, the purely organic single-component OURTP small molecules can be generally designed in two steps by subsequently introducing (1) lone-pair electron containing atoms, such as O, N, and P atoms, to enhance the spin-orbital coupling according to the El-Sayed's rule; (2) appropriate moieties to promote the formation of stable H-aggregates or compact crystals to trap, stabilize, and protect the generated triplet excitons via ISC. Indeed, H-aggregated fluorophores typically have low luminescence efficiencies, because of the emission-forbidden feature of the lowest energy levels formed by the strong interactions of the transition dipoles between parallelly stacked molecules; nevertheless, the stable non-emissive packing structure in H-aggregation can effectively stabilize the triplet states, resulting in significantly elongated lifetime of OURTP under ambient conditions. This design rule for organic afterglow was experimentally validated in a series of organic molecules (compounds **1–5**), showing significantly tuned excited states for OURTP with lifetimes up to 1.35 s [12] (Scheme 5.1).

Crystal-induced phosphorescence (CIP) was also proposed to realize OURTP for organic afterglow at room temperature [39]. With the increase of concentrations,  $\pi$ -conjugated materials suffer from reduced luminescence intensity in most cases, and even become non-radiative in a solid state known as aggregation-caused quenching (ACQ). In contrast, aggregation-induced emission and/or aggregation-enhanced emission (AIE and/or AEE) effects were also observed in some organic  $\pi$ -conjugated molecules, which are called as AIEgens. AIE effects can significantly promote the luminescence of organic materials by restricting inter- and intramolecular motions to minimize the non-radiative and quenching process for higher luminescence from a crystal. [40] CIP effects with limited intermolecular motions in crystals for OURTP phenomenon were observed in a series of molecules (compounds **6–11**), which contain ketone to enhance the ISC to populate the triplet excited states [41–44]. The effects of CIP in achieving long-lived OURTP through reducing exciton quenching and non-radiative decay rates can be summarized as follows: (1) protecting excitons from moisture and oxygen quenching by crystallization; (2) restricting C-H vibrations via strong short connection, i.e., intermolecular hydrogen bonds to increase the rigidity of the molecules; (3) dense crystal packing to firmly lock the molecules and thereby rigidify their conformations via severe crystallization.

Manipulating intermolecular heavy atom effects is also important in acquiring strong OURTP from metal-free organic molecules. Strong spin-orbit coupling will facilitate intersystem crossing and radiative deactivation of triplet excited state at the same time, leading to high efficiency and short lifetime of the luminescence, simultaneously. Therefore, careful tuning of heavy atom effect for the balanced lifetime and efficiency of OURTP is important in achieving high-performance organic



**Scheme 5.1** Molecular structures of the purely organic single-component OURTP small molecules

afterglow. With a luminophore of carbazole, a flexible linking chain, and a terminal bromine atom, aromatic carbonyls (compounds **12–15**) were found to show long luminescence lifetime up to 0.2 s and ultrahigh ambient phosphorescent quantum yield up to 39.5% in crystal. [45] In addition, these compounds can emit white light under UV irradiation (365 nm) with total luminescent efficiency of 72.6% ascribed to dual emission of both strong fluorescence and phosphorescence. Importantly, the distance between bromine atom (as heavy atom) and carbazole determines whether the OURTP occurs; the intermolecular weak interactions strongly influence the lifetime and efficiency of OURTP for organic afterglow. The introduction of a heavy heteroatom to increase the ISC rate was also valid in constructing carbazolyl and

sulfonyl/carbonyl groups containing afterglow molecules (compounds **16–20**) for efficient OURTP with a lifetime up to 0.49 s and quantum yield of 6% [41, 46].

Recently, a series of simple arylboronic esters (compounds **21–39**) were observed to emit phosphorescence in the solid state at room temperature with a lifetime in the order of several seconds [10, 47]. These molecules undergo an out-of-plane distortion at the (pinacol)B-C<sub>ipso</sub> moiety in the excited T<sub>1</sub> state, leading to facilitated mixing of  $\pi$  and  $\sigma$  orbitals with promoted spin-orbit coupling and enhanced phosphorescence at the room temperature. Moreover, a systematic compound survey with 19 arylboron compounds indicates that rather than determined by the patterns and numbers of boron substituents on the aryl units, the OURTP properties are dominated by solid-state molecular packing.

### 5.2.2 Multicomponent Materials

According to Eq. (5.9), it is theoretically easy to elongate OURTP for afterglow by minimizing the non-radiative decay and exciton quenching effects simultaneously in a rigid host, when the radiative decay for the phosphorescent emission is already very slow. However, it is experimentally challenging to develop such a host–guest material system containing both emissive phosphorescent guest and efficient hosts capable of separating humidity and oxygen as well as restricting non-radiative vibration simultaneously. Basic requirements for the multicomponent organic afterglow material designed in a host–guest system are as follows. First, the host and guest molecules should be highly compatible for good dispersion of guest molecules in the host matrix. Second, host molecule should have higher T<sub>1</sub> and S<sub>1</sub> energy levels than that of the guest phosphors to prevent the luminescent quenching by energy transfer from the guest to the host. Third, the host materials should be optically and chemically inert for both photoexcitation and luminescence extraction, and be electronically active for charge injection and transport to the guest emitters when used in OLEDs via electronic excitation.

In 2013, Hirata et al. succeeded in achieving efficient OURTP from purely organic amorphous multicomponent host–guest systems in the air by using rigid hydroxyl steroidal compounds (compound H1 in Scheme 5.2) as the host matrix and a secondary amino-substituted deuterated carbon (compound G1) as the guest [34]. Deuteration of the guest slows down its non-radiative decay rate, while the amino group promotes the ISC to populate the T<sub>1</sub> state. Benefitted from the high rigidity and oxygen barrier of the steroidal host, the exciton quenching of the guest caused by diffusional motion and is significantly minimized after well dispersed in the host matrix. Moreover, high T<sub>1</sub> energy level of the host and small concentration of the guest further suppress the quenching processes. Consequently, red-green-blue OURTP with outstanding afterglow performance ( $\tau > 1$  s,  $\Phi > 10\%$ ) in ambient condition is realized in a purely organic system.

Following such a material design strategy, Hirata et al. further dispersed two kinds of guests in the amorphous hydroxyl steroidal host (H1). One guest is an aro-

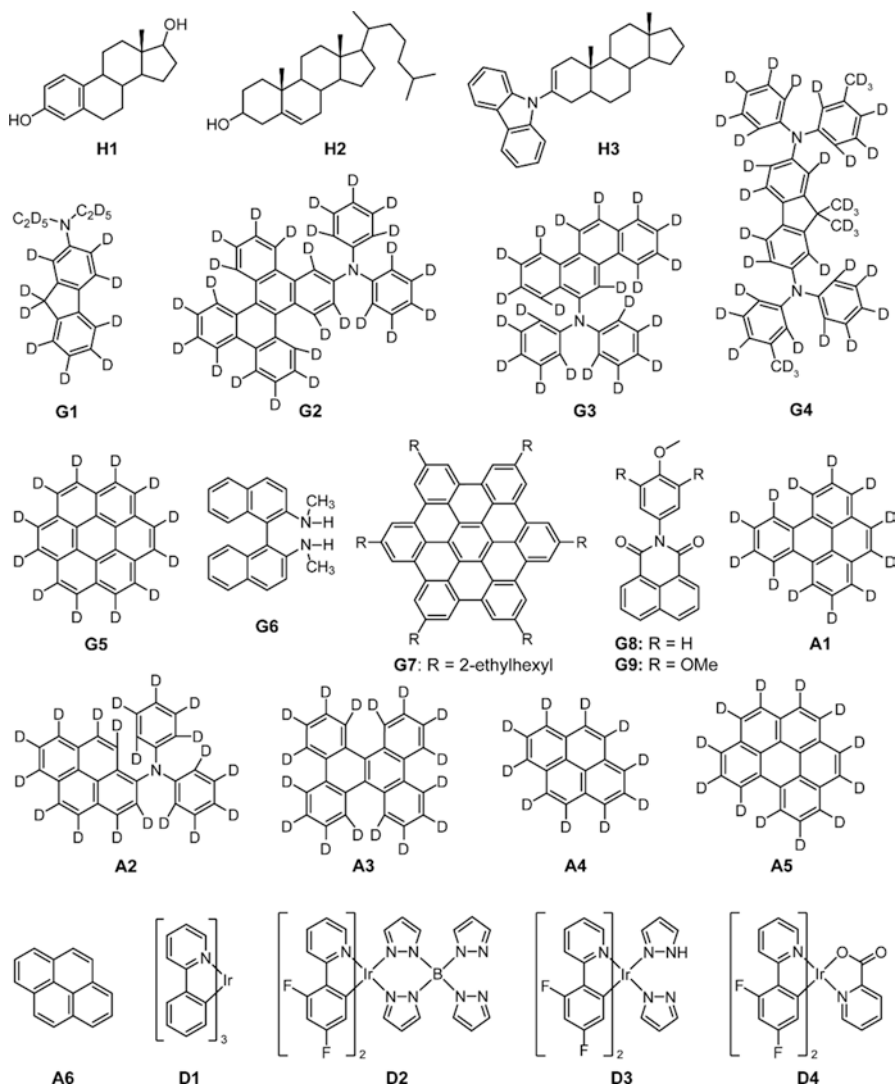
matic species that acts as an acceptor (A1-6) and a phosphor for the afterglow, while the other is a transition metal complex (D1-4) functioned as a triplet donor to populate the triplet excited state of the acceptor by photosensitization [48]. Through this three component co-guest method, the afterglow lifetime can reach 2.77 s with a total quantum yield of 44%. In a similar way, they also demonstrated a photo-reversible red OURTP by using a persistent phosphorescent guest (compound G2), a photochromic guest, and an amorphous steroidal host (compound H1) together [49]. The afterglow from the red-emitting guest was observed with a lifetime longer than 1 s; this red afterglow emission can be erased and recovered by UV/green light irradiation, corresponding to the reversible photocyclization and decyclization of the secondary photochromic guest. The photoisomerization of the photochromic compound determines the occurrence and cease of dual dipole–dipole energy transfer from the excited states of the phosphorescent guest to the ground state of the photochromic guest, and thus triggers the deactivation and activation of the red OURTP for on–off switching, respectively. Circularly polarized OURTP has been also realized by doping chiral binaphthyl enantiomers of **G6** into **H1**, showing circular polarized yellow afterglow (560 nm) in air with a lifetime of 0.67 s and quantum yield of 2.3% [50].

Besides the hydroxyl steroid host, other host materials have been also developed. Adachi et al. introduced a hole-transporting carbazole unit into the steroid androstene to prepare a semiconductive hydrophobic steroid derivative, which is effective in supporting OURTP with a lifetime up to 4.3 s (with the guest emitter of compound **G5**) and is especially attractive for electronic device applications [51]. Blue electroluminescence was observed under an applied voltage, and the device shows green OURTP emission after ceasing of power supply, demonstrating the first success in preparing afterglow OLEDs. Transparent plastic of poly(methyl methacrylate) (PMMA) can also suppress the non-radiative decay and quenching processes significantly to support the organic afterglow. When N-substituted naphthalimides of G8 and G9 were doped into PMMA, the lifetimes of the emission are about 0.23 s [52]. An even longer lifetime up to 5.58 s was reached when coronene (G5-h<sub>12</sub>) was dispersed in the PMMA host [11] (Scheme 5.2).

### 5.2.3 Polymers

Polymers or macromolecules play an important role in many aspects of scientific investigations. In this newly emerged research field of OURTP, polymers were also found to be applicable as afterglow emitters. It can be dated back to 2007, when Fraser and coworkers connected boron difluoride-based phosphors to polylactic acid (PLA) to develop afterglow polymer with a lifetime longer than 0.1 s (P1–P3 in Scheme 5.3). PLA acts as a host matrix to protect luminophore from contacting with oxygen and suppress non-radiative deactivation, thus extending phosphorescent lifetime. The boron difluoride  $\beta$ -diketonate-based afterglow polymer P1 shows intense fluorescence and OURTP (509 nm) with a lifetime of 0.17 s and a persistent

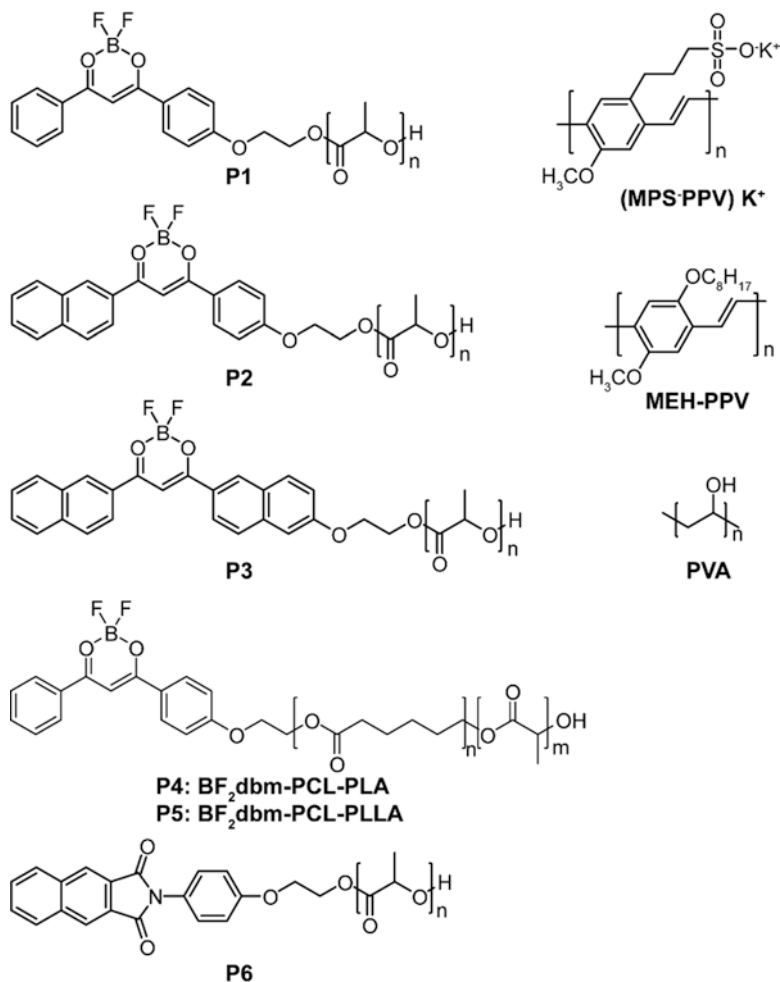




**Scheme 5.2** Multicomponent organic afterglow materials in host–guest system

time of 5–10 s in a solid film [53]. Replacing one phenyl group of P1 with naphthyl group produces P2, which has typical intramolecular charge transfer bands in absorption and emission spectra for red-shifted and molecular weight-dependent afterglow emission with a lifetime of  $\sim 0.1$  s in a solid film [54]. When both two phenyl groups of P1 were replaced with naphthyl groups, the resulting P3 exhibits much longer afterglow lifetime up to 0.38 s in a film state [55]. Similarly, afterglow from P4 and P5 was also observed when poly( $\epsilon$ -caprolactone) was inserted between the phosphor and PLA or PLLA (*L*-PLA) [56]. A longer organic afterglow lifetime





**Scheme 5.3** Organic afterglow polymers

of 1.2 s was realized by connecting a new phosphor of N-substituted naphthalimides to PLA matrix (P6) [52].

For other types of organic afterglow polymers, Rao and coworkers reported that the nano-precipitated MEH-PPV nanoparticles show persistent luminescence lasting for nearly 1 h after a single excitation [36]. Although the mechanism of persistent phosphorescence of the conjugated polymer nanoparticle is unclear, the pivotal role of MEH-PPV in achieving OURTP is confirmed because the OURTP is absent in other conjugated polymer nanoparticles. Moreover, dispersion of water-soluble conjugated polymers such as (MPS-PPV)K<sup>+</sup> into rigid polymers (i.e., polyvinyl alcohol (PVA) and poly(vinyl-pyrrolidone) (PVP)) also enables afterglow emission [57]. More efforts are required to figure out the fundamental mechanisms for effi-

cient OURTP in polymers, and to develop new series of organic afterglow polymers.

### 5.2.4 Carbon Dots

As an important class of photoluminescent nanomaterials in recent years among the nanocarbon family and traditional semiconductor quantum dots, carbon dots have various attractive properties and potential applications due to not only their excellent optical performance and small size effect, but also the great biocompatibility and ease to achieve surface functionalization [58–61]. Strong fluorescence of carbon dots was generally observed and investigated with much less attention paid to the phosphorescent phenomenon and related applications.

In 2013, Zhao et al. reported the first example of carbon dots-based afterglow materials by dispersing carbon dots into a matrix of polyvinyl alcohol (PVA) [38]. Under the excitation of ultraviolet light, obvious phosphorescence with a lifetime of 0.38 s was detected at 500 nm. This long-lived OURTP emission is suggested to be originated from triplet excitons of aromatic carbonyls above the carbon dots and protection of PVA matrix by restricting the rotation and vibration energy loss through hydrogen bonds between carbonyls and PVA molecules. Potash alum ( $\text{KAl}(\text{SO}_4)_2 \cdot x(\text{H}_2\text{O})$ ) is also a good host material for carbon dots to generate notable OURTP emission upon excitation by UV light [37]. The  $\text{KAl}(\text{SO}_4)_2 \cdot x(\text{H}_2\text{O})$  seems to be able to more effectively protect the triplet excitons and suppress the non-radiative deactivation pathways, leading to longer lifetime up to 0.71 s.

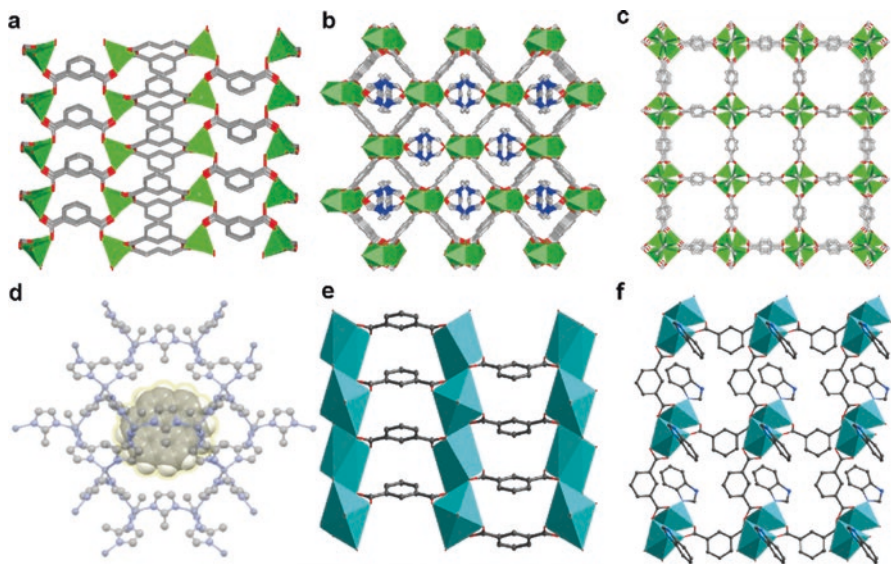
Two-component matrices have been also used to suppress the vibrational dissipation of long-lived triplets with apparent advantages over a single-component matrix. By combining the rigidity of the melting recrystallization urea (the first matrix) and hydrogen bonding between biuret (the second matrix) and carbon dots, the composite matrices enable the N-doped carbon dots to show an OURTP lifetime of 1.06 s and a high phosphorescence quantum yield of 7% in air [62]. The C=N bonds on the surface of the N-doped carbon dots can create new energy level structures, which are supposed to be the origin of the OURTP phenomenon. Triple-mode emission [63] and amphiphilic carbon dots [64] were also developed further extending fields of afterglow applications.

### 5.2.5 Metal-Organic Frameworks (MOFs)

Metal-organic frameworks (MOFs) are a class of inorganic-organic coordination hybrids, whose structures and properties can be tuned effectively via proper selection of both metal ions and ligands. According to the basic luminescent mechanism

of OURTP, coordination of organic phosphor units with metal ions in MOFs is effective in producing afterglow because (1) metal ions involving heavy atom effect can accelerate the spin-orbit coupling of excited electrons for the population of triplet excitons and (2) organic-metal hybrids based on strong coordination interaction usually have enhanced rigidity of molecular conformations and restricted molecular motions/vibrations to minimize the non-radiative loss of excitons and facilitate the phosphorescence emission. The first example of afterglow MOFs is developed by Yang and Yan by coordinating organic phosphors of terephthalic acid (TPA), isophthalic acid (IPA, compound **6** in Scheme 5.1), and trimesic acid (TMA, compound **7** in Scheme 5.1) with noble-metal-free and rare-earth-free ions of  $\text{Zn}^{2+}$  and  $\text{Cd}^{2+}$ ; the Zn-IPA MOFs exhibit efficient green OURTP with the longest lifetime of 1.3 s [65]. Also, they succeeded in preparing dynamic MOFs of Zn-TPA-DMF and MOF-5 that can reversibly change the structures upon solvation and/or guest adsorption for highly tunable OURTP with lifetimes of 0.47 s and 0.15 s, and colors from cyan to yellow and from green to red, respectively [66].

The MOF structure can be also used as a host matrix to suppress non-radiative decay processes for afterglow emission because their rigid porous structure and pore structures can trap and stabilize emitter molecules [11]. By introducing deuterated coronene (G5) into the pores of the zeolitic imidazolate framework ZIF-8, an ultra-long lifetime of 22.4 s was observed at the room temperature, and of 0.4 s at 460 K. Such an ultra-long lifetime and excellent thermal stability of OURTP at high



**Scheme 5.4** Afterglow MOFs of (a) Zn-IPA, (b) Zn-TPA-DMF, (c) MOF-5, (d) G4@ ZIF-8, (e) CP1, and (f) CP2

temperature indicate the great potential of MOF structures in encapsulating, isolating, and modulating the excited organic emitters for organic afterglow.

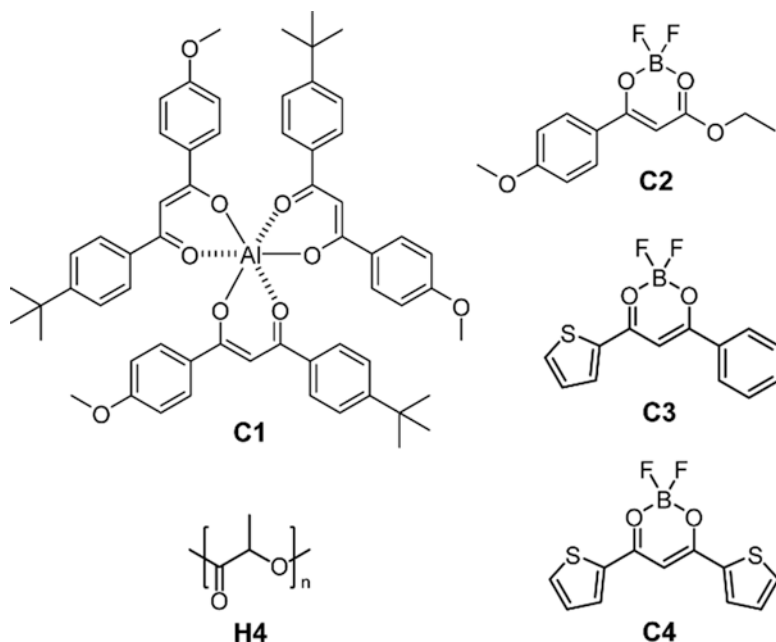
Afterglow emissions can also be achieved by metal coordination polymers (CPs). Yan and coworkers coordinated 1,3-benzenedicarboxylic acid and benzimidazole with  $\text{Cd}^{2+}$  respectively to produce two-dimensional layered CP1 and CP2 (Scheme 5.4e, f). Interlayer C-H- $\pi$  and  $\pi$ - $\pi$  interactions allow ultra-long persistent luminescence with lifetimes of 0.70, 0.40 s and 0.76, 0.54 s for CP1 and CP2 under ambient condition and in water, respectively. Afterglow lifetime of CPs can be further tuned via modulation of coordination situation and packing fashion of ligands. Surprisingly, CP2 shows a linear and reversible sensitivity to pH value of surrounding environment indicating its potential to function as a pH-sensor.

### 5.2.6 Complexes

As discussed in Sect. 5.1.2, heavy metal complexes are efficient in promoting spin-orbit coupling for phosphorescent emission with a typical lifetime of several microseconds. Due to the significantly enhanced ISC processes in both exciton transformation and triplet state radiative decay, it is impossible to achieve organic afterglow emission from heavy metal complexes. Nevertheless, if a light metal with less spin-orbital coupling property is used to balance the exciton transformation and the radiative decay, organic afterglow from complexes can be also expected. An avobenzene (AVB) complex of Al(III) named as  $\text{Al}(\text{AVB})_3$  (C1 in Scheme 5.5) shows afterglow emission around 500 nm with a lifetime of 0.4 s at room temperature, when dispersed in H4 matrix [67]. Another series of ketone-Lewis acid model complexes of difluoroboron- $\beta$ -diketones also show dual-emission phenomenon with simultaneous fluorescence and organic phosphorescence originated from Lewis-acid-induced charge transfer state and carbonyl-enhanced ISC, respectively. Especially, the crystal of difluoroboron ethyl 3-(4-methoxyphenyl)-3-oxopropanoate (BF2EMO, C2) exhibits OURTP with a lifetime of 0.22 s for organic afterglow due to the multiple weak interactions among the molecules in the crystal which rigidify the matrix and effectively shut down thermal decay. Another two B-complexes (C3 and C4) in the similar molecular structure using different substituents also exhibit afterglow properties with lifetime about 0.1 s, when blended with PLA matrix [68] (Scheme 5.5).

## 5.3 Applications of Organic Afterglow Phosphors

The intrinsic OURTP at ambient conditions with significantly elongated luminescence lifetime over 1 s is suitable for a large variety of fundamental research and advanced applications which can hardly be achieved using conventional short-lived organic fluorescence, phosphorescence, or TADF materials. Considering the intrinsic advantages of organic molecules, the lightweight and flexible organic afterglow



**Scheme 5.5** Organic afterglow complexes

materials capable of persistent luminescence with lifetime over 0.1 s are attractive in providing numerous opportunities for potential applications in a large range of aspects, including afterglow OLEDs, anti-counterfeiting, optical recording, biochemistry, ultrahigh-density data storage and ultra-complex information encryption, especially after rational and integrated arrangements of their emitting colors, luminescent lifetimes, and excitation and emission wavelengths.

### 5.3.1 Afterglow OLEDs

OLEDs are considered to be the next-generation technology for lighting and displays with many advantages of lightweight, ultrathin, and highly flexible. To improve the OLED efficiencies to maximum extent, the 75% electrically generated excitons in triplet states should be harvested for luminescence [69–71]. Therefore, the first-generation OLEDs based on fluorescent organic materials have been updated to the second-generation phosphorescence OLEDs using room-temperature phosphorescent organic complex emitters, and very recently, to the third-generation TADF OLEDs based on TADF molecules, which can harvest triplet excitons for fluorescence via reverse intersystem crossing (RISC).

Organic afterglow materials generally exhibit dual emission of fluorescence and phosphorescence; the long-lived OURTP component will be attractive for the fabri-

cation of afterglow lamps, which show persistent luminescence even after shutting off the power. Instead of coating inorganic afterglow phosphors on the surface of a lamp, organic OURTP emitters in afterglow OLEDs allow direct generation of long-lived triplet exciton for electroluminescence. This organic afterglow lamp, without adding an additional photoluminescence-producing layer, is highly attractive for future lighting applications.

Adachi et al. was the first to prepare an organic afterglow OLED by depositing an OURTP emitter (compound **G5**) into a semiconductive matrix (compound **H3**) which can serve as a host to minimize the non-radiative decay of the guest emitters and, on the other hand, can act as electron and hole transporters to electronically excite the deposited guest molecules [51]. In this way, the electronically excited organic afterglow was realized via hole and electron injection and combination in a device structure of indium tin oxide (ITO)/4,4'-bis[*N*-(1-naphthyl)-*N*-phenyl-amino]biphenyl ( $\alpha$ -NPD) (30 nm)/1,3-bis(*N*-carbazolyl)benzene (mCP) (10 nm)/1% DMFLTPD-d36:CzSte (30 nm)/1,3,5-tris(*N*-phenylbenzimidazol-2-yl)benzene (TPBi) (60 nm)/LiF (0.8 nm)/Al (80 nm) (Fig. 5.3a). This first organic afterglow OLED showed blue fluorescence under an applied voltage and green OURTP after ceasing the driving voltage. With compound **G5**, the lifetime of the green electroluminescent OURTP is 0.39 s, which is shorter than the corresponding lifetime of the photoluminescent OURTP (0.61 s). When a planar coronene-d<sub>12</sub> (compound **G8**) was used as the organic afterglow OLED emitter, the lifetime can be extended to 4.3 s.

### 5.3.2 Anti-counterfeiting

To prevent falling into a situation with great chances of fraud, huge efforts have been devoted to developing methods to distinguish the real and the fake. Among them, anti-counterfeiting label is one of the most efficient ones. The distinguishable lifetimes of OURTP luminophores from traditional organic materials offer OURTP materials a great opportunity for data security and anti-counterfeiting.

As shown in Fig. 5.4a, codes “2014” written by compound **3** with a lifetime of 1.36 s are above the codes of “8888,” which is written with short-lifetime (<3 ns) fluorescent material on a flexible substrate [12]. Under the irradiation of 365 nm UV light, only blue pattern of “8888” can be observed. The encrypted pattern of “2014” in yellow afterglow appears only after removing the excitation source. A similar application was shown in Fig. 5.4b, in which characters “1357” were written by fluorescent starch while “2468” were written by afterglow carbon dots [62]. All characters emitted blue fluorescence under UV irradiation, while only “2468” could be seen after turning off the UV lamp. In other attempts (Fig. 5.4c) [45], commercial anti-fake stamps and two patterns of compounds **13** and **15** in a common receipt show red and blue fluorescence under 365 nm excitation, respectively; when the excitation light is turned off, the red and blue fluorescence disappears immediately, leaving yellow afterglow of compounds **13** and **15** that gradually disappears in the following several seconds.



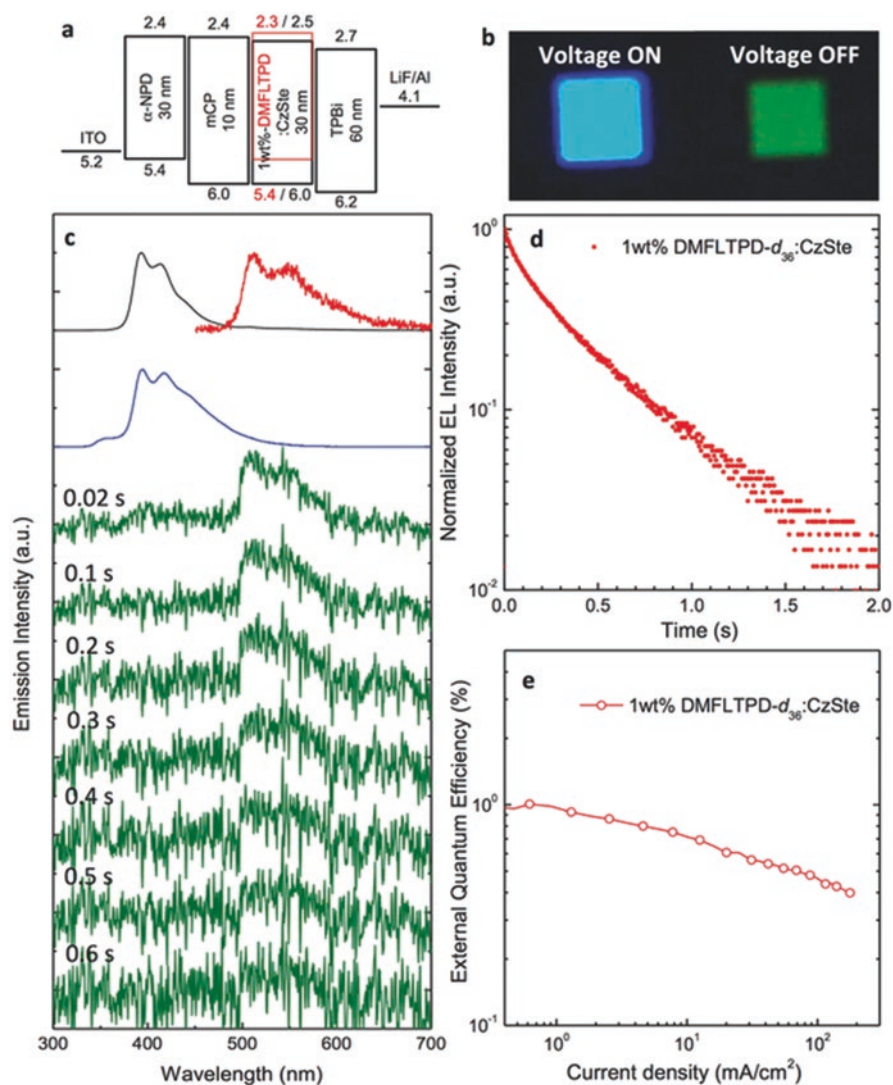


**Fig. 5.3** (a) Organic afterglow OLED structure (energy levels in eV). (b) Device photographs during (left) and after (right) the electronic excitation of the device using H3 as a host and G5 as a guest. (c) Fluorescence (black) and phosphorescence (red) spectra of compound H3 doped film, and EL spectra with H3 as the host during (blue) and after (green) electrical excitation. (d) Transient EL decay curve of the device after the applied voltage was turned off. (e) External quantum efficiency (EQE)–current density characteristics of the OLED [51].

Triple-mode emission of PVA/m-CDs enables a more complicated application [63]. As illustrated in Fig. 5.4d, two patterns were drawn on a banknote beside the existing anti-counterfeiting picture which is invisible under daylight. When excited by UV light, both drawn patterns and existing picture can be observed. The drawn



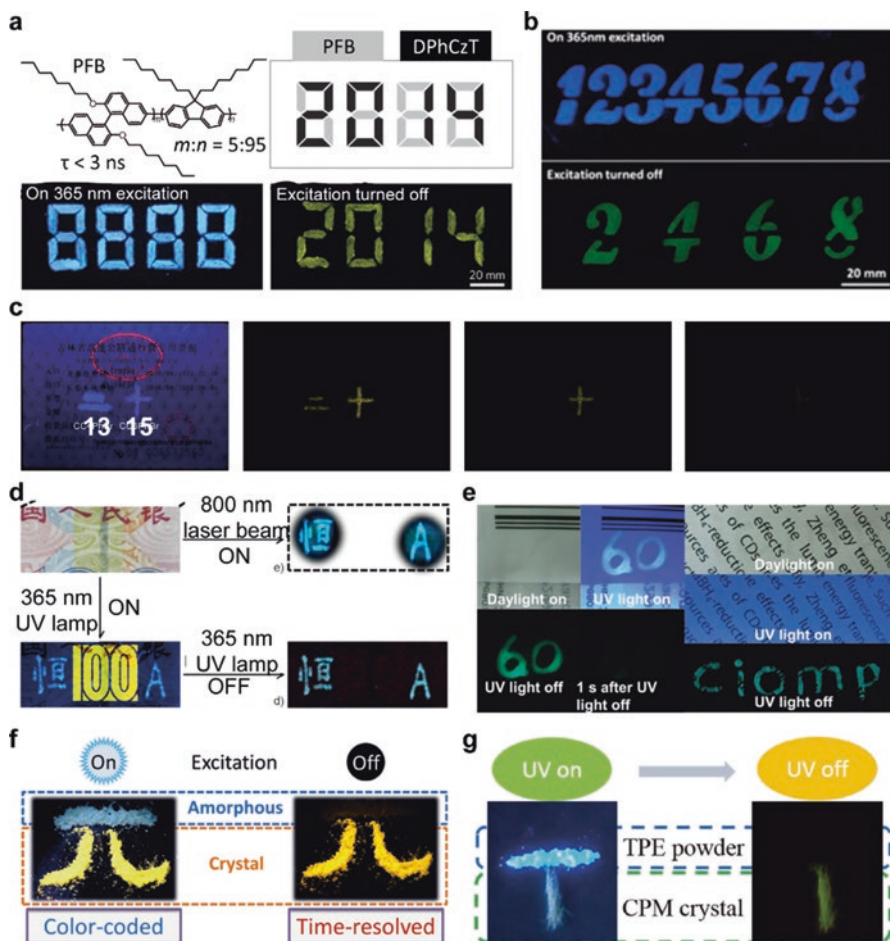


**Fig. 5.4** The prototype applications of organic afterglow materials in anti-counterfeiting using (a) compound **3** [12], (b) urea/CDs [62], (c) compounds **13** and **15**, (d) PVA/m-CDs [63], (e) PVA/CDs [38], (f) compound **11** [41], and (g) compound **18** [46]

patterns are also visible under 800 nm laser beam. Once UV excitation was turned off, the original anti-counterfeiting picture disappears immediately and only the drawn patterns can be seen. By taking both advantages of different luminescent color and lifetime codes, these flexible organic afterglow materials can provide rich encoding information for high-level anti-counterfeiting. Using carbon dots, a concept of time-resolved phosphorescence anti-counterfeiting was also shown in Fig. 5.4e [38]. Letters written by carbon dot-PVA mixed ink solution can be hardly observed from background paper under UV and daylight irradiation, owing to the strong fluorescence of the background paper. However, after ceasing the UV light, the encrypted secret information of characters “ciomp” can be observed with strong afterglow emission in several seconds after the immediate disappearance of back-

ground fluorescence of paper. As demonstrated in Fig. 5.4f [41], a dual-responsive security protection application based on OURTP molecule of compound **11** has been prepared. The light blue part of letter “ $\pi$ ,” which represents the amorphous state of **11**, can be easily distinguished from the yellow part referring to crystal state under 365 nm ultraviolet irradiation; after removing the lighting source, only the bottom part of letter “ $\pi$ ” with orange afterglow from the crystal can be observed. When using fluorescent tetraphenylethylene (TPE) and dual-emissive afterglow compound **18**, a similar application can be realized as shown in Fig. 5.4g [46].

### 5.3.3 Optical Recording

Information recording is important in the daily life. As a process of recording signals on a medium through the use of light, optical recording is convenient in recording signals that can be reproduced after a subsequent time. The key material for optical recording is the recording medium, which varies from photographic film to optical disk in the history. Considering the crystallization-dependent luminescence feature with different emission spectra in different solid states of organic afterglow, as well as reversible solid-state emission upon fuming, grinding, and shearing, it is promising for the organic afterglow materials to serve as recording medium of optical recording devices.

Compound **9** has an OURTP lifetime of 0.37 s and a facile transform between four crystal states (1CA, 1CB, 1CC, and 1CD) and an amorphous state (1GP) under different situations upon vapor fuming and mechanical stimuli. To take advantages of this mechanochromic luminescence mechanism, an application of optical recording was succeeded in using compound **9** (Fig. 5.5a). Under the UV irradiation, blue fluorescence was observed after grinding component **9** on a filter paper owing to the amorphous solid feature (1GP). After fuming with chloroform for 1 min, phase transition from amorphous to crystal state (1CA) occurs followed by color change from blue to deep blue. On this deep-blue background, characters “Learn” can be written with mechanical stimuli to reverse the 1CA to 1GP. The blue amorphous “Learn” can transform to blue-greenish at 1CB crystal state after a fast fuming (0.5 min) of acetone, without changing the deep-blue background. Thus, more words can be recorded in amorphous 1GP state with blue emission under UV light. Moreover, chloroform fuming treatment for 5 min can erase all the characters in different colors by phase transition to 1CA for the background deep-blue emission.

Another OURTP molecule of compound **8** was also applicable in optical recording based on the reversible phosphorescence-to-fluorescence switching in response to the mechanical stimulus (Fig. 5.5b) [43]. The pink OURTP emission of **8** with a lifetime of 0.54 s can be suppressed by grinding to make the compound amorphous with enhanced intramolecular free rotation and vibration motion, leading to reduced OURTP with dominated blue fluorescence. But, when the grinding was stopped, the luminescence color changes after several minutes due to the combined luminescence containing both fluorescences (430 nm) from the amorphous state and OURTP

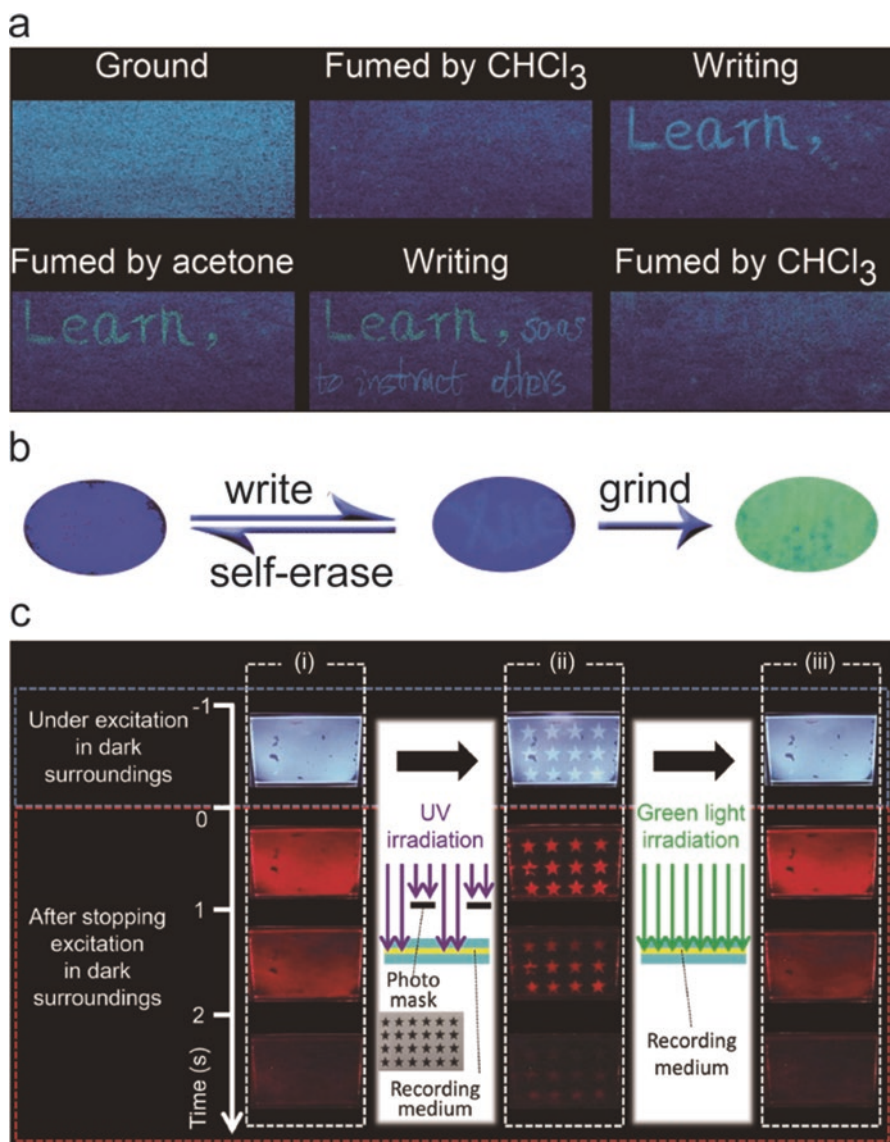


**Fig. 5.5** Applications of organic afterglow materials in optical recording. (a) The smart emissive paper based on switchable PL of compound **9**; [43] (b) The self-erased behavior and shear sensitive emission of compound **8**; [44] (c) Photo-reversible on-off OURTP patterning using H1, G2, and a photochromic molecule [49]

(550 nm) from crystals after aging. Therefore, the word “Xue” with blue emission can be observed by writing with a stainless pin on the surface of compound **8** deposited on a filter paper. The mechanical stimulus turns the partly crystallized purple-red emissive powder to amorphous for blue fluorescence. This optical recording can

be only observed within 1 min owing to the quick aggregation transformation of the compound to form crystals. However, strong shearing of the powder on the filter paper leads to strong blue-green emission, possibly attributed to hydrogen-bonding formation between the OURTP compound and the hydroxyl groups on the filter surface.

A photo-reversible on-off recording can be also constructed by using a multi-component host-guest OURTP material system containing an hydroxyl steroidal host, a photochromic guest as an acceptor, and a red aromatic phosphorescent guest as a donor (Fig. 5.5c). The red OURTP of compound G2 was observed over the whole area for a few seconds after removing the UV irradiation of 385 nm. After 320 nm radiation through a photomask to excite the photochromic guest for dipole-dipole energy transfer from  $S_1$  and  $T_1$  of the OURTP donor (compound G2) to the  $S_1$  of the closed form of the photochromic guest, the OURTP molecules close to the photochromized guest is quenched, leading to a red OURTP image that can be observed for a few seconds after ceasing the excitation source. An overall irradiation of 540 nm to turn the photochromic guest in open form can lead to the elimination of recorded OURTP image by minimizing the energy transfer from the excited OURTP donor to photochromic guest in open form. By cycling the UV and green light irradiation alternately, the optical recording of on-off reversible OURTP images has been successfully realized.

### 5.3.4 Sensors

Organic afterglow is sensitive to external stimuli, which enables organic afterglow materials to act as efficient sensors for these stimuli. Oxygen can quench phosphorescence efficiently by deactivating triplet excitation through collision with triplet oxygen at ground state. Therefore, OURTP luminophores can be designed as reversible, highly sensitive and selective oxygen sensors at room temperature. In addition, the much longer lifetime of afterglow emission than the traditional rare-metal complex phosphors makes it possible to realize not only intensity-resolved but also lifetime-resolved real-time oxygen sensing.

Thanks to the dual emission of organic afterglow materials containing both oxygen-stable fluorescence and oxygen-sensitive phosphorescence with large stokes shift between them for obvious color change before and after contacting oxygen molecules, organic afterglow materials based on difluoroboron  $\beta$ -diketone (P1, P2, and P3) can provide real-time imaging of oxygen concentration in a dynamic environment by determining the lifetime of pixels. Further, these organic afterglow materials can be also designed as biological oxygen sensors by introducing heavy atoms for enhanced spin-orbit coupling. For example, the iodine-substituted P3 (P3-I) with increased OURTP quantum efficiency shows clear green fluorescence and orange phosphorescence; when P3-I nanoparticles were taken by T41 mouse mammary cells, excellent ratiometric oxygen sensor as lifetime-based

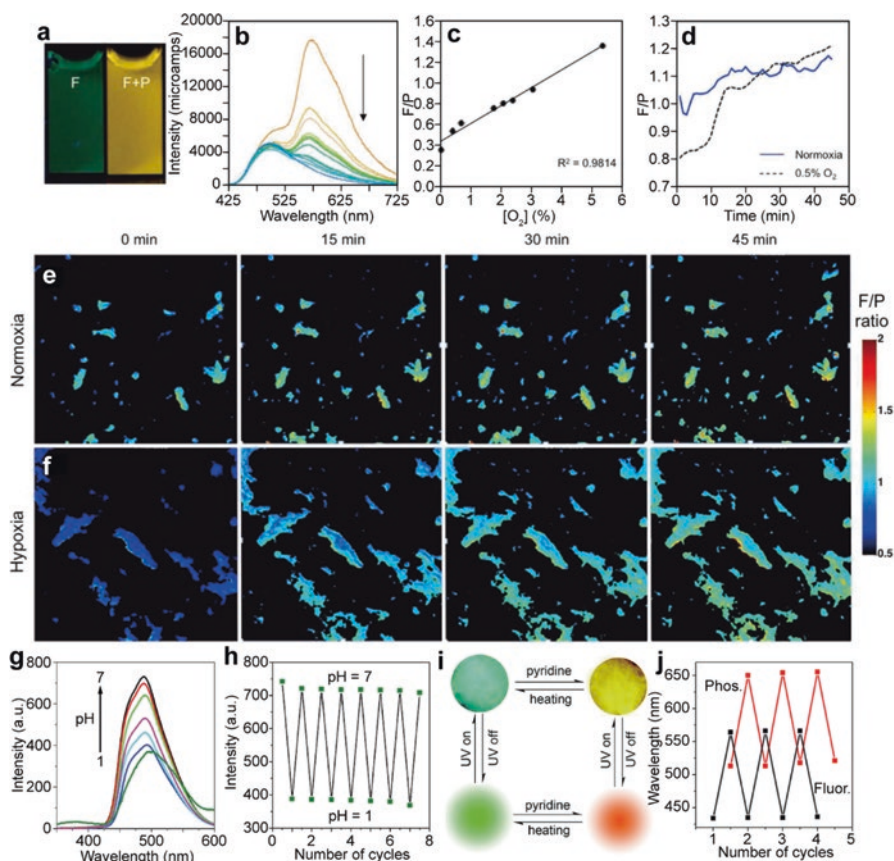


**Fig. 5.6** Applications of organic afterglow materials in oxygen, pH, and solvent sensors. (a) Fluorescence (F) and phosphorescence (P) images of **P3-I** nanoparticle in air (F) and  $N_2$  (F + P) ( $\lambda_{ex} = 354$  nm) [55]. (b) Total emission spectra of **P3-I** nanoparticle at increased  $O_2$  levels from 0% to 21%. (c) Fluorescence intensity (505 nm) over phosphorescence intensity (565 nm) (F/P) calibration plot showing a linear fit in the 0–5.3%  $O_2$  range. (d) QuadView microscope quantification of F/P intensity ratio monitored for 45 min. (e) QuadView microscope images of **P3-I** within 4T1 cells under normoxia (air; ambient). (f) QuadView microscope images of the hypoxia (0.5%  $O_2$ ) to normoxia transition. (g) Afterglow spectra of **Zn-IPA** detected in different pH values; [65] (h) Reversible variation of the afterglow response upon alternation between pH 7 and 1. (i) **MOF-5** crystal image under fluorescence microscopy before and after treatment with a solvent of pyridine (up) and schematic representation of the tunable afterglow emission under the heating and pyridine reabsorption process [66]. (j) Reversible variation of fluorescence (Fluor.) and afterglow phosphorescence (Phos.) emission wavelengths between the desolvation and solvent reabsorption process of **MOF-5**

sensors for gated emission detection of intracellular oxygen levels has been realized (Fig. 5.6a-f).

MOF-based afterglow materials are sensitive to pH and solvent because these environmental variations can change the MOF structure for varied luminescent



behaviors. The rigid Zn-IPA MOF exhibits a reversible afterglow mission under alternating acid conditions from pH = 1 to pH = 7; weaker afterglow emission is observed under acid condition (pH = 1) due to the diminished coordination between  $\text{Zn}^{2+}$  and oxygen in carboxylic group by increased interactions between  $\text{H}^+$  and oxygen atoms (Fig. 5.6g-h). In the case of dynamic MOFs of MOF-5, solvent molecules can potentially be a guest in its nanochannel, resulting in varied host-guest interactions and guest-induced structural transformation for tunable afterglow emission from green to red. This color tuning is reversible; the green afterglow recovers when the absorbed solvents were removed from the MOFs (Fig. 5.6i-j).

### 5.3.5 Bioimaging

Luminescence bioimaging offers a unique approach for visualizing morphological details of tissues with subcellular resolution for the investigation of microspecies from living cells. The background fluorescence of the tissues may disturb the fluorescent bioimaging significantly, leading to reduced imaging resolutions and faked signals. The long-lived phosphorescence can be easily distinguished from background fluorescence and scattered light, which is a beneficial property for bioimaging. Most reported bioimaging phosphorescent probes are based on Ir(III) complexes, which are expensive and environmentally unfriendly. Moreover, relatively short luminescence lifetimes of microseconds restrict the further extending of signal-to-noise ratio. The ideal materials for bioimaging should have simple structure as well as much longer emission lifetime in ambient conditions.

Compared to the well-developed fluorescent and phosphorescence bioimaging, afterglow emission with persistent luminescence has been rarely used for imaging applications, although the long lifetime of the afterglow is highly appalusive to better separate the short-lived autofluorescence ( $\sim\text{ns}$ ) from target fluorescence signal via time-resolved luminescence measurements. In addition, persistent luminescence of afterglow should last for minutes even hours after removing the light source, allowing for distinguishing signal from the background without the need of additional instrumentation. Therefore, similar to the nanoparticles fabricated by inorganic counterparts reported for *in vivo* imaging, organic afterglow materials are very attractive in bioimaging such as low toxicity for high biocompatibility [72].

Rao et al. reported that MEH-PPV nanoparticles can emit afterglow emission (500–700 nm) lasting for an hour after single excitation [36]. They further encapsulated a near-infrared dye (NIR775) in the MEH-PPV nanoparticle to design a persistent near-infrared luminescence through resonance energy transfer from the organic afterglow polymer to the near-infrared dye. The persistent luminescence spectrum closely resembles the steady-state fluorescence emission spectrum with a broad emission (500–700 nm) originated from the MEH-PPV and a sharp peak at 780 nm corresponding to the NIR775 dye. The *in vivo* imaging was performed by subcutaneous injection of the NIR775-doped MEH-PPV nanoparticles (excited with a white light) on the back of anesthetized mice (Fig. 5.7). The animal imaging

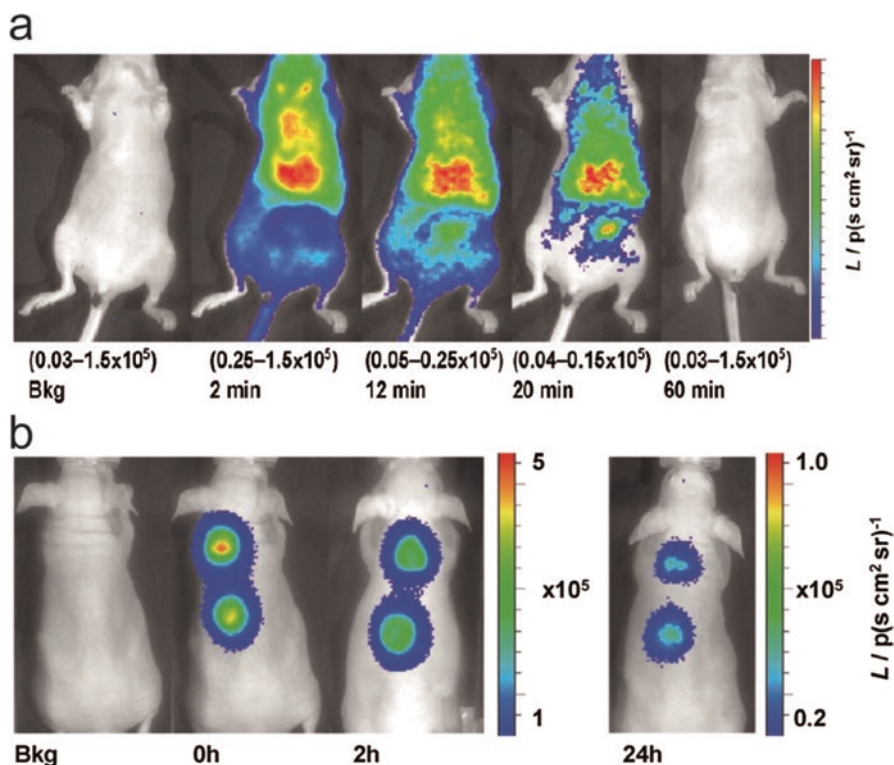


**Fig. 5.7** In vivo bioimaging using MEH-PPV organic afterglow nanoparticles. Images of a mouse before (Bkg) and after intravenous injection of excited nanoparticles and imaged (a) at 2, 12, 20, and 60 min as well as (b) at 2 and 24 h (the subcutaneous injection site was exposed to white light for 3 min before the collection of afterglow emission); the *number in brackets* indicates the intensity scale of the images

was performed in the absence of excitation source. A maximum radiance was observed immediately after the injection, and the continuously imaged afterglow emission shows that there is an initial high uptake of nanoparticles in the heart and liver with much improved signal-to-noise ratio in comparison to fluorescence imaging. Moreover, the injected nanoparticles can be re-excited by exposure of the animal under an excitation source. Only a small decrease in emission intensity can be observed after 2 h of the injection. Further decrease can be discovered after 24 h, which can be ascribed to the metabolism of the nanoparticles (Fig. 5.7).

## 5.4 Concluding Remarks

The significant breakthrough in lifetime tuning of the excited states of organic molecules at ambient conditions has posed and will continuously pose profound impacts on the development of organic electronics. The significantly elongated OURTP



**Table 5.1** Structural and photophysical properties of organic afterglow materials<sup>a</sup>

Compound	Formula/doping density	Fluorescence			Organic afterglow			Ref.
		$\lambda$ (nm)	$\tau$ (ns)	$\eta$ (%)	$\lambda$ (nm)	$\tau$ (s)	$\eta$ (%)	
<b>1</b>	C <sub>10</sub> H <sub>14</sub> O <sub>2</sub>	332	2.8	9.1	515, 547	0.71, 0.69	0.3	[12]
<b>2</b>	C <sub>19</sub> H <sub>18</sub> N <sub>4</sub> O <sub>2</sub>	393	5.5	20.5	529, 574	1.28, 1.35	0.6	[12]
<b>3</b>	C <sub>27</sub> H <sub>18</sub> N <sub>4</sub>	440	4.4	4.4	530, 575	1.06, 1.05	1.3	[12]
<b>4</b>	C <sub>15</sub> H <sub>8</sub> Cl <sub>2</sub> N <sub>4</sub>	408	2.0	13.1	543, 591	0.47, 0.49	2.1	[12]
<b>5</b>	C <sub>30</sub> H <sub>21</sub> N <sub>2</sub> P	406	6.6	4.9	587, 644	0.21, 0.29	0.1	[12]
<b>6</b>	C <sub>8</sub> H <sub>6</sub> O <sub>4</sub>	380	1.8	–	506	0.29	–	[73]
<b>6</b>	C <sub>8</sub> H <sub>6</sub> O <sub>4</sub>	356	–	–	497	0.63	3.3	[65]
<b>7</b>	C <sub>9</sub> H <sub>6</sub> O <sub>6</sub>	384	–	–	524	0.15	2.2	[65]
<b>8</b>	C <sub>19</sub> H <sub>13</sub> NO	439	1.9	28.0 <sup>b</sup>	550	0.54	–	[44]
<b>9</b>	C <sub>37</sub> H <sub>24</sub> N <sub>2</sub> O	430	–	1.0	553, 600	0.37, 0.37	–	[43]
<b>10</b>	C <sub>25</sub> H <sub>17</sub> NO	436	3.5	12.3	552, 569	0.52	1.4	[42]
<b>10</b>	C <sub>25</sub> H <sub>17</sub> NO	431	2.5	–	570, 624	0.48, 0.47	–	[41]
<b>11</b>	C <sub>25</sub> H <sub>16</sub> BrNO	421	0.3, 1.6	–	549, 602	0.29, 0.28	5.0	[41]
<b>12</b>	C <sub>14</sub> H <sub>12</sub> BrN	407	3.4	1.1	544	0.16	1.6	[45]
<b>13</b>	C <sub>22</sub> H <sub>20</sub> BrNO	373, 415	4.8, 9.7	26.1	555	0.34	9.5	[45]
<b>14</b>	C <sub>23</sub> H <sub>22</sub> BrNO	373, 414	1.6, 4.0	8.4	555	0.20	2.8	[45]
<b>15</b>	C <sub>24</sub> H <sub>24</sub> BrNO	376, 420	3.9, 11.7	33.1	554	0.20	39.5	[45]
<b>16</b>	C <sub>24</sub> H <sub>17</sub> NO <sub>2</sub> S	410	8.3	–	562	0.39	–	[41]
<b>17</b>	C <sub>24</sub> H <sub>16</sub> BrNO <sub>2</sub> S	410	2.7	–	558	0.12	6.0	[41]
<b>18</b>	C <sub>19</sub> H <sub>13</sub> NO	445	1.4	–	530	0.75	–	[46]
<b>19</b>	C <sub>20</sub> H <sub>15</sub> NO	442	1.1	–	540	0.34	–	[46]
<b>20</b>	C <sub>20</sub> H <sub>15</sub> NO <sub>2</sub>	425	0.4	–	545	0.11	–	[46]
<b>21</b>	C <sub>6</sub> H <sub>7</sub> BO <sub>2</sub>	325	0.5 s	–	482	1.20	–	[47]
<b>22</b>	C <sub>6</sub> H <sub>8</sub> B <sub>2</sub> O <sub>4</sub>	329	0.4 s	–	494	0.95	–	[47]
<b>23</b>	C <sub>12</sub> H <sub>17</sub> BO <sub>2</sub>	290	–	–	465	1.79		[10]
<b>24</b>	C <sub>13</sub> H <sub>19</sub> BO <sub>3</sub>	298	–	–	502	1.39		[10]
<b>25</b>	C <sub>13</sub> H <sub>16</sub> BNO <sub>2</sub>	306	–	–	519	0.44		[10]
<b>26</b>	C <sub>8</sub> H <sub>8</sub> BFO <sub>2</sub>	370	0.9 s	–	488	1.70		[47]
<b>27</b>	C <sub>8</sub> H <sub>8</sub> BClO <sub>2</sub>	339	0.1 s	–	498	0.25		[47]
<b>28</b>	C <sub>8</sub> H <sub>8</sub> BrO <sub>2</sub>	331	–	–	501	0.18		[47]

(continued)

**Table 5.1** (continued)

Compound	Formula/doping density	Fluorescence			Organic afterglow			Ref.
		$\lambda$ (nm)	$\tau$ (ns)	$\eta$ (%)	$\lambda$ (nm)	$\tau$ (s)	$\eta$ (%)	
<b>29</b>	C <sub>10</sub> H <sub>12</sub> B <sub>2</sub> O <sub>4</sub>	329	0.6 s	—	503	1.60	—	[47]
<b>29</b>	C <sub>10</sub> H <sub>12</sub> B <sub>2</sub> O <sub>4</sub>	316	—	—	471, 506	1.65	—	[10]
<b>30</b>	C <sub>14</sub> H <sub>24</sub> B <sub>2</sub> N <sub>4</sub>	400	—	—	457	0.79	—	[10]
<b>31</b>	C <sub>18</sub> H <sub>28</sub> B <sub>2</sub> O <sub>4</sub>	305	—	—	460, 500	1.85	—	[10]
<b>32</b>	C <sub>18</sub> H <sub>26</sub> B <sub>2</sub> F <sub>2</sub> O <sub>4</sub>	351	—	—	507	0.56	—	[10]
<b>33</b>	C <sub>24</sub> H <sub>32</sub> B <sub>2</sub> O <sub>4</sub>	343	—	—	536	0.20	—	[10]
<b>34</b>	C <sub>18</sub> H <sub>28</sub> B <sub>2</sub> O <sub>4</sub>	302	—	—	500	1.73	—	[10]
<b>35</b>	C <sub>18</sub> H <sub>28</sub> B <sub>2</sub> O <sub>4</sub>	297	—	—	469, 500	1.57	—	[10]
<b>36</b>	C <sub>19</sub> H <sub>30</sub> B <sub>2</sub> O <sub>4</sub>	305	—	—	452, 478	0.49	—	[10]
<b>37</b>	C <sub>19</sub> H <sub>30</sub> B <sub>2</sub> O <sub>5</sub>	329	—	—	480	0.69	—	[10]
<b>38</b>	C <sub>19</sub> H <sub>27</sub> B <sub>2</sub> NO <sub>4</sub>	306	—	—	449, 473	0.42	—	[10]
<b>39</b>	C <sub>18</sub> H <sub>15</sub> B <sub>3</sub> O <sub>3</sub>	302	—	—	461, 495	0.46	—	[10]
<b>PMMA/G5-h<sub>12</sub></b>	99.4%/0.6%	—	—	10.6	—	5.58	1.7	[11]
<b>H2/G1/THEB<sup>c</sup></b>	90%/1%/9%	365	—	19.1	480	1.40	3.1	[74]
<b>H1/G2</b>	99%/1%	—	—	—	—	1.12	5.3	[49]
<b>H1/R-G6<sup>d</sup></b>	99.7%/0.3%	420	6.0	30.0	560	0.67	2.3	[50]
<b>H1/G7</b>	99.7%/0.3%	450–550	—	6.7	450–800	3.90	2.6	[75]
<b>H3/G4</b>	99%/1%	450	—	18.7	570	4.70, 4.30 <sup>e</sup>	5.3	[51]
<b>H3/G5</b>	99%/1%	400	—	36.2	515	0.61, 0.39 <sup>e</sup>	4.1	[51]
<b>PMMA/G8</b>	99.5%/0.5%	—	—	—	541	0.23	3.1	[52]
<b>PMMA/G9</b>	99.5%/0.5%	—	—	—	541	0.23	3.9	[52]
<b>H1/G3</b>	97%/3%	—	—	—	405	1.05	18 <sup>f</sup>	[48]
<b>H1/D1/A2</b>	94%/5%/1%	—	—	—	500	0.46	41 <sup>f</sup>	[48]
<b>H1/D2/A3</b>	94%/5%/1%	—	—	—	444	1.39	44 <sup>f</sup>	[48]
<b>H1/D3/A6</b>	94%/5%/1%	—	—	—	468	0.67	36 <sup>f</sup>	[48]
<b>H1/D2/A5</b>	94%/5%/1%	—	—	—	405	1.40	36 <sup>f</sup>	[48]
	96%/3%/1%	—	—	—	405	1.65	25 <sup>f</sup>	[48]
<b>H1/D2/A1</b>	96%/3%/1%	—	—	—	405	2.77	27 <sup>f</sup>	[48]
<b>H1/D2/A4</b>	96%/3%/1%	—	—	—	405	0.49	25 <sup>f</sup>	[48]
<b>H1/D4/A5</b>	96%/3%/1%	—	—	—	405	1.38	22 <sup>f</sup>	[48]
<b>PVA/CDs</b>	—	400	—	—	500	0.38	—	[38]
<b>PVA/m-CDs</b>	—	420	6.4	—	506	0.46	—	[63]
<b>PA/CDs</b>	—	408, 480	—	—	500	0.66	—	[37]

(continued)

**Table 5.1** (continued)

Compound	Formula/doping density	Fluorescence			Organic afterglow			Ref.
		$\lambda$ (nm)	$\tau$ (ns)	$\eta$ (%)	$\lambda$ (nm)	$\tau$ (s)	$\eta$ (%)	
<b>PVA/ACDs</b>	85%/15%	375	6.8	–	375, 450	0.23, 0.45	–	[64]
<b>Urea/HN-CDs</b>	–	–	9.5	29.0	490	0.93	7.0	[62]
<b>Urea/MN-CDs</b>	–	–	14.4	–	490	0.64	–	[62]
<b>Urea/LN-CDs</b>	–	–	17.4	–	490	0.62	0.4	[62]
<b>H4/C1</b>	99.5%/0.5%	422	–	–	491	0.40	–	[67]
<b>C2</b>	–	452	14.0	–	500	0.22	–	[67]
<b>H4/C3</b>	99.9%/0.1%	415	–	–	557	0.11	–	[68]
	99%/1%	433	1.0	–	555	0.11	–	[68]
<b>H4/C4</b>	99.9%/0.1%	433	1.1	–	572	0.14	–	[68]
	99%/1%	448	1.3	–	576	0.12	–	[68]
	98%/2%	457	1.2	–	572	0.11	–	[68]
<b>P1</b>	Mn = 8.8 kDa	440	1.2, 4.4	–	509	0.17	–	[53]
<b>P2</b>	Mn = 7.7 kDa	496	8.8	–	555	0.10	–	[54]
<b>P2</b>	Mn = 16.1 kDa	461	2.6	–	552	0.13	–	[54]
<b>P3</b>	Mn = 31.8 kDa	494	7.1	–	509	0.16	–	[55]
<b>P3b</b>	1% <sup>e</sup>	484	3.3	–	499	0.38	–	[55]
<b>P4</b>	Mn = 18.6 kDa	446	3.5	–	518	0.27	–	[56]
<b>P5</b>	Mn = 11.1 kDa	450	4.1	–	522	0.11	–	[56]
	Mn = 15.0 kDa	446	3.8	–	527	0.15	–	[56]
<b>P6</b>	Mn = 12.8 kDa	–	–	–	510	1.20	3.9	[52]
<b>Zn-TPA</b>	C <sub>8</sub> H <sub>8</sub> ZnO <sub>6</sub>	360	–	–	508	0.48	3.4	[65]
<b>Zn-11</b>	C <sub>16</sub> H <sub>8</sub> Zn <sub>2</sub> O <sub>8</sub>	387	–	–	484	1.32	3.4	[65]
<b>Zn-12</b>	C <sub>27</sub> H <sub>21</sub> Zn <sub>3</sub> O <sub>26</sub>	334	–	–	533	0.20	2.7	[65]
<b>Cd-TPA</b>	C <sub>25</sub> H <sub>29</sub> Cd <sub>2</sub> N <sub>3</sub> O <sub>11</sub>	340	–	–	497	0.16	–	[65]
<b>Cd-11</b>	C <sub>11</sub> H <sub>11</sub> CdNO <sub>5</sub>	363	–	–	489	0.32	–	[65]
<b>1-DMF</b>	C <sub>11</sub> H <sub>6</sub> ZnNO <sub>5</sub>	326	–	2.2	503	0.47	4.8	[66]
<b>MOF-5</b>	C <sub>11</sub> H <sub>6</sub> ZnNO <sub>5</sub>	434	–	46.3	513	0.15	0.2	[66]
<b>G5@ZIF-8</b>	–	–	–	10.1	–	22.40	3.7	[11]
<b>G5-h<sub>12</sub>@ZIF-8</b>	–	427–506	25.0	8.7	509–610	7.40	1.8	[11]
<b>CP1</b>	–	392	–	4.1	514	0.70	2.1	[76]
<b>CP2</b>	–	396	–	4.3	514	0.76	3.1	[76]

<sup>a</sup>The emission peaks ( $\lambda$ ), lifetimes ( $\tau$ ), and quantum yields ( $\eta$ ) of the fluorescence and OA of the organic afterglow materials in solid state

<sup>b</sup>In solution

<sup>c</sup>THEB refers to  $\alpha, \alpha', \alpha''$ -tris(4-hydroxyphenyl)-1-ethyl-4-isopropylbenzene

<sup>d</sup>G6 in R-configuration

<sup>e</sup>Lifetime of electroluminescence

<sup>f</sup>Integration of phosphorescence yield of the donor and energy transfer from the T<sub>1</sub> state of the donor to the ground state of the acceptor

<sup>g</sup>Blends prepared by P3 and PLA in order to achieve 1% dye loading

emission from organic afterglow materials exhibits luminescent lifetime up to seconds, which are eight and three orders of magnitude longer than conventional fluorescence and phosphorescence, respectively. This amazing extension of emission lifetime in organic materials is promising for a large variety of applications in numerous fields. At the current stage of the initial study, the organic afterglow materials have already been successfully applied in OLEDs, document security with anti-counterfeiting, optical recording, sensors, and bioimaging based on either single-component, multicomponent small molecules, MOFs, or polymers. Although the luminescent intensity and efficiency of organic afterglow are still relatively low and the number of available materials is rather limited, these advances are important for not only updating the photophysical understandings and material engineering principles of organic optoelectronic materials, but also providing important clues to revolutionize the present study of organic semiconductors and their applications, leading to the rise of a new generation of organic optoelectronic materials and afterglow materials (Table 5.1).

## References

1. Ostroverkhova, O.: Organic optoelectronic materials: mechanisms and applications. *Chem. Rev.* **116**, 13279 (2016)
2. Wang, K., Liu, C., Meng, T., Yi, C., Gong, X.: Inverted organic photovoltaic cells. *Chem. Soc. Rev.* **45**, 2937 (2016)
3. Kim, S., Kwon, H.J., Lee, S., Shim, H., Chun, Y., Choi, W., Kwack, J., Han, D., Song, M., Kim, S., Mohammadi, S., Kee, I., Lee, S.Y.: Low-power flexible organic light-emitting diode display device. *Adv. Mater.* **23**, 3511 (2011)
4. Tao, Y., Xu, L., Zhang, Z., Chen, R., Li, H., Xu, H., Zheng, C., Huang, W.: Achieving optimal self-Adaptivity for dynamic tuning of organic semiconductors through resonance engineering. *J. Am. Chem. Soc.* **138**, 9655 (2016)
5. Tao, Y., Guo, X., Hao, L., Chen, R., Li, H., Chen, Y., Zhang, X., Lai, W., Huang, W.: A solution-processed resonance host for highly efficient Electrophosphorescent devices with extremely low efficiency roll-off. *Adv. Mater.* **27**, 6939 (2015)
6. Lower, S.K., El-Sayed, M.A.: The triplet state and molecular electronic processes in organic molecules. *Chem. Rev.* **66**, 199 (1966)
7. Horie, K., Mita, I.: Photochemistry in polymer solids. Decay of benzophenone phosphorescence in poly(methyl methacrylate). *Chem. Phys. Lett.* **93**, 61 (1982)
8. Horie, K., et al.: Photochemistry in polymer solids. 3. Kinetics for Nonexponential decay of benzophenone phosphorescence in acrylic and Methacrylic polymers. *Macromolecules.* **17**, 1746 (1984)
9. Xu, S., et al.: Excited state modulation for organic afterglow: materials and applications. *Adv. Mater.* **28**, 9920 (2016)
10. Shoji, Y., Ikabata, Y., Wang, Q., Nemoto, D., Sakamoto, A., Tanaka, N., Seino, J., Nakai, H., Fukushima, T.: Unveiling a new aspect of simple Arylboronic esters: long-lived room-temperature phosphorescence from the heavy Atom-free molecules. *J. Am. Chem. Soc.* **139**, 2728 (2017)
11. Mieno, H., et al.: Long-lived room-temperature phosphorescence of Coronene in Zeolitic Imidazolate framework ZIF-8. *Adv. Opt. Mater.* **4**, 1015 (2016)
12. An, Z., et al.: Stabilizing triplet excited states for Ultralong organic phosphorescence. *Nat. Mater.* **14**, 685 (2015)

13. Yuan, J., et al.: Purely organic optoelectronic materials with ultralong-lived excited states under ambient conditions. *Chn. Sci. Bull.* **60**, 1631 (2015)
14. Qin, X., et al.: Lanthanide-activated phosphors based on 4f-5d optical transitions: theoretical and experimental aspects. *Chem. Rev.* **117**, 4488 (2017)
15. Baldo, M.A., et al.: Excitonic singlet-triplet ratio in a semiconducting organic thin film. *Phys. Rev. B*, **60**, 14422 (1999)
16. Kasha, M.: Phosphorescence and the role of the triplet state in the electronic excitation of complex molecules. *Chem. Rev.* **41**, 401 (1947)
17. Chen, R.F., et al.: Fluorescence decay times: proteins, coenzymes, and other compounds in water. *Science*, **156**, 949 (1967)
18. Huang, W., et al.: *Organic Electronics*. Science Press, China (2011)
19. Kenkre, V.M., et al.: Effect of transport coherence on trapping-quantum-yield calculations for excitons in molecular-crystals. *Phys. Rev. B*, **23**, 3748 (1981)
20. Butler, W.L., et al.: Lifetime of the long-wavelength chlorophyll fluorescence. *Biochim. Biophys. Acta*, **66**, 72 (1963)
21. El-Sayed, M.A., et al.: Intramolecular heavy-Atom effect on the polarization of naphthalene phosphorescence. *J. Chem. Phys.* **39**, 1899 (1963)
22. Adachi, C., et al.: Nearly 100% internal phosphorescence efficiency in an organic light-emitting device. *J. Appl. Phys.* **90**, 5048 (2001)
23. Ma, Y.G., et al.: Electroluminescence from triplet metal-ligand charge-transfer excited state of transition metal complexes. *Synth. Met.* **94**, 245 (1998)
24. Baldo, M.A., et al.: Highly efficient phosphorescent emission from organic electroluminescent devices. *Nature*, **395**, 151 (1998)
25. Endo, A., et al.: Thermally activated delayed fluorescence from  $\text{Sn}^{4+}$ -porphyrin complexes and their application to organic light-emitting diodes-a novel mechanism for electroluminescence. *Adv. Mater.* **21**, 4802 (2009)
26. Tao, Y., et al.: Thermally activated delayed fluorescence materials towards the breakthrough of organoelectronics. *Adv. Mater.* **26**, 7931 (2014)
27. Endo, A., et al.: Efficient up-conversion of triplet excitons into a singlet state and its application for organic light emitting diodes. *Appl. Phys. Lett.* **98**, 83302 (2011)
28. Goushi, K., et al.: Organic light-emitting diodes employing efficient reverse intersystem crossing for triplet-to-singlet state conversion. *Nat. Photon.* **6**, 253 (2012)
29. Yang, Z., et al.: Recent advances in organic thermally activated delayed fluorescence materials. *Chem. Soc. Rev.* **46**, 915 (2017)
30. Li, W., et al.: Employing similar to 100% excitons in OLEDs by utilizing a fluorescent molecule with hybridized local and ChargeTransfer excited state. *Adv. Funct. Mater.* **24**, 1609 (2014)
31. Pan, Y., et al.: High yields of singlet excitons in organic electroluminescence through two paths of cold and hot excitons. *Adv. Opt. Mater.* **2**, 510 (2014)
32. Krishna, V.G.: Delayed fluorescence due to triplet-triplet annihilation: a theoretical study. *J. Chem. Phys.* **46**, 1735 (1967)
33. Parker, C.A., et al.: Delayed fluorescence from solutions of anthracene and phenanthrene. *Proc. R. Soc. A*, **269**, 574 (1962)
34. Hirata, S., et al.: Efficient persistent room temperature phosphorescence in organic amorphous materials under ambient conditions. *Adv. Funct. Mater.* **23**, 3386 (2013)
35. Kuno, S., et al.: Visible room-temperature phosphorescence of pure organic crystals via a radical-ion-pair mechanism. *Phys. Chem. Chem. Phys.* **17**, 15989 (2015)
36. Palner, M., et al.: Semiconducting polymer nanoparticles with persistent near-infrared luminescence for in vivo optical imaging. *Angew. Chem. Int. Edit.* **54**, 11477 (2015)
37. Dong, X., et al.: Efficient long lifetime room temperature phosphorescence of carbon dots in a potash alum matrix. *J. Mater. Chem. C*, **3**, 2798 (2015)
38. Deng, Y., et al.: Long lifetime pure organic phosphorescence based on water soluble carbon dots. *Chem. Commun.* **49**, 5751 (2013)

39. Yuan, W.Z., et al.: Crystallization-induced phosphorescence of pure organic luminogens at room temperature. *J. Phys. Chem. C*. **114**, 6090 (2010)
40. Hong, Y., et al.: Aggregation-induced emission. *Chem. Soc. Rev.* **40**, 5361 (2011)
41. Yang, Z., et al.: Intermolecular electronic coupling of organic units for efficient persistent room-temperature phosphorescence. *Angew. Chem. Int. Edit.* **55**, 2181 (2016)
42. Gong, Y., et al.: Achieving persistent room temperature phosphorescence and remarkable mechanochromism from pure organic Luminogens. *Adv. Mater.* **27**, 6195 (2015)
43. Li, C., et al.: Reversible luminescence switching of an organic solid: controllable on-off persistent room temperature phosphorescence and stimulated multiple fluorescence conversion. *Adv. Opt. Mater.* **3**, 1184 (2015)
44. Xue, P., et al.: Luminescence switching of a persistent room-temperature phosphorescent pure organic molecule in response to external stimuli. *Chem. Commun.* **51**, 10381 (2015)
45. Xue, P., et al.: Bright persistent luminescence from pure organic molecules through a moderate intermolecular heavy atom effect. *Chem. Sci.* (2016). doi:[10.1039/C5SC03739E](https://doi.org/10.1039/C5SC03739E)
46. Xie, Y., Ge, Y., Peng, Q., Li, C., Li, Q., Li, Z.: How the molecular packing affects the room temperature phosphorescence in pure organic compounds: ingenious molecular design, detailed crystal analysis, and rational theoretical calculations. *Adv. Mater.* (2017). doi:[10.1002/adma.201606829](https://doi.org/10.1002/adma.201606829)
47. Kuno, S., et al.: Long persistent phosphorescence of crystalline phenylboronic acid derivatives: photophysics and a mechanistic study. *ChemPhotoChem.* **1**, 102 (2017)
48. Hirata, S., et al.: Large reverse saturable absorption under weak continuous incoherent light. *Nat. Mater.* **13**, 938 (2014)
49. Katsurada, Y., et al.: Photoreversible on-off recording of persistent room-temperature phosphorescence. *Adv. Opt. Mater.* **3**, 1726 (2015)
50. Hirata, S., et al.: Circularly polarized persistent room-temperature phosphorescence from metal-free chiral aromatics in air. *J. Phys. Chem. Lett.* **7**, 1539 (2016)
51. Kabe, R., et al.: Afterglow organic light-emitting diode. *Adv. Mater.* **28**, 655 (2016)
52. Chen, X., et al.: Versatile room-temperature-phosphorescent materials prepared from N-substituted Naphthalimides: Emission enhancement and chemical conjugation. *Angew. Chem. Int. Edit.* **55**, 9872 (2016)
53. Zhang, G., et al.: Multi-emissive difluoroboron dibenzoylmethane polylactide exhibiting intense fluorescence and oxygen-sensitive room-temperature phosphorescence. *J. Am. Chem. Soc.* **129**, 8942 (2007)
54. Samonina-Kosicka, J., et al.: Dual-emissive difluoroboron naphthyl-phenyl beta-diketonate polylactide materials: effects of heavy atom placement and polymer molecular weight. *Macromolecules.* **47**, 3736 (2014)
55. DeRosa, C.A., et al.: Oxygen sensing difluoroboron dinaphthoylmethane polylactide. *Macromolecules.* **48**, 2967 (2015)
56. Zhang, G., et al.: Difluoroboron dibenzoylmethane PCL-PLA block copolymers: matrix effects on room temperature phosphorescence. *Macromolecules.* **42**, 3162 (2009)
57. Al-Attar, H.A., et al.: Room-temperature phosphorescence from films of isolated water-soluble conjugated polymers in hydrogen-bonded matrices. *Adv. Funct. Mater.* **22**, 3824 (2012)
58. Deng, J., et al.: Electrochemical synthesis of carbon Nanodots directly from alcohols. *Chem-Eur. J.* **20**, 4993 (2014)
59. Zhou, L., et al.: Carbon nanodots as fluorescence probes for rapid, sensitive, and label-free detection of Hg<sup>2+</sup> and biothiols in complex matrices. *Chem. Commun.* **48**, 1147 (2012)
60. Zhang, Y., et al.: Graphitic carbon quantum dots as a fluorescent sensing platform for highly efficient detection of Fe<sup>3+</sup> ions. *RSC Adv.* **3**, 3733 (2013)
61. Sun, Y.P., et al.: Quantum-sized carbon Dots for bright and colorful photoluminescence. *J. Am. Chem. Soc.* **128**, 7756 (2006)
62. Li, Q., et al.: Efficient room-temperature phosphorescence from nitrogen-doped carbon Dots in composite matrices. *Chem. Mater.* **28**, 8221 (2016)
63. Jiang, K., et al.: Triple-mode Emission of carbon Dots: applications for advanced Anti-counterfeiting. *Angew. Chem. Int. Edit.* **55**, 7231 (2016)

64. Tan, J., et al.: Synthesis of amphiphilic carbon quantum Dots with phosphorescence properties and their multifunctional applications. *J. Mater. Chem. C*. **4**, 10146 (2016)
65. Yang, X., et al.: Strongly enhanced long-lived persistent room temperature phosphorescence based on the formation of metal–organic hybrids. *Adv. Opt. Mater.* **4**, 897 (2016)
66. Yang, X., Yan, D.: Long-afterglow metal-organic frameworks: reversible guest-induced phosphorescence tunability. *Chem. Sci.* **7**, 4519 (2016)
67. Zhang, X., et al.: General design strategy for aromatic ketone-based single-component dual-emissive materials. *ACS Appl. Mater. Int.* **6**, 2279 (2014)
68. Kolpaczynska, M., et al.: Thienyl difluoroboron beta-diketones in solution and polylactide media. *Aust. J. Chem.* **69**, 537 (2016)
69. Gather, M.C., et al.: White organic light-emitting diodes. *Adv. Mater.* **23**, 233 (2011)
70. Xu, H., et al.: Recent progress in metal-organic complexes for optoelectronic applications. *Chem. Soc. Rev.* **43**, 3259 (2014)
71. Tao, Y., et al.: Organic host materials for phosphorescent organic light-emitting diodes. *Chem. Soc. Rev.* **40**, 2943 (2011)
72. Kim, J.H., et al.: Bright red-emitting electrophosphorescent device using osmium complex as a triplet emitter. *Appl. Phys. Lett.* **83**, 776 (2003)
73. Gong, Y., et al.: Crystallization-induced dual emission from metal- and heavy atom-free aromatic acids and esters. *Chem. Sci.* **6**, 4438 (2015)
74. Hirata, S., et al.: Reversible thermal recording media using time-dependent persistent room temperature phosphorescence. *Adv. Opt. Mater.* **1**, 438 (2013)
75. Hirata, S., Vacha, M.: White afterglow room-temperature emission from an isolated single aromatic unit under ambient condition. *Adv. Opt. Mater.* **5**, 1600996 (2017)
76. Yang, Y., et al.: Ultralong persistent room temperature phosphorescence of metal coordination polymers exhibiting reversible pH-responsive emission. *ACS Appl. Mater. Int.* **8**, 15489 (2016)



# Index

## A

Absorption, 2, 3, 5, 7, 9, 12, 14, 36, 37, 39, 62, 87–90, 103, 106, 111, 124, 130  
Absorption spectrum, 89  
Activator, 3, 4, 7, 15, 16, 40, 42, 97  
Adachi, C., 129, 136  
Afterglow, 6–18, 21, 22, 24, 25, 28–34, 36–41, 43–51, 58, 60, 62–71, 90, 92–94, 98, 102, 103, 105, 107, 108, 110, 117, 118, 122–144  
Afterglow time, 25, 28, 29  
Alkaline earth nitridosilicates, 32  
Aluminate phosphors, 25, 28, 65  
Anti-counterfeiting, 135–139  
Autofluorescence, 1, 2, 21, 106, 111, 112, 143  
Azamatov, Z.T., 15

## B

Band structure, 7, 8  
Bessière, A., 47  
Bioimaging, 2, 32, 45, 48, 51, 63, 101, 106, 108, 143, 144

## C

$\text{Ca}_2\text{MgSi}_2\text{O}_7$ , 23, 28, 29, 43  
Carbon dots, 125, 132, 136, 138  
Carnall, W.T., 12  
Chang, C., 27  
Chen, I., 66  
Combustion method, 56, 92  
Coordination environment, 9, 25, 27, 42, 65

Crystal field theory (CFT), 10  
Crystal structure, 12, 17, 29, 49, 97, 98

## D

Debye–Scherrer equation, 99  
Decay constant, 94  
Decay curve, 25, 29, 36, 44, 45, 48, 50, 51, 69–71, 76, 119, 137  
Defect, 2, 6–8, 16, 17, 26, 39, 49, 52, 53, 71, 97  
Display, 21, 22, 117

## E

Electric-dipole transition, 25  
Emission, 1–5, 7–10, 12, 14–16, 21, 22, 25–32, 34–42, 45–52, 60–63, 65–67, 72, 73, 76, 87, 88, 90–94, 97, 101, 103, 106–108, 110, 111, 117, 118, 120–122, 124–135, 137, 139–143  
Energy bands, 16, 89  
Energy level, 2, 4, 5, 7–10, 12, 14–16, 24, 36, 47, 68, 90, 91, 97, 120, 124, 126, 128, 132, 137  
Energy transfer, 3, 4, 39, 40, 42, 43, 111, 128, 129, 141, 143  
Excitation spectrum, 32, 37, 39, 41, 46, 48, 49, 62, 87, 110  
excited state, 2–7, 11, 15, 35, 36, 94, 117–122, 124–126, 129

## F

f-f transition, 8, 9, 25, 34  
FRET, 111–113

**H**

H-aggregation, 124–126  
 Hirata, S., 128  
 Hydrothermal method, 57, 60, 108

**I**

Impurities, 2, 6–8, 16, 17, 21, 55, 89, 97  
 In vivo, 2, 21, 48, 54, 67, 73, 74, 106, 108, 113, 143  
 Inorganic host, 7, 8, 42  
 Intersystem crossing, 118, 120, 126, 135

**J**

Jia, D., 36, 47

**L**

Lateral flow assay, 113, 114  
 Lei, B., 42  
 Li, Y.Q., 31  
 Lighting, 22, 101–106, 117, 135, 136, 139  
 Lin, Y., 30, 32  
 Liu, L., 32  
 Liu, Y., 37  
 Lu, X.D., 72  
 Luminescence, 1–7, 12, 14–16, 21, 22, 24–29, 32, 34–38, 40, 42–51, 53, 58, 60, 64–71, 87, 88, 90, 93–95, 97, 101, 102, 106, 108, 110–113, 117–128, 131, 134–136, 139, 143  
 Luminescence decay, 25, 36, 44, 48, 87, 93–95, 97  
 Luminescence material, 2  
 Luminescent Center, 1, 5, 9, 12–16  
 Luminous fiber, 101, 105, 106  
 Luminous paint, 1, 6, 21, 62, 101, 104  
 Luminous watch, 104–105

**M**

Maldiney, T., 67, 108  
 Matsuzawa, T., 6  
 Max von Laue, 97  
 Miyamoto, Y., 32

**N**

NIR-light emitting phosphor, 6, 22, 28, 39, 40, 47  
 Non-radiative deactivation, 122, 123, 125, 129, 132

**O**

OLEDs, 121, 128, 129, 135, 136  
 Optical recording, 135, 139–141  
 Optoelectronic, 117, 118, 121, 122

**P**

Pan, Z., 40  
 Pang, R., 32  
 Particle size, 45, 54, 60, 95, 96, 99  
 Paterson, A.S., 113  
 Persistent luminescence, 1, 2, 6, 7, 14–16, 21, 25–27, 32, 35, 36, 94, 101, 102, 106, 108, 110, 111, 113, 125, 134, 136, 143  
 Persistent luminescence nanoparticle, 15, 75  
 Persistent luminescent material, 1, 14, 87  
 Phosphor, 1–3, 5, 6, 12, 14–16, 21–76, 87, 90–98, 101–105, 113, 117, 123, 128–130, 133, 136, 141  
 Polymer-grafted phosphor, 76

**Q**

Qiu, G., 50  
 Quantum dots, 106, 113, 132

**R**

Rao, 131, 143  
 Rasheed, F., 15  
 Reaction assay, 113  
 Reflection spectrum, 90  
 Room-temperature phosphorescence, 117, 122–124

**S**

Sensitizer, 3, 4, 40, 44  
 Sensor, 121, 134, 141–143  
 Silicate phosphor, 28  
 Sol-gel method, 53–55, 106, 108  
 Spin-orbit coupling, 9, 125, 126, 128, 133, 134, 141  
 $\text{Sr}_2\text{MgSi}_2\text{O}_7$ , 12, 14, 28, 29, 35, 64, 91, 101, 102, 108, 113  
 $\text{Sr}_3\text{Al}_2\text{O}_6$ , 27, 53, 57, 58, 66, 70  
 $\text{Sr}_4\text{Al}_{14}\text{O}_{25}$ , 12, 14, 23, 24, 27, 63, 64, 68, 69

**T**

Takasaki, H., 24  
 Targeted tumor imaging, 74, 108  
 Term symbol, 9, 10, 12

Thermally activated delayed fluorescence  
(TADF), 120–122, 134, 135  
Thermoluminescence, 3, 62, 69, 87, 90–92  
Time-resolved luminescence, 93, 143  
Trap, 6, 14–17, 28, 45, 64, 67–69, 90–92, 124,  
126, 133  
Trap depth, 45, 64, 67, 69, 90, 92  
Triplet exciton, 121–126, 132, 133, 135, 136

**V**

Van den Eeckhout, K., 32

**W**

Wang, X.-J., 42  
White-emitting phosphor, 61

**X**

X-ray powder diffraction, 97, 98

**Z**

Zhao, 132  
Zinc gallogermanate phosphor, 48